ASPECTS OF ATMOSPHERIC TRANSPORT AND DISPERSION WITHIN AN AIR BASIN

Thesis by
Robin Scott Horrell

In Partial Fulfillment of the Requirements
for the Degree of
Doctor of Philosophy

California Institute of Technology
Pasadena, California

1991
(Submitted January 10, 1991)

This thesis is dedicated

to

my parents and
Andrea, my lovely wife

Acknowledgements

It is impossible to thank everyone for every contribution which has ultimately been manifested in the final dissertation. To this end, I would first like to thank everyone from whom I received help and suggestions and which I might have inadvertently omitted in the following acknowledgements.

I would like to thank the Air Quality Management District for access to equipment, and extensive access to personnel. For access to their computer systems and telemetry system I would like to thank Ron Sweet and Chris Marlia. The help of the meteorologists Bruce Selik and Jerry Arnold especially during the South Coast Air Quality Study of 1987 was highly appreciated. Within the planning division I would especially like to thank Chung Liu, Henry Hogo, and Tom Chico for their helpful suggestions and assistance during my research. I wish to give special thanks to Julia Lester, also of the planning division, for her suggestions, corrections, and constructive criticisms of many sections of this thesis.

I owe a special thank you to Joe Cassmassi, the AQMD's Senior Meteorologist. His suggestions in the development of the WIND simulation package were numerous and constructive. On a personal level I would also like to acknowledge Joe for his genuine interest in my professional development. I admire his ability to integrate people and in my case, in doing so, make me strive to bring out my best. Interaction with Joe will have a lasting influence on my measure of what excellence is in the work place.

The California Air Resources Board (CARB) has supported a large fraction of this research. Within the CARB I would like to thank Bart Croes, Lowel Ashbaugh and especially Chuck Bennett for favors too numerous to list. I would also like to thank Don Lehrman of Technical and Business Systems for supplying me with preliminary upper air data from the SCAQS.

At Caltech I owe special thanks to Mike Deem who has been both an assis-

tant, friend, and inspiration. His conceptualization of the WIND program from my original coarse formulation is exceptional. Peter Wyckoff and Scott Halliday also at Caltech have contributed significantly to the development and coding of many of my computer programs. I would like to thank four people whose friendship made my time at Caltech more enjoyable, Chris Guske, Greg Sullivan, Ron Benson and Mike Loewenberg.

A special thanks is due to my wife, Andrea, who made suggestions, corrections, and overall endured me at times when I could hardly endure myself. Her efforts and tolerance will long be remembered and appreciated.

Finally, I would like to thank my advisor Dr. Fred Shair who has patiently taught me a great deal about science and engineering. Without his help and guidance, none of this would have been possible. I would like to extend that thanks to him for his generosity with his time and his willingness to allow me to explore subjects which did not directly contribute to this thesis but greatly contributed to my education.

Thank you.

Abstract

Atmospheric transport and dispersion and their relationship to observed pollution levels are analyzed using three methods. Two traditional methods, (1) dimensional analysis and (2) atmospheric sulfur hexafluoride tracer experiments are applied to new problems; the third, (3) neural computation is a new method of looking at incomplete ozone data reconstruction, and short term ozone forecasting.

A comprehensive dimensional analysis of buoyantly driven slope wind is presented to unify the subject. The functional relationship between thickness, velocity, Reynolds, Froude, Rossby and Richardson numbers of the buoyant layer and the characteristic slope parameters is established. A detailed study of the velocity and temperature profiles is done using the Von Karman-Pohlhausen (KP) integral technique. Generated profiles are in agreement with field measurements. The technique is extended to handle transient slope flows using a combination of the KP method and the method of characteristics.

The transport and dispersion of airborn emissions from Los Angeles are studied using tracer during the Southern California Air Quality Study of 1987. Emphasis is placed on emissions generated during the morning land breeze/sea breeze transition periods. Analysis of tracer transport patterns indicates emission transport from downtown Los Angeles was by two routes, and the relative importance of each route was determined by a diurnally occurring divergence zone. This zone, resulting from geography and pressure gradients, was shown to migrate east to west in the air space above Los Angeles. The zone routes a majority of morning emissions northwest of Los Angeles, contrary to the commonly held belief that morning emissions were routed east. Results were verified using surface wind trajectories constructed from telemetry data.

Artificial neural computing strategies are applied to two air quality data sets for the purpose of ozone data reconstruction and forecasting at Newhall, California. The Madaline III algorithm is used to reconstruct data at a single site. The

reconstruction is done to add missing data. This method is advantageous when peaks in the data are missing, and traditional interpolation methods inapplicable. Williams and Zipser's recurrent algorithm is used to make short-term ozone forecasts at a single location based on past history of ozone observations at that site. The results are systematically better than regression methods.

Table of Contents

List of Figures

Chapter One

Section 1.1

Section 1.2

Section 1.6

Section 1.7

Section 1.8

Section 1.9

List of Tables

Chapter One

Section 1.6

Section 1.9

A1.9 Appendix

Chapter Two

Section 2.1

Section 2.2

Section 2.3

Section 2.4

Introduction

This thesis is divided into three chapters, and each chapter is divided into sections. The tables and figures of each section are numbered independently. Each equation is numbered by chapter, section, then sequentially within the section, e.g., Equation 1.2.7 refers to Chapter One, Section 2, Equation 7. The contents of the chapters are summarized as follows. Chapter One is a dimensional analysis of atmospheric slope wind including several applications of the resulting analysis. Chapter Two is a study of atmospheric transport and disperison near a two-dimensional divergence zone. Chapter Three is a discussion of the application of neuro-computing strategies to air quality modeling, and to processing air quality data.

The Sections 1.1 and 1.2 of Chapter One introduce the subject of buoyantly driven slope wind. In Sections 1.3-1.5 a boundary layer analysis of this subject is performed. In Section 1.6 the characteristic and dimensionless parameters from the boundary layer analysis are summarized and compared to worldwide observations. In Sections 1.7, the approximate boundary layer technique devised by von Karman and Pohlhausen is applied to the results of Sections 1.4 and 1.5 for steady state slope flows. Section 1.8 extends the analysis of Section 1.7 to include transient slope flows. Finally, in Section 1.9 ten sites in the Los Angeles Basin which exhibit slope flows are analyzed using the above framework. This analysis makes clear how the mesoscale slope flows associated with the mountains surrounding a basin can be transporting natural and anthropogenic emissions both into and out of the basin by upslope and downslope winds.

While reading Chapter One keep in mind a few conventions used throughout the text. One, slope winds are often difficult to observe during the day because they are obscured by other stronger winds, e.g., a sea breeze. Thus, when observations of slope winds are discussed, they are in general downslope wind and may be referred to only as *slope wind.* Two, a general word *katabatic* exists, meaning of a nighttime wind which gravitates downslope due to a density differ-

ence between surface and ambient air. Katabatic is used interchangeably with downslope as a desciptor. Three, the terminology *slope wind* and *slope flow* are also synonymous.

Chapter Two addresses the general problem how to assess the atmospheric transport and dispersion within an air basin in which the multiple inlets and outlets create convergence and divergence zones. The Los Angeles-Glendale divergence zone of Los Angeles Basin is studied by atmospheric tracer experiments and the use of surface winds. In this case the incoming westerly and southerly sea breeze is divided by the divergence zone in the vicinity of downtown Los Angeles. The emissions put into the breeze prior to the branch point of the divergence zone are split and routed through the basin through two seperate and distant exits. Chapter Two Section 2.1 describes four sulfur hexafluride tracer studies done in the proximity of the branch point as part of the Southern California Air Quality Study (SCAQS) of 1987. A part of Section 2.1 is devoted to performing mass balances on the tracer, and Section 2.2 is a detailed description of the measurements of the vertical atmospheric structure required to close the mass balances. Section 2.3 places the observations made in the two summer sulfur hexafluoride studies into the context of the air flow patterns from an entire summer season. Finally, Section 2.4 describes a new, alternative method for examining the air flow dynamics at a single site, by comparing the dynamics at that site to a well chosen reference. This method is applied to the wind fields near downtown Los Angeles on the two summertime tracer days, and to summer season averages from all of the South Coast Air Quality Managements Districts Air Monitoring sites.

An inplicit theme of Chapter Two is visual and interactive automation of meteorological and air quality data processing. Each section of the analysis is assisted by WIND, a PC-based collection of interactive programs to process meteorological (MET) and air quality (AQ) data, written to accomplish the analyses in Chapter Two. The philosopy that guided the entire development of

WIND was the ability for the end user of the MET and AQ data to be able to (1) view the data graphically in nearly real time, (2) view MET and AQ data simultaneously, (3) interactively perform a large number of tasks which are desirable to repeat, such as simulating air parcel trajectories, conducting mass balances, and determining fluxes at any location. In addition, the philosophy was adopted that the program should be capable of being used in any geographic location where data was available, and be written in well structured C code so as to be portable to other computer environments if at some later time this became desirable. WIND programs are briefly discussed in each section where they are used, and are documented by a seperate user's guide, currently version 2.0, and the seperate technical guide of C language source code.

Chapter Three begins with a motivation for examining neuro-computing strategies as they relate to the study of air quality (Section 3.1). Section 3.2 is a summary of how neuro-computers of a particular sort perform their calculation, and are trained. Section 3.3 demonstrates the use of a feedforward network to reconstruct incomplete ozone data and 3.4 demonstrates the use of a recurrent network to do ozone forecasting.

Chapter One

A Boundary Layer Analysis of Buoyantly Driven Slope Flow

Table of Nomenclature

C_p	Heat capacity
g	Gravitational constant, 9.8 ms^{-1}
k	von Karman constant, 0.4
K, K_T	Turbulent transfer coefficients
l	Critical length, either l_c or l_{Co}
L	Characteristic length in the flow direction
n	Dimensional direction normal to the slope
p, p_c	Pressure, characteristic pressure
s	Dimensional direction along the slope
t	Time
t_c	Characteristic time
$\bar{t}$	Dimensionless time
T	Denotes thermal boundary layer or turbulent, as in eddy viscosity, ν_T
u	Dimensional velocity in the s direction
U	Dimensionless velocity in the slope direction
$U^\star$	Characteristic velocity, b.l. analysis
$\ddot{U}$	Dimensionless ratio of $\frac{U_\infty}{U^\star}$
$\mathbf{v}$	Vector velocity
v	Dimensional velocity in the y direction
V	Dimensionless cross slope velocity
w	Dimensional velocity in the n direction
W	Dimensionless velocity normal to the slope
x	Dimensional distance non-rotated frame
y	Dimensional distance in the width dimension
z	Dimensional dist. in vertical non-rotated frame

α	Thermal difussivity
β	Coefficient of expansivity, ideal gas $\beta = \frac{1}{T}$
δ	Boundary layer thickness, as a function of χ
f	Coriolis parameter
Δ	Boundary layer vertical characteristic length
Γ	Adiabatic lapse rate
λ	Dimensionless number, effect of lapse rate
Θ	Dimensionless temperature
μ	Viscosity
ν	Kinematic viscosity
ξ	Dimensionless distance along y direction
Ω	Earth's rotation rate
ψ	Latitudinal angle off the equator
ρ	Density
ϕ	Slope angle
τ	Shear stress, both molecular and Reynolds stresses
χ	Dimensionless direction in the slope direction
ζ	Dimensionless direction normal to the slope
∞	Denotes ambient atmospheric conditions
Fr	Froude number
Gr	Grashof number
Pr	Prandtl number
Re	Reynolds number
Ri	Richardson number
Ro	Rossby number
Sc	Schmidt number

A Comprehensive Dimensional Analysis for Assessing the Transport Properties of Atmospheric Slope Flows

(Sections 1.1 - 1.6)

Abstract

A boundary layer analysis of buoyantly driven atmospheric slope flow is presented. From this analysis a complete set of scaling parameters and dimensional groups are obtained. Among the results from this analysis is a scaling parameter for the heretofore undefined thickness of the buoyant layer. Other simple relationships are derived from this result. These relationships include simple formulations for the characteristic velocity, the Reynolds number, the Rossby number, the Grashof number, and the bulk Richardson number, which can all be expressed in terms of the fundamental parameters of slope length, slope angle, ambient temperature, differential temperature, atmospheric lapse rate, and eddy diffusivity. The characteristic velocity, $U^{\star}$, is regressed against observations of maximum velocity and is found to follow the relationship $U_{Obs}^{Max} = 0.625U^{\star}$ with a correlation coefficient of 0.913. This suggests that the more complex formulations for maximum velocities in the literature may be unnecessary. In total, the analysis serves to unify the subject of slope flow and to guide investigators at a simple, but fundamental level.

1.1 Introduction

Slope wind is a ubiquitous feature of non-level terrain where a differential temperature between the ground and the ambient air produces a buoyant force that motivates air flow. See Figure 1. Observations show the buoyant force is often large enough in magnitude to oppose the synoptic pressure force and generate and sustain mesoscale air flows along the slope, bearing no similarity to those anticipated by examining synoptic data alone. Buoyantly-driven mesoscale wind, traverse to and cocurrent with the synoptic pressure gradients, can noticeably alter the vertical wind profile near the ground by creating a low level jet. See Figure 2.

Mesoscale slope winds are generally a recurrent, semi-predictable feature of a particular geographic region. Radiative ground cooling, ground heating by insolation, evaporative cooling and the rapid passage of a front, are the most common factors leading to the atmospheric conditions required for buoyantly-driven wind. A particular geographic region and its surroundings may be prone to one or more of the above factors. Consequently, meteorological forecasts that anticipate the occurance of such factors also preempt the likely observance of mesoscale buoyantly driven wind. The diurnal nature of these factors generally limits the observance of mesoscale slope wind to time scales less than a day, with few exceptions.

Mesoscale buoyantly driven flows are common above and surrounding uneven terrain. Therefore, any serious investigation and interpretation of atmospheric transport in a domain susceptible to the phenomena should not overlook their possible influences. In this respect, three general categories of influence exist for a given geographic region: (1) buoyancy plays little or no role compared to the synoptically driven winds, (2) buoyant effects explain certain anomalous

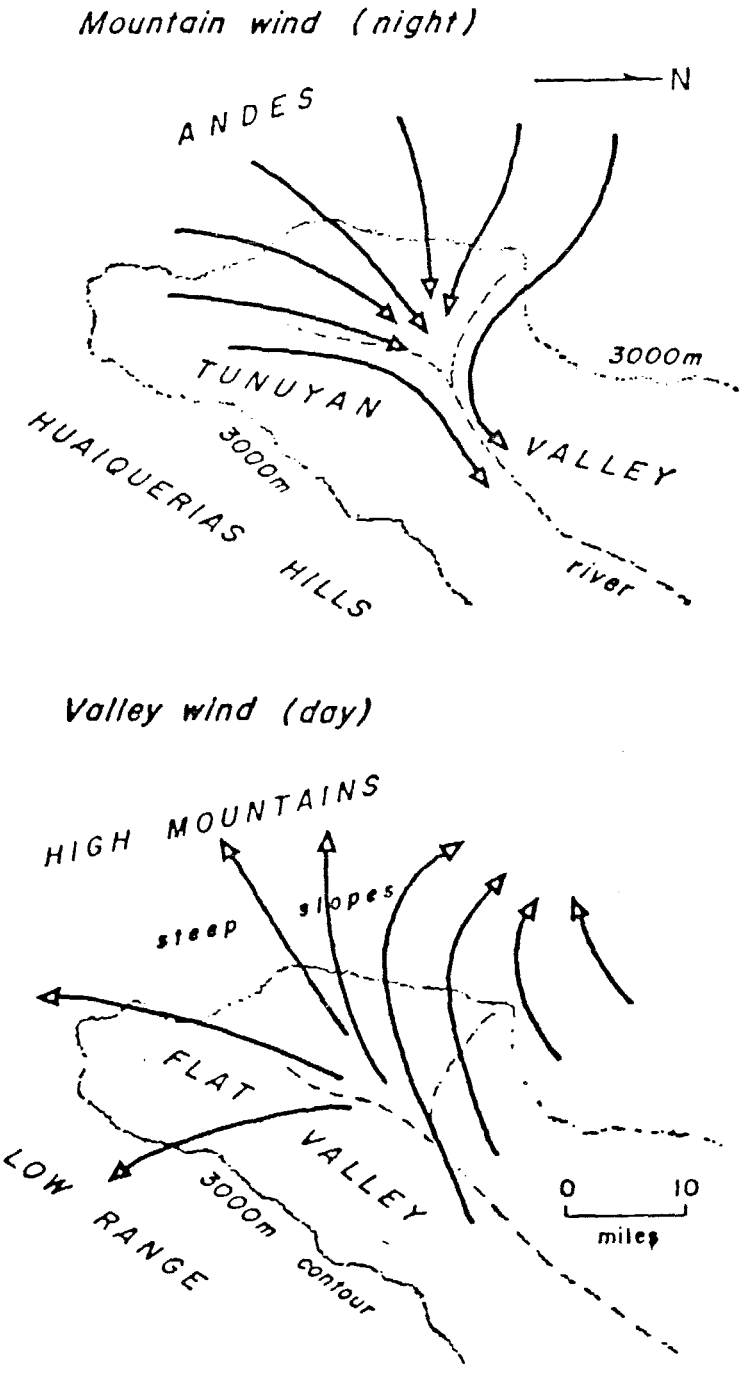

An excellent example of the complete reversal of air flow patterns with the change from day to night is found in the Tunuyan Valley, in the foothills of the Andes. Arrows show how the winds sweep down the cooled slopes into the valley at night but rush up the heated valley slopes during the day.

Figure 1. An example of the geography giving rise to slope flow. (Reproduced from "Watching for the Wind," Edinger, 1967).

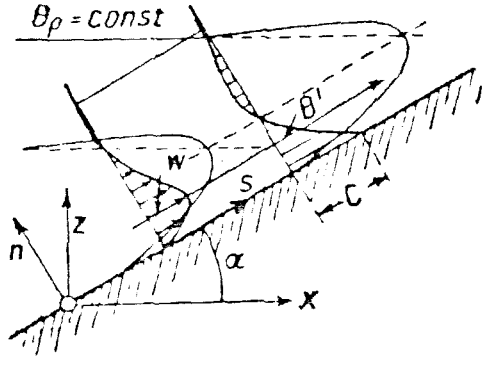

Fig. 5.57.—Wind at a slope

Figure 2. An example of the potential temperature and velocity profiles in a slope flow. (Reproduced from "Essentials of Fluid Dynamics," Prandtl, 1952).

but generally repeatable observations that occur rather unpredictably, and (3) buoyancy accounts for the principle mechanism of local transport. The third category of influence is generally predictable and is only influenced by the passage of very dominant weather systems or seasonal variations.

The work of previous investigators provides insight into the wide range of observations and the present analytical and computational methods used to examine buoyantly driven slope flows. The discussion will be limited to relatively flat geography, i.e., sloping terrain that does not channel or force convergence of the wind as it moves in the flow direction.

Observational Studies

The literature contains many observational studies of atmospheric phenomena dedicated to slope flow, and other studies indirectly present observations pertinent to the subject. Many locations throughout the globe provide persistent, seasonally semi-permanent examples of the slope flow phenomena. The conditions necessary to produce slope wind exist on a wide variety of length, slope and differential (ground to ambient air) temperature scales. The range of these scales is limited only by the physical dimensions and energy budget of the earth. On a continental scale, for instance, the 1000 km slopes with a 0.3 degree angle and small differential temperature of about 0.5 degrees C are responsible for observations made in Antarctica. These produce high velocities, reaching 45 ms^{-1} (around 90 mph), making them the most extreme observation of this phenomena on earth and an interesting subject for study (Ball 1956, 1957, Chiba et al. 1986, Gosink 1987). Other examples on a smaller scale are the slope winds observed on mountain slopes and broad mountain basins, where the slope angle is likely to be greater than those of the Antarctic, but the length of the slope is much shorter. Within the United States, studies have been done in the Rocky Mountains (Banta 1982), in Washington at Rattlesnake Mountain (Horst and Doran 1982-3) and near Mt. Rainier (Buettner and Thyer 1966). Studies in Mexico (Fitzjarrald 1984) and in Europe (Defant 1949) have also been done. One of the typically smaller (i.e., occurring over a shorter slope length) atmospheric downslope flows that has been studied is along the surface of glaciers or snow patches (Ohata and Higuchi, 1979), where the length along the slope may only be a few hundred meters. The phenomena is known as glacier wind, and can develop over such short lengths because of the sharp slope angle and the sustained cooling provided by evaporation and the existence of ice. Glacier winds are often observed during summer months because of the advection of warm air over the

surface of the glacier from the surroundings creates sharp temperature gradients normal to the slope.

Atmospheric slope flows can exist on even smaller length scales than those mentioned above, but the likelihood of observing them occurring naturally is small. There are two reasons: (1) any ambient wind or turbulence will obscure the effect, (2) and the velocity and thickness of the flow layer are small. The dimensional analysis done in a later section of this paper provides the tools required to perform a convincing analysis of the conditions under which slope flows are going to be observed. For practical reasons laboratory scale experiments are done with fluids other than air and often involve concentration gradients and crystalization rather than temperature gradients for example (Turner and Ellison 1959, and Huppert et al. 1986). This paper is limited to atmospheric conditions.

Computational Studies

The computational advances made over the past 15 years have made obtaining numerical results from the complete set of governing equations an appealing alternative to seeking analytical solutions. Because of the strongly coupled, nonlinear nature of the slope flow equations, analytical solutions may require restrictive assumptions. Several authors (Leslie and Smith 1974, Rao and Snodgrass 1981, and Arritt and Pielke 1987) have taken advantage of available computational capacity in investigating slope flows. In addition to the advantage of seeking solutions using the full governing equations, numerical solutions can incorporate boundary conditions that further confound any attempt to obtain a purely analytical solution to the same problem. For buoyantly driven flows, the vertical velocity and temperature field will most commonly be desired when ambient, synoptically driven or larger domain mesoscale winds are present. Analytical solutions are often simplified to avoid this necessary complexity. Computational techniques provide an avenue to investigate a broad class of conditions under which slope winds are observed.

Leslie and Smith begin with the general conservation of mass, momentum and energy equations, retaining only the terms pertaining to short mesoscale buoyancy driven flows where the Boussinesq approximation has been made. A stream function is introduced, and the resulting set of equations is integrated numerically. Turbulence is treated through a constant eddy diffusivity, K, equal to $4 \cdot 10^4\ cm^2 \cdot s^{-1}$. The particular two-dimensional geographic arrangement is a shallow flat sloping region trailing off into a horizontal region. The associated meteorology places a ceiling on the region of influence by the existence of a strong high level inversion. Simulated ground cooling provides the driving temperature gradient for a katabatic wind. The air is initially quiescent within the domain. The reported simulation results are consistent with general observations of buoy-

ancy driven winds, but are not quantitatively compared with observations.

Arritt and Pielke describe their simulation method in much the same way as Leslie and Smith. However, the intervening period of more than a decade has provided sufficiently faster computers which afford a more comprehensive description of turbulence. In this case a prognostic turbulent energy provides the parameterization on which the exchange coefficients (analogs of the eddy diffusivity mentioned above) are based. The geometry for which the simulation was verified is the geography of Rattlesnake Mountain. Unlike Leslie and Smith, the meteorology provides no high level inversion, only the low level inversion created by radiative cooling that provides the impetus for the nocturnal katabatic wind. A comparison of the vertical velocity and potential temperature obtained by the simulation to data reveals qualitative and reasonably good quantative results.

The effects of the ambient wind on the boundary layer thickness and vertical wind profile is a separate issue addressed by Arritt and Pielke using their simulation model.

Analytical Studies

Two general approaches have been used to obtain analytical solutions for buoyantly driven winds: (1) hydrolic methods and (2) conservation equation methods. The hydrolic method provides information on the bulk properties of the buoyant layer. In contrast, the conservation equation techniques provide detailed information about the velocity and temperature profiles inside the layer. The hydrolic techniques are generalizations of open channel hydrolics which have added the buoyant term to the governing equations Defant (1951) and Ball (1956). Hydrolic methods account for the acceleration of the buoyant layer by entrainment through the interface with the ambient air. Some hydrolic models have relied on the assumption of a constant buoyant layer thickness, an assumption shown in this paper to be invalid for most common observations of slope wind. Manins and Sawford (1979) use the hydrolic formulation to provide a one-dimensional model for slope flow. Extensions of this technique have been used to study slope wind in the presence of ambient wind Fitzjarrald (1984). Kondo and Sato (1988) have reformulated the hydrolic method by adding the paramerization of the interfacial stresses between the ground and ambient air. This method treats the buoyant layer as a parcel rather than a hydrolic channel. The hydrolic technique is perhaps limited most by its inability to provide detailed information about the flow and temperature profile within the jet. The first analytical approach to use the conservation equations to study slope wind was presented by Prandtl (1942). Prandtl solved one of the limiting cases of slope wind, which is seldom observed, but one of the few cases that lends itself to a simple solution. Unfortunately, his simple solution to the model equations is the basis for comparison of much of the subsequent analysis in the field. Later analyses by Rao and Snodgrass (1980), Gutman (1983), as well as the computational work mentioned earlier were also developed directly from the conservation equations. Because detailed informa-

tion about the flow is often desired, the conservation method has received more attention in recent times.

Motivation for the Present Analysis

The analysis presented by the previous authors has served to describe many features of slope wind. However, the subject of slope wind itself is rather disjoint, lacking a comprehensive unification of the observations, theoretical developments, and computational results presented by previous authors. As a consequence, persons wishing to make quick estimates of the impact of buoyant winds at a particular location have to perform relatively detailed calculations or computer simulations for the case they are examining. Unfortunately, the comparisons made by many of the authors of their findings and those of previous authors was done for cases not in the same physical regime; thus, misleading conclusions that have been expressed about slope winds in general which should have only been made for specific flow regimes. For example, Rao and Snodgrass state without explanation, "The Coriolis effects are negligible except for very small slope angles." The work of Mahrt (1982) attempts to tackle some of the problems by unifying the field, but falls short of this goal primarily because the work does not contain a comprehensive dimensional analysis. It only has scaling arguments. In particular, it side steps some of the fundamental issues of the dimensional analysis, such as determining the characteristic thickness for the buoyant air flow layer.

The comprehensive dimensional analysis done in this paper establishes the fundamental dimensionless groups necessary to perform a rapid preliminary analysis of slope wind. The potential impact of slope winds in a particular region can quickly be assesed based only on the fundamental characteristic parameters of slope length, slope angle, ambient temperature, atmospheric lapse rate, and surface to air temperature differential. Using these parameters, as indicated in this paper one can quickly establish such factors as (1) the characteristic depth of the buoyant layer, (2) the characteristic time frame required for flow to develop, (3)

the characterictic velocity, (4) the Reynolds number, (5) the importance of Coriolis forces through the Rossby number, (6) and the importance of entrainment through the bulk Richardson number. This boundary layer analysis provides a coherent picture of the interconnections between the model equations, computer simulations, and observations made under various conditions.

The ability to rapidly assess the impact of slope wind is important to the studies of other fields besides meteorology, e.g., air pollution and air quality. Individuals, in these and other fields, may wish to investigate the likelihood of slope wind occurring in a particular system without becoming an expert at the analytical and numerical methods for slope winds. The transport and dispersion resulting from slope winds in and surrounding populated areas is widespread, and the number of sites likely to be investigated for influence by buoyant wind effects is large. Finally, when more detailed studies are required, they should be undertaken with the appropriate equations for the particular regime of slope flow to be studied. The same holds true for observational field studies where *a priori* knowledge of the important parameters to measure will allow for the best characterization of the flow.

In the four sections that follow (1.2 - 1.5) an attempt is made to unify the subject of slope flow by performing a complete dimensional analysis. Sections 1.3 - 1.5 present the momentum, energy, and mass conservation equations. These equations are made dimensionless, noting which equations apply under which physical circumstances. Section 1.6 summarizes all of the dimensionless groups which were found.

1.2 Theory

Starting Equations

For momentum, the positionally averaged Navier-Stokes equation (1.2.1) which includes the effects of the earth's rotation and groups the Reynolds stresses into τ is the fundamental starting point for studying atmospheric buoyantly driven slope flow.

$$\rho \frac{D\mathbf{v}}{Dt} = -\nabla p - (\nabla \cdot \tau) + \rho g \; - \; 2\rho\Omega \times \mathbf{v} \tag{1.2.1}$$

The analogous equation for conservation of energy, balances the convective derivative of temperature with conduction and compressibility.

$$\rho C_p \frac{DT}{Dt} \; = \; -\nabla \cdot q \; - \; p(\nabla \cdot \mathbf{v}) \tag{1.2.2}$$

As stated earlier, the density equations that motivate the flow are a function of temperature, thus 1.2.1 and 1.2.2 are coupled. The incompressible continuity equation (1.2.3) applies (Pielke, 1984).

$$\nabla \cdot \mathbf{v} \; = \; 0 \tag{1.2.3}$$

As a result, 1.2.2 can be simplified to eliminate the effect of local compression on the temperature field.

The shear stress tensor, τ, is composed of viscous, s, and turbulent, σ, (or Reynolds stress) components as denoted by Equation 1.2.4.

$$\tau \; = \; s \; + \; \sigma \tag{1.2.4}$$

As is most commonly done when modeling atmospheric transport, viscous transfer of momentum is neglected ($s \approx 0$) compared to turbulent transfer (Lumley and Tennekes, 1972). For the purpose of this analysis, the mixing length theory is applied in order to obtain an analytical representation of the remaining

turbulent term. The shortcomings of this approach are recognized, but as will be demonstrated below, the results obtained using this formulation are qualitatively representative of the observations. The mixing length hypothesis provides a simple way of representing turbulence using a constant exchange coefficient, K, as is shown in Equation 1.2.5.

$$\tau = -K\nabla \mathbf{v} \tag{1.2.5}$$

By analogy, heat is transported according to the relationship given in Equation 1.2.6.

$$q = -K_T \nabla T \tag{1.2.6}$$

Equations 1.2.1 - 1.2.6 are a closed set of equations and provide the basis for studying buoyantly driven slope flow.

The Scaled Equations

As mentioned before, the absence of obvious characteristic parameters to use in scaling the governing equations may explain the lack of material in the literature on the appropriate way of approaching a dimensional analysis for slope flow. Two crucial areas lack obvious characteristic variables: lengths and velocities. While the slope length, L, provides a characteristic length along the slope, there is not a natural choice of a characteristic length vertical to, or when applicable, in the width dimension of the slope. The velocity has no natural choices in any of the three slope coordinates. With the characteristic length and velocity scales not explicitly available, one must attempt to construct them via other methods.

The work of previous authors provides insight into possible approaches to scaling the model equations. This includes the discusions presented by Prandtl, Mahrt, and the recent paper of Kondo and Sato, all mentioned previously. The

principal drawback of these presentations is that the full conservation equations were seldom the starting point for the analysis. In other words, terms in the model equations are disposed of or retained in an *ad hoc* fashion prior to actually doing a dimensional analysis. In Prandtl's presentation, terms appear to have been chosen partly on the basis of obtaining an easy analytical solution. Work since Prandtl has increasingly dealt with identifying which terms need to be retained to provide a realistic yet not analytically or computationally overburdening model for treating slope flow. Unfortunately, however, this decision process often preceeds doing any dimensional analysis. Consequently, the results are valid for the particular case that fits the starting equation, yet how this case fits into the bigger picture of slope flows in general is never made clear.

Many authors have treated slope flow in the way described above. The collective efforts which have been put forth, in a case by case way, provides some direction for doing a complete dimensional analysis. This previous work is put into context by this analysis.

In our method the characteristic scaling parameters are assumed to exist, and then obtained implicitly in terms of other known parameters through knowledge of the physical mechanisms of buoyantly driven slope flow. Having obtained the implicit characteristic scaling parameters in this way, it is then possible to completely specify dimensionless conservation equations for different regimes of buoyancy driven slope flow. This section, and the one following, serve to present the scaled equations and to define the characteristic constants, along with the pertinent dimensionless groups which arise.

Boundary Layer Analysis

The analyses presented below are derived in detail to elucidate the origin of the dimensionless groups and implicitly defined scaling parameters. The equations developed in Sections 1.3 - 1.5 build successively upon one another. In Section 1.3 the continuity equation (1.3.1) is scaled to show which forms are appropriate for long and short distances along the slope. In Section 1.4 the energy equation (1.4.1) is scaled and serves to implicitly define the vertical scaling thickness, Δ, for two regimes of the dimensionless number λ. In Section 1.5 the momentum equation (1.5.1) is non-dimensionalized. The complete set of dimensionless equations are developed for buoyantly driven slope flow in these sections.

1.3 Making the Continuity Equation Dimensionless

The continuity equation in the slope coordinates is made dimensionless first. Only one of the 6 characteristic parameters to do the scaling is known *a priori*, this is, L, the slope length. The unknown characteristic parameters are named, and subsequently defined in terms of the other parameters as physical constraints on the equations are enforced. When these parameters become known by correctly scaling the other conservation equations, they are then inserted into the definitions, and completely specifing the characteristic variables. The slope coordinate system is defined in Figure 1. The dimensional form of the equation is written out below.

$$\frac{\partial u}{\partial s} + \frac{\partial v}{\partial y} + \frac{\partial w}{\partial n} = 0 \qquad (1.3.1)$$

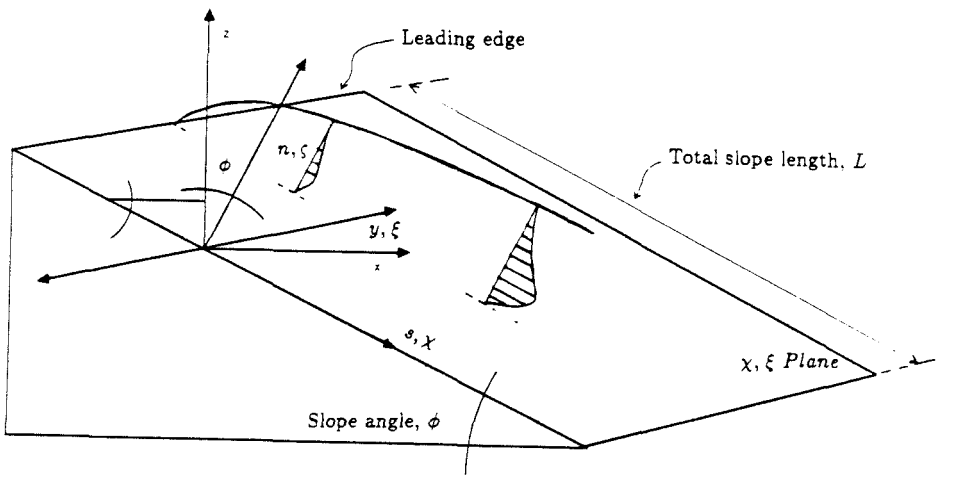

Figure 1. Slope coordinates relative to the rectangular coordinates of level ground.

The first step is to introduce the following, dimensionless variables:

$$\begin{aligned} U &= \frac{u}{U^*} \\ \chi &= \frac{s}{L} \\ V &= \frac{v}{V^*} \\ \xi &= \frac{y}{L_y} \\ W &= \frac{w}{W^*} \\ \varsigma &= \frac{n}{\Delta} \end{aligned} \qquad (1.3.2 - 1.3.7)$$

Equation 1.3.1 is then rewritten in terms of the above, and divided through by $\frac{U^*}{L}$.

$$\frac{\partial U}{\partial \chi} + \frac{V^* L}{U^* L_y}\frac{\partial V}{\partial \xi} + \frac{W^* L}{U^* \Delta}\frac{\partial V}{\partial \varsigma} = 0 \qquad (1.3.8)$$

At this point, a little reasoning provides an assumption that saves a lot of trouble later and will be proven a little later in the discussion. Recall that at the leading edge of the boundary layer, the slope is uniform in the width dimension (by the original formulation of the problem), hence any fluid that is entrained into the boundary layer must be drawn downward from the air above the layer. Consequently, at the boundary layer's leading edge,

$$\frac{W^*}{\Delta} \gg \frac{V^*}{L_y} \qquad (1.3.9)$$

and the appropriate form of the dimensionless continuity equation in this regime is

$$\frac{\partial U}{\partial \chi} + \frac{\partial W}{\partial \varsigma} = 0. \qquad (1.3.10)$$

The necessity that the remaining two terms balance forces the coefficient, $\frac{W^* L}{U^* L_y}$, to be equal to unity. This defines

$$W^* = \frac{\Delta}{L} U^* \qquad (1.3.11)$$

in terms of the as yet undefined characteristic slope velocity and vertical scale length. The converse argument is possible when one looks at a slope flow that spans a long distance (long will be defined shortly). In this case,

$$\frac{W^*}{\Delta} \ll \frac{V^*}{L_y}, \tag{1.3.12}$$

the Coriolis forces, which would be hardly detectable over a short distance, have begun to bend the flow away from being colinear with the slope. Thus, over this distance the applicable continuity equation needs to be a balance of the gradients of the surface winds. In short this leads to the analogous relationships and equations to those presented above.

$$\frac{\partial U}{\partial \chi} + \frac{\partial V}{\partial \xi} = 0 \tag{1.3.13}$$

$$V^* = \frac{L_y}{L} U^* \tag{1.3.14}$$

For completeness it is also important to mention that when

$$\frac{W^*}{\Delta} = \frac{V^*}{L_y} \tag{1.3.15}$$

the full continuity equation,

$$\frac{\partial U}{\partial \chi} + \frac{\partial V}{\partial \xi} + \frac{\partial W}{\partial \varsigma} = 0 \tag{1.3.16}$$

must be applied. In this case both 1.3.11 and 1.3.14 define the implicit characteristic velocities.

1.4 Making the Energy Equation Dimensionless

For buoyantly driven slope flows the energy equation represents a balance of slopewise advection with vertical transport of energy via turbulent diffusion. Though over long distances energy tranport may be affected by the bending of the flow field due to Coriolis forces, the energy equation is primarily two-dimensional for the geometry being considered (a flat sloping surface with a near uniform surface temperature). It will be treated as such for all the model equations developed in this document. With this in mind

$$\rho C_p \frac{DT}{Dt} = -\nabla \cdot q - p(\nabla \cdot \mathbf{v}) \tag{1.4.1}$$

is combined with

$$q = -K_T \nabla T \tag{1.4.2}$$

and is written out in detail, eliminating the compressive term because of continuity, and keeping only the terms in the slope, s, and slope normal, n, directions as discussed above.

$$\rho C_p \left(\frac{\partial T}{\partial t} + u\frac{\partial T}{\partial s} + v\frac{\partial T}{\partial n}\right) = K\left(\frac{\partial^2 T}{\partial s^2} + \frac{\partial^2 T}{\partial n^2}\right) \tag{1.4.3}$$

The relationship between the true temperature and the potential temperature is used, and the tranposition to the coordinates of the slope is made using Equations 1.4.4 - 1.4.6 below.

$$\frac{dT}{dz} = \frac{d\theta}{dz} - \Gamma \tag{1.4.4}$$

$$z = \chi \sin\phi \tag{1.4.5 and 1.4.6}$$

$$z = \varsigma \cos\phi$$

Additional dimensionless variables are introduced for the time and potential temperature.

$$\bar{t} = \frac{t}{t^*} \tag{1.4.7}$$

$$\Theta = \frac{\theta - \theta_\infty}{\theta_0 - \theta_\infty} \tag{1.4.8}$$

The dimensionless potential temperature, Θ, is defined in terms of the slope's surface potential temperature, θ_0, and the upper air reference temperature, θ_∞. Equation 1.4.3 is made dimensionless using the above, and those terms already defined in Equations 1.3.2 - 1.3.7, yielding,

$$\frac{1}{t^\star}\frac{\partial\Theta}{\partial\bar{t}} + \frac{U^\star}{L}U\frac{\partial\Theta}{\partial\chi} + \frac{\Gamma\sin\phi U^\star}{\theta_0-\theta_\infty}U + \frac{U^\star}{L}V\frac{\partial\Theta}{\partial\varsigma} - \frac{\Gamma\cos\phi U^\star}{\theta_0-\theta_\infty}\frac{\Delta}{L}V$$

$$= \frac{\alpha_T}{L^2}\frac{\partial^2\Theta}{\partial\chi^2} + \frac{\alpha_T}{\Delta^2}\frac{\partial^2\Theta}{\partial\varsigma^2}. \tag{1.4.9}$$

It is then rearranged, and terms of order $\frac{\Delta}{L}$ and smaller are lumped together as $O(\frac{\Delta}{L})$ terms.

$$\frac{L}{U^\star}\frac{1}{t^\star}\frac{\partial\Theta}{\partial\bar{t}} + U\frac{\partial\Theta}{\partial\chi} + V\frac{\partial\Theta}{\partial\varsigma} + \frac{\Gamma\sin\phi L}{\theta_0-\theta_\infty}U = \frac{\alpha_T L}{\Delta^2 U^\star}\frac{\partial^2\Theta}{\partial\varsigma^2}$$

$$+ O(\frac{\Delta}{L}) \text{ and smaller terms.} \tag{1.4.10}$$

Defining the dimensionless group, $\frac{\Gamma\sin\phi L}{\theta_0-\theta_\infty}$ as λ Equation 1.4.10 is rewritten.

$$\frac{L}{U^\star}\frac{1}{t^\star}\frac{\partial\Theta}{\partial\bar{t}} + U\frac{\partial\Theta}{\partial\chi} + V\frac{\partial\Theta}{\partial\varsigma} + \lambda U = \frac{\alpha_T L}{\Delta^2 U^\star}\frac{\partial^2\Theta}{\partial\varsigma^2}$$

$$+ O(\frac{\Delta}{L}) \text{ and smaller terms.} \tag{1.4.11}$$

When Equation 1.4.11 is written in this form it is apparent that the characteristic time for a slope flow to develop is $t^\star = \frac{L}{U^\star}$. Steady state is reached when $t^\star$ is small relative to the time frame of the flow duration, a condition that needs to be checked from case to case, but often holds for diurnal changes on the mesoscale.

At this point in the dimensional analysis a decision must be made as to which terms balance in order to define the different regimes under which various

forms of the dimensionless equation can be applied. For the slopeflow energy equation, there are two regimes which arise. To see how the two regimes arise, consider Equation 1.4.11.

The turbulent diffusion of energy to or from the ground's surface is an essential feature of the physical process, hence the first term right of the equality in 1.4.11 which embodies this effect is always retained. Excluding the unsteady term, the remaining terms that are left to balance the diffusive term are either of order 1 (the advective terms) or of order λ (the effect of transport through a stratified atmosphere). One can observe that λ scales with increasing length, L along the slope. Consequently, λ ranges from 0 at the slopes leading edge to some finite value depending on the length of the slope. For $\lambda < 1$ the advective terms balance the diffusive term. As a consequence, the cofficient of the diffusive terms must equal unity.

$$\frac{\alpha_T L}{U^\star \Delta^2} = 1 \tag{1.4.12}$$

From this the vertical scaling parameter, Δ, is implicitly defined.

$$\Delta = \left[\frac{\alpha_T L}{U^\star}\right]^{\frac{1}{2}} = L\left[\frac{\alpha_T}{\nu_T}\right]^{\frac{1}{2}}\left[\frac{\nu_T}{LU^\star}\right]^{\frac{1}{2}} = LPr^{-\frac{1}{2}}Re^{-\frac{1}{2}} \tag{1.4.13}$$

This leads to Equation 1.4.14, which is valid for $\lambda \leq 1$; this occurs at the leading edge of all buoyantly driven slopeflows.

$$\frac{\partial \Theta}{\partial \bar{t}} + U\frac{\partial \Theta}{\partial \chi} + \lambda U + V\frac{\partial \Theta}{\partial \varsigma} - \lambda\frac{\Delta}{L}\cot\phi V = \frac{\partial^2 \Theta}{\partial \varsigma^2}$$

$$+ O(\frac{\Delta}{L}) \text{ and smaller terms.} \tag{1.4.14}$$

When $\lambda \geq 1$ the diffusive term must be of order λ.

$$\frac{\alpha_T L}{U^\star \Delta^2} = \lambda \tag{1.4.15}$$

This results in the definition of the vertical scaling thickness for cases when $\lambda \geq 1$,

$$\Delta = Pr^{-\frac{1}{4}} \left[\frac{\alpha_T^2}{\Gamma(sin^2\phi)g\beta} \right]^{\frac{1}{4}} \tag{1.4.16}$$

and in the equation that is valid in this same regime.

$$\frac{1}{\lambda}\frac{\partial\Theta}{\partial\bar{t}} + \frac{1}{\lambda}U\frac{\partial\Theta}{\partial\chi} + U + \frac{1}{\lambda}V\frac{\partial\Theta}{\partial\varsigma} - \frac{\Delta}{L}\cot\phi V = \frac{\partial^2\Theta}{\partial\varsigma^2}$$

$$+ O(\frac{\Delta}{\mathrm{L}}) \text{ and smaller terms.} \tag{1.4.17}$$

Equations 1.4.14 and 1.4.17 provide a set of equations that can be applied to slope flows over a full range of slope lengths. Equation 1.4.14 is always applied at the leading edge of the boundary layer regardless of whether λ exceeds 1. Equation 1.4.17 becomes applicable at the point along the slope when λ computed at that point is unity. This is analogous to the critical length, l_c, used by Kondo and Sato.

1.5 Making the Momentum Equation Dimensionless

The momentum boundary layer is a direct consequence of an unstably stratified density gradient above the surface of the slope. Thus the density term that embodies this effect in the momentum conservation equation must be balanced by the appropriate advective, diffusive and Coriolis terms in order to model the flow field correctly. This section presents the dimensional analysis that allows the correct balancing of terms to be obtained without the *ad hoc* speculation that has plagued some previous authors on the subject. A hierarchy of regimes will be found when this analysis is complete. Over short distances where Coriolis forces can be neglected, i.e., the Rossby number is large, two regimes exist as a result of restrictions imposed by the energy equation. These regimes are defined as regions along the slope where $\lambda \leq 1$ and $\lambda \geq 1$. Over long distances where Coriolis forces are important i.e., the Rossby number is small $Ro \leq O(1)$, there exists a third regime. Generally, λ is likely to be of $O(1)$ or larger in this regime, so it is not deemed necessary to subdivide small Ro like what was done above for large Ro.

The conservation of momentum equation,

$$\rho \frac{D\mathbf{v}}{Dt} = -\nabla p - (\nabla \cdot \tau) + \rho g, \tag{1.5.1}$$

can be separated into its horizontal component equations and similarly scaled as was done to the conservation equations of Sections 1.3 and 1.4. The hydrostatic approximation is made in the direction normal to the slope. The results are Equations 1.5.2 and 1.5.3.

$$\frac{\partial u}{\partial t} + u\frac{\partial u}{\partial s} + v\frac{\partial u}{\partial y} + w\frac{\partial u}{\partial n} = \nu_T \left[\frac{\partial^2 u}{\partial s^2} + \frac{\partial^2 u}{\partial y^2} + \frac{\partial^2 u}{\partial n^2}\right] +$$

$$-\frac{1}{\rho}\frac{\partial p}{\partial s} + g\frac{T - T_\infty}{T_\infty}\sin\phi v + 2\omega \sin\psi v - 2\omega\cos\psi w \tag{1.5.2}$$

$$\frac{\partial v}{\partial t} + u\frac{\partial v}{\partial s} + v\frac{\partial v}{\partial y} + w\frac{\partial v}{\partial n} = \nu_T\left[\frac{\partial^2 v}{\partial s^2} + \frac{\partial^2 v}{\partial y^2} + \frac{\partial^2 v}{\partial n^2}\right] + -\frac{1}{\rho}\frac{\partial p}{\partial y} + g\frac{T - T_\infty}{T_\infty}\cos\phi v + 2\omega\sin\psi u \qquad (1.5.3)$$

In addition, the relationship between the pressure gradient and the boundary layer's external flow, u_e and v_e is described by the following two relationships assuming the flow is inviscid outside of the buoyant layer.

$$-\frac{1}{\rho}\frac{\partial p}{\partial s} = u_e\frac{\partial u_e}{\partial s} \qquad (1.5.4)$$

$$-\frac{1}{\rho}\frac{\partial p}{\partial y} = v_e\frac{\partial v_e}{\partial y} \qquad (1.5.5)$$

The two dimensionless momentum equations applicable to the front edge of the bondary layer for $\lambda \leq 1$ and for $\lambda \geq 1$ are determined first. Recall that at the leading edge of the boundary layer the flow field is arguably two-dimensional in the s and n coordinates. Combining Equation 1.5.2 with 1.5.4, restricting the equations to two dimensions, non-dimensionalizing using the characteristic variables appropriate to the front end of the boundary layer (1.3.1 - 1.3.6, 1.3.10) and, lumping all terms of order $\frac{\Delta}{L}$ into $O(\frac{\Delta}{L})$ gives Equation 1.5.6.

$$\frac{\partial U}{\partial \bar{t}} + U\frac{\partial U}{\partial \chi} + W\frac{\partial U}{\partial \xi} = \ddot{U}\frac{\partial \ddot{U}}{\partial \chi} + Pr\frac{\nu_T L}{U^*\Delta^2}\frac{\partial^2 U}{\partial \chi^2} + \frac{g(\sin\phi)\beta(\theta_0 - \theta_\infty)L}{U^{*2}}\Theta + O(\frac{\Delta}{L}) \qquad (1.5.6)$$

Additional information from the results of Section 1.4 can be used to simplify the coeffients of Equation 1.5.6. Ambient winds are now assumed to be quiescent. Notice that the coefficient of the diffusive term contains the dimensionless grouping 1.4.12 or 1.4.15, which is unity when $\lambda < 1$ and is λ when $\lambda \geq 1$. Also, since for turbulent flow the Prandtl number is approximately 1 the order of the diffusive coefficient depends only on λ. This results in Equations 1.5.7a ($\lambda \leq 1$) and 1.5.7b ($\lambda \geq 1$).

$$\frac{\partial U}{\partial \bar{t}} + U\frac{\partial U}{\partial \chi} + W\frac{\partial U}{\partial \xi} = Pr\frac{\partial^2 U}{\partial \chi^2} + \frac{g(\sin\phi)\beta(\theta_0 - \theta_\infty)L}{U^{*2}}\Theta + O(\frac{\Delta}{L}) \qquad (1.5.7a)$$

$$\frac{\partial U}{\partial \bar{t}} + U\frac{\partial U}{\partial \chi} + W\frac{\partial U}{\partial \xi} = Pr\lambda\frac{\partial^2 U}{\partial \chi^2} + \frac{g(\sin\phi)\beta(\theta_0 - \theta_\infty)L}{U^{\star 2}}\Theta + O(\frac{\Delta}{L}) \quad (1.5.7b)$$

The characteristic velocity colinear with the slope is determined directly from Equations 1.5.7a and b. Since the buoyant term, $(\frac{g(\sin\phi)\beta(\theta_0-\theta_\infty)L}{U^\star}\Theta)$, must be retained, it is balanced with the largest of the remaining terms. For Equation 1.5.7a, the largest remaining term has a lead coefficient of 1; consequently $\frac{g(\sin\phi)\beta(\theta_0-\theta_\infty)L}{U^{\star 2}}$ is equated to 1. Solving for $U^\star$ defines the characteristic velocity,

$$U^\star = [g(\sin\phi)\beta(\theta_0 - \theta_\infty)L]^{\frac{1}{2}} \quad (1.5.8)$$

Farther along the slope where λ exceeds 1, and 1.5.7b applies, the balance is between the buoyant force and the $O(\lambda)$ diffusive term. This leads to a modified definition of the characteristic velocity in this regime,

$$U^\star = Pr^{-\frac{1}{2}}\left[\frac{g(\sin\phi)\beta|\theta_0 - \theta_\infty|^2}{\Gamma}\right]^{\frac{1}{2}}. \quad (1.5.9)$$

1.5.8 and 1.5.9 specifies the characteristic velocity $U^\star$ in terms of the measureable physical parameters of the particular slope and potential temperature gradient being examined for the two regimes of λ. Finally, the most simplified forms for the momentum equation for the two regimes are given as follows.

$$\frac{\partial U}{\partial \bar{t}} + U\frac{\partial U}{\partial \chi} + W\frac{\partial U}{\partial \xi} = Pr\frac{\partial^2 U}{\partial \chi^2} + \Theta + O(\frac{\Delta}{L}) \quad (1.5.10a)$$

$$\frac{\partial U}{\partial \bar{t}} + U\frac{\partial U}{\partial \chi} + W\frac{\partial U}{\partial \xi} = Pr\lambda\frac{\partial^2 U}{\partial \chi^2} + \lambda\Theta + O(\frac{\Delta}{L}) \quad (1.5.10b)$$

When Coriolis Forces Predominate

When a slope flow extends over lengths scales on the order of hundreds of kilometers, as is the case in Antarctica, the effects of Coriolis forces are evident in the horizontal bending of the flow from the coordinate of the slope. This

bending is accounted for in the dimensional analysis of the momentum equation along the slope through its coupling with the momentum equation in the cross slope direction. The continuity equation, which is appropriate on these longer slopes, 1.3.13, provides the relationship between characteristic velocities in the horizontal plane that allows a dimensional analysis to be done. Proceeding in a fashion similar to that done in the first part of this section, the model equations appropriate over long distances in a buoyantly driven boundary layer flow are developed.

Starting with 1.5.2 and 1.5.3, the dimensionless forms of these equations appropriate for slope flow influenced by Coriolis forces can be derived. To isolate the Coriolis effect, synoptic pressure gradients are dropped from the model equations. Using Equations 1.3.14, 1.3.2 - 1.3.7, and 1.5.8 or 1.5.9, the momentum equations are non-dimensionalized, and the smaller terms in the vertical direction eliminated.

$$\frac{\partial U}{\partial \bar{t}} + U\frac{\partial U}{\partial \chi} + V\frac{\partial U}{\partial \xi} = \frac{1}{Re}\left[\frac{\partial^2 U}{\partial \chi^2} + \frac{L^2}{L_y^2}\frac{\partial^2 U}{\partial \xi^2}\right] + \Theta + \frac{fL_y}{U^\star}V. \quad (1.5.10)$$

$$\frac{\partial V}{\partial \bar{t}} + U\frac{\partial V}{\partial \chi} + V\frac{\partial V}{\partial \xi} = \frac{1}{Re}\left[\frac{\partial^2 V}{\partial \chi^2} + \frac{L^2}{L_y^2}\frac{\partial^2 V}{\partial \xi^2}\right] - \frac{fL}{V^\star}U. \quad (1.5.11)$$

The only source of motion in Equation 1.5.11 arises from the Coriolis force, thus the advective terms must balance it. Consequently, using 1.5.13,

$$\frac{fL}{V^\star} = \frac{fL}{U^\star}\frac{L}{L_y} = \frac{1}{Ro}\frac{L}{L_y} = 1. \quad (1.5.12)$$

Solving for the characteristic length, L_y, in the cross slope direction, ξ, gives

$$L_y = \frac{L}{Ro}. \quad (1.5.13)$$

Using 1.5.13, and the knowledge that the Reynolds number, Re, is very large compared to 1 further reduces Equations 1.5.10 and 1.5.11 to those given below.

$$\frac{\partial U}{\partial \bar{t}} + U\frac{\partial U}{\partial \chi} + V\frac{\partial U}{\partial \xi} = \Theta + V. \quad (1.5.14)$$

$$\frac{\partial V}{\partial \bar{t}} + U\frac{\partial V}{\partial \chi} + V\frac{\partial V}{\partial \xi} = -U. \tag{1.5.15}$$

With this step completed the entire specification of all the pertinent dimensionless groups is done.

1.6 Characteristic and Dimensionless Slope Flow Parameters

The boundary layer analysis discussed above in Sections 1.3 - 1.5 gives rise to a set of dimensional scaling parameters and dimensionless groups. These can be used for assessing the impact of bouyantly driven flow in a particular geograpical area, from estimates or measurements of only a few important parameters: slope length, slope angle, ambient potential temperature, potential temperature difference, atmospheric lapse rate, and an atmospheric diffusivity. The parameters are denoted respectively as (L, ϕ, θ, $\acute{\theta}$, Γ, *and* K). The dimensionless groups and scaling parameters are also useful in designing field studies and assessing the realism of laboratory scale experiments.

The characteristic, or scaling, parameters that arise from the analysis are discussed first. An attempt is made to introduce the implicit parameters in a logical, sequential order.

The energy equation serves to specify implicitly the characteristic boundary layer thickness, Δ, depending on the importance of other terms in the energy equation. As the buoyant wind drives the air to a different altitude, compressional heating or cooling can and will take place. The extent to which this will affect the buoyant flow depends completely on the air surrounding the jet, and the speed at which the jet rushes through the surrounding air. The dimensional analysis provides the dimensionless group, λ, which assesses the importance of the elevation change on the conservation of energy equation. The magnitude of λ determines which of the terms will be balanced.

$$\lambda = \frac{\Gamma \sin\phi L}{\Theta_0 - \Theta_\infty} = \frac{L}{l_c} \tag{1.6.1}$$

The critical length, l_c, is then defined explicitly.

Two definitions for the characteristic vertical length, Δ, exist. First when $\lambda \leq 1$, Equation 1.4.13 (in Section 1.4), the balance between advective and

diffusive mechanisms for energy transport yields,

$$\Delta \;=\; LPr^{-\frac{1}{2}}Re^{-\frac{1}{2}} \;\sim\; L^{\frac{1}{4}} \qquad (1.6.2a)$$

where the Reynolds, Re, and Prandtl, Pr, numbers are defined in terms of the groups below. Since the Reynolds number scales as $L^{\frac{3}{2}}$ (when $\lambda \leq 1$,) for buoyantly driven flows (see 1.6.7 below), one can quickly obtain the result that the characteristic boundary layer thickness, Δ, for the case $\lambda < 1$, grows as $L^{\frac{1}{4}}$. The second case is when $\lambda \geq 1$, and the balance between advective and diffusive mechanisms is replaced by a balance between the $O(\lambda)$ term and the largest diffusive term, Equation 1.4.15 (in Section 1.4). This leads to the definition of the characteristic thickness as

$$\Delta \;=\; Pr^{-\frac{1}{4}}\left[\frac{\alpha_T^2}{\Gamma(sin^2\phi)g\beta}\right]^{\frac{1}{4}} \sim L^0. \qquad (1.6.2b)$$

The L^0 dependancy of Δ indicates the effect of compressional heating or decompressional cooling eventually prevents the boundary layer thickness from growing along the slope. Note that this is the exact result obtained by Prandtl.

From the χ direction momentum equation comes the characteristic velocities for $\lambda \leq 1$ (1.6.2a) and for $\lambda \geq 1$ (1.6.2b),

$$U^\star \;=\; Pr^{-\frac{1}{2}}\left[g(\sin\phi)\beta|\theta_0-\theta_\infty|L\right]^{\frac{1}{2}} \sim L^{\frac{1}{2}}, \qquad (1.6.3a)$$

$$U^\star \;=\; Pr^{-\frac{1}{2}}\left[\frac{g\beta|\theta_0-\theta_\infty|^2}{\Gamma}\right]^{\frac{1}{2}} \sim L^0, \qquad (1.6.3b)$$

as a consequence of balancing the order 1, $O(1)$, advective and diffusive transport terms or the $O(\lambda)$ diffusive term with the buoyant term. Previous authors (Mahrt, Sato and Kondo) have recognized Equation 1.6.3a as being important to the study of buoyantly driven flows, but Equation 1.6.3b has not previously been identified with buoyantly driven flows. Equation 1.6.3b is suggested in the

original work of Prandtl, who notes that the speed becomes independent of slope length and length for these conditions. (Hereafter $\acute{\theta}$ will refer to the quantity $|\theta_0 - \theta_\infty|$.) The characteristic velocity normal to the slope, where $\lambda \leq 1$, comes directly from the continuity equation and can be written in terms of the above definitions.

$$W^\star = \frac{\Delta}{L} U^\star = Pr^{-\frac{1}{2}} Re^{-\frac{1}{2}} U^\star \tag{1.6.4}$$

When λ is bigger than 1 the velocity normal to the slope vanishes, because there is no entrainment.

To verify the correctness of $U^\star$ as the characteristic velocity, a comparison of $U^\star$ (using Equation 1.6.3a only) versus the observed maximum velocity, U_{Obs}^{Max}, is presented in Figure 1 for a number of observations (see Tables 1 and 2). The data is fit with a line obtained by linear regression,

$$U_{Obs}^{Max} = 0.625 U^\star, \tag{1.6.5}$$

having the regression coefficient (Pearson r value) of 0.81. The regression is forced through the origin. Though this value of r is certainly indicative of a linear fit between U_{Obs}^{Max} and $U^\star$, a better correlation might be obtained were more comprehensive data available. For instance, when vertical wind profiles are measured, the incremental vertical measurement heights are not guaranteed to capture the true maximum velocity. In addition, several of the papers from which the data were obtained did not provide comprehensive information on θ, $\Delta\theta$, ϕ, and L from which to compute $U^\star$. In such cases estimates were made for the variables based on other information supplied, such as topographical maps, and the likely climate and ground conditions of the area where measurements were made. (Table 2 from Sato and Kondo supplied information on several locations in Japan, and additional information from Antarctica.) Hopefully, authors of the results from future investigations will adopt the convention of comprehensively reporting

Site no.	Site name	Location	Author
1	Scholl Canyon	USA	Shair
2	Mt. Tsurugi	Japan	[Ohata and Higuchi]
3	Rattlesnake Mountain, 7/1980	USA, Washington	Horst and Doran
4	Rattlesnake Mountain, 7/1981	USA, Washington	Horst and Doran
5	Hakatajima	Japan	[Imaoka]
6	Cobb Mountain	USA	[Dickerson and Gudiksen]
7	Glacier de St. Sorlin	France	[Martin]
8	South Park	USA, Colorado	Banta and Cotton
9	Glacier San Rafael	Chile	[Ohata et al.]
10	Mizuho Station	Antarctica	[Adachi and Kawaguchi]
11	Mizuho Station	Antarctica	Chiba and Kobayashi
12	Syowa Station	Antarctica	[Adachi]
13	Adelie Land	Antarctica	Gosink

Table 1. Locations, sites, and authors.

[ ] indicate data obtained directly from Kondo and Sato, Table 2.

Site no.	L (m)	ϕ (degrees)	$\acute{\theta}$ (K)	θ (K)	$U^{\star}$ (ms^{-1})	U_{Obs}^{Max} (ms^{-1})
1	225	22	0.25	290	0.86	1.0
2	250	9	4.0-6.4	270	2.3-3.0	1.4-2.2
3	422	21	3.9	299	4.4	2.3
4	422	21	2.4	300	3.4	2.1
5	690	12.3	2.0	270	3.3	2.4
6	2400	10.6	5.0	270	8.95	1.2
7	2500	7	2.0-6.6	270	4.7-8.5	1.4-4.4
8	14000	3.3	4.5	320	10.3	4.0
9	40000	4.0	3.5	270	18.8	5.0
10	300000	0.15	7.2	260	14.6	14.0
11	300000	0.15	7.0	248	14.7	10.0
12	550000	0.31	3.8	260	20.6	15.4
13	800000	0.28	5.0	260	27.4	15.0-22.0

Table 2. Critical parameters, characteristic and observed velocities.

the necessary data for making the above correlation. Regardless of shortcomings in the data used for the correlation, the implicit definition of the characteristic velocity, $U^{\star}$, does appear to be the correct natural scaling parameter for buoyancy driven flows. The correlated equation (1.6.5) is useful in approximating the maximum velocity along a slope with only a few parameters needing to be estimated or measured.

Knowledge of the characteristic velocity allows for a number of other parameters to be obtained. These include the characteristic time for the flow to develop, as well as dimensionless groups common to fluid mechanics in general.

The characteristic time for the transient portion of the flow (all boundary conditions being constant), $t^{\star} = \frac{L}{U^{\star}}$ comes from either the energy or the momentum equation and is defined in terms of $U^{\star}$. Table 3 shows characteristic times obtained from the data used to generate Figure 2. The characteristic times span the range from minutes to nearly half a day. As was mentioned previously, most katabatic winds exist on the order of hours as governed by the diurnal cycle. Thus, winds which have characteristic times much smaller than several hours are generally in steady or pseudo steady state, and the dynamics which are observed are related to the dynamics of the boundary conditions. Examples are changes in ground and air temperatures due to radiation and air movement aloft of the katabatic boundary layer. The winds which have characteristic times on the order of hours are likely to be either developing or ceasing with the exception of one notable category. The katabatic winds of Antarctica, as Table 3 shows, require times exceeding a half day to develop. It must be kept in mind, however, that the proper conditions for strong katabatic winds to develop and reach steady state at the polar region may exist over several days. When this is not the case, the Antarctic katabatic wind will not reach steady state. Thus, the above definition of the characteristic time is useful in determining the dynamics

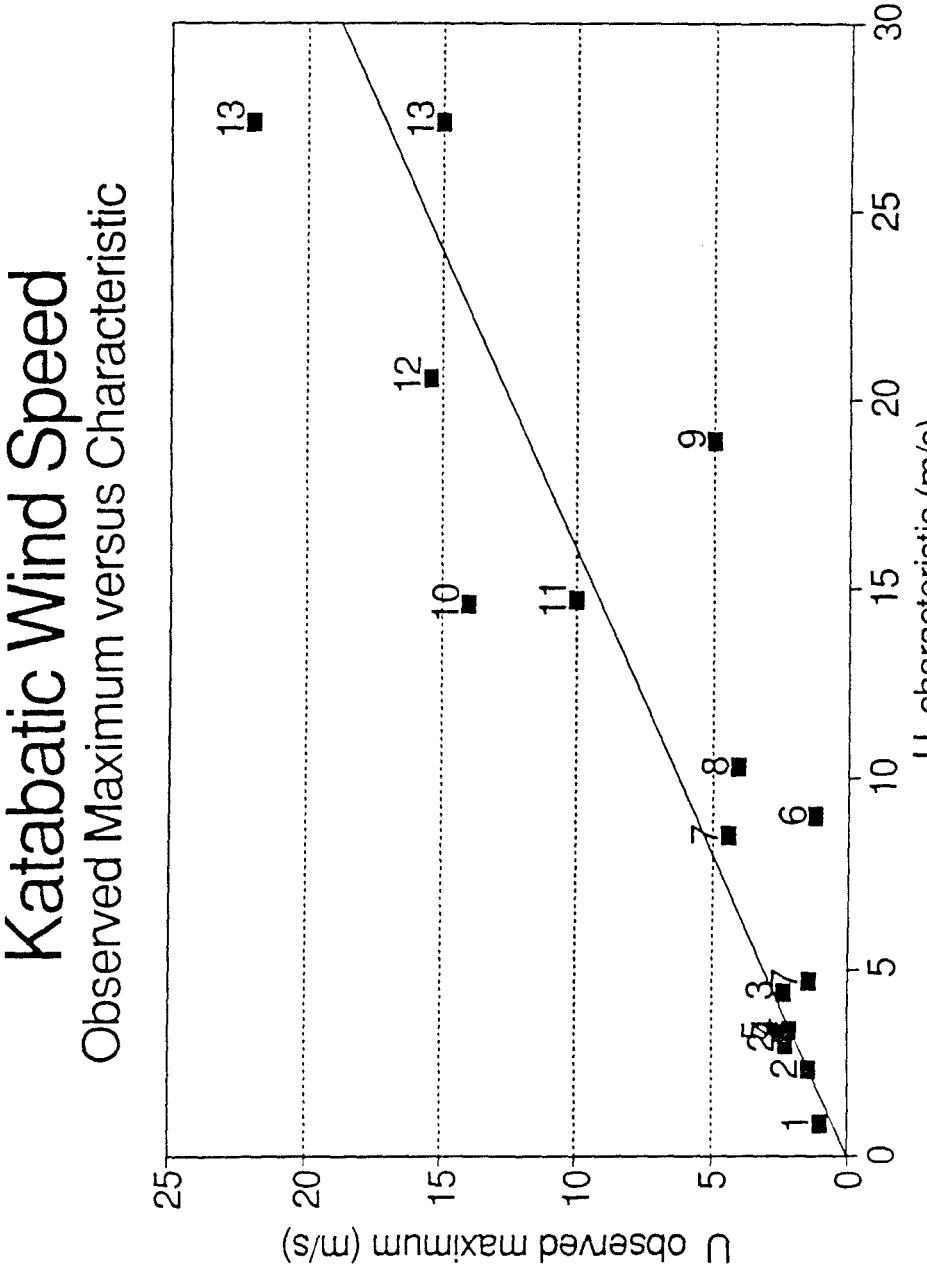

Figure 1. Linear correlation between the observed maximum velocity, U_{Obs}^{Max}, of the low level jet and the characteristic velocity, U^*, obtained via dimensional analysis. Numbers above the data points indicate the source of the data in Table 1.

Site no.	$\bar{t}$ (minutes)	λ	Coriolis parameter f, (s^{-1})	Longitude ψ, (degrees)	Rossby no. Ro
1	4.5	3.37	$1.3 \cdot 10^{-5}$	34 N	294
2	1.8	0.06-0.09	$1.3 \cdot 10^{-5}$	35 N	920
3	1.6	0.23	$1.7 \cdot 10^{-5}$	47 N	610
4	2.0	0.37	$1.7 \cdot 10^{-5}$	47 N	470
5	3.5	0.44	$1.3 \cdot 10^{-5}$	35 N	360
6	4.5	0.53	$1.6 \cdot 10^{-5}$	45 N	230
7	8.8	0.27-0.91	$1.8 \cdot 10^{-5}$	50 N	190
8	23	1.07	$1.5 \cdot 10^{-5}$	40 N	49
9	36	4.78	$-1.7 \cdot 10^{-5}$	47 S	28
10	342	0.65	$-2.2 \cdot 10^{-5}$	70 S	2.1
11	340	0.67	$-2.2 \cdot 10^{-5}$	70 S	2.1
12	445	4.69	$-2.2 \cdot 10^{-5}$	70 S	1.6
13	487	4.69	$-2.2 \cdot 10^{-5}$	70 S	0.81-1.2

Table 3. Characteristic time, λ, and Rossby number.

of katabatic winds, but should also be placed in the context of the dynamics of surrounding environment to avoid accidently neglecting the time dependent terms of the conservation equations.

The familiar dimensionless groups to fluid analysis are summarized below, where the implicit definition of $U^{\star}$ is inserted as the characteristic velocity. Consequently, these dimensionless groupings take on some interesting forms and relations to one another. The Grashof number, Gr, is central to the study of bouyancy driven flows. Physically, the Grashof number represents a ratio of the buoyant forces to the viscous forces.

$$Gr = \frac{L^3\rho^2 g(\sin\phi)\beta\acute{\theta}}{K^2} \tag{1.6.6}$$

The Reynolds number, Re, which is the characterictic dimensionless ratio of inertial to viscous forces, can be written in terms of the Grashof number for buoyant slope flow as a consequence of the convective, viscous and buoyant forces all balancing in the analysis. Note that the turbulent kinematic viscosity is defined as $\nu_t = \frac{K}{\rho}$ and that two definitions are presented depending on the value of λ. The definition valid for $\lambda \leq 1$ is

$$Re = \frac{LU^{\star}}{\nu_T} = Pr^{-\frac{1}{2}}\left[\frac{L^3\rho^2 g(\sin\phi)\beta\acute{\theta}}{K^2}\right]^{\frac{1}{2}} = Pr^{-\frac{1}{2}}Gr^{\frac{1}{2}} \sim L^{\frac{3}{2}}. \tag{1.6.7a}$$

The Reynolds number definition valid for $\lambda \geq 1$ is in terms of Equation 1.6.3b and l_c.

$$Re = \frac{l_c U^{\star}}{\nu_T} = \frac{Pr^{-\frac{1}{2}}}{\nu_T}\left[\frac{g\beta\acute{\theta}^4}{sin^2\phi\Gamma^3}\right]^{\frac{1}{2}} \sim L^0. \tag{1.6.7b}$$

It is not surprising that the Froude number, Fr, which represents the relative importance of the inertial forces to the gravitational forces, becomes independent of gravity as a result of the inertial forces being spawned by buoyant (i.e.,

gravitational) forces. For $\lambda \leq 1$

$$Fr = \frac{U^{\star 2}}{gL} = Pr^{-1}(\sin\phi)\beta\acute{\theta}. \tag{1.6.8}$$

The Prandtl number,

$$Pr = \frac{\nu_T}{\alpha_T} = \frac{\rho C_p}{K_T}\frac{K}{\rho}, \tag{1.6.9}$$

which represents the ratio of the thermal diffusivity to the momentum diffusivity, is approximately 1 for turbulent flows, since the effective diffusive transport mechanism for both is the same. This may be used to simplify the previous dimensionless groups which include the Prandtl number.

The importance of Coriolis effects for a given geometry and differential temperature can be determined by computing the Rossby number, *Ro*. The Rossby number is specified in terms of the above characteristic variables, $\lambda \leq 1$,

$$Ro = \frac{U^{\star}}{fL} = \frac{l_{Co}}{L} = Pr^{-\frac{1}{2}}\left[\frac{g(\sin\phi)\beta\acute{\theta}}{f^2 L}\right]^{\frac{1}{2}}, \tag{1.6.10a}$$

and for $\lambda \geq 1$,

$$Ro = \frac{U^{\star}}{fL} = \frac{l_{Co}}{L} = Pr^{-\frac{1}{2}}\left[\frac{g\beta\acute{\theta}^2}{f^2 L^2 \Gamma}\right]^{\frac{1}{2}}, \tag{1.6.10b}$$

by the analysis performed in Section 1.5. Note the critical length along the slope at which Coriolis forces become important is called l_{Co}. The Coriolis parameter, f, is defined in terms of the earth's rotation rate, Ω, and the latitudinal angle, ψ, as $f = 2\Omega\sin\psi$. Table 3 contains the Rossby number for the observed slope flows. Note that $Ro \leq 1$ indicates Coriolis effects strongly affect the flow. For $1 \leq Ro \leq 20$ the Coriolis terms have a noticeable affect on the flow, while values of *Ro* greater than 100 indicate Coriolis effects are not likely to be observed in the particular circumstance being evaluated. Also, note that *Ro* is parenthetically

defined in terms of λ depending on the value of $U^\star$ which applies where Ro is being computed. Notice that the critical length, l_{Co}, after which Coriolis forces become dominant along χ (the slope) is defined in 1.6.10. The condition of l_{Co} being greater than L is equivalent to Ro being greater than 1. It may be clearer to use the critical length $_{C}o$ than to use $Ro \geq 1$ in some circumstances. For instance this allows direct comparison with the critical length l_c at which the effect of the buoyant jet traversing the stratified air becomes important for a given flow. Note that most slope flows have $Ro > 1$.

Once the Rossby number has been defined it is possible to explicitly define a characteristic velocity in the cross slope direction, $V^\star$, which results from the Coriolis force. The cross slope scaling parameter width, L_y, comes from balancing terms in the ξ direction momentum equation, Section 1.5

$$L_y = \frac{L}{Ro} \tag{1.6.11}$$

$$V^\star = \frac{L_y}{L} U^\star = \frac{U^\star}{Ro} = fL \tag{1.6.12}$$

Thus for a given location $V^\star$ is quickly determined in terms of the slope length and Coriolis parameter.

The last traditional dimensionless group is the Richardson number, Ri, and it can be expressed in terms of the above groupings by the following rearrangement.

$$Ri = -g(\cos\phi)\beta\acute{\theta}\frac{\Delta}{U^{\star 2}} \tag{1.6.13}$$

The Richardson number is a measure of the stability of a stratified shear flow. The Richardson number presented above is the bulk form.

When thermally driven slope winds coexist with ambient winds, as they often do, it is important to ascertain the influence that the interaction has on transport. Two principle interactions summarize the extremes, the ambient wind can flow

counter current ,i.e., oppose the slope flow, or it can flow cocurrent ,i.e., with the slope flow. Obviously the effects of cross winds require a three-dimensional formulation, but such cases are not treated herein. The dimensionless group governing this interaction is a natural choice, $\ddot{U}$, in that it is a ratio of the ambient flow velocity to the characteristic velocity of the slope flow, for $\lambda \leq 1$

$$\ddot{U} = \frac{U_\infty}{U^*} = \left[\frac{U_\infty^2}{g(\sin\phi)\beta\acute{\theta}L}\right]^{\frac{1}{2}}. \qquad (1.6.14)$$

A similar relationship can be developed using the characteristic velocity for $\lambda \geq 1$ using Equation 1.6.3b. The magnitude of $\ddot{U}$ indicates whether the buoyantly driven wind is a first or second order effect relative to the ambient wind. When $|\ddot{U}| < 1$ the buoyantly driven wind is the first order effect and the low level jet is likely to be observed. When $|\ddot{U}| > 1$ the ambient winds dictate the nature of the flow field. In this case buoyantly driven winds perturb the ambient flow field and their effect may be obscured.

Conclusions

Probably the most striking feature of buoyantly driven slope flows brought out by this analysis is the functional relationship between the boundary layer thickness and the slope length (1.6.2a and 1.6.2b). The two regimes are controlled by the mechanisms by which energy flows across the buoyant layer. At the leading edge of the slope, advective and diffusive transport balance, while further along the slope diffusive transport is balanced by the heating (or cooling) effect of entraining ambient air into the momentum boundary layer. The demarcation point between the two regimes is set by the value of the parameter λ. For $\lambda \leq 1$ the former case above holds, while for $\lambda \geq 1$ the latter case applies. Of course, in the overlap region around $\lambda = 1$ all three mechanisms for energy transport are in balance. It is very important when assessing the potential for slope flow to first calculate λ. The steeper and shorter the slope or the smaller the ground to air temperature gradient, the more likely λ will exceed 1. Based on λ's value, one can calculate the remaining parameters of interest.

The growth of the buoyantly driven boundary layer at its leading edge as a function of the slope length to the quarter power ($\Delta \sim L^{\frac{1}{4}}$) is one aspect that has important implications with regard to pollution transport. The reason for this lies in the connection between boundary layer thickness and the entrainment of air from above the layer. A boundary layer which grows as $\chi^{\frac{1}{4}}$, where χ is used instead of L since one can choose to scale the slope length anywhere along the slope, entrains a large fraction of air at first and less and less with increasing distance along χ. This means that a buoyant boundary layer acts like a pump, preferentially extracting air at its leading edge and depositing it at the end of the slope.

This has two major effects on the transport of pollutants, depending on their origin relative to the buoyant flow. First, if elevated pollution levels exist at the

front of the buoyant boundary layer, the polluted air is drawn in and transported within the layer until the end of the slope is reached. Dilution of the pollutant by air from above the layer farther along the slope is limited because the slow growth of the layer imposed by the $\chi^{\frac{1}{4}}$ law provides minimal entrainment into the layer. If the slope is long enough such that λ exceeds 1 ($\Delta \sim L^0$), then the boundary layer thickness becomes constant, i.e., no entrainment into the layer from above, and dilution is limited completely to turbulent transport across the boundary layer. Second, if the slope along which the boundary layer develops is a source of pollutant, for instance a landfill, then by the same arguments presented above, the pollutant is trapped and transported within the boundary layer. In this way the emissions from a ground source can be moved at ground level from one location with limited dilution to another location.

The dimensional analysis can be used to determine the kind of interaction the slope wind will have with the ambient wind. The nature of the slope wind-ambient wind interaction has been discussed in several papers. The observations presented therein substantiate the persistence of slope wind in the presence of ambient wind. Interpretation, and use of equation 1.6.14, is by an attempt to provide a quick method for estimating whether a slope wind will persist and be observable in the presence of cocurrent or counter current ambient wind.

The following guidelines are proposed when interpreting the value of $\ddot{U}$. For $|\ddot{U}| \gg 1$ the effects of the slope wind will not be observed. Under such circumstances the atmospheric conditions that produce slope wind are not likely to be maintained. When $|\ddot{U}| \approx 1$ the effect of the slope wind may be evident as a distortion in the logarithmic ground level wind velocity profile, but a true jet will not be observed. When $1 > |\ddot{U}| > 0$ the observed wind profile will have a low level jet, but will also show the influence of the ambient wind with increased vertical height. Naturally, when $\ddot{U} = 0$ ambient winds are not present and the

low level jet will be observed undisturbed. Because observations available from the literature are insufficient to substantiate these criteria, the above are simply guidelines and may need to be revised as more data becomes available.

Slope winds are often nested within other mesoscale meteorological regimes, for example, the mountain-valley system. Thus it may be possible to obtain estimates of the ambient wind potential in an area also susceptible to slope wind, by techniques developed for these other mesoscale regimes. This information, plus the pertinent parameters available for the slope wind can be combined and used in Equation 1.6.14 to serve as a predictive tool for estimating the near ground behavior of winds along a slope.

It is useful to place several previous papers into the context of the dimensional analysis just presented. Examination of Prandtl's solution reveals that it is the solution of a slope flow for the dimensionless case of $\lambda \gg 1$. In other words, Prandtl's solution is a realistic solution of the extreme case where entrainment of the ambient air leads to a reversal of the potential temperature gradient atop of the boundary layer. If Ohata and Higuchi (1979) had known this, they probably would not have expected their observations on a snow patch, which had a λ of $0.04 - 0.06$ (Table 3), to match well with Prandtl's solution. The paper by Rao which suggests that Coriolis effects are negligible except for small slope angles should be amended based on Equation 1.6.10. The statement should also include cases where the slope is long, the ground to ambient air temperature gradient is small, or the Coriolis parameter is large; specifically, cases where the Rossby number is 1 or smaller.

Acknowledgements

The assistance of M. Deem and P. Wyckoff in the preparation of this document was greatly appreciated.

1.7 Application of the von Karman – Pohlhausen Method to Bouyantly Driven Boundary Layers

Introduction

The boundary layer equations developed in Sections 1.2 - 1.5 cannot, in general, be solved to give closed form solutions except for the case when the critical slope parameter, λ, is much larger than one (Prandtl, 1952). Atmospheric slope flows exist for smaller values of λ, and so it would be desirable to have a method of acquiring the detailed temperature and velocity profiles for these conditions. Computer generated profiles are possible but not always practical, and hydrolic techniques do not allow for the computation of temperature and velocity profiles within the slope flow boundary layer.

The boundary layer method devised by von Karman and Pohlhausen, and described by Schlicting (1979), is an alternative approximate solution strategy capable of satisfying the above mentioned criteria. Through the method the detailed temperature and velocity profiles are obtained, often without the need for any computer assistance. The drawback of the technique is that it is approximate. However, the error introduced in other similar problems is generally small, usually less than ten percent, when implemented as it will be below. Some of the physical parameters on which any solution would rely are not known more accurately than to ten percent, and field measurements of the slope wind speed profiles contain errors of this magnitude. The ability to obtain the velocity and temperature profiles far outweighs the small error introduced by this method when it is utilized for comparison with field measurements and modeling atmospheric conditions.

Method

The boundary layer equation for energy (Equation 1.4.11), and for momentum (Equation 1.5.6), are integrated from the ground, 0, to the edge of the slope flow boundary layer at $\delta(\chi)$. A uniform speed external to the flow, U_∞, is assumed. It has been made dimensionless by the characteristic slope velocity, $U^\star$. The resulting equations are combined with the continuity equation, and Liebniz's differentiation of an integral rule is applied. After rearrangement this gives Equation 1.7.1 and 1.7.2. These equations are very similar to the standard boundary layer integral equations for flow over a flat plate, with the addition of the terms which couple the momentum to the energy.

Energy

$$\frac{d}{d\chi}\int_0^{\delta_T(\chi)} U\Theta \, d\varsigma \; + \lambda \int_0^{\delta_T(\chi)} U \, d\varsigma \; = \; -\frac{\partial \Theta}{\partial \varsigma}\bigg|_{\varsigma=0} \tag{1.7.1}$$

Momentum

$$\frac{d}{d\chi}\int_0^{\delta(\chi)} U(U-U_\infty) \, d\varsigma \; = \; -Pr\frac{\partial U}{\partial \varsigma}\bigg|_{\varsigma=0} + \int_0^{\delta(\chi)} \Theta \, d\varsigma \tag{1.7.2}$$

The δ's are made dimensionless in order to be compatible with the dimensionless forms of the boundary layer equations and are defined below.

$$\delta_T(\chi) \; = \; \frac{\delta_{Therm}}{\Delta} \tag{1.7.3}$$

$$\delta(\chi) \; = \; \frac{\delta_{\rho v}}{\Delta} \tag{1.7.4}$$

The boundary layer thicknesses, δ_{Therm} for the thermal layer, and $\delta_{\rho v}$ for the momentum layer, are dimensional. To complete the specification of the method, polynomial profiles are assumed for the temperature and velocity and fit to the boundary conditions which are known or may be imposed by physical arguments.

Boundary Conditions and Profiles

I. Temperature: Define $\eta \equiv \frac{\zeta}{\delta(x)}$, $\eta_T \equiv \frac{\zeta}{\delta_T(x)}$, and $h \equiv \frac{\delta_T(x)}{\delta(x)}$

Boundary Conditions:

1. $\Theta(\eta_T = 0) = 1$
2. $\Theta(\eta_T = 1) = 0$
3. $\Theta'(\eta_T = 1) = 0$
4. $\Theta''(\eta_T = 0) = 0$

Meaning of the Boundary Conditions

See Section 1.4 Equation 1.4.8 which defines the temperature variable, Θ. Boundary condition 1 and 2 specify the dimensionless potential temperature difference function at ground level and at the edge of the thermal boundary layer. Boundary condition 3 guarantees the temperature profile joins the external temperature field smoothly. Boundary condition 4 is obtained directly from Equation 1.4.14.

Assumed profile:

$$\Theta = a_1 + a_2\eta_T + a_3\eta_T^2 + a_4\eta_T^3$$

After applying the boundary condtions:

$$\Theta = 1 - \frac{3}{2}\frac{\eta}{h} + \frac{1}{2}(\frac{\eta}{h})^3 \qquad (1.7.5)$$

II. Velocity (quiescent external flow): Define $\eta \equiv \frac{\zeta}{\delta(x)}$

Boundary Conditions:

1. $U(\eta = 0) = 0$
2. $U(\eta = 1) = 0$
3. $U'(\eta = 1) = 0$
4. $U''(\eta = 0) = -Pr^{-1}$

Meaning of the Boundary Conditions

See Section 1.5 Equations 1.5.8 which defines the dimensionless velocity, U. Boundary condition 1 and 2 specify the dimensionless velocity at ground level and at the edge of the momentum boundary layer is zero. Boundary condition 3 guarantees the velocity profile joins the external velocity field smoothly. Boundary condition 4 is obtained directly from Equation 1.5.10a.

Assumed profile: $U = b_1 + b_2\eta + b_3\eta^2 + b_4\eta^3$

After applying the boundary conditions:

$$U = \frac{\delta^2}{4Pr}\eta(1-\eta)^2 \tag{1.7.6}$$

III. Velocity (Uniform external flow): Define $\eta \equiv \frac{\zeta}{\delta(x)}$

Boundary Conditions:

1. $U(\eta = 0) = 0$
2. $U(\eta = 1) = U_\infty$
3. $U'(\eta = 1) = 0$
4. $U''(\eta = 0) = -Pr^{-1}$

Meaning of the Boundary Conditions

Same as the velocity conditions in II. above, except boundary condition 2 specifies the dimensionless velocity at the edge of the momentum boundary layer is U_∞.

Assumed profile: $U = b_1 + b_2\eta + b_3\eta^2 + b_4\eta^3$

After applying the boundary conditions:

$$U = \left[\frac{3}{2}U_\infty + \frac{\delta^2}{4Pr}\right]\eta - \frac{\delta^2}{2Pr}\eta^2 - \left[\frac{1}{2}U_\infty - \frac{\delta^2}{4Pr}\right]\eta^3 \qquad (1.7.7)$$

Velocity and Temperature Boundary Layer Thickness

Inserting the assumed profiles, i.e., Equations 1.7.5 and 1.7.6, into the integral form of the boundary layer equations and evaluating the integrals leads to a set of equations for the unknown functions, $\delta(\chi)$, $\delta_T(\chi)$, *or* $h(\chi)$. The solution of this set of equations requires additional assumptions since there are 3 unknown functions and only 2 equations. The assumption that the ratio of the boundary layer, h, is a constant, at least to first order, can be argued on the basis that the existence of the momentum boundary layer results directly from the thermal boundary layer. This leaves the following pair of differential equations to be solved and manipulated. The Prandtl number is assumed to be unity.

From the energy equation comes Equation 1.7.8.

$$\delta(\chi)^3 \frac{d\delta(\chi)}{dx} = \frac{Pr}{2}\left(\frac{h^3}{40} - \frac{h^4}{48} + \frac{3h^5}{560}\right)^{-1}. \tag{1.7.8}$$

From the momentum equation and velocity profile, Equation 1.7.6, comes Equation 1.7.9.

$$\delta(\chi)^3 \frac{d\delta(\chi)}{dx} = 336Pr^2\left(\frac{3}{4} - \frac{3}{4h} + \frac{1}{8h^3}\right) \tag{1.7.9}$$

The boundary condtion is $\delta(\chi = 0) = 0$.

From the momentum equation and velocity profile, Equation 1.7.7, comes Equation 1.7.10.

$$\frac{d\delta(\chi)}{dx} = \frac{-\frac{3}{2}PrU_\infty + \delta^2\left(\frac{3}{4} - \frac{3}{4h} + \frac{1}{8h^3}\right)}{a_1 U_\infty^2 \delta + a_2 U_\infty \delta^3 + Pr^{-2}\delta^5} \tag{1.7.10}$$

The constants are defined as: a1 = 0.6107, a2 = 0.05895, a3 = 0.002976 and the boundary condition is $\delta(\chi = 0) = 0$. This relationship can be used to study the influence of an external wind on the boundary layer thickness.

The value of h is the first piece of information available directly. By dividing Equation 1.7.8 by Equation 1.7.9, rearranging, and then solving the resulting

fifth order polynomial for its zeros, a set of possible solutions for h are obtained. The most probable value is $h = 1.05$. The other possible values to choose from were either complex or physically unrealistic. With h known, $\delta(\chi)$ can now be evaluated from Equation 1.7.9 and the boundary condition for δ. This gives:

$$\delta(\chi) = 3.7226\chi^{\frac{1}{4}}. \tag{1.7.11}$$

Maximum and Average Velocity

The average velocity is found from the approximate velocity profile, Equation 1.7.6, by integration.

$$U^{Ave}(\chi) = \int_0^1 U(\eta)\, d\eta = \frac{\delta^2(\chi)}{48Pr} \tag{1.7.12}$$

The maximum velocity is found from the approximate velocity profile by differentiation. It occurs at $\eta = \frac{1}{3}$, i.e., one third the total boundary layer thickness.

$$U^{Max}(\chi) = \frac{\delta^2(\chi)}{27Pr} \tag{1.7.13}$$

The ratio of the maximum velocity to the average velocity is

$$\frac{U^{Max}}{U^{Ave}} = \frac{48}{27} = 1.77. \tag{1.7.14}$$

Dimensional Relationship of Velocity Maximum

The maximum dimensional velocity, U_{Dim}^{Max}, is related to the dimensional boundary layer thickness as:

$$U_{Dim}^{Max}(s) = \frac{U^{*2}}{27LK}\delta_{\rho v}^2(s). \tag{1.7.15}$$

The dimensional slope coordinate is s. This is found by taking Equation 1.7.13 and using the relationships found in Section 1.5 to reconsitute a dimensional equation. This relationship holds for $\lambda \leq 1$. The parameter K is the effective eddy diffusivity for momentum.

Comparison of the Velocity Profile to Field Observations

During field measurements sufficient data has not been collected to do a comprehensive comparison between observations and the boundary layer analysis previously described. Though numerous field investigations of slope winds have been done, none of them have thoroughly studied the development of the buoyant boundary layer along the slope. Most downslope studies have been at the end of the slope, where the winds are the strongest, and thus at the end of the boundary layer. From an observational point of view, this is where the speed is at a maximum, and so it makes sense to take measurements there. From a modeling and verification-of-theory point of view, measurements should be taken at numerous places along the slope.

The assumption that slope flows can be approximated by a nearly constant thickness all along the slope must have been used to design most field studies. This assumption appears never to have been tested except in the large scale slope flows in Antarctica. The boundary layer analysis given in Sections 1.2-1.5 describes the different regimes for slope flow and shows this approximation is only valid for $\lambda \gg 1$. Whereas this assumption is valid in the flows in Antarctica, it does not hold for many of the studies which have been done on smaller scales.

A consequence of assuming the boundary layer thickness is constant is the ability to neglect the evolution of the flow along the slope when taking measurements. Remember from Section 1.5 and 1.6 that the boundary layer and slope wind profile have become independent of the slope coordinate. This assumption is not valid case for all regimes of slope wind. However, some investigators have treated measurements as if they are in this regime irrespective of whether they are or not. In no observational paper read to date has the author attempted to describe the slope flow regime on the basis of the fundamental characteristic scalings. Not surprising is fact that the measurements are then being compared

to models of the wrong physical regime of the slope flow. Because of this, the conclusions drawn by some authors about the applicability of their models are still to be proven.

Unfortunately, the model proposed above cannot be thoroughly tested either because of the absence of measurements at multiple places along a single slope. Only a fit of theory and profiles are possible at single locations along the slope. One plot is shown here, Figure 1, where the model was compared to measurements reported by Banta and Cotton (1982). The plot is generated by inserting the measured boundary layer thickness in Equation 1.7.6, using a slope length of 3300 meters, slope angle of 3.3 degrees, and a potential temperature difference of 4 degrees. This data could be extracted from plots in Banta and Cotton's paper. The model produces results which are qualitatively correct, but to draw a comparison between this model and other models would be inappropriate. When better data exists such comparisons can be undertaken.

One point on which it is appropriate to draw a conclusion is the correctness of assuming the maximum boundary layer speed will occur one third the height up from the ground. From the plot this seems to be a good assumption. This has also been noted in other comparisons not reported herein.

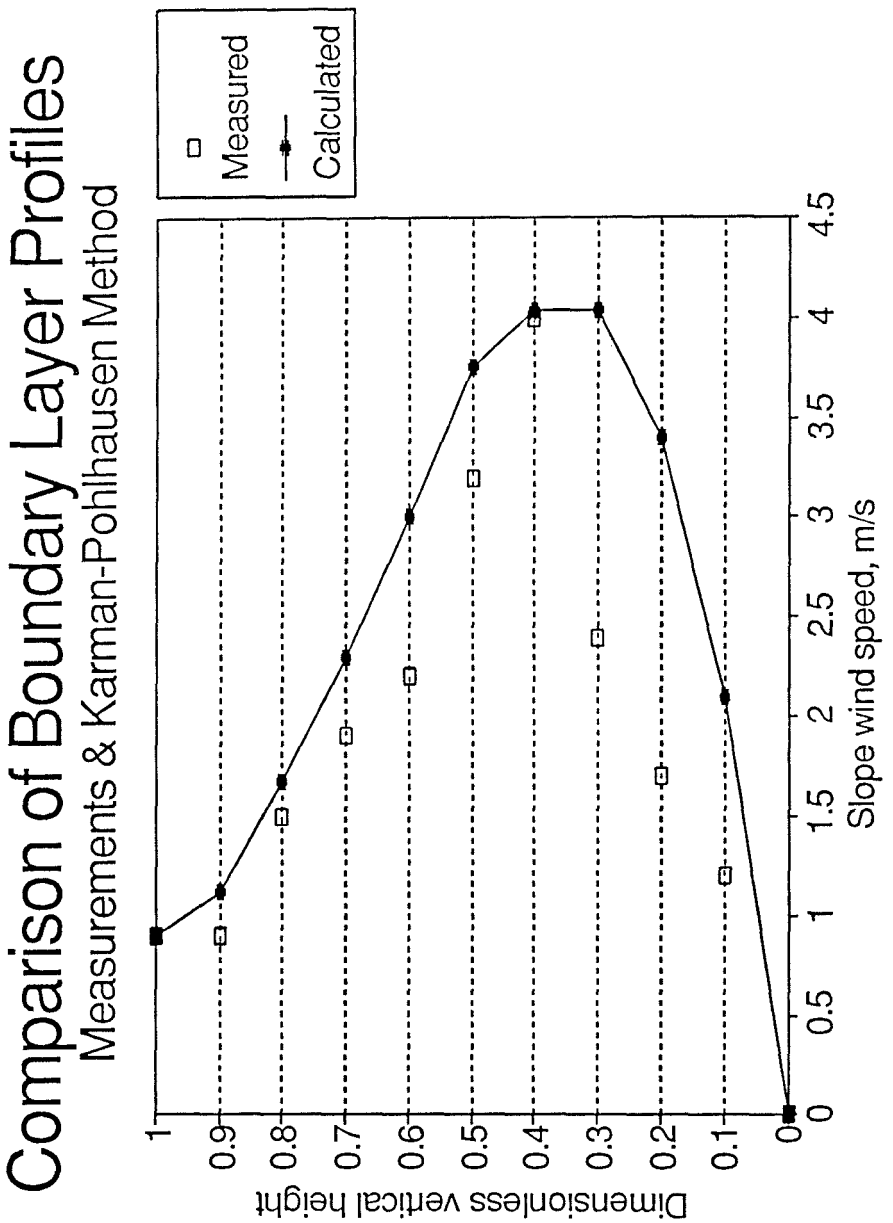

Figure 1. Comparison of the velocity profile given by Equation 1.7.7 with measurements made by Banta and Cotton (1982).

Effect of an External Wind on the Boundary Layer Thickness

The flux of momentum towards the ground resulting from an external wind has the capacity to change the thickness of the boundary layer along the slope. Equations 1.7.7 and 1.7.10 are used to study the quantitative changes in the boundary layer thickness resulting from a uniform external flow. The influence is studied for two reasons: (1) most often slope winds occur in the presense of a breeze or wind, and (2) changes in the boundary layer thickness affect the dilution of emissions in the layer.

To study the change in boundary layer thickness, Equation 1.7.10 is integrated numerically to the end of the slope, i.e., the boundary layer. For the dimensionless equation this is from $\chi = 0$ to 1. All boundary layer thicknesses reported below are given at $\chi = 1$. Seven simulations were done for external wind speeds which ranged from -0.5 (minus indicates opposing flow) to 0.2 of the characteristic slope velocity. Figure 2 shows the results of these simulations plotted as the boundary layer thickness δ normalized by the boundary layer height when $U_\infty = 0$ (Equation 1.7.11). The simulations were done using a dynamic simulation package, ACSL, using a fourth order Runga-Kutta as the numerical integration scheme. One assumption which was implicit in the simulation was the value of the ratio of the thermal to momentum boundary layer thickness, h, was constant. In the presence of an external wind, the momentum boundary layer thickness is no longer completely determined by the thermal layer. No method was able to be devised to determine how the error in this assumption grew with increasing U_∞. However, this assumption is valid in the neighborhood of the external wind speed being zero, $U_\infty = 0$. It was extended to the range of U_∞ used in the calculations.

In the following discussion when the boundary layer is referred to, this means the end of the boundary, $\chi = 1$. Since h was found to be approximately equal to

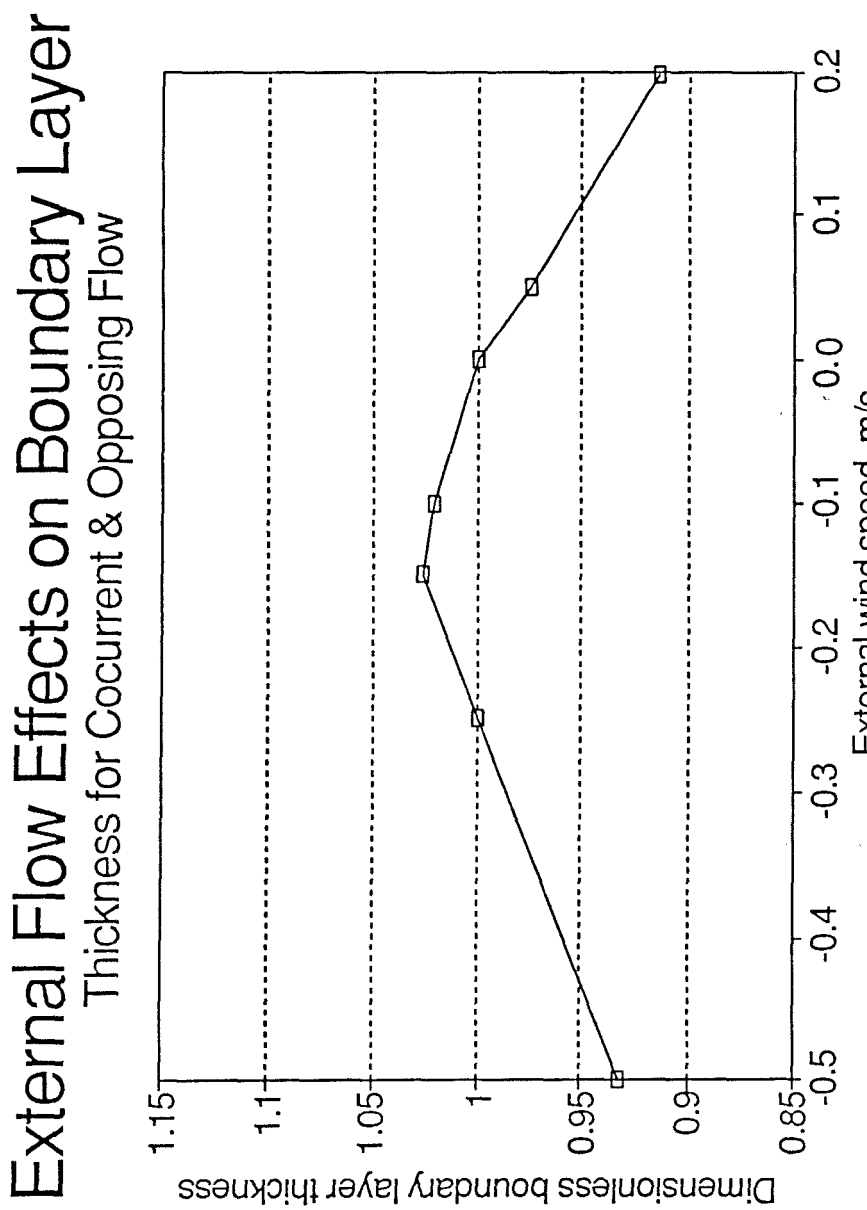

Figure 2. Changes in the slope flow momentum boundary layer thickness in the presence of an external constant flow. Both opposing flows and flows moving with the boundary layer are depicted. Notice the maximum height occurs for a small opposing flow. The external wind speed is made dimensionless by the characteristic slope flow speed, U^*.

one, the thermal and the momentum boundary layer are interchangeable. The phenomena being discussed are for the entire boundary layer, but the calculations are examined at the end of the layer.

A maximum in the boundary layer thickness occurs for an opposing flow which is flowing fifteen percent of the characteristic slope flow speed, U^*. Ostensibly two parameters control the thickness of the layer: (1) the height of the velocity maximum above ground and (2) the magnitude of the maximum velocity. Knowing that a maximum boundary layer thickness occurs, the interaction of the two factors can be explained as follows. For small opposing flows little momentum is being diffused into the layer to reduce the maximum velocity. Under these conditions it takes the original length $\delta(U_\infty = 0)$ to reach zero speed at the outer edge of the boundary layer, plus a little amount more to go from a speed of zero to the small opposing speed. At increased speeds the opposing flow sends more momentum into the layer. This retards the speed at the center of the flow, thus the maximum velocity is smaller and lower to the ground. These two effects are in balance at the maximum, and then larger opposing flow causes the boundary layer to decrease in size. The boundary layer has the same thickness when $U_\infty = 0.25U^*$ as it does when there is no external flow.

When the external flow is in the same direction as the slope flow, the boundary layer thickness decreases. In this case the flux of momentum into the top of boundary layer allows it to reach the external flow speed across a shorter distance. When the external speed roughly reaches the slope speed, the boundary layer will again need to grow because the transfer of momentum from the external flow will begin to be slowed by momentum transfer to the ground.

In either case, i.e., opposing or similar flows, when the external flow speed is approximately greater than the characteristic slope speed, the boundary layer thickness will be determined by the opposing flow.

Conclusions

Five major conclusions can be drawn from the previous section.

1. The von Karman-Pohlhausen technique is successfully applied to slope flows.
2. The velocity profile which is obtained compares well with measurements.
3. The slope flow boundary layer thickness grows slightly in a breeze opposing the direction of its flow, reaching a maximum height when the external flow is fifteen percent the size of the characteristic slope flow speed, $U_\infty = 0.15U^*$.
4. The slope flow boundary layer thickness decreases steadily in a breeze flowing in the same direction as the flow.
5. A carefully designed, comprehensive slope flow field study will have to be done to determine the adequacy of the above technique. This field study should consider the following advice:
   a. Use the results from the dimensional analysis to assess/pick a site for the measurements. A site with a gradual slope on the order of 10 km would be ideal, perhaps a glacier.
   b. Do simultaneous measurements at many locations along the slope. Make certain the leading edge of the flow can be located by first doing diagnostic measurements.
   c. Estimate the boundary layer thickness for the slope flow *a priori*, confirm it with diagnostic measurements, and then do extensive measurements from ground level up to this height including a reasonable margin for variations. Definitely find the maximum speed at each point along the slope, since testing the theory depends on knowing it.
   d. A simultaneous atmospheric tracer release might be considered to parameterize turbulence, mixing, and transport in and of the flow. If real time visualization of the slope flow were being done by reconstructing the data as it were being taken, a very controlled tracer release into the

leading edge of the flow would be possible.

1.8 Modeling the Evolution of a Two – Dimensional Thermally Driven Atmospheric Boundary Layer

Introduction

The objective of this section is to present a non-numerical approach for modeling the transient development of a buoyantly driven slope flow boundary layer. No prior work in this area exists in the literature except for that done by computer simulations, e.g., Leslie and Smith (1974), Arritt and Pielke (1986). The approach to be considered is to extend the von Karman-Pohlhausen method discussed in Section 1.7 to incorporate the transient terms of the momentum equation. A similar approach was used to analyze the impulsive motion of a semi-infinite flat plate at speed U, by Stewartson (1950). In this study, Stewartson determined the boundary layer development beyond an essential singularity at $Ut = x$, away from the leading edge, was independent of the horizontal coordinate, x. By analogy slope flows will also have this same type of essential singularity. This result then has very interesting implications to slope flows, and especially to interpreting field measurements.

Field observations taken along a slope could mistakenly be interpreted to support that a particular flow had become independent of slope length when in reality the flow was still undergoing its transient boundary layer development. In Sections 1.4 - 1.7 the conditions when a steady state slope flow becomes independent of slope length are thoroughly studied. The study of the transient slope flow introduces another caveat that investigators must understand before field measurements can be properly compared against theory.

Similar to the previous sections, the boundary layer is due to a temperature

difference between the ground and the air. In this case the temperature difference will be assumed to occur instantaneously. Such air/ground temperature differences do not really occur in nature, but the dynamics involved in creating a temperature difference by radiative heat transfer, or advection of an unequilibrated air mass over the slope, are generally fast compared to the development of the boundary layer. This assumption represents the most abrupt conditions which would start a boundary layer to develop. Field observations are likely to be less dramatic.

Method

The essence of the following method is the reduction of the coupled momentum and energy partial differential equations (PDE) to a single first order PDE describing the momentum boundary layer thickness as a function of time and position. The method of characteristics is applied to this equation, giving a simple technique to determine the extent of boundary layer development in a transient slope flow.

The transient problem is approached identically to the steady-state boundary layer solution given in Section 1.7. By analogy the following unsteady integral equations can be derived. The critical slope length parameter, λ, is assumed to be zero. Physically, this restricts the solutions to boundary layers which are steady state functions of the distance along the slope.

$$\frac{d}{dt}\int_0^{\delta(\chi,t)} U d\varsigma + \frac{d}{d\chi}\int_0^{\delta} U(U-U_\infty)d\varsigma + \frac{dU_\infty}{d\chi}\int_0^{\delta} U d\varsigma = -Pr\frac{\partial U}{\partial \varsigma}|_{\varsigma=0} + \int_0^{\delta}\Theta d\varsigma \tag{1.8.1}$$

$$\frac{d}{dt}\int_0^{\delta_T(\chi,t)} \Theta d\varsigma + \frac{d}{d\chi}\int_0^{\delta_T} U(\Theta-\Theta_\infty)d\varsigma + \frac{d\Theta_\infty}{d\chi}\int_0^{\delta_T} U d\varsigma = -\frac{\partial \Theta}{\partial \varsigma}|_{\varsigma=0} \tag{1.8.2}$$

In the problem under consideration, the upper air is assumed to be quiescent and it remains at a constant temperature. Consequently, U_∞ and Θ_∞ are zero. This leads to Equations 1.8.3 and 1.8.4.

$$\frac{d}{dt}\int_0^{\delta(\chi,t)} U d\varsigma + \frac{d}{d\chi}\int_0^{\delta} U^2 d\varsigma + = -Pr\frac{\partial U}{\partial \varsigma}|_{\varsigma=0} + \int_0^{\delta}\Theta d\varsigma \tag{1.8.3}$$

$$\frac{d}{dt}\int_0^{\delta_T(\chi,t)} \Theta d\varsigma + \frac{d}{d\chi}\int_0^{\delta_T} U\Theta d\varsigma = -\frac{\partial \Theta}{\partial \varsigma}|_{\varsigma=0} \tag{1.8.4}$$

The technique of von Karman and Pohlhausen is employed next, thereby providing polynomial approximations for $U(\chi,\eta,t)$ and $\Theta(\chi,\eta,t)$ which satisfy the boundary conditions mentioned in Section 1.7.

$$U(\chi,\eta,t) = \frac{\delta^2(\chi,t)}{4Pr}\eta(1-\eta)^2 \tag{1.8.5}$$

$$\Theta(\chi,\eta,t) \;=\; 1-\frac{3}{2}\frac{\eta}{h}+\frac{1}{2}(\frac{\eta}{h})^3 \qquad (1.8.6)$$

In the above profiles, δ is the momentum boundary layer thickness, h is the ratio of the thermal boundary layer thickness to the momentum boundary layer thickness, and η is the dimensionsionless vertical height, $\frac{\zeta}{\delta}$. The value of h is a constant. See Section 1.7 which describes this more completely.

The above profiles are then substituted into Equation 1.8.3 for momentum, and the integrals and partial derivatives are evaluated. This leaves the following partial differential equation for the boundary layer thickness.

$$\frac{\partial}{\partial t}\delta^2 \;+\; \frac{3}{14Pr}\frac{\partial}{\partial \chi}\delta^4 \;=\; 36Pr[\frac{3}{4}(1-\frac{1}{h})+\frac{1}{8h^3}] \qquad (1.8.7)$$

This equation should be contrasted with the steady-state Equation 1.7.9. This equation is solved by the method of characteristics, bringing in the boundary condition $\delta(\chi=0,t)=0$ and the initial condition $\delta(\chi,t=0)=0$.

Results

The characteristic lines obtained are shown in Figure 1 on the following page. Two sets of lines are obtained; those beginning on the χ axis yield the value $\delta = [\frac{b}{a}\chi]^{\frac{1}{4}}$ and those beginning on the t axis $\delta = [bt]^{\frac{1}{2}}$, $(a = \frac{3}{14Pr}$, $b = 36Pr[\frac{3}{4}(1-\frac{1}{h}) + \frac{1}{8h^3}]$, $h = 1.05)$. The two regions overlap on the line $x = abt^2$.

Figure 2 shows the boundary layer height, $\delta(\chi)$, for various fixed times, generated by using Figure 1. This is the dimensionless plot times the lead coefficient of 2.21. The steady state solution obtained in Section 1.7 Equation 1.7.11 has a lead coefficient of 3.72. The difference in the two methods is a result of the extra polynomial which is introduced into the Equation 1.8.7 in the transient term. At the present there is no way to determine which of the two is most accurate. Lead coefficients excepted, functionally the two solutions are identical.

The essential singularity for the slope flow occurs at $U^*t = s$. The velocity, U^*, is the characteristic slope velocity defined in Equation 1.6.3a, t is time and s is the slope coordinate.

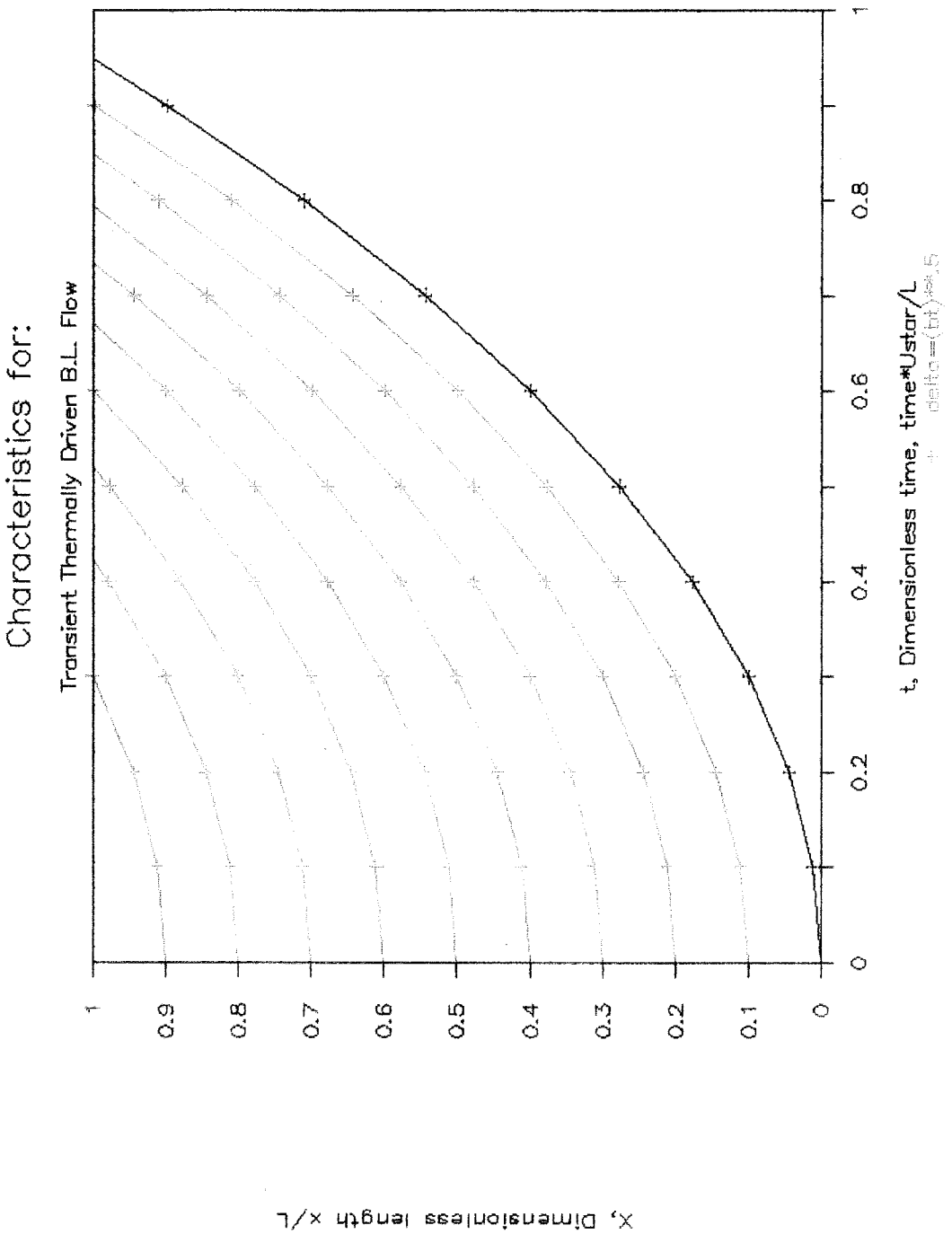

Figure 1. Characteristic lines for general transient slope flow.

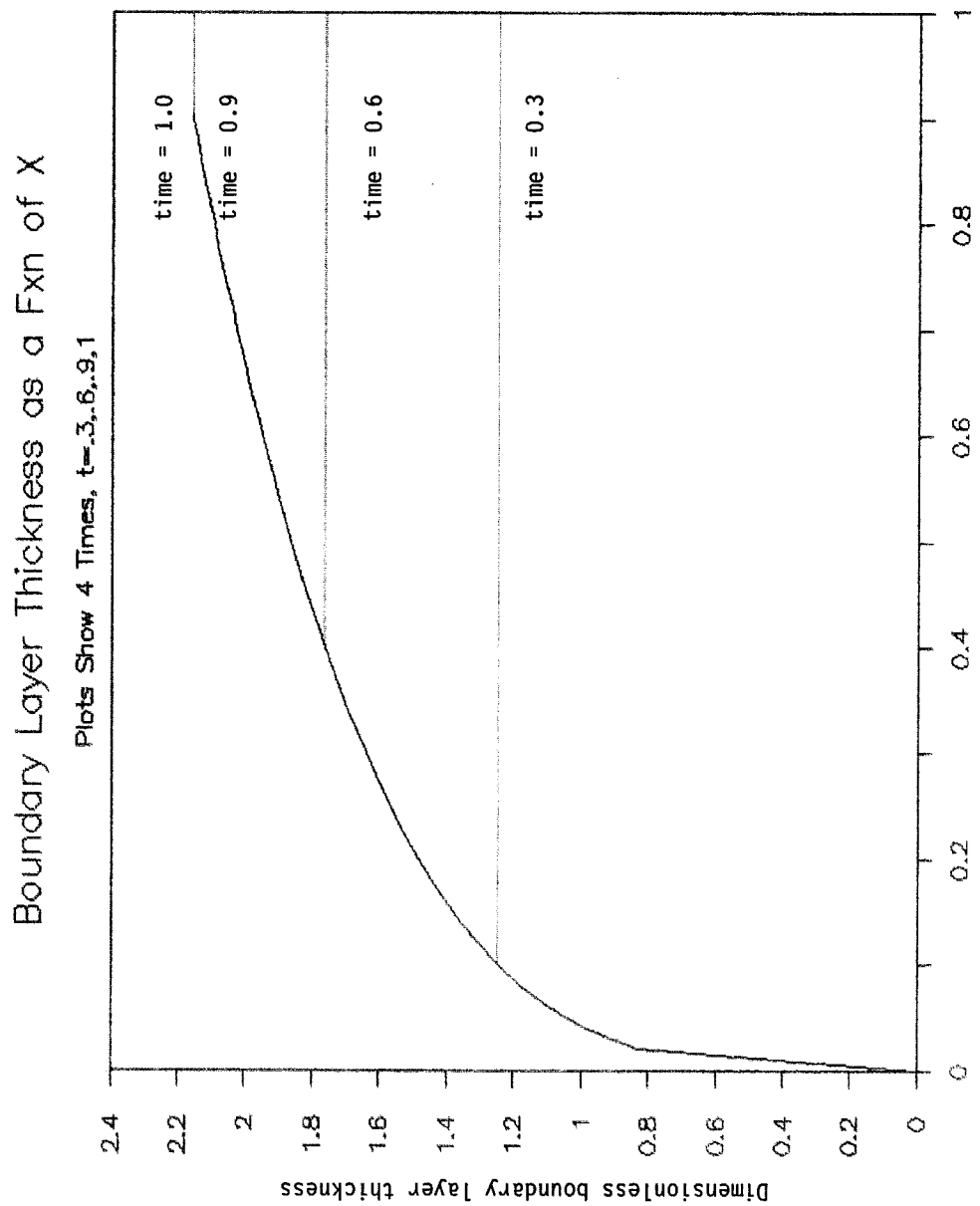

Figure 2. Boundary layer thickness as a function of dimensionless slope length and dimensionless time.

Conclusions

Four conclusions can be drawn from the above study of the transient flow.

1. The above method described herein provides a route for investigating systems of coupled PDE's derived from boundary layer analysis. Though approximate, the technique preserves a physical interpretation as to the origin of each term and does not require numerical techniques to complete the analysis. The next extension is to apply the technique to a more complete description of the problem discussed above.
2. Transient slope flows may be difficult to discern from steady slope flows which have boundary layers which have become independent of slope length.
3. Observations must be made with exceptional care so as to document every pertinent parameter to the flow as described in Section 1.6. Only then will it be possible to determine where along the slope of a given flow the boundary layer should become independent of slope length and where the observed flow was still experiencing transients.
4. When a high quality field study is done, these results should be compared with it and the existing models of other authors.

1.9 Katabatic Wind Along the Mountain Slopes Bordering the Los Angeles Basin

Abstract

A theoretical framework is developed to interpret certain characteristics of the nighttime downsloping drainage winds from sloping terrain adjacent to a basin. The impact of the slope winds upon air pollution within a basin is discussed.

Specific data from ten South Coast Air Quality Management District (AQMD) Air Monitoring Sites along the base of the mountain slope which face the Los Angeles Basin were analyzed in order to determine the ground-to-ambient air differential temperature needed to generate the observed wind speeds.

Introduction

The mountains surrounding the Los Angeles Basin create conditions capable of producing light slope winds along their slopes. During the daytime, the influence of upslope winds witinin the basin is often obscured by the stronger sea breeze and larger scale dominant winds. However, at night and especially the early morning, these stronger winds subside and the local downslope winds may dominate. Downslope, or katabatic winds in the basin are low level parabolically shaped jets affecting the vertical region of air between the ground and about a hundred meters; typical temperature and velocity profiles are shown in Figure 1. Although these winds are generated on the mountain slopes, their impact is observed at the base of the mountains and many kilometers further into the basin as indicated by Figure 2. These nighttime drainage winds may be quite extensive and tend to reinforce each other along the perimeter of the basin. For example, the relatively straight east/west orientation of the San Gabriel and San Bernardino mountain ranges which bound the basin to the north causes downslope winds (from a northerly direction) from Pasadena to Riverside.

The significance of these pre-sunrise winds is their ability to alter the spatial distribution of the extensive morning automobile emissions and any other existing natural or anthropogenic gaseous pollutants throughout the basin. Katabatic winds alter the spatial pollutant distribution by three basic mechanisms: (1) new emissions are relocated from their source, (2) existing ambient emissions are pushed up and/or out of the way by the drainage, and (3) aged emissions or emissions from natural sources from higher elevations along the slope are transported down into populated areas. Furthermore, the stable stratification in the nighttime slope winds retains emissions near the ground because of reduced vertical mixing across the boundary layer.

Though difficult to separate from the sea breeze during the day, these winds

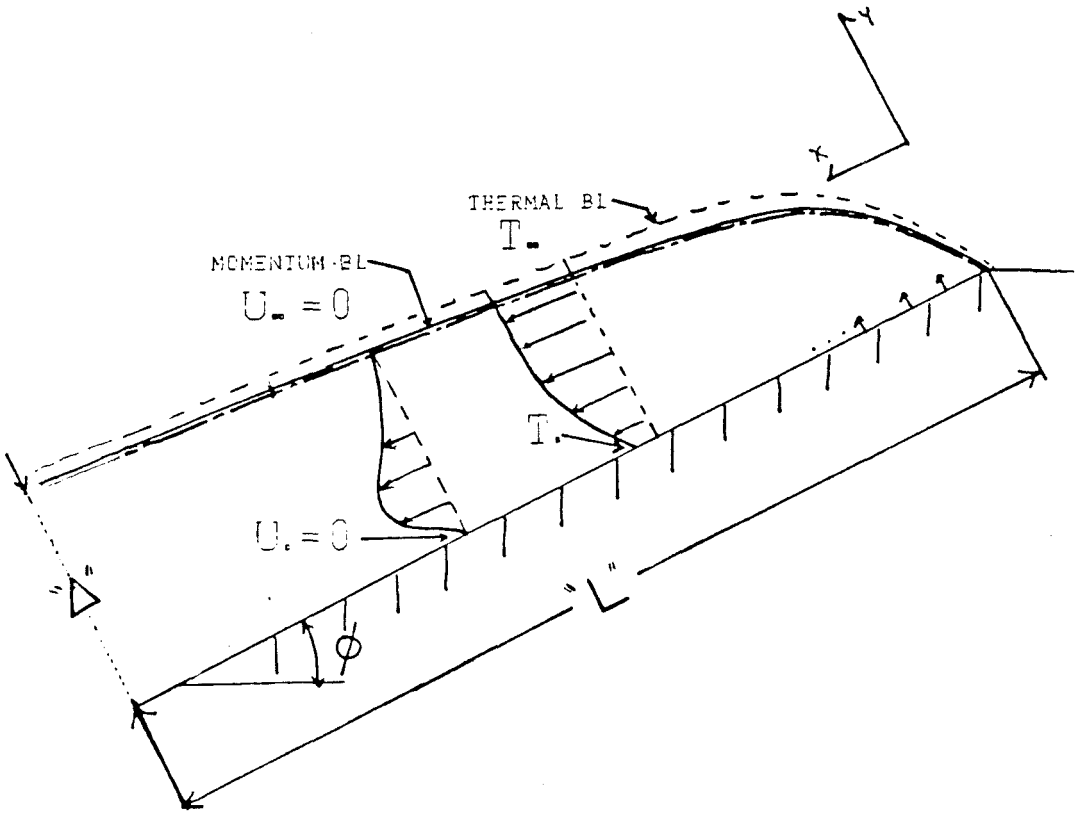

Figure 1. Velocity and temperature profiles in an idealized slope flow. The boundary layer thickness, Δ, the slope angle, ϕ, and slope length, L, are labeled.

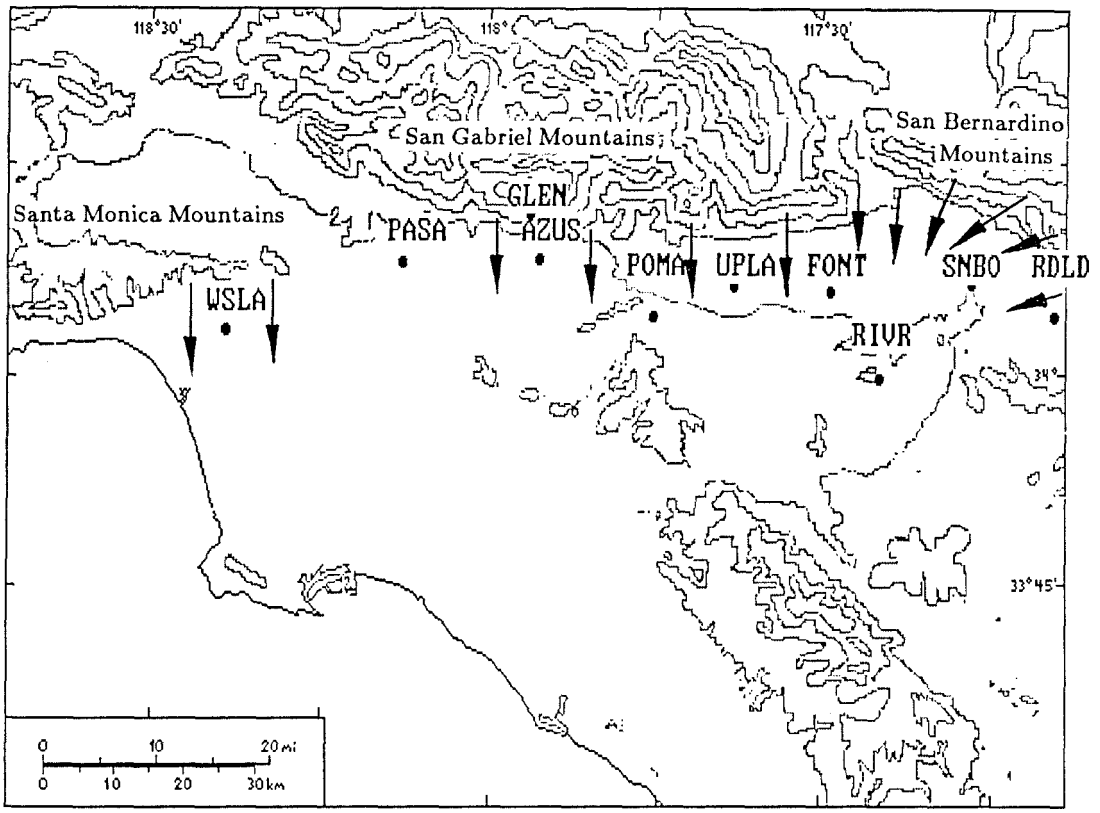

Figure 2. Slope wind measuring sites in the Los Angeles Basin. The arrows depict the nighttime downslope flow. The site abbreviations are defined in Table 1. The background lines are contour lines of elevation to highlight the location of the mountains in the basin.

may also affect the emission transport in local areas, causing variation in the wind field and mixing heights. Understanding the physics of the nighttime winds from a particular site may provide the means of analyzing the contributions of daytime slope winds at the same site.

In this paper two questions are addressed: (1) what is the nighttime ground to ambient air temperature difference which creates the buoyant conditions which drives the slope wind, and (2) why do observed nighttime slope winds from steep slopes tend to have lower speeds than their counter parts from gradual slopes?

This work was motivated primarily to provide a means to assess the particular wind fields generated by air flow simulations of the Los Angeles Basin, such as those from the Urban Airshed Model (see Chico, 1990). However, these two issues are relevant to explaining observations in any basin, both for up and downslope winds.

Method

The average wind speed, direction and associated standard deviations for each hour of the day at 31 wind monitoring sites in the basin were examined for the the summer of 1988. See Appendix A 2.3 of the section entitled "A Smog Season Examination of the LA-Glendale Divergence Zone." From this set of 31 sites, the 10 sites bordering the San Gabriel, San Bernardino, and Santa Monica Mountains were selected. See Table 1, which also includes the average slope angle and slope length associated with the mountains near each site. The time period when each site was experiencing local winds, i.e., generated on the mesoscale, was determined from the plots in Appendix A 2.4 of the section entitled, "Examination of Wind Field Dynamics Using Cross Differencing." From these data the hour of the day, the direction and the maximum speed of the wind during the period of local wind was calculated. See Table 2. The above mentioned data and the equations derived in the chapter entitled "A Comprehensive Dimensional Analysis of the Transport Properties of Atmospheric Slope Flows" are combined to estimate the maximum slope wind speed. From this estimate the differential temperature between the ground and the ambient air (above the slope wind layer) is calculated.

Site Label	Site Name	Adjacent Slope's Angle, ϕ (in degees)	Adjacent Slope's Length, L (in meters)
AZUS	Azusa	7.0	8000
FONT	Fontana	11.0	6000
GLEN	Glendora	7.7	4500
PASA	Pasadena	14.0	6000
POMA	Pomona	5.7	10000
RDLD	Redlands	3.8	30000
RIVR	Riverside	1.6	30000
SNBO	San Bernardino	3.8	30000
UPLA	Upland	13.2	10000
WSLA	West Los Angeles	2.5	7000

Table 1. Observation sites, and nearby slope's angle and length

Site Label	Hour of the Day (midnight = 0)	Max. Observed Avg. Speed, U_{Obs}^{Avg} (in m/s)	Observed Avg. Direction (degrees off north)
AZUS	5	0.9	351
FONT	4	0.5	15
GLEN	5	0.7	52
PASA	5	0.1	278
POMA	5	0.4	315
RDLD	4	0.5	108
RIVR	3	0.9	327
SNBO	4	0.4	98
UPLA	5	0.2	354
WSLA	3	0.5	348

Table 2. Nighttime slope/drainage wind characteristics

Estimation of the Maximum Slope Wind Speed

Wind data is measured at only one height above ground level, usually 9.1 meters (30 feet), at each of the sites. This presents a problem since without additional vertical wind data there is no direct way to determine how the measured speed compares to the maximum speed in the slope wind's vertical profile. However, an indirect method of determining the maximum speed from the measured speed at 9.1 meters has been devised. It proceeds through the following four steps: (1) the correct regime of the slope flow is determined from dimensional analysis, (2) the thickness of the slope flow layer is bounded, (3) the thickness is compared with the height of the measurement to see if it falls within the bounds, (4) given "(3)" is satisfied, the relationship between the maximum and measured speed is approximated. The method is developed in detail below.

To determine if the measurement height is within the slope flow boundary layer, and its relationship to the height of the actual speed maximum, the vertical thickness of the jet must be obtained. The most tenable method for obtaining this height, when it is not available by measurement, is to calculate it from its characteristic relationship to the slope parameters. To do this calculation correctly, the appropriate scaling regime for the slope flow must be determined.

The first step to determining the correct scaling regime for a slope flow is to compute the ratio of the slope's length, L, to its critical length, l_c. This ratio, defined to be

$$\lambda = \frac{\Gamma \sin\phi L}{\Theta_0 - \Theta_\infty} = \frac{L}{l_c}, \tag{1.9.1}$$

represents the most common demarkation point between regimes of atmospheric slope flows. In Equation 1 the parameters are as follows: the atmospheric lapse rate Γ, slope length L and angle ϕ, and the potential temperature difference $\Theta_0 - \Theta_\infty$. Practically, Equation 1.9.1 marks the distance, l_c, along the slope of

total length L, where the boundary layer ceases to increase in thickness. The characteristic and dimensionless parameters have different forms depending on the value of λ.

Determination of λ seems to require even more knowledge about the flow, i.e., the slope length and angle, the driving temperature difference, and the lapse rate. This turns out not to be true for several reasons, but before explaining why, consider a few facts about the parameters which make up λ. These facts may be helpful later in verifying some of the assumptions which are about to be made. In practice it can be difficult to determine L without extensive field measurement. The non-idealities in the slope surface and adequate knowledge of where the boundary layer begins along the slope being the main reasons. Frequently L is simply estimated (for downslope flows) by designating the apex of the slope as the leading edge (beginning of the boundary layer), then assigning L to the distance from there to a point along the slope. The uncertainties obtained by this approach are large, possibly 50 percent or more. (The actual boundary layer begins where a temperature difference exists, which is not necessarily the top of the slope). Next, the average potential temperature difference between the ground and the ambient air is the reason for this analysis, and if it were known this would be unnecessary. Third, the atmospheric lapse rate varys only in a small range so it presents no problems. The final parameter, the slope angle ϕ, is the key to finding λ, and mitigates the need to know the other three parameters accurately. The reason is the sinusoidal dependency of the critical length, l_c on ϕ, and the high accuracy to which ϕ can be known. Under atmospheric conditions, i.e., a wide range of lapse rates, slope lengths, and temperature differences, steep slopes (5 degrees or more) generally have $\lambda \geq 1$, and gradual slopes (1 degree or less) generally have $\lambda \geq 1$. The bounding mountains in the basin have steep slopes, and for this reason the entire analysis below is based on $\lambda \geq 1$.

The validity of this assumption is verified at a later point. Estimation of the Boundary Layer Thickness

When $\lambda \geq 1$ the relationship for the boundary layer thickness is as follows:

$$\Delta = Pr^{-\frac{1}{4}} \left[\frac{\alpha_T^2}{\Gamma(sin^2\phi)g\beta} \right]^{\frac{1}{4}}. \tag{1.9.2}$$

To evaluate Equation 1.9.2 the following values were used. The eddy diffusivity, α_T, is estimated range from 1 to 3 m^2/s, typical for the neutral to stable nighttime conditions in the basin. The lapse rate is 0.01 $(degrees\ K/m)$ which is an upper bound for this parameter. The slope angles for the cases being considered range from 1.6 to 14 degrees. The average summertime surface temperature (T) during the early morning hours is between 285 - 290 K. The thermal coefficient of volumetric expansion, $\beta = 1/T$, comes from the ideal gas law. The gravitational constant is 9.8 m/s. The Prandtl number is assumed to be of order 1. For these conditions the calculated boundary layer thickness falls between 18 and 96 meters. The wind profile due to a buoyantly driven layer is roughly parabolic, with a maximum speed approximately one third of the boundary layer up from the ground (Shair, 1987). Taking a third of this gives an estimated maximum height of from 6 to 32 meters, which bounds the height at which measurements are being taken.

Even though the wind measurements are being taken inside the slope wind boundary layer, the probability that the maximum speed is observed in any measurement is low. Thus, a reasonable assumption is the average of the observed speeds, at a site, is the average speed of the vertical boundary layer. This takes into account changes in the height of the maximum speed from measurement to measurement. The maximum boundary layer speed, U_{Obs}^{Max}, has been determined to be 1.77 times the average speed, U_{Obs}^{Avg}, by means of the approximate Von Karman-Pohlhausen solution for buoyant flows. The maximum observed speed,

U_{Obs}^{Max}, has already been shown to be 0.625 times the characteristic velocity, $U^{\star}$, under a wide range of conditions. Based on the above analysis, the wind speed that is measured at each site will be assumed to be the vertical average slope wind speed. Consequently, the characteristic velocity for the flow will be calculated as

$$U^{\star} = 2.84 U_{Obs}^{Avg}. \tag{1.9.3}$$

Without additional data it is inappropriate to refine the estimate of $U^{\star}$ further.

Determination of the Differential Temperature

The temperature driving force is determined by rearranging the characteristic equation for the slope wind velocity given below. The characteristic velocity for slope wind for $\lambda \geq 1$ is related to the slope and temperature parameters by Equation 1.9.4.

$$U^{\star} = Pr^{-\frac{1}{2}} \left[\frac{g\beta|\theta_0 - \theta_\infty|^2}{\Gamma} \right]^{\frac{1}{2}} \tag{1.9.4}$$

Rearranging Equation 1.9.4 and combining it with Equation 1.9.3 provides a means of estimating the average differential temperature for the slope flows at each site.

$$|\theta_0 - \theta_\infty| = 2.84 Pr^{\frac{1}{2}} \left[\frac{\Gamma}{g\beta} \right]^{\frac{1}{2}} U_{Obs}^{Avg} \tag{1.9.5}$$

For the calculations described in the Results section, the parameters Pr, g, β, and Γ have the values given above. The values for $U^{\star}$ were obtained from Table 2.

Slope Wind Speed and Slope Length

A graph, Figure 3, is created to show the relationship between the characteristic slope wind velocity and slope length (for $\lambda \leq 1$) which also conveys the relationship between slope angle and the critical slope length. Thus the transition to $\lambda \geq 1$ is also made clear for a wide range of slope angles. The characteristic slope wind velocity for $\lambda \leq 1$,

$$U^{\star} = Pr^{-\frac{1}{2}} \left[g(\sin\phi)\beta|\theta_0 - \theta_\infty|L \right]^{\frac{1}{2}} = \left[Pr^{-1}\sigma^2 gL \right]^{\frac{1}{2}} \tag{1.9.6}$$

is plotted as lines of constant slope strength, $\sigma = \left[(\sin\phi)\beta|\theta_0 - \theta_\infty| \right]^{\frac{1}{2}}$. Three lines of constant slope angle, ϕ, 25, 5, and 1 degree(s), are plotted on top of the first plot, such that their intersection points with the lines of constant slope strength are the critical slope length, l_c. This graph is general and can be applied under the full range of atmospheric conditions worldwide. (It has even been applied when diagnosing the potential for slope flow in the polar regions of Martian atmosphere).

From Figure 3 it is clear that the same steep slopes responsible for a large slope strength also create conditions which hasten reaching a maximum speed along the slope. This is consistent with observations of katabatic winds worldwide, i.e., the shallow slopes of Antarctica generate strong katabatic winds and the steep slopes of mountains exhibit gentle breezes.

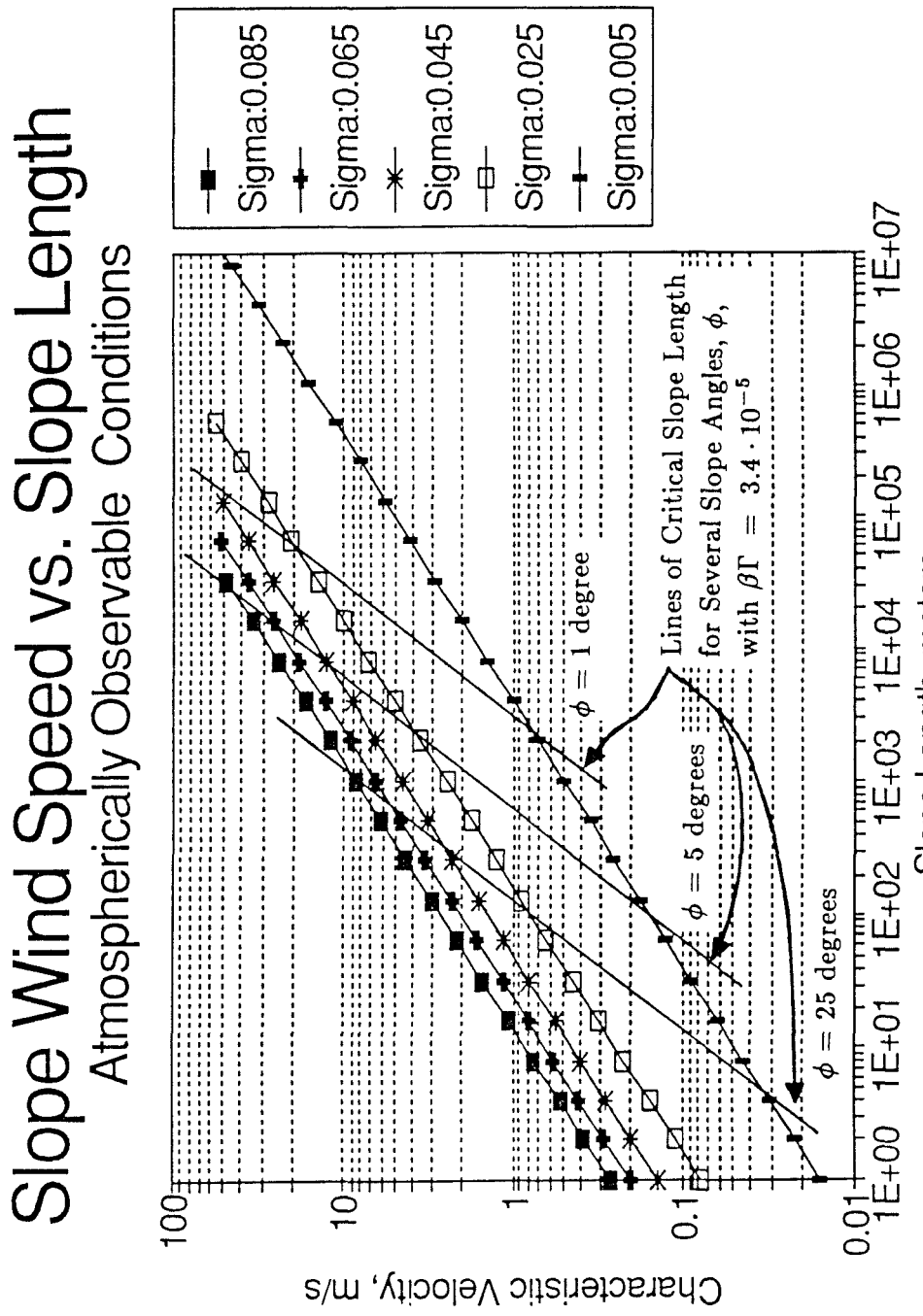

Figure 3. Characteristic slope wind velocity as a function of slope length and slope strength also showing lines of critical slope length for different slope angles.

Results

Temperature Differential

The ground-to-ambient-air temperature difference for the 10 sites, as computed from Equation 1.9.5, are compiled in Table 3. The values range from a 0.1 to 1.5 K, which is consistent with the isolated measurements made at Scholl Canyon by Shair; refer to Table 3 in the chapter entitled "A Comprehensive Dimensional Analysis of the Transport Properties of Atmospheric Slope Flows." With the temperature difference known, the critical length and λ can be determined from equation 1. The values obtained verify the original assumption that λ was in excess of 1.

Spatial Distribution of Driving Forces

Nine of the ten sites experience drainage from katabatic winds on the average. Pasadena is the only anamolous site, i.e., its average wind direction during the local wind period does not flow perpendicular to the nearby mountain range. But when one notes the slopes near Pasadena are among the steepest of those studied, and the potential for slope wind is extremely small, it is not surprising slope wind is not observed.

Quick Estimation of Slope Wind Speed

Figure 3 can be used to rapidly estimate slope flow speeds worldwide. To use the graph, compute a slope strength, σ. Using this slope strength and the slope angle, find their intersection on the graph. The velocity at this point is the maximum for that slope under the chosen conditions, the slope length at this point is l_c. The wind speed does not increase with increasing slope length beyond this point. If the actual slope length is less than l_c, then follow the line of constant slope strength down and to the left to this slope length, and read off the characteristic velocity. The parameters $\beta\Gamma = 3.4 \cdot 10^{-5}$ were picked to

Site Label	**Temp. Diff.** $\lvert\theta_0 - \theta_\infty\rvert$ (degrees K)	**Critical Slope Length,** l_c (in meters)	λ
AZUS	1.37	1100	7.3
FONT	0.77	400	15
GLEN	1.07	800	5.6
PASA	0.15	70	85
POMA	0.61	600	17
RDLD	0.77	1100	27
RIVR	1.37	4900	6.1
SNBO	0.61	900	33
UPLA	0.31	90	110
WSLA	0.77	1100	6.3

Table 3. Nighttime differential temperature, critical slope length, and dimensionless slope parameter

be average atmospheric conditions. If the values of these parameters are known very accurately for particular circumstances, it might be desirable to recompute the lines of constant ϕ. Under most conditions these lines will not be in error by more than a few percent.

If the slopes of the Los Angeles Basin were not subject to the limiting physical restrictions associated with $\lambda \geq 1$, they would be capable of generating downslope wind speeds in excess of 10 m/s. However, because these restrictions do exist, observations in the basin are restricted to the lower left regions of the plot in Figure 3. In addition, the observations presented herein support the relationship between steeper slopes having slower observed katabatic winds.

Conclusions

The critical slope length, l_c, may be more aptly called the effective slope length for steep slopes, since it really is the maximum segment of the total slope length which must be experiencing a potential temperature difference in order to create a flow. For steep slopes, the place along the slope where the katabatic wind develops may be of little importance because the critical slope length is short compared to the total slope length. For the slopes which surround the Los Angeles basin, the critical length is modest compared to the total slope lengths, 20 percent or less in all cases studied. In terms of the computation interval of numerical models, this means energy and momentum calculations along slopes should be done at intervals of 0.5 km at the most. The small temperature differences which drive the flow, on the order of a degree, and the vertical bound on the slope flow thickness of 100 meters means vertical computational resolution on the order of 30 meters or less. It is clear that considerable computational power is required to reproduce these flows accurately above any large surfaces.

Though no documented evidence is known by the author to support this claim, it is suggested that the intrusion of a large amount of stable slope air centering around Glendora and Azusa may on certain mornings initially slow the transport of western basin emissions eastward. Furthermore, the emissions from the late afternoon and evening of the previous day may be revisiting the basin by means of the slope flow drainage through Azusa and Glendora. The detailed physics of the flow from this area could be studied quite effectively using atmospheric tracers. The knowledge obtained would benefit both the conceptual model and the numerical calculations at this and other locations.

A 1.9 Appendix : Average Wind Speed and Direction for the Summer of 1988 at 31 AQMD Wind Monitoring Sites

Introduction

A number of the experiments and studies described in this thesis benefit from having a seasonal average wind speed and direction for each hour of the day at each of the 31 Air Quality Management District wind monitoring sites. The data from this composite average day can be used directly, as it is in this paper where the data from individual days would not suffice, or it can be used as a reference, as it is in later sections where the average summertime day is used to make comparisons to individual day's measurements.

The year 1988 was chosen for many reasons. One, the data was current. Two, the quality of the data could be checked through direct contact with the AQMD personnel currently responsible for it. Three, 1988 was a good year for ozone observations relative to other recent years, which is important for later uses. Only the data from one summer was used to compute the average because it eliminated possible year to year variations.

Averaging Method

Wind data was obtained from the South Coast Air Quality Management District's Telemetry System from May to September of 1988. This data was measured at 31 sites, on an hourly basis, and consists of vector-averaged wind speed and direction. The data is put into binary files consisting of one month blocks, i.e., the WIND format as described by the WIND Manual Version 2.0.

The data was averaged using the special purpose program AVEWIND, designed to accept WIND formatted data. The data averaging algorithm used by AVEWIND converts the wind speed and direction data into its vector components, performs the vector averaging and then converts the data back to its original speed and direction format. Standard deviations of the speed and direction at each site and hour are also computed by AVEWIND. These are computed from the average speed and direction. In the calculation of the wind direction standard deviation, angle differences are limited to 180 degrees.

All hours are given in Pacific Daylight Savings Time (PDT). Hour 0 is midnight (PDT), and corresponds to the data gathered from midnight up to hour 1, and so on for the remaining 23 hours.

Averaged Data

Tables 1 - 4 show the results of the averaging and the standard deviations for wind speed and direction. These results will be used and referred to throughout this thesis.

The four data sets are useful for a variety of reasons, including characterizing each site on average, and providing a means of interpreting the averages based on their uncertainty. Similarities and differences in the sites based on geographical location can also be examined using Tables 1 - 4.

Figures 1 - 10 were compiled to provide a qualitative and quantitative method by which the sites from similar geographic areas could be compared on the basis of their wind direction standard deviations. These plots provide a measure of both the site and the regional uncertainties in the wind direction at every hour.

The wind direction standard deviation plots provide a unique method of assessing the influence of certain wind patterns in a given region. To see how, consider the following example. The San Fernando Convergence zone may move across three wind monitoring sites in the Los Angeles Basin: Burbank, Reseda, and Newhall in the afternoon of any day. The zone is known to move from west to east, often impacting Reseda, frequently passing Newhall, and seldom reaching Burbank. When the divergence zone passes a site, the wind direction changes by roughly 120 degrees. Figure 1 clearly demonstrates how the east to west migration of the zone increases the uncertainty in: (1) Reseda's wind direction at about 15 PDT, (2) Newhall's wind direction two hours later, and (3) Burbank's wind direction slightly another two hours later.

Similar inferences may be made from the other figures, and using the other three sets of data.

HOUR	0	1	2	3	4	5	6	7	8	9	10	11
STATION												
CELA	1.1	0.5	0.4	0.7	0.6	0.9	0.5	0.5	1.1	1.9	2.8	3.8
WSLA	0.2	0.2	0.1	0.5	0.3	0.3	0.0	0.9	1.8	3.2	5.1	6.5
HAWT	1.4	1.2	0.8	0.5	0.6	0.6	0.4	0.7	1.1	2.6	4.8	6.9
LGBH	0.3	0.6	0.4	0.4	0.6	0.5	0.8	0.9	1.2	1.9	2.5	3.5
WHIT	0.3	0.1	0.1	0.1	0.2	0.3	0.3	0.3	0.5	1.0	1.2	2.0
RESE	0.3	0.2	0.1	0.2	0.2	0.3	0.2	0.2	0.4	0.8	0.8	1.0
BURK	1.9	1.6	1.2	1.0	0.6	0.9	0.8	1.0	1.1	1.9	2.6	3.1
PASA	0.1	0.1	0.1	0.0	0.1	0.1	0.0	0.2	0.3	0.6	0.8	1.1
AZUS	1.6	1.4	0.8	0.8	0.5	0.9	0.7	0.3	1.2	1.9	3.1	3.9
GLEN	0.3	0.3	0.4	0.5	0.6	0.7	0.6	0.2	0.6	1.4	2.1	2.7
POMA	0.9	0.8	0.6	0.5	0.4	0.4	0.4	0.3	0.7	1.1	1.8	2.8
PICO	1.9	1.1	1.0	0.9	0.7	0.5	0.8	1.1	1.5	2.8	3.9	4.7
LYNN	1.3	0.9	0.7	0.6	0.6	0.6	0.7	0.7	1.0	1.5	2.3	4.0
NEWL	0.1	0.3	0.3	0.2	0.0	0.1	0.0	0.1	0.1	0.7	2.3	4.2
LANC	1.5	1.2	1.2	0.9	1.0	0.8	0.7	0.7	1.1	1.1	1.1	0.7
LAHB	0.5	0.5	0.4	0.4	0.2	0.1	0.2	0.5	0.8	1.5	2.6	3.2
ANAH	1.1	1.0	0.9	0.8	1.0	0.7	0.9	0.9	1.4	1.9	2.8	3.8
LSAL	0.6	0.5	0.5	0.4	0.3	0.4	0.4	0.6	0.8	1.5	2.7	4.1
COST	0.4	0.3	0.2	0.1	0.2	0.3	0.3	0.4	0.8	1.6	2.2	3.0
TORO	0.9	0.6	0.6	0.7	0.6	0.6	0.8	0.8	0.8	0.8	1.1	1.4
NORC	0.7	0.7	0.5	0.4	0.4	0.3	0.5	0.5	1.1	1.3	2.6	3.8
RIVR	1.4	1.0	0.8	0.9	0.4	0.3	0.5	0.7	0.6	1.3	2.6	4.4
PERI	0.0	0.2	0.1	0.0	0.1	0.1	0.2	0.5	0.6	0.5	0.5	1.2
HEME	1.4	1.1	0.7	0.9	0.7	0.6	0.5	0.4	1.0	1.5	2.1	2.9
BANN	5.1	5.1	4.7	4.3	4.3	4.1	4.1	3.9	3.8	4.0	4.2	4.9
PLSP	6.4	5.8	5.0	4.7	4.2	3.7	3.3	2.8	1.5	0.7	0.2	0.0
UPLA	0.5	0.4	0.3	0.3	0.2	0.2	0.2	0.2	0.6	1.0	1.5	2.0
FONT	0.4	0.4	0.2	0.3	0.5	0.3	0.4	0.3	0.5	1.7	2.3	3.3
SNBO	1.3	0.9	0.8	0.5	0.4	0.2	0.4	0.4	0.5	1.0	2.0	2.7
RDLD	0.1	0.3	0.2	0.4	0.5	0.4	0.2	0.1	0.5	0.8	1.9	2.2
CRES	1.5	1.4	1.4	1.0	1.0	0.9	1.1	1.4	2.4	3.2	3.3	3.2

HOUR	12	13	14	15	16	17	18	19	20	21	22	23
STATION												
CELA	5.8	7.4	9.0	8.9	9.0	8.3	6.8	5.7	3.8	2.7	2.0	1.5
WSLA	7.5	7.5	7.9	7.6	7.2	6.3	4.7	3.0	1.7	0.9	0.7	0.3
HAWT	8.6	9.9	10.0	9.9	9.1	8.7	7.5	6.1	5.1	3.7	3.0	2.3
LGBH	4.1	4.3	4.6	4.8	5.8	5.1	4.7	3.9	3.0	1.8	0.9	0.5
WHIT	2.9	4.3	4.5	5.2	4.2	4.0	3.3	2.5	1.8	1.0	0.6	0.2
RESE	1.7	1.9	2.1	1.5	0.2	0.1	0.7	0.5	0.5	0.4	0.3	0.4
BURK	3.1	3.6	3.8	3.6	3.7	3.4	3.2	3.4	3.0	2.6	2.6	2.4
PASA	1.6	2.3	2.4	2.9	2.2	2.1	1.5	0.7	0.3	0.2	0.0	0.1
AZUS	4.6	5.9	6.5	7.0	7.3	6.6	6.3	5.3	4.0	2.9	2.3	1.8
GLEN	2.9	3.6	4.2	4.8	4.2	3.7	2.5	1.2	0.6	0.3	0.1	0.1
POMA	3.6	4.0	5.2	5.4	5.1	5.1	4.2	3.5	2.6	1.9	1.5	1.2
PICO	5.4	7.1	8.0	8.4	8.2	7.5	6.9	5.5	4.7	3.4	2.8	2.4
LYNN	6.1	7.4	8.2	8.4	8.4	7.8	7.0	6.0	4.4	3.4	2.5	1.6
NEWL	4.9	4.6	4.7	4.8	4.2	3.0	1.8	1.3	0.5	0.4	0.3	0.3
LANC	1.3	2.2	3.5	3.9	4.4	3.9	3.8	3.6	2.8	1.9	1.7	1.9
LAHB	4.4	5.4	6.0	5.9	5.9	5.2	4.8	4.1	3.0	2.1	1.5	0.8
ANAH	5.4	6.1	6.6	6.7	6.3	6.0	4.9	4.2	3.6	2.4	1.8	1.6
LSAL	4.9	5.3	5.8	5.1	4.5	3.9	3.1	2.1	1.7	1.1	0.7	0.6
COST	3.6	4.0	4.0	3.6	3.5	2.9	2.4	1.7	1.2	0.8	0.7	0.5
TORO	2.3	2.9	3.0	2.9	2.3	2.6	1.8	1.2	1.0	0.6	0.7	0.8
NORC	6.7	9.1	10.6	11.4	10.9	9.9	8.5	6.1	4.0	2.6	1.7	1.1
RIVR	5.9	7.6	8.9	10.4	10.8	9.6	7.2	4.6	3.5	2.6	2.3	1.6
PERI	2.7	3.8	5.5	6.1	7.3	6.3	4.0	1.2	0.6	0.3	0.2	0.3
HEME	4.2	5.1	5.4	7.0	7.3	7.2	6.2	4.7	3.6	2.6	2.6	1.8
BANN	4.7	4.8	5.2	6.5	7.1	8.0	7.9	7.8	6.8	5.9	5.2	5.2
PLSP	0.6	1.0	1.5	2.3	3.5	4.8	6.3	8.4	9.4	8.8	8.4	7.6
UPLA	2.5	2.8	3.1	3.4	3.4	3.2	2.9	2.6	1.9	1.5	0.9	0.6
FONT	4.3	5.3	6.4	8.0	8.2	7.7	6.6	4.4	3.2	1.6	0.9	0.6
SNBO	3.7	4.5	4.8	6.9	8.1	7.9	7.2	5.4	4.2	3.2	2.3	1.7
RDLD	3.1	3.6	4.3	4.9	5.0	4.6	3.4	2.0	1.2	0.6	0.2	0.2
CRES	3.8	3.8	4.1	4.0	4.3	3.8	3.1	2.5	2.2	1.9	1.5	1.5

Table 1. Average wind speed from 31 SCAQMD Telemetry System Sites for the period May - September 1988 at all 24 hours. Data is in units of miles per hour.

HOUR STATION	0	1	2	3	4	5	6	7	8	9	10	11
CELA	2.6	3.2	3.1	3.0	2.6	2.8	3.2	3.2	2.8	2.9	2.6	3.3
WSLA	2.4	2.8	2.3	2.2	2.4	2.3	2.8	2.5	2.4	3.0	3.4	3.6
HAWT	2.8	2.9	2.5	2.9	2.7	2.3	2.6	2.8	3.0	3.2	3.1	3.4
LGBH	2.9	2.4	2.3	2.5	2.5	2.5	2.2	2.5	2.7	2.7	2.7	2.6
WHIT	2.0	1.9	1.9	1.8	1.7	1.5	2.0	2.1	2.2	2.7	2.5	2.5
RESE	1.9	1.9	2.1	1.6	1.8	1.8	1.8	2.1	2.2	2.4	2.5	3.5
BURK	2.1	2.4	1.9	2.0	1.5	1.8	1.7	2.1	2.4	2.5	2.5	2.6
PASA	0.7	0.6	0.5	0.5	0.5	0.6	0.8	0.9	1.0	1.4	1.5	1.7
AZUS	2.1	2.0	2.2	2.3	2.5	2.3	2.4	2.6	2.1	2.4	2.2	2.4
GLEN	0.9	1.0	1.0	1.0	1.2	1.2	1.0	1.1	1.1	1.5	1.8	2.0
POMA	1.2	1.4	1.1	1.0	1.1	0.9	1.1	1.1	1.5	1.7	2.3	2.4
PICO	2.4	2.3	2.0	2.1	1.9	2.4	2.4	2.8	2.6	3.2	2.9	3.1
LYNN	2.5	2.3	2.1	2.1	2.0	1.9	2.2	2.3	2.5	2.6	3.1	3.3
NEWL	2.2	1.7	1.3	1.6	1.5	1.0	1.3	2.0	2.5	3.5	3.8	4.0
LANC	2.2	2.5	2.4	2.0	2.5	2.0	1.9	2.5	3.0	3.2	4.3	4.7
LAHB	2.3	2.2	2.1	2.2	2.2	2.3	2.4	2.5	2.4	3.0	2.7	2.7
ANAH	2.0	2.0	2.0	2.1	2.2	2.2	2.5	2.6	2.4	2.6	2.7	2.8
LSAL	2.5	2.5	2.2	2.2	2.2	2.1	2.3	2.5	2.8	2.8	3.3	3.6
COST	1.7	1.5	1.4	1.5	1.2	1.2	1.9	1.5	1.8	2.1	2.5	2.7
TORO	1.8	1.4	1.9	1.5	1.6	1.7	1.8	2.0	2.7	2.6	3.2	3.3
NORC	2.4	2.3	2.1	1.8	2.0	1.9	2.2	2.2	2.5	3.7	3.8	4.6
RIVR	3.0	2.8	2.9	3.0	2.9	2.8	3.0	5.7	3.0	4.0	3.8	3.6
PERI	1.5	1.6	1.3	1.4	1.2	1.3	1.6	2.2	2.2	3.0	3.5	4.3
HEME	2.2	2.1	1.8	2.2	1.9	1.7	2.1	2.1	2.5	2.6	2.9	3.5
BANN	3.1	3.5	3.3	3.2	3.4	3.4	3.8	4.2	5.5	6.1	6.7	6.4
PLSP	4.3	4.6	4.5	4.8	4.9	4.2	4.1	5.1	5.2	5.1	5.9	6.7
UPLA	1.0	0.8	0.8	0.9	0.8	0.9	0.9	0.9	1.0	1.2	1.2	1.2
FONT	1.7	2.2	2.0	2.0	2.0	1.9	2.6	3.2	2.5	2.8	3.5	3.3
SNBO	2.4	1.9	1.6	1.4	1.5	1.8	1.7	1.8	2.3	3.2	3.3	3.2
RDLD	1.4	1.3	1.3	1.2	1.0	1.0	1.3	1.6	2.0	2.3	2.4	2.4
CRES	3.2	3.0	3.1	3.0	2.5	3.0	3.3	3.3	3.4	3.6	4.0	4.1

HOUR STATION	12	13	14	15	16	17	18	19	20	21	22	23
CELA	3.3	3.8	3.6	3.6	3.2	3.2	3.1	3.1	2.8	2.6	2.3	2.5
WSLA	3.4	3.0	3.2	3.0	3.0	2.5	2.4	2.7	2.5	2.6	2.5	2.4
HAWT	3.1	3.6	3.0	3.0	3.1	3.3	3.4	3.1	3.4	3.0	3.0	3.0
LGBH	3.1	3.6	3.9	3.4	3.5	3.5	2.9	2.7	2.4	2.6	2.3	2.4
WHIT	3.0	3.2	3.1	3.4	2.9	3.2	2.9	2.4	2.6	2.5	2.0	2.0
RESE	2.7	3.3	3.2	4.0	5.2	5.0	4.2	3.2	2.6	2.3	1.7	1.5
BURK	3.0	3.0	2.9	3.0	2.9	3.2	2.6	2.6	2.5	2.4	2.0	2.1
PASA	1.9	2.1	2.1	2.3	2.2	1.7	1.6	1.3	0.8	0.5	0.9	0.7
AZUS	2.7	2.5	2.8	2.6	2.2	2.1	2.0	2.2	2.1	2.1	2.0	1.9
GLEN	2.4	2.6	2.7	2.6	2.4	2.5	2.1	1.6	1.6	1.4	1.1	1.1
POMA	2.7	2.9	3.1	2.7	2.7	2.7	2.6	2.3	2.2	1.9	1.8	1.5
PICO	3.4	3.7	3.3	2.8	3.4	2.7	2.6	2.4	2.7	2.3	2.3	2.5
LYNN	3.2	3.4	3.3	3.2	3.0	3.1	2.3	2.6	2.3	2.2	2.3	2.5
NEWL	4.0	3.8	3.3	3.6	3.8	3.5	3.3	2.7	2.1	1.8	1.5	1.5
LANC	4.9	4.8	4.3	4.1	4.2	4.2	3.5	3.2	2.7	2.5	2.1	2.4
LAHB	2.9	2.9	3.0	2.8	3.0	2.8	2.6	2.6	2.4	2.7	2.4	2.3
ANAH	2.9	2.5	2.8	2.6	2.8	2.4	2.4	2.3	2.2	2.5	2.2	2.1
LSAL	4.0	4.2	4.8	4.5	4.1	3.8	3.5	2.9	2.5	2.2	1.9	1.7
COST	3.0	3.3	3.0	3.0	2.9	2.8	2.4	2.1	1.8	1.6	1.6	1.3
TORO	3.7	3.7	3.9	3.6	3.5	3.1	2.8	2.4	2.0	1.8	1.6	1.7
NORC	4.9	4.6	4.6	4.3	4.2	3.9	3.9	3.2	3.0	2.9	2.8	2.5
RIVR	3.8	4.3	4.3	4.9	4.8	4.2	3.7	3.1	2.9	2.6	2.5	2.4
PERI	4.5	4.7	4.5	4.5	4.7	4.3	4.3	4.5	3.8	3.2	3.0	2.6
HEME	3.7	4.2	4.1	3.7	3.5	2.7	2.6	2.0	2.0	2.1	2.3	2.3
BANN	6.5	6.3	5.7	5.2	4.8	5.0	4.5	4.2	3.4	3.6	3.3	3.4
PLSP	7.1	7.4	7.3	6.6	6.2	5.9	5.6	5.8	6.1	5.5	5.4	5.2
UPLA	1.2	1.4	1.2	1.3	1.3	1.2	1.2	1.1	1.1	1.2	1.1	1.1
FONT	3.0	3.6	3.4	6.3	3.4	3.1	2.9	2.5	5.3	2.2	2.0	1.9
SNBO	3.4	3.6	3.9	3.9	3.7	3.5	2.8	2.8	2.4	2.1	1.9	1.9
RDLD	2.6	3.0	3.0	3.1	2.8	2.5	2.4	1.9	1.7	1.3	1.6	1.2
CRES	3.8	4.5	3.9	4.0	3.5	3.7	3.7	3.6	3.4	3.4	3.5	3.8

Table 2. Standard deviation of the wind speed from 31 SCAQMD Telemetry System Sites for the period May - September 1988 at all 24 hours. Data is in units of miles per hour.

HOUR	0	1	2	3	4	5	6	7	8	9	10	11
STATION												
CELA	253	259	311	346	3	30	28	143	185	200	197	213
WSLA	333	341	356	348	332	344	327	181	190	211	219	222
HAWT	235	218	204	186	147	155	118	163	184	230	251	257
LGBH	298	238	178	70	80	95	107	114	163	184	191	200
WHIT	258	59	46	27	44	65	61	97	183	211	202	216
RESE	105	107	125	129	143	152	189	162	122	109	112	125
BURK	144	151	170	177	196	196	202	194	180	164	145	151
PASA	228	240	258	273	270	278	247	163	159	184	185	196
AZUS	264	275	280	298	318	351	352	258	232	228	229	233
GLEN	42	37	40	42	48	52	61	175	203	222	225	232
POMA	306	301	310	321	315	321	302	234	231	251	270	279
PICO	195	189	182	167	161	167	209	229	219	211	221	220
LYNN	249	244	226	223	216	198	194	196	199	204	210	226
NEWL	103	107	121	111	107	111	85	1	306	293	176	164
LANC	188	187	172	169	167	169	184	190	198	190	198	178
LAHB	242	280	329	354	73	29	138	200	250	249	246	249
ANAH	195	186	178	162	162	140	131	162	187	202	217	220
LSAL	278	315	308	342	17	358	13	19	302	264	255	251
COST	244	245	285	2	18	33	32	12	206	190	208	209
TORO	121	118	121	114	116	106	115	153	177	218	248	256
NORC	224	224	216	211	191	192	196	226	318	326	294	290
RIVR	318	318	326	327	314	313	281	202	215	254	271	290
PERI	317	113	77	117	133	194	151	123	130	83	49	16
HEME	186	183	179	176	160	166	191	288	274	265	255	248
BANN	265	264	264	265	275	273	263	253	247	235	226	223
PLSP	317	319	316	315	314	314	312	297	224	188	151	148
UPLA	315	326	336	343	350	354	354	149	184	217	226	240
FONT	315	348	354	0	15	12	18	157	194	219	235	233
SNBO	194	193	151	141	98	53	83	101	183	215	218	216
RDLD	99	103	108	108	108	110	108	343	297	289	282	285
CRES	251	254	243	257	257	255	246	204	148	152	167	187

HOUR	12	13	14	15	16	17	18	19	20	21	22	23
STATION												
CELA	226	238	244	247	249	253	249	249	242	234	229	237
WSLA	233	238	238	243	240	240	234	228	213	209	210	292
HAWT	260	262	264	271	270	269	272	267	262	254	245	246
LGBH	210	222	236	248	260	270	269	273	273	281	278	285
WHIT	216	212	220	223	238	243	249	251	254	241	254	232
RESE	113	126	123	117	110	83	101	105	128	119	104	106
BURK	159	169	180	175	164	148	140	135	135	132	136	137
PASA	208	205	218	224	225	233	230	229	227	214	211	215
AZUS	237	237	234	238	242	243	242	240	246	246	248	257
GLEN	233	227	235	233	233	235	241	249	264	288	338	28
POMA	270	273	268	270	265	271	275	279	287	289	292	294
PICO	220	221	226	226	230	231	227	227	222	213	209	197
LYNN	241	245	252	258	259	258	259	260	257	254	247	242
NEWL	164	172	166	175	181	190	196	199	148	126	108	112
LANC	177	186	181	188	190	181	199	202	202	195	192	190
LAHB	245	246	238	246	244	244	242	245	238	237	237	245
ANAH	227	229	229	226	226	223	224	224	219	213	211	202
LSAL	248	244	249	250	257	266	275	278	283	281	283	275
COST	211	219	224	226	230	238	237	232	238	231	224	230
TORO	261	257	250	255	264	254	253	246	236	209	160	145
NORC	281	279	283	285	289	289	294	293	300	299	281	255
RIVR	287	284	281	285	279	282	277	281	286	292	301	314
PERI	348	341	324	322	317	321	330	3	55	92	131	54
HEME	245	239	236	232	234	232	232	223	222	204	193	187
BANN	219	231	236	243	243	242	244	241	248	257	265	263
PLSP	146	111	170	91	315	329	325	319	322	321	324	324
UPLA	249	255	253	251	256	255	254	257	264	271	285	299
FONT	241	244	254	257	255	255	248	245	247	244	258	265
SNBO	219	220	216	220	225	222	216	212	210	212	208	201
RDLD	285	285	285	275	271	267	271	278	294	298	358	93
CRES	200	198	207	223	218	204	194	202	224	232	242	244

Table 3. Average wind direction from 31 SCAQMD Telemetry System Sites for the period May - September 1988 at all 24 hours. Data is in units of degrees; the direction is that from which the wind is blowing.

HOUR STATION	0	1	2	3	4	5	6	7	8	9	10	11
CELA	80	91	86	85	92	93	95	89	73	66	54	54
WSLA	93	91	89	77	85	87	89	86	75	59	44	38
HAWT	77	81	85	87	84	79	91	81	76	72	51	38
LGBH	96	101	102	102	96	94	95	86	78	74	63	54
WHIT	98	93	88	85	78	78	82	88	90	80	76	66
RESE	70	75	78	85	87	91	97	94	86	74	77	75
BURK	61	65	69	73	74	71	69	74	78	67	61	63
PASA	79	85	84	84	76	90	94	79	74	74	68	65
AZUS	62	70	77	78	85	79	84	99	74	62	50	45
GLEN	92	85	82	69	65	60	66	85	69	57	47	45
POMA	61	62	72	80	89	84	94	80	67	69	59	48
PICO	55	67	70	77	81	90	100	89	76	61	46	49
LYNN	64	68	73	78	79	77	79	78	71	64	61	45
NEWL	77	76	77	67	70	74	73	86	84	91	79	66
LANC	55	72	67	74	66	67	80	90	82	83	88	88
LAHB	95	98	95	98	101	94	102	95	87	71	59	54
ANAH	68	75	77	78	79	82	83	76	70	66	55	47
LSAL	88	96	99	96	98	96	94	95	89	79	73	66
COST	91	95	94	88	94	97	90	94	101	91	77	74
TORO	80	80	82	77	81	80	74	80	82	77	67	72
NORC	76	74	76	78	79	77	76	87	88	78	68	66
RIVR	75	76	89	74	90	86	89	84	82	80	67	62
PERI	101	99	96	101	97	93	94	82	89	86	88	90
HEME	61	62	74	73	84	77	89	82	63	64	58	58
BANN	32	34	38	43	38	43	54	60	70	72	71	68
PLSP	34	42	38	44	41	49	52	79	82	87	91	93
UPLA	61	66	64	68	63	60	72	81	66	63	50	44
FONT	77	72	79	70	70	68	73	93	69	54	50	49
SNBO	78	91	84	88	85	92	81	86	80	75	64	60
RDLD	84	79	75	70	64	64	67	92	80	66	50	53
CRES	58	57	63	60	61	58	70	74	55	57	59	59

HOUR STATION	12	13	14	15	16	17	18	19	20	21	22	23
CELA	40	35	29	30	25	23	29	33	44	54	66	73
WSLA	32	30	29	28	29	31	36	52	68	85	90	99
HAWT	23	19	19	17	20	16	22	25	39	40	51	68
LGBH	51	53	52	50	49	55	39	42	51	65	81	90
WHIT	62	48	44	42	47	51	52	53	57	67	76	91
RESE	70	67	66	77	94	93	104	100	88	83	79	75
BURK	57	60	59	60	56	62	59	51	59	61	52	57
PASA	54	48	41	36	40	34	31	43	51	60	68	72
AZUS	43	33	34	30	27	25	22	27	45	54	59	65
GLEN	48	41	41	37	34	32	37	60	74	82	90	92
POMA	48	40	40	33	33	30	32	33	35	46	49	59
PICO	42	39	30	28	30	29	27	29	29	35	42	44
LYNN	39	32	29	27	22	27	27	25	29	34	45	55
NEWL	60	52	53	51	56	62	78	88	97	89	77	77
LANC	87	75	65	64	63	60	58	49	47	50	50	49
LAHB	48	38	32	35	35	38	37	40	46	62	71	88
ANAH	39	33	28	29	32	32	34	37	39	49	57	64
LSAL	66	64	63	64	64	62	63	64	64	73	80	86
COST	71	68	67	67	66	63	64	66	70	74	80	81
TORO	65	57	57	58	61	55	59	62	74	87	96	89
NORC	49	40	36	30	30	30	26	29	44	58	68	76
RIVR	46	40	35	34	30	28	32	39	49	53	56	72
PERI	82	72	61	57	57	60	68	88	88	97	98	89
HEME	59	58	60	48	43	41	34	32	42	45	42	51
BANN	66	68	66	57	50	48	46	36	31	30	29	30
PLSP	101	93	102	99	102	95	83	54	35	25	32	35
UPLA	35	35	33	29	30	30	29	27	37	45	48	60
FONT	39	40	34	32	26	24	25	26	41	61	67	81
SNBO	51	47	49	38	36	35	28	34	42	45	64	75
RDLD	47	45	38	39	35	33	34	47	73	92	88	91
CRES	54	58	57	58	54	57	66	69	66	65	69	66

Table 4. Standard deviation of the wind direction from 31 SCAQMD Telemetry System Sites for the period May - September 1988 at all 24 hours. Data is in units of degrees.

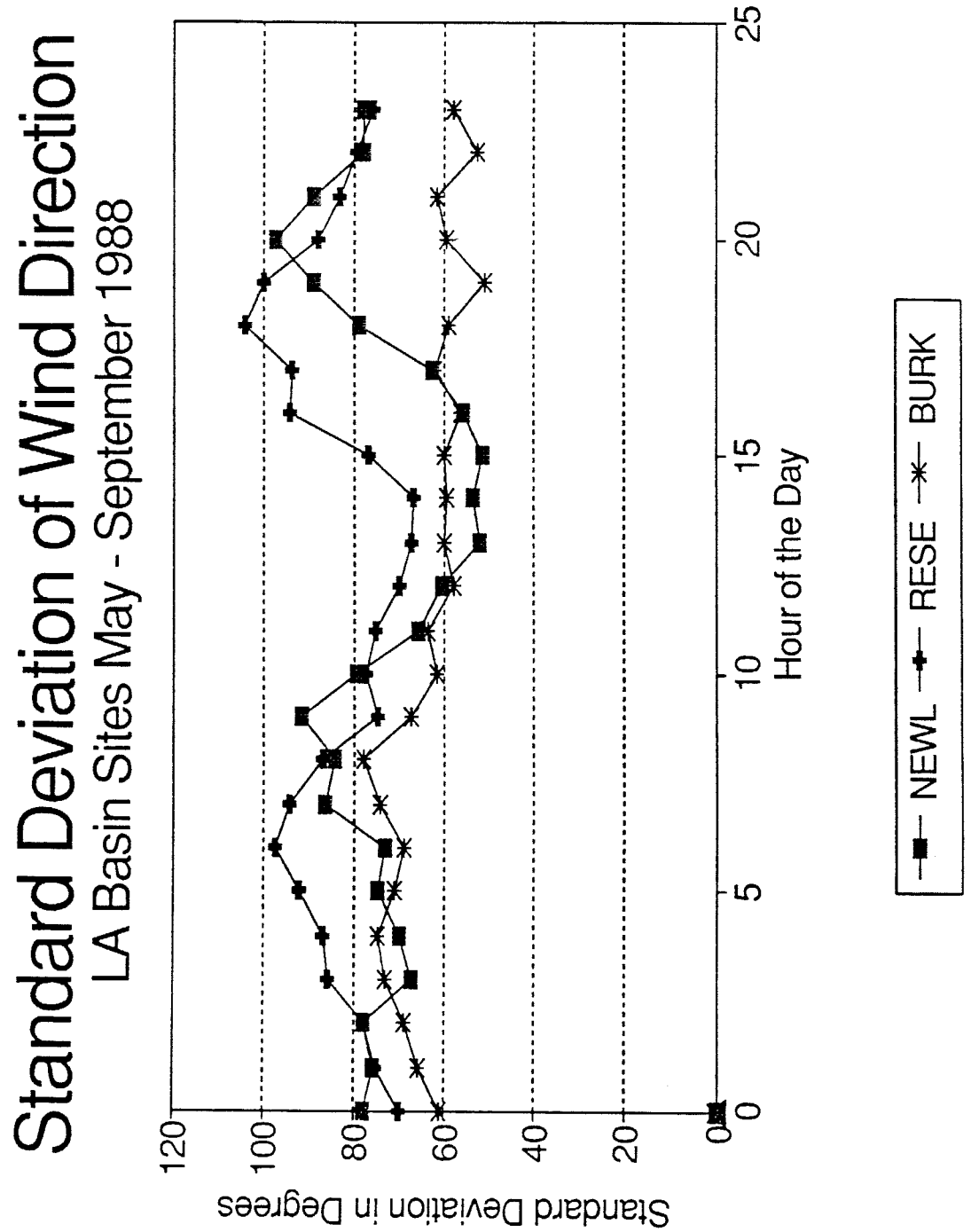

Figure 1. Northwestern Basin Sites in the San Fernando Valley

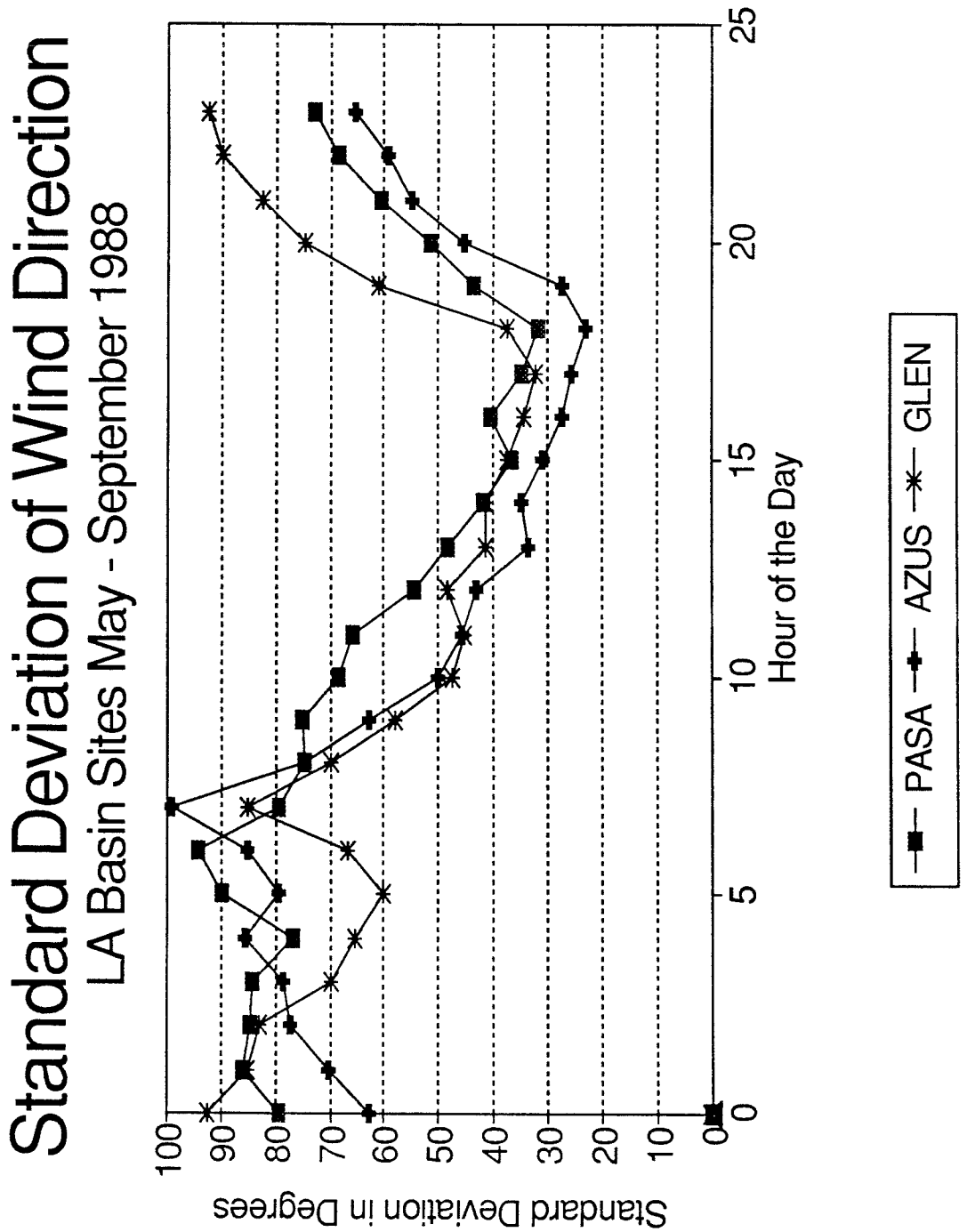

Figure 2. Northern Basin Sites Bordering Mountains

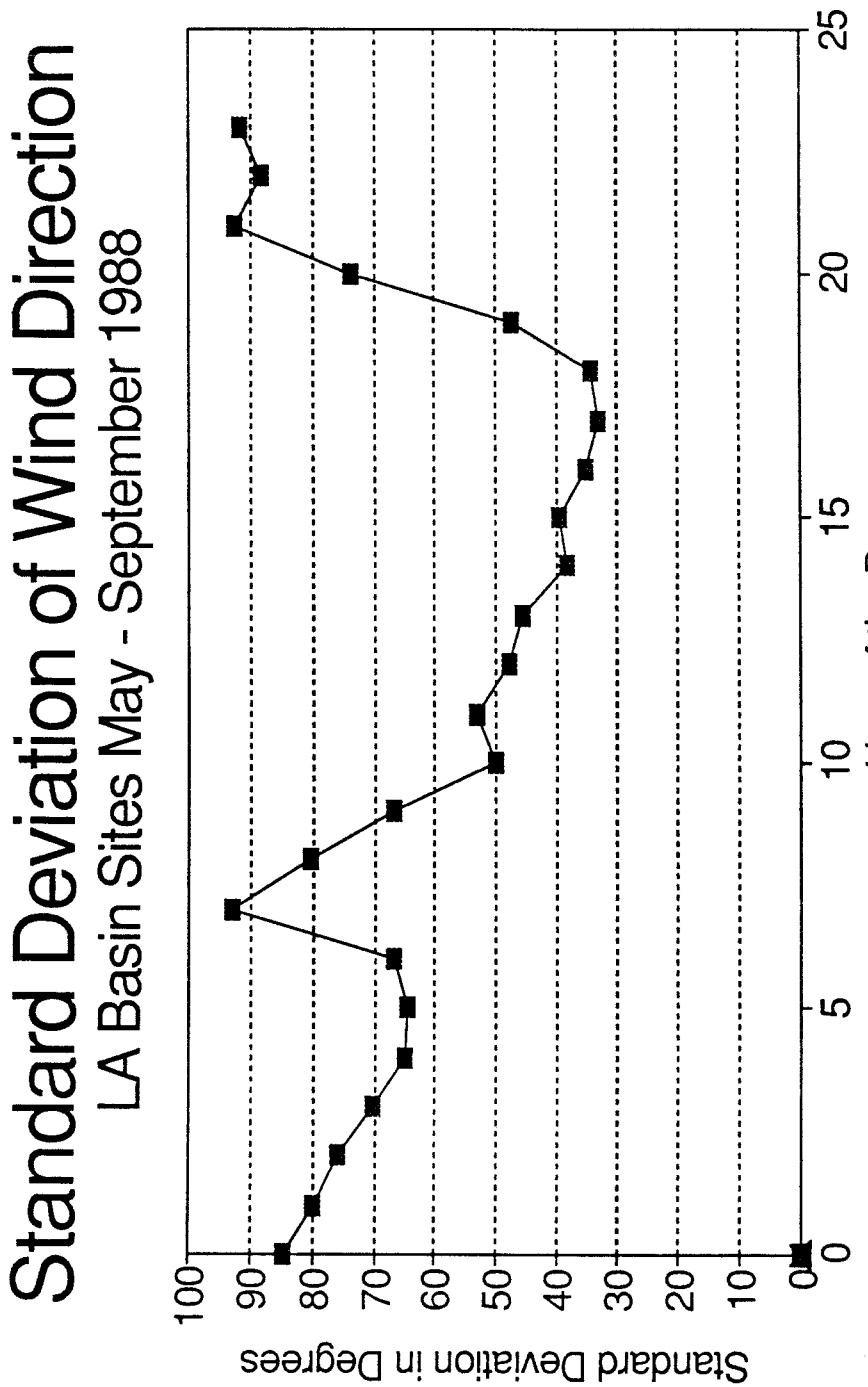

Figure 3. North Central Site Bordering Mountains with a Strong Nightime Slope Flow

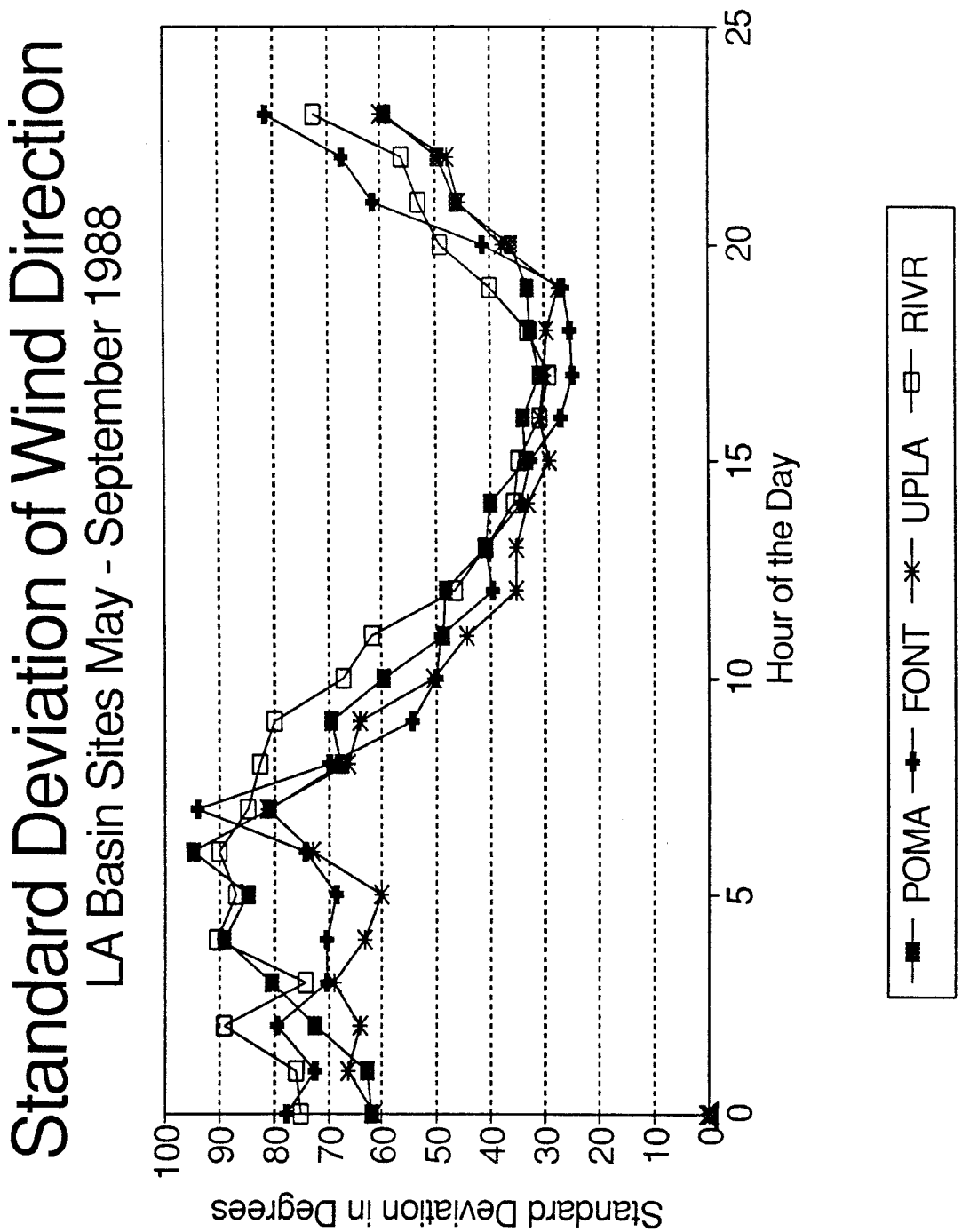

Figure 4. Eastern Basin Sites (1)

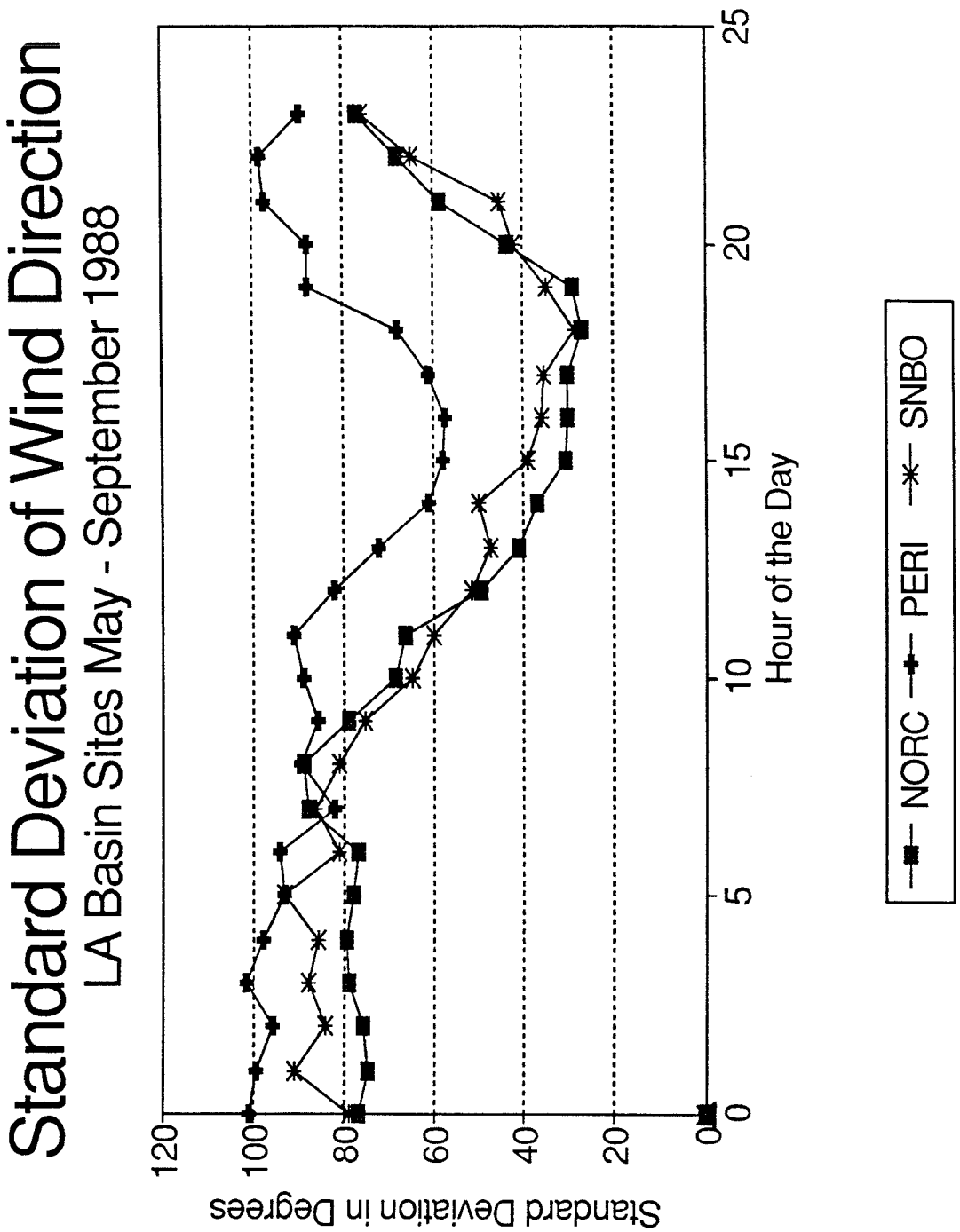

Figure 5. Eastern Basin Sites (2)

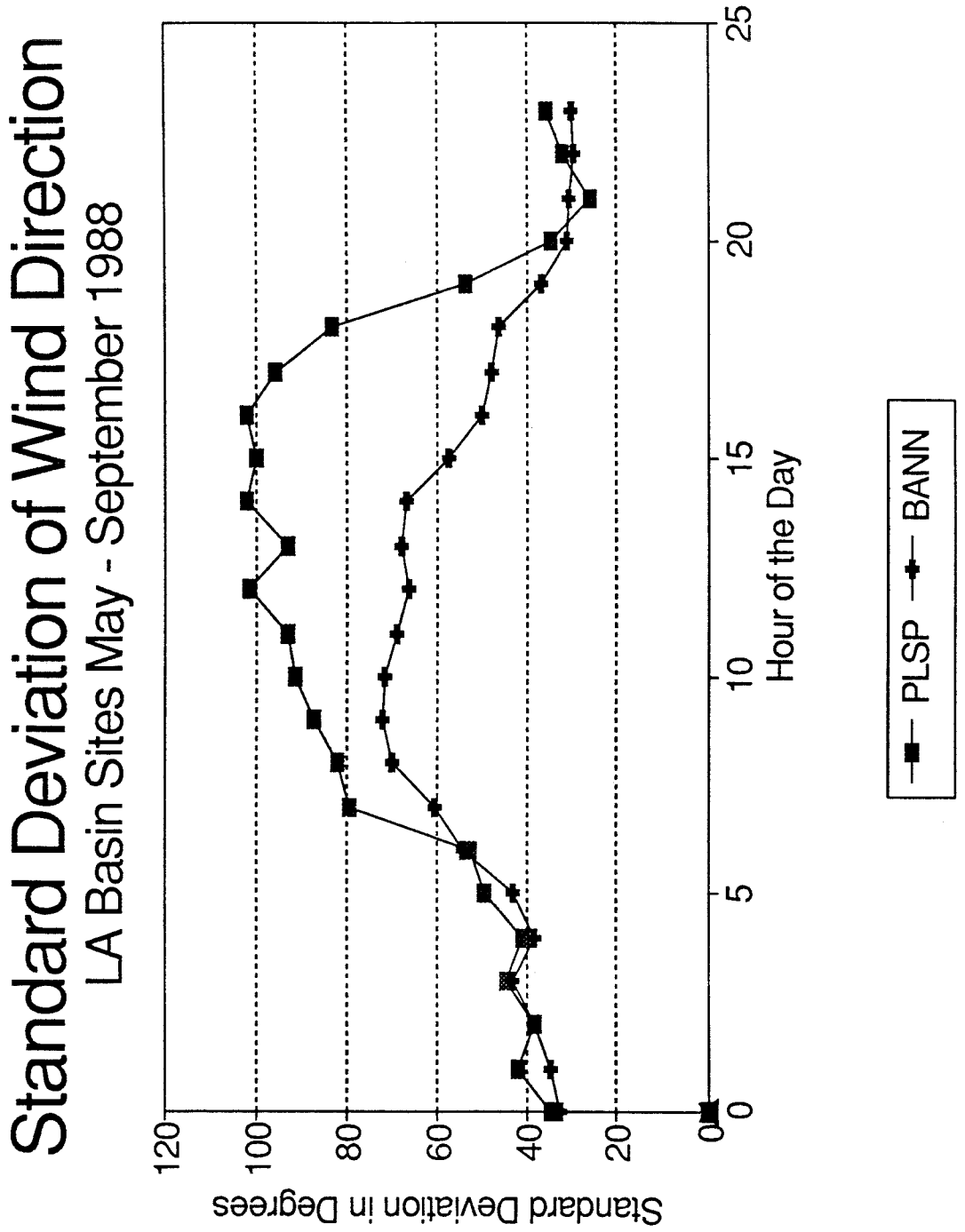

Figure 6. Eastern Desert Sites

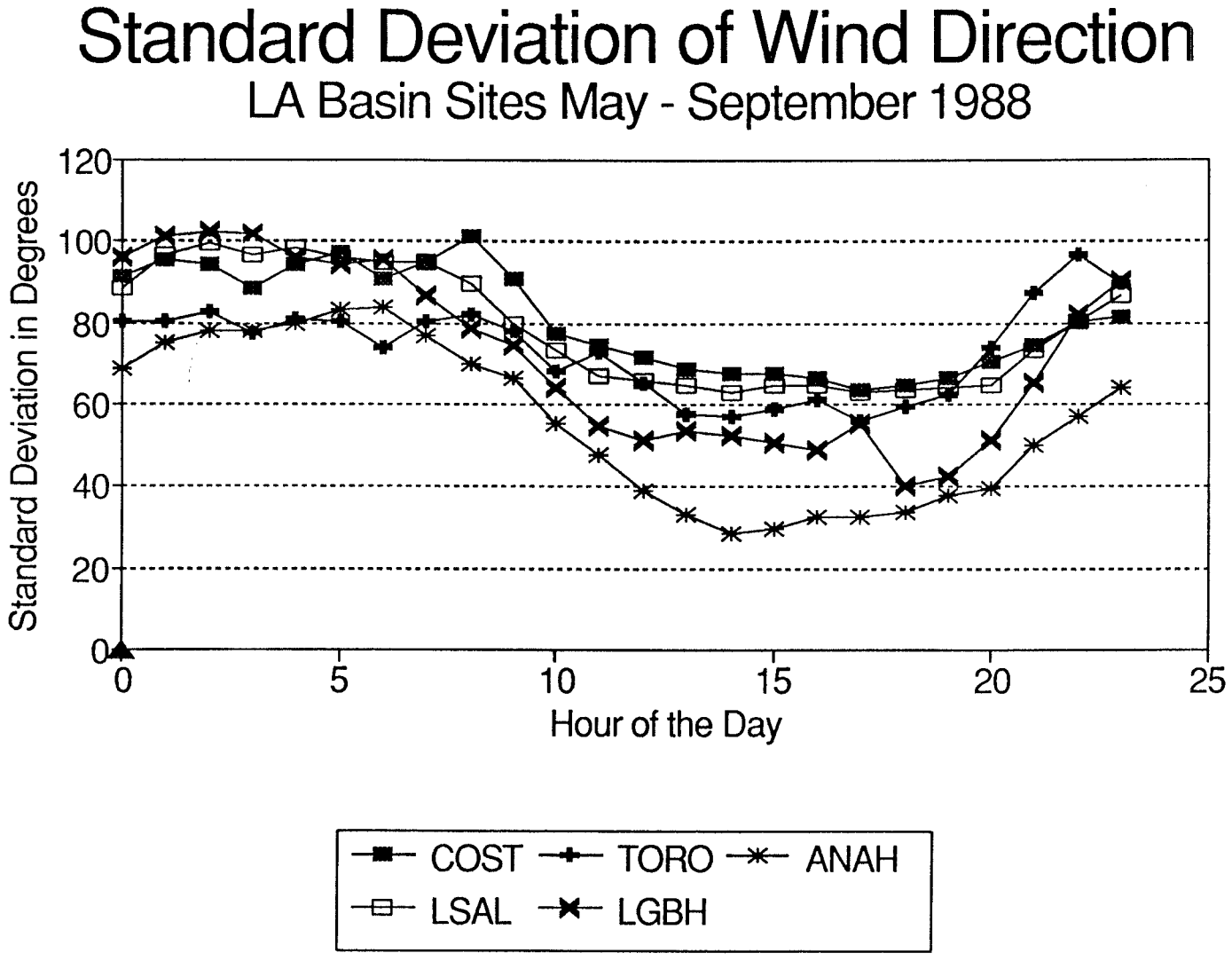

Figure 7. Southwestern Coastal Regions

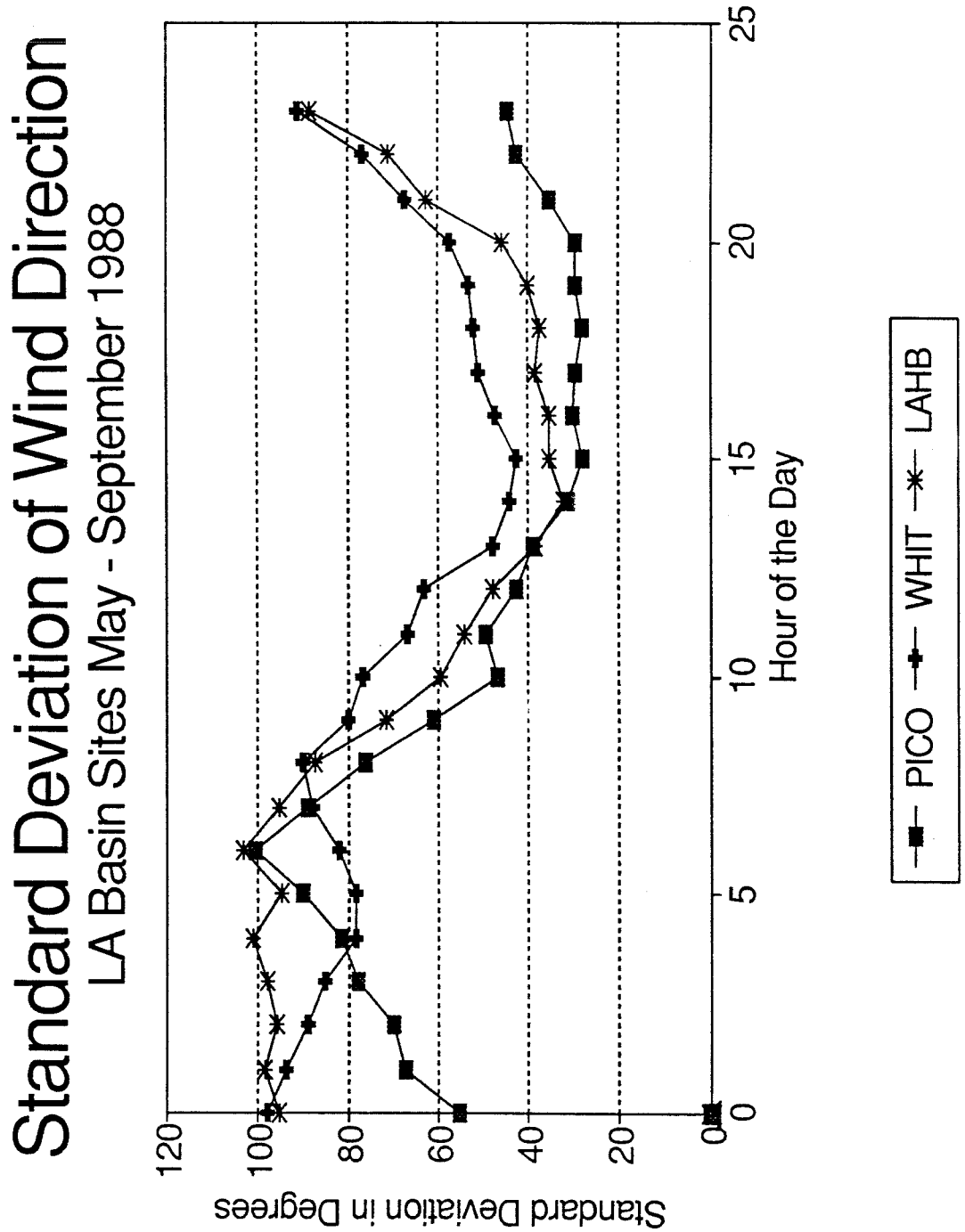

Figure 8. Central Basin Sites

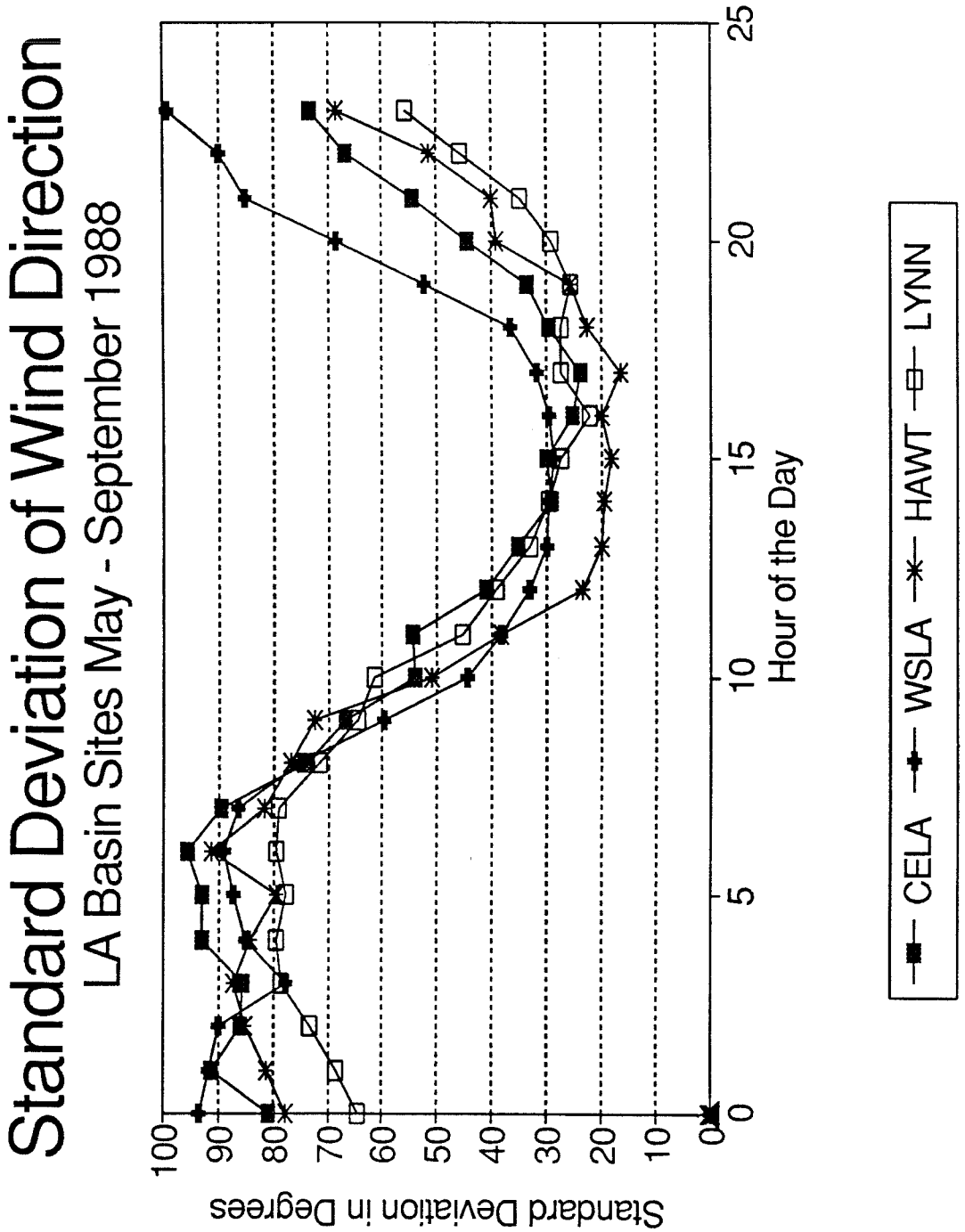

Figure 9. Downtown and Western Coastline Sites

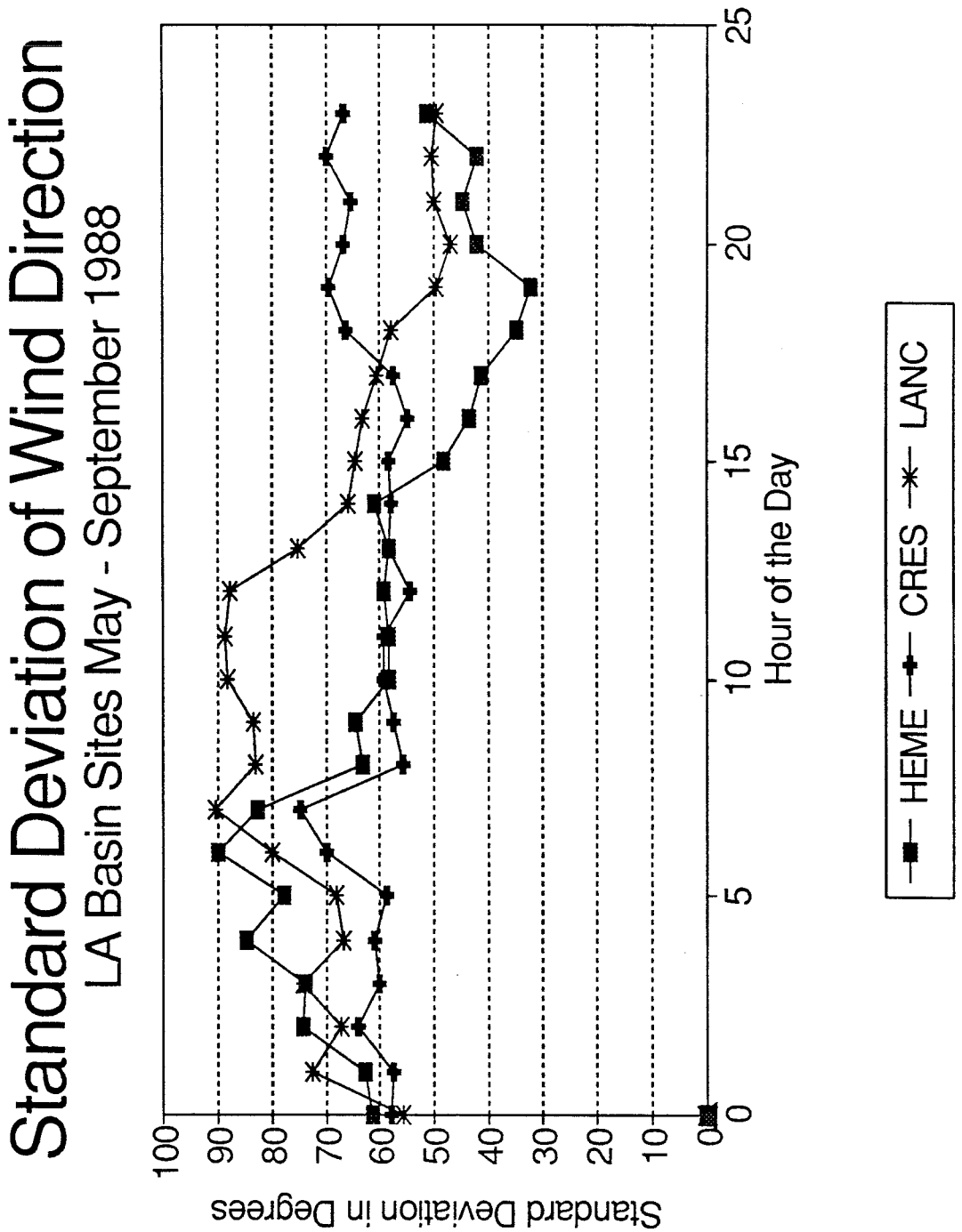

Figure 10. Sites on the Basin's Perimeter

References

1. Arritt R. W. and Pielke A. R. (1986), Interactions of nocturnal slope flows with ambient winds, Boundary-Layer Meteorology, **37** no. 1/2, pp. 183-195.
2. Ball F. K. (1956), The theory of strong katabatic winds, Aust. J. Phys., **9**, pp. 373-386.
3. Banta R. M. (1982), Thesis: An observational and numerical study of mountain boundary-layer flow, Department of Atmospheric Science, Colorado State University, paper no. 350.
4. Buettner K. J. K. and Thyer N. (1966), Valley winds in the Mt. Reinier area, Arch. Met. Geoph. Biok., **14**, pp. 125.
5. Burmeister L. C. (1983), Convective Heat Transfer, Chapter 12, John Wiley and Sons, pp. 511-575.
6. Chiba O. and Kobayashi S. (1986), A study of the structure of low-level katabatic winds at Mizuho Station, East Antartica, Boundary-Layer Meteorology, **37** no. 1/2, pp. 343-355.
7. Chico T. et al. (1990), Assessing urban airshed model performance in the South Coast air basin using tracer gases, Air Quality Mangagement Draft Report.
8. Defant F. (1951), Local winds. Compendium of Meteorology. American Met. Soc. Boston, pp. 655-672.
9. Doran J. C. and Horst T.W. (1982-3), Observations and models of simple nocturnal slope flows, J. Atmos. Sci., **40**, pp. 708-717.
10. Ellison T.H. and Turner J.S. (1959), Turbulent entrainment in stratified flows, J. Fluid Mech., **6**, pp. 423-448.
11. Fitzjarrald D. R. (1984), Katabatic wind in opposing flow, J. Atmos. Sci. **41**, pp. 1143-1158.
12. Gosink J. P. (1987), Entrainment by katabatic winds in Adelie Land, Antarctica, Preprints Third International Symposium on Stratified Flows, **2**.
13. Gutman L. N. (1983), On the theory of the katabatic slope wind, Tellus, **35A** no 3, pp. 213-218.
14. Horrell R. S. (1987), Atmospheric buoyancy driven downslope flows with entrainment from a ground source, Masters Thesis, Department of Chemical Engineering, California Institute of Technology, Pasadena, CA 91125.
15. Huppert E., Stephen R., Sparks J., Wilson J. R. and Hallworth M. A. (1986), Cooling and crystallization at an inclined plane, Earth and Planetary Science Letters, **79**, pp. 319-328

16. Kondo J. and Sato T. (1988), A simple model of drainage flow on a slope, Boundary-Layer Meteorology, **43**, pp. 103-123.
17. Leslie L. M. and Smith R.K. (1974), A numerical study of katabatic winds and their effect on pollutant dispersal in urban areas, Australasian Conf. on Hydraul and Fluid Mech, 5th, Proc, Univ. of Canterbury, Christchurch, NZ pp. 553-560.
18. Mahrt L. (1982), Momentum Balance of Gravity Flows, American Met. Soc., **39**, pp. 2701-2711.
19. Manins P. C. and Sawford B. L. (1979), Katabatic winds: A field case study, Quart J. R. Met. Soc., **105**, pp. 1011-1025.
20. Manins P. C. and Sawford B. L. (1979), A model of katabatic winds, Journal of Atmospheric Sciences, **36**, pp. 619-630.
21. Ohata T. and Higuchi K. (1979), Gravity Wind on a Snow Patch, Journal of the Meteorological Society of Japan, **36**, pp. 254-263.
22. Pielke R. A. (1984), Mesoscale Meteorological Modeling, Academic Press, Inc., pp. 23-41.
23. Prandtl L. (1952), Essentials of Fluid Dynamics, Blackie and Son Limited, pp. 452. (Also available in its original form in German, 1942.)
24. Rao K. S. and Snodgrass H. F. (1981), A nonstationary nocturnal drainage flow model, Boundary-Layer Meteorology, **20**, pp. 309-320.
25. Tennekes H. and Lumley J. L. (1972), A First Course in Turbulence, The MIT Press, pp. 27-58.

Chapter Two

A Study of Atmospheric Transport and Dispersion Near a Two-Dimensional Divergence Zone

Section 2.1

Published and presented as part of the Air and Waste Management Association's 82nd Annual Meeting, June, 1989.

Submitted for Publication in Atmospheric Environment.

89-138.2

Ground Release SF_6 Tracer Experiments Used to Characterize Transport and Dispersion of Atmospheric Pollutants During the Southern California Air Quality Study of 1987

Robin Scott Horrell, Michael Deem, Peter Wyckoff, and Fred Shair
Chemical Engineering, California Institute of Technology
Pasadena, CA 91125

and

Neil Crawford
Chemical Engineering, University of California, Berkeley
Berkeley, CA 94704

March 25, 1989

ABSTRACT

As part of the 1987 South Coast Air Quality Study (SCAQS) program, 4 SF_6 tracer tests were conducted. The tracer results help document the transport and dispersion of the air over downtown Los Angeles. An objective trajectory algorithm was developed in order to use both surface and upper level winds to help interpret the tracer data.

Based upon the spread of the tracer during the summer, the effective horizontal eddy diffusivity was estimated to be of order 10^4 meters^2/second. Negligible "carry over" was observed during the summer.

The extent of "carry over" during the winter was estimated from mass balances of the tracer. During the winter studies, the residence time of the tracer within the Los Angeles Basin exceeded 36 hours.

The relationship of the tracer to observations of elevated pollutant concentrations are examined.

INTRODUCTION

Los Angeles has had one of the most comprehensive pollution control programs in the country. Despite this effort many of the inhabitants of the LA Basin are exposed to ozone concentrations which exceed the federal standard more than 1 out of every 3 days, Davidson[1], (1986). By carefully considering the effects of meteorology, Davidson has shown that the control program has lead to a steady decline in ozone exposure. Yet the rate of decline he reports over the 1976-1984 period, if extrapolated, is not enough to bring Los Angeles into compliance with the Clean Air Act until beyond the year 2000. In addition to ozone, other airborne pollutants such as carbon monoxide, nitrogen dioxide, and PM_{10} often exceed both state and federal standards. Clearly measures which go beyond those already in effect need to be devised, studied, and then implemented in order to improve the basin's air quality.

Relatively speaking, a great deal is known about the transport and dispersion that takes place during the daily on-shore flow meteorological regime. Much less is known about the characteristic of the **nighttime off-shore flow** meteorological regime. Still less is known about the **morning and evening transition regimes** which often coincide with the so-called "rush hours". Almost nothing is known about the impact of emissions which are **transported out to sea** during the night and then returned during the subsequent on-shore flow. Likewise, almost nothing is known about pollutants that are transported into the surrounding mountains during the daytime **up-slope flow** and returned during the subsequent nighttime **down-slope flow.** Finally, almost nothing is has been documented regarding the influence of the **winds "aloft"** upon the transport and dispersion of pollutants throughout the Los Angeles basin. In short, more needs to be documented and understood about **(i) flows across the boundaries of the region of interest, (ii) the transition regimes, and (iii) the flows aloft.** This information is essential for the efficient development of new control measures aimed at improving air quality.

Thus, four sulfur hexafluoride (SF_6) tracer studies were conducted in order to document the transport and dispersion of certain ground level emissions during the Southern California Air Quality Study (SCAQS) in 1987. Although not all of the above mentioned needs could be addressed in only 4 tests, the above issues were kept in mind during the planning the tracer tests. The SF_6 tracer releases were coordinated with experiments conducted by Tracer Technologies Inc. and Southern California Edison that involved the release of perfluorocarbons near ground level and aloft, England[2] et al., (1989).

The tracer studies were conducted (i) to help improve forecast models, and (ii) to provide data to test numerical model simulations which attempt to predict pollution levels throughout the Los Angeles basin. The SF_6 tracer studies were designed to quantitatively document the transport and dispersion of emissions released in downtown Los Angeles during the morning and evening transition

regimes. Two SF_6 studies were conducted during the summer, and two during the fall.

An objective interpolation and extrapolation model, referred to as **WIND**, was developed in order to rapidly utilize the South Coast Air Quality Management's (SCAQMD) wind telemetry data. Currently **WIND** is run on an IBM PS2 personal computer with a high resolution color monitor. **WIND** used both surface and upper level air data to develop trajectories. The tracer data and the wind trajectories were used to help clarify the mechanisms and patterns of atmospheric transport.

The purpose of this report is (i) to present the pertinent data concerning the transport and dispersion of morning and evening emissions from downtown Los Angeles, and (ii) to discuss the implications of these data.

Brief Review of Previous Studies

Various aspects of the local meteorology have long been known. Edinger[3,4] (1959) described the marine layer and its affect on the meteorology of the basin, and the distribution of photochemical smog (1973). Information on the three-dimensional transport of pollutants, and carry over in the Los Angeles region during a smog episode was reported by Blumenthal[5] et al. (1977), and Bytnerowitcz[6] et al. (1987).

Shair[7] et al. were the first to use a gaseous tracer to quantitatively study the transport and dispersion associated with the land breeze/sea breeze circulation system. They found that elevated emissions released during the nighttime off-shore flow could significantly impact the air quality during the subsequent on-shore flow regime. They also found certain quantitative aspects of the circulation pattern to be rather persistent.

Hayes[8], (1984) has organized the surface winds in Los Angeles into seven categories. During the summer, the winds fall almost exclusively into 4 of the 7 categories. During the nighttime, between 22:00 PDT and 4:00 PDT, 71% of the time the surface winds were either downslope or calm. During the daytime, between 10:00 PDT and 16:00 PDT, the surface winds fall into either the onshore south or sea breeze categories; both these regimes involve an onshore flow from Santa Monica to the Palos Verdes Peninsula. During the winter, the surface winds are distributed more evenly into the 7 categories. For example, at 4:00 PDT the surface winds are likely to be calm (29%), offshore (25%), downslope (17%), and Santa Ana (17%). At 10:00 PST the flows are similarly grouped but the likelihood of a southerly flow has increased to 15%, while that of the other categories has decreased by a few percent. The afternoon winter winds, like those in the summer, fall primarily into two categories, sea breeze (51%) and onshore south (24%). The evening winds are again diverse and nearly like the winds observed at 4:00 PST.

EXPERIMENTAL

The techniques used during the SCAQS SF_6 were similar to those used by previous investigators. For example see Drivas and Shair[9] (1974), Drivas[10] (1975), Lamb[11] (1978), and Reible[12] (1982). Basically, these investigations consist of releasing SF_6 at a constant known rate from a source (or source region) of interest, and (ii) collecting a large number of air samples throughout region and time of interest. The tracer concentrations within the air samples are determined by means of electron-capture gas chromatography. Such studies have elucidated many source/receptor relationships of interest.

Tracer Releases

Sulfur hexafluoride, (having a molecular weight of 146), was released at a constant rate from 6:00 to 9:00 PDT during July 15, September 3, November 11, and from 16:00 to 19:00 PST during December 10, 1987. The first three tests were to probe the morning transition regime during which the morning "rush hour" occurs. The last day was to probe the evening transition, during which the evening "rush hour" occurs. These days were chosen on the basis of the SCAQS short term meteorological forecasts. The hope was to release the tracer on days during which elevated pollution levels within the Los Angeles region would be observed within the following 36 hours. The release site for each test was the Southern California Edison Office in Vernon, California. This site, (longitude: 118 degrees 14 minutes, latitude: 34 degrees) was chosen because (i) it is centered approximately in the middle of the hydrocarbon emissions of the downtown area, and (ii) representatives of SCE permitted us to use their facility.

During the July 15th study, SF_6 was released at a rate of 426 grams per minute leading to a total release of 76.7 kilograms (or 169 pounds). During the September 3rd study, SF_6 was released at a rate of 1151 grams per minute leading to total release of 207.2 kilograms (or 456 pounds). During the November 11th study, SF_6 was released at a rate of 772 grams per minute leading to a total release of 139 kilograms (or 306 pounds). During the December 10th study SF_6 was released at a rate of release 1362 grams per minute leading to a total release of 245 kilograms (or 539 pounds). In order to compare the results of different tracer experiments, the downwind tracer concentrations must be normalized by means of their molar release rates. The molar release rates for tests 1,2,3 and 4 were 175, 473, 317, and 560 gram moles per hour respectively.

Air Sample Collection

Air samples were collected by means of two methods. First, 5-second "grab" samples were collected by passengers along auto traverses. Second, hourly averaged samples were collected by means of automatic samplers located at several "fixed" sites of interest. All samples were collected in 30 cc plastic syringes that had been previously vacuum cleaned and tested. The auto traverse data were used to recreate a "snap shot" of the tracer cloud.

During Test 1, 30 automatic samplers were deployed at 20 sites. Tables I, II, and III list the telemetry, upper air, and fixed sampling sites; figures 1 and 2 show their locations. During Test 2, 29 automatic samplers were deployed at the same sites as in Test 1. During Test 3, 12 automatic samplers were deployed at 10 different sites. In Test 4, 22 automatic samplers were deployed at 11 different sites.

Unfortunately during Tests 1 and 2, a divergence zone lay to the east of the release site and most of the tracer was transported northward into the San Fernando Valley. Although good descriptions of the clouds were obtained via auto traverses, few hourly averaged SF_6 tracer data were collected since the fixed sites were chosen in anticipation of atmospheric transport from downtown Los Angeles towards the east. The hourly averaged SF_6 tracer data for Test 3 are listed in Tables IVa and IVb. The hourly averaged SF_6 tracer data for Test 4 are listed in Tables Va, Vb, and Vc. Sampling begins on the hour reported and continues for 1 hour.

Analysis of SF_6

The air samples were analyzed by the means of electron capture gas chromatography. The apparatus and technique are described by Drivas and Shair (1975). Concentrations of SF_6 can be readily detected in concentrations down to 1 part tracer per trillion parts (ppt) of air by volume.

TRANSPORT TRAJECTORIES OBTAINED FROM METEOROLOGICAL DATA

A computer model, **WIND**, was developed to objectively interpolate and extrapolate the surface and upper level winds throughout the SCAQS region of interest. **WIND** was used to generate two-dimensional transport trajectories at various elevations. These trajectories were compared to those inferred by the SF_6 tracer data. For any location within the region of interest, a trajectory may be calculated and displayed on the computer's high resolution color screen. A topographical map of the SCAQS region of interest provides the background on which the transport trajectories are displayed. **WIND** also permits rectangles to be drawn around any zone within the SCAQS region of interest; the volume flux of air may be calculated and displayed around the rectangle. Such diagrams indicate the presence of convergence and divergence zones.

The algorithm for interpolation and extrapolation was based upon the desire to have the wind at any point within the SCAQS region of interest to be calculated from at least two telemetry reporting stations. First, the average distance between a telemetry station and its **two nearest neighbors** is determined for each such station. The average value of the all these distances, R_e, is called the "critical radius".

When the **WIND** program is executed, R_e is first calculated and remains constant throughout the subsequent calculations unless changed manually. The **WIND** program automatically calculates a new value of R_e for each new set of

telemetry stations. The interpolation and extrapolation schemes are based upon the following algorithm. To obtain the velocity vector at a point P_1 on the map, a circle of radius R_c is drawn with P_1 at its center. An imaginary right circular cone of height R_c is constructed having as its base the circle drawn previously. In this way the center of the cone lies at a height R_c above the point P_1. The surface of the cone represents the weighting function which describes how stations surrounding P_1 are used to determine the velocity vector at that point. The weight, i.e. the influence a particular telemetry station has on the local velocity is determined by projecting the point which represents the location of that station vertically onto the cone. The height of the point of intersection with the cone is the amount which that station influences the calculation of the velocity vector. Points that lie outside of the radius R_c are given a weight of zero, while the ones inside have weights ranging from 0 to R_c. A single component direction of the velocity vector at a given point is then the normalized sum of all the corresponding single component direction vectors interior to R_c multiplied by their respective weighting factors. The normalization constant is the sum of the weighting factors of all the stations. Thus, this construction is geometrical in nature and, in accordance with intuition, does not attribute influence to telemetry stations far from the point in question. This method is extremely quick because of the minimal computational requirements, and thus is ideal for the PC.

Trajectories are determined by the successive application of the following recursive algorithm at each hourly interval. A point P_1 is specified on the map which represents the center of the "parcel" of air being tracked. The local velocity at that point is calculated in the manner described above. The location of the parcel of air an hour later, P_2, is estimated by calculating the vector displacement which would occur if the parcel moved at the local velocity at P_1 for an hour. The estimate is assessed and improved according to the following method. The line segment formed by P_1 and P_2 is bisected at P_3. The velocity at P_3 is determined, and the parcel is allowed to travel at this velocity for half the time of the preceding interval, in this case one half hour, ending up at position P_4. If the absolute difference between P_2 and P_4 is less than a tolerance (which is inversely proportional to the level of the recursion, in this case 1/2) then P_2 is accepted as the new location of the air parcel after one hour. However, if the absolute difference between P_2 and P_4 is greater than the tolerance, then the process is repeated at a time interval equal to one half of the previous time interval. That is, the line segment formed by P_1 and P_3 is then bisected and the sequence of steps described above is repeated on this smaller length interval. This process is continued until the tolerance is satisfied on a sub-segment of the total segment P_1P_2. The recursion then backs its way out satisfying the tolerance requirement at each interval, progressively calculating the intermediate position of the air parcel as it moves during one hour.

The use of the recursion algorithm permits the development of trajectories which are very sensitive to regions where convergence, divergence and abrupt directional changes occur. The increased sensitivity results from assessing the

velocity at more than just one point along the route of an hour long trajectory.

Currently **WIND** is used to examine the wind fields within the Los Angeles region. The region of coverage spans from 117 degrees 7 minutes to 118 degrees 17 minutes in latitude, and from 33 degrees 15 minutes to 34 degrees 25 minutes in longitude. The region corresponds to that bounded at the north west corner by Newhall, at the north east corner near Crestline, at the south east corner near Perris and at the south west corner in the Pacific Ocean. The inputs for **WIND** are the data obtained from the SCAQMD's telemetry system along with the upper level wind data gathered during the SCAQS program. The stations within the telemetry system are listed in Table I and depicted in Figure 1. The upper level wind stations are listed in Table II, and depicted in Figure 2 (Lehrman[14], 1988).

RESULTS

July 15, 1987

About 12.5 cubic meters (at normal conditions) of pure SF_6 were released from 6:00 - 9:00 PDT, (the morning transition period) near ground level from the Vernon site. The extent to which the tracer dispersed during the morning transition period was determined from data collected via auto traverses. As shown in Figure 3, by 9:30 PDT the tracer cloud had dispersed over a region with horizontal dimensions 22 kilometers in the north/south direction by 17 kilometers in the east/west direction. Although not apparent in Figure 3, the tracer cloud was almost circular - with an approximate radius of 11 kilometers (7 miles). By considering the solution to the transient radial diffusion equation, the "effective eddy diffusivity" was estimated to be of the of order of 10^4 meters^2/second.

The mixing depth over the downtown area at 9:30 PDT was estimated to be about 500 meters (Bennett[13], 1988; Lehrman[14], 1988). Thus, by 9:30 PDT, the tracer had mixed through a volume of approximately equal to 1.8×10^{11} cubic meters. The average concentration of the tracer within this volume was calculated to be 80 ppt. Consequently, the tracer cloud was estimated to contain 14.4 cubic meters of pure SF_6. Thus, **taking into account the inherent uncertainties in the mass balance calculation**, it is reasonable to conclude that the tracer cloud contained essentially all of the tracer that was released.

The mid day surface and upper level winds swept the tracer northward and then westward into the San Fernando Valley. The **WIND** generated trajectories are shown in Figure 5a. As indicated, the morning southerly winds shifted into the typical onshore flow. Upper level wind trajectories which start at 6:00 PDT from Vernon, and continue for 18 hours, are depicted in Figure 5c. The surface wind trajectories lagged behind the transport of the tracer. The observation that the surface winds underestimate the transport distance of a tracer is in agreement with the observations of Neiburger[15], 1955. However, the faster upper level wind trajectories are in excellent agreement with the tracer data shown in Figures 2 and

3. Between 100 and 400 meters AGL over Vernon, the upper level winds were observed to rotate counter clockwise with increasing altitude, (see Figure 5c).

September 3, 1987

About 34.7 cubic meters, (at normal conditions) were released from 6:00 - 9:00 PDT near ground level at the Vernon site. As shown in Figures 4a and 4b, the extent to which the tracer had dispersed at various times were again determined from auto traverse data. As shown in Figure 4a, rather high concentrations of tracer were observed up to 7 miles **south** of Vernon between 9:00 - 10:00 PDT. It should be noted that neither the available surface winds nor the available upper level winds gave any indication of transport to the **south** of the release site.

As in the previous test, the mid day winds swept the tracer northward and then westward into the San Fernando Valley. As in the previous test, the winds between 100 and 400 meters AGL over Vernon were found to rotate counter clockwise with increasing altitude, (see Figure 5d). The winds aloft were stronger than those in the previous test. Note that in both the summer tests, the morning transition period was characterized by light, but directional, surface winds.

The **WIND** generated trajectories indicate that the upper level winds are required to explain the location of the tracer cloud that was observed during the afternoon. Trajectories of the surface winds were found to lie to the east of the tracer in the afternoon. The 100 and 200 meter AGL trajectories were found to coincide with the location of the tracer. The 300 and 400 meter AGL trajectories were found to lie to the west of the tracer. As in the first test upper level wind trajectories were required to explain the location of the tracer.

Ozone Concentrations during Tests 1 and 2

The concentrations and distributions of ozone during Tests 1 and 2 were remarkably similar. For example in both tests, maximum hourly averaged ozone concentrations occurred between 13:00 and 15:00 PDT. These times coincided with the approximate arrival times of the tracer. The maximum ozone concentrations at Burbank, Reseda, and Newhall were 12-14 pphm, 13-17 pphm, and 17-18 pphm respectively. Thus, the tracer data indicate that the atmospheric pollutants, residing north and west of the divergence zone, contributed to the observed ozone in the San Fernando Valley. During the morning, the divergence zone existed along a strip which passed south and east of Vernon, and extended to Pasadena.

Elevated ozone concentrations were also observed in the eastern part of the Los Angeles Basin. For example the maximum hourly averaged ozone concentrations at Fontana, San Bernardino, Redlands, and Crestline were 16-18 pphm, 18-19 pphm, 13-17 pphm, and 20-22 pphm respectively. Trajectories shown in Figures 5a and 5b indicate that atmospheric pollutants to the south and east of the divergence zone - and north of Costa Mesa, contributed to the ozone in the eastern region of the Los

Angeles Basin. The trajectories starting at Costa Mesa indicate that the transport of atmospheric pollutants south of Costa Mesa was influenced by the Elsinor convergence zone.

By 14:00 PDT the tracer cloud had reached the dimensions of 43 kilometers x 27.5 kilometers (see Figure 4b). The "effective eddy diffusivity" associated with this cloud was calculated to be of the order of 10^4 meters^2/second - in excellent agreement with that calculated from the previous test. The mixing depth was estimated to be 300 meters (Bennett[13], 1988; Lehrman[14], 1988). Thus, during the afternoon, the tracer was dispersed within a volume of about 3.5×10^{11} cubic meters within which the average concentration of tracer was 108 ppt. Consequently, the amount of tracer contained within the cloud was estimated to be 37.8 cubic meters of pure SF^6 - indicating that the tracer cloud shown in Figure 4b accounted for essentially all of the tracer that was released.

Also shown in Figure 5b are the trajectories for sites located in Orange County. It is interesting to note that the southern most site shows trajectories that exhibit an abrupt change in direction in the region of the Elsinor convergence zone.

November 12-13, 1987

About 23.3 cubic meters of pure SF_6 were released from 6:00 - 9:00 PDT. The hourly averaged tracer data are listed in Table 4a. The northern most station at which SF_6 was observed was Burbank. The low concentrations seen at Burbank (from 13:00 - 15:00 PDT) may have transported by the surface level winds depicted in Figure 8a. During the release, the tracer was transported to the west and apparently offshore. Following the flow reversal which transported the tracer onshore, the West Los Angeles site experienced and hourly averaged concentration of 136 ppt. Furthermore, significant tracer concentrations were observed as far south as Lynwood (from 9:00 - 14:00 PDT). As indicated by the trajectory in Figure 9a, the tracer at Lynwood may have been transported by the 100 meter AGL winds. These observations indicate the great extent to which the tracer spread as a result of a flow reversal. It should be noted that SF_6 was observed at sites within the basin up to 36 hours following the start of the release.

Auto traverse data collected from 6:00 - 8:00 PDT on November 13 indicated the presence of large cloud of tracer (with dimensions 37 km x 37 km) as indicated in Figure 6a. The average concentration of tracer within this region was 21 ppt. Assuming a mixing depth of 200 meters would account for about 25% of the tracer released during the morning of the previous day. By then, the tracer had undergone at two flow reversals. The amount of tracer lost due to vertical mixing during these flow reversals in unknown.

It should be noted that 36 hour surface wind trajectories, and 18 hour upper level wind trajectories, do not leave the SCAQS region of interest. The computed

trajectories, shown in Figure 8a indicate that much of the tracer may have been transported into the San Gabriel Mountains. However, the location of the maximum concentration of SF_6,(observed between 6:00 - 8:00 PDT on November 13), was 35-45 kilometers to the east of the corresponding trajectories.

December 10-11, 1987

Approximately 41.1 cubic meters of pure SF_6 were released from 16:00 - 19:00 PST (during the evening transition period) on December 10. The transport of the tracer, offshore and then onshore, can be inferred from the hourly averaged data listed in Tables Va, Vb, and Vc. Tracer concentrations above 1000 ppt were seen in central Los Angeles for 7 hours following the end of the release. From 1:00 - 6:00 PST on December 11, concentrations above 100 ppt were seen moving eastward over West Hollywood; between 2:00 and 3:00 PST the average concentration was 311 ppt. Eleven hours later this cloud apparently was transported along the foothills of the San Gabriel mountains; the average SF_6 concentration from 13:00 - 14:00 was 290 ppt. The surface wind trajectories, in qualitative agreement with above mentioned observations, indicated a clockwise transport of a portion of the tracer. However, the trajectories do not show indicate the fact that the majority of the tracer was transported over the ocean - where there were no meteorological data available. Following the release, the westward transport of the tracer is shown in Figure 6b.

As shown in Figures 7a and 7b, the majority of the tracer was seen moving onshore south of Vernon during the morning and afternoon of December 11. The average concentrations of tracer within the dashed boxes of Figures 7a and 7b are 54 ppt and 46 ppt respectively. Assuming a mixing depth of 200 meters indicates that during the morning of December 11, 87% of the tracer was contained in the dashed box (with dimensions of 61 km x 53 km) shown in Figure 7a. Even in the afternoon, about 21% of the tracer was observed over the western region of the Los Angeles Basin (see Figure 7b); the dimensions of the box are 24 km x 36 km. During the morning and early afternoon, the surface winds along the coast were on shore. These observations indicate that a considerable portion of the SF_6 returned to the Los Angeles region after having resided offshore overnight. The extent of the offshore flow 19 hours earlier can be inferred from the fact that SF_6 was coming onshore during the **afternoon of December 11.** Offshore meteorological data would be needed to predict the degree to which the tracer was dispersed south of the release site.

Some of the tracer was transported offshore around the Palos Verdes Peninsula, and then onshore as far south as Corona Del. Emissions, from a single low level point source, were transported and dispersed over an area of 3000 square kilometers surrounding the release site.

Elevated concentrations of carbon monoxide were observed in the south west portion of the basin. Values near the 20 ppm California state standard,

(for a 1 hour average concentration) were observed Lynwood from 6:00 - 8:00 PDT on December 11. The corresponding concentration of tracer was 45 ppt.

CONCLUSIONS

(1) In both summer studies, during the hour following the end of a three hour release, the tracer was dispersed over an area of approximated 400 square kilometers.
(2) During the summer, an effective eddy diffusivity of around 10, meters^2/second characterized the dispersion of the tracer.
(3) Mass balances of the tracer indicated that essentially off of the tracer was accounted for all of the tracer.
(4) An objective trajectory model was developed to help interpret the tracer data.
(5) Both the surface and upper level winds are needed to explain the transport of the tracer.
(6) The morning downtown emissions did not impact the ozone in the eastern region of the Los Angeles region.
(7) In both winter studies, a vast majority of the tracer was carried over. The residence time within the SCAQS area of interest was greater than 36 hours.
(8) Mass balances indicated that a more complex pattern of dispersion occurred during the winter as compared to that during the summer.
(9) The convoluted surface wind trajectories help verify the presence of flow reversals.
(10) In both cases the tracer was transported outside of the boundary for which adequate meteorological data are available.
(11) Increased meteorological data, included (i) winds over the ocean, (ii) winds in the mountains, and (iii) upper levels winds are needed to adequately reconstruct all of the transport and dispersion patterns.
(12) During December 11, 1987, the tracer was observed to coincide with the elevated carbon monoxide levels at Lynwood.

Acknowledgements:

This work was funded in part by a grant from the California Air Resources Board. We are delighted to acknowledge the excellent support given to us by (i) Charles Bennett, Frank DiGenova, Eric Fugita, and Manjit Ahuja of the California Air Resources Board in Sacramento, and (ii) Howard Bakes, Don Daymon, Pat Harrington, Lee Lewis, Loudes Menes, Janet Nguyen, Frank Ong, and King Yu of the California Air Resources Board in El Monte. We also wish to thank William Bope and Joseph Cassmassi of the South Coast Air Quality Management District for their valuable help and insight. Neil Crawford was supported by an NSF Research Experience for Undergraduate (REU) grant administered through the Caltech Summer Undergraduate Research Fellowship (SURF) program. We wish to thank Carolyn Merkel, Joan Spears, and Jean Cass of the SURF office.

REFERENCES

1. A. Davidson, "Comment on ten-year ozone trends in California and Texas," APCA Journal, **36** (5): 597 (1986).
2. W. G. England, L. H. Teuscher, S. Marsh, "Perfluorocarbons Tracer Experiments during the Southern California Air Quality Study," Air and Waste Management Association, paper 89-138.1 (1989).
3. J. G. Edinger, "Changes in the depth of the marine layer over the Los Angeles Basin," J. Met. **16** 3 219 (1959).
4. J. G. Edinger, "Vertical distribution of photochemical smog in Los Angeles Basin," Env. Sci and Tech. **7** 3 247 (1973).
5. D. L. Blumenthal et al., "Anatomy of a Los Angeles smog episode: pollutant transport in the daytime sea breeze regime," Atmos. Env. **12** 893 (1977).
6. A. Bytnerowicz et al., "Gaseous and particulate air pollution in the San Gabriel Mountains of Southern California," Atmos. Env. **21** 8 1805 (1987).
7. F. H Shair et al., "Transport and dispersion of airborne pollutants associated with the land breeze-sea breeze system," Atmos. Env. **16** (9) 2043 (1982).
8. T. Hayes et al., *California Surface Wind Climatology*, State of California Air Resources Board Aerometric Data Division, 12 (1984).
9. P. J. Drivas and F. H. Shair, "A tracer study of pollutant transport and dispersion in the Los Angeles area," Atmos. Env. **8** 1155 (1974).
10. P. J. Drivas, *Investigation of Atmospheric Dispersion Problems by Means of a Tracer Technique*, Doctoral Thesis California Intitute of Technology, Pasadena CA 91125 (1975).
11. B. K. Lamb, *Development and Application of Dual Atmospheric Tracer Techniques for the Characterization of Pollutant Transport and Dispersion*, Doctoral Thesis California Intitute of Technology, Pasadena CA 91125 (1978).
12. D. D. Reible, *Investigations of Transport in Complex Atmospheric Flow Systems*, Doctoral Thesis California Intitute of Technology, Pasadena CA 91125 (1982).
13. C. Bennett, Personal communication, California Air Resources Board, Sacremento CA 95812 (1988).
14. D. Lehrman, Personal communication, Technical and Business Systems, Santa Rosa, CA 95404 (1988).
15. M. Neiburger, "Tracer tests of the accuracy of trajectories computed from the observed winds in the Los Angeles area," Air Pollution Foundation, (1955).

Table I Station Code and Name for SCAQMD Telemetry Stations

Code	Station Name	Code	Station Name
ANAH	ANAHEIM	AZUS	AZUSA
BANN	BANNING	BURK	BURBANK
CELA	LOS ANGELES	COST	COSTA MESA
CRES	CRESTLINE	FONT	FONTANA
GLEN	GLENDORA	HAWT	HAWTHORN
HEME	HEMET	LAHB	LA HABRA
LANC	LANCASTER	LGBH	LONG BEACH
LSAL	LOS ALAMITOS	LYNN	LYNWOOD
NEWL	NEWHALL	NORC	NORCO
PASA	PASADENA	PERI	PERRIS
PICO	PICO RIVERA	PLSP	PALM SPRINGS
POMA	POMONA	RDLD	REDLANDS
RESE	RESEDA	RIVR	RIVERSIDE
SNBO	SAN BERNARDINO	TORO	EL TORO
UPLA	UPLAND	WSLA	WEST LOS ANGELES
WHIT	WHITTIER		

Table II Station Code and Name for SCAQS Upper Air Stations

Code	Station Name
BURB	BURBANK
EL	EL MONTE
LONG	LONG BEACH
LOYO	LOYOLA MARYMOUNT UNIV.
ONTA	ONTARIO
RIVE	RIVERSIDE

Table III Code and Name for Additional Automatic Sampler Locations

Code	Station Name
ALTA	ALTADENA
CORO	CORONA DEL MAR
LADE	LADERA HEIGHTS
PALO	PALOS VERDES PENINSULA
RUBI	RUBIDOUX
WHLL	WEST HOLLYWOOD

Tables 1, 2, and 3.

Table IVa Automatic Sampler Results, November 12-13
November 12, 1987

TIME	6	7	8	9	10	11	12	1	2	3	4	5	PST
SITE													
HAWT	0	0	0	405	382	48	30	14	11	5	6	4	
WSLA	0	0	0	0	9	58	136	77	17	2	0	0	
GLEN	0	0	0	0	0	0	0	0	4	6	9	83	
ELMO	0	0	0	0	0	0	0	50	33	18	16	28	
BURK	0	0	0	0	0	0	0	18	20	0	5	5	
ANAH	0	0	0	0	0	0	0	12	18	2	4	5	
PICO	0	0	0	0	0	0	35	11	0	37	7	4	
LYNN	0	0	0	36	24	367	8	44	19	2	4	5	
POMA	0	0	0	0	0	0	0	0	0	0	0	47	
PASA	0	0	0	0	0	0	0	0	47	34	25	11	

Table IVb
November 13, 1987

TIME	6	7	8	9	10	11	12	1	2	3	4	5	PST
SITE													
HAWT	4	6	9	10	14	6	9	6	12	14	11	15	
PASA	20	32	28	14	26	21	23	12	6	9	3	7	

Tables 4a and 4b.

Table Va Automatic Sampler Results, December 10-11

December 10, 1987

TIME	3	4	5	6	7	8	9	10	11	12	1	2 PST
SITE												
PASA	0	0	0	0	0	0	0	0	0	0	0	0
LYNN	0	0	0	84	69	46	27	19	22	31	25	28
HAWT	0	0	49	38	48	70	100	210	10	19	186	38
CELA	0	6	79	237	1176	1349	2254	1146	828	1353	1418	67
LGBH	0	0	0	0	0	0	0	0	0	16	17	20
WHLL	0	0	0	0	0	0	0	0	0	0	261	311

Table Vb

December 11, 1987

TIME	3	4	5	6	7	8	9	10	11	12	1	2 PST
SITE												
PASA	0	0	0	0	0	0	0	8	40	34	290	257
ALTA	0	0	0	0	0	0	0	0	19	13	48	41
CORO					13	8	12	53	13	9	11	
LADE	61	18	40	29	33	33	49	44	38	36	30	47
WHLL	205	119	128	138	67	21	32	35	27	33	101	22
PICO			0	0	0	10	13	7	48	24	28	
RUBI									0	0	0	

Table Vc

December 11, 1987

TIME	3	4	5	6	7	8	9	10	11	12	1	2 PST
SITE												
PASA	270	240	115	79	41	54	23	26	42	17	22	24
ALTA	19	20	18	10	14	9	13	14	6	9	10	13
CORO	19	18	23	11	10							
PICO	27	0	0									
RUBI	0	0	0	0	0	0	15	3	15			

Tables 5a, 5b, and 5c.

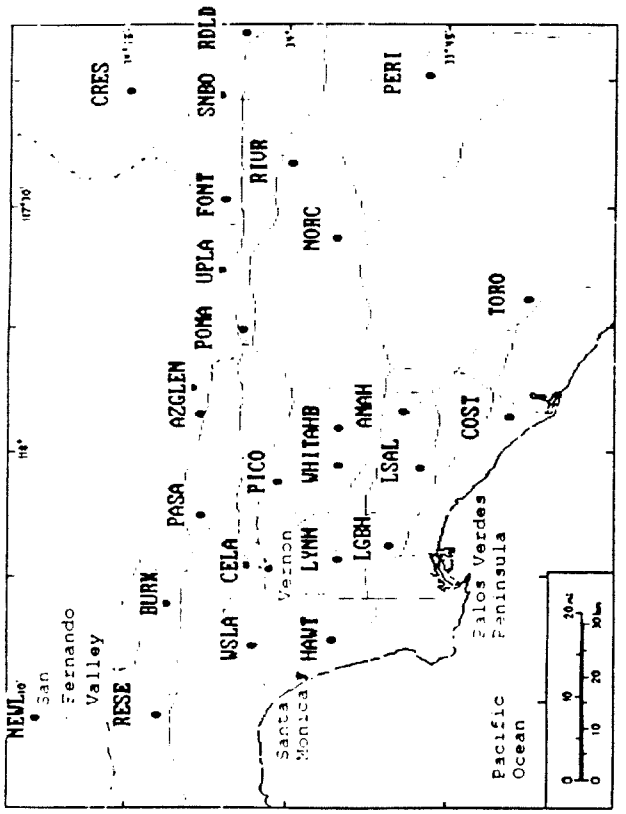

Figure 1. Location of reporting sites for the SCAQMD Telemetry System in the western Los Angeles Basin. The LA freeway system is depicted in the background.

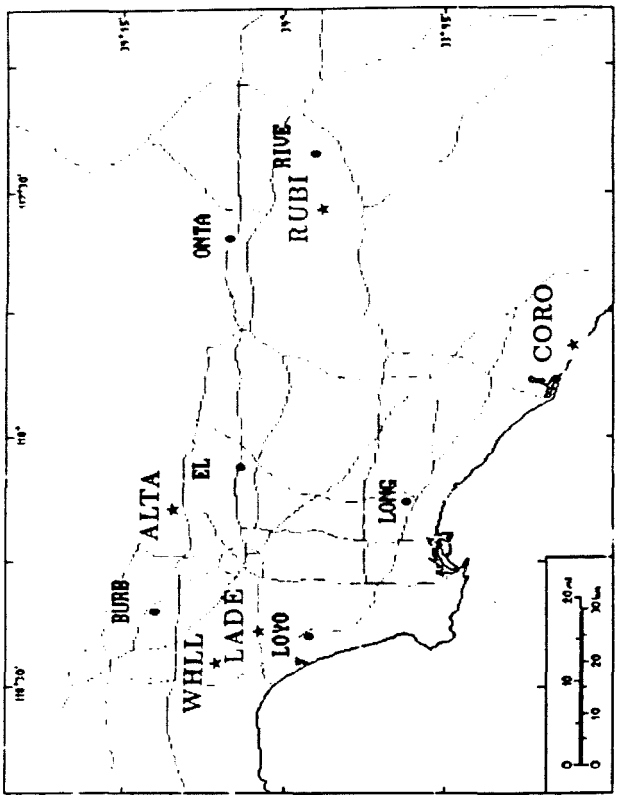

Figure 2. Location of upper air network stations •, and additional one hour average sample board locations ★.

(a)

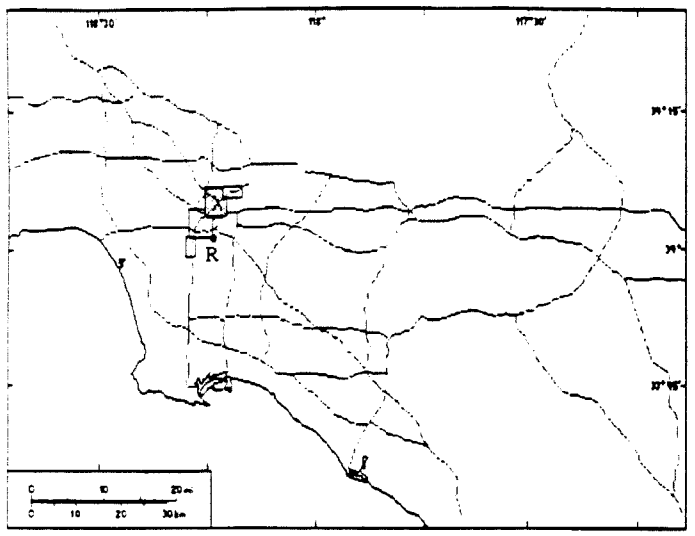

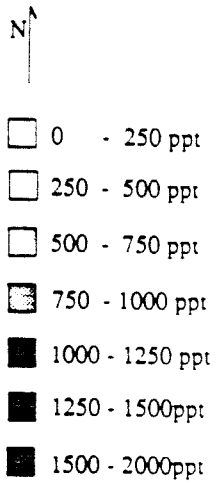

(b)

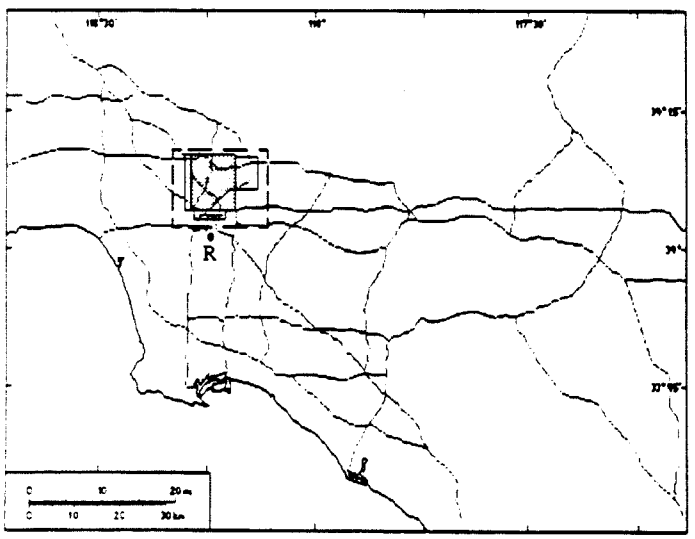

Figure 3. SF_6 tracer cloud as seen by auto traverses on July 15, 1987, (a) 9:00 - 9:30 PDT and (b) 9:30 - 10:30 PDT .

(a)

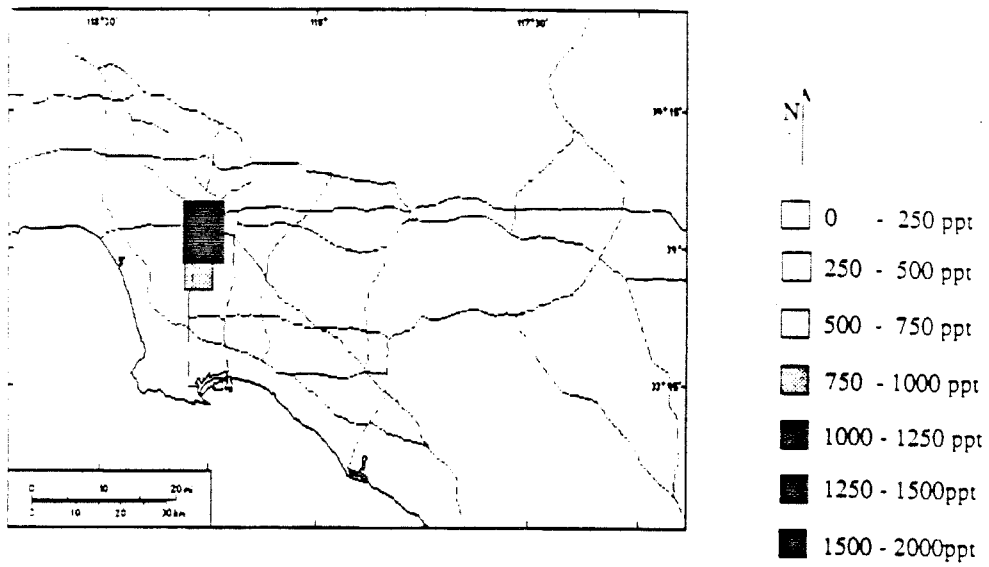

(b)

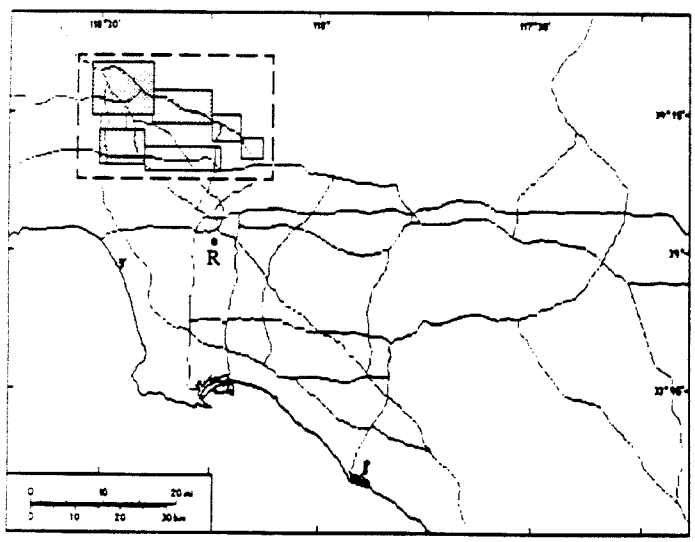

Figure 4. SF_6 tracer cloud as seen by auto traverses on September 3, 1987, (a) 9:00 - 10:00 PDT. and (b) 13:00 - 14:00 PDT.

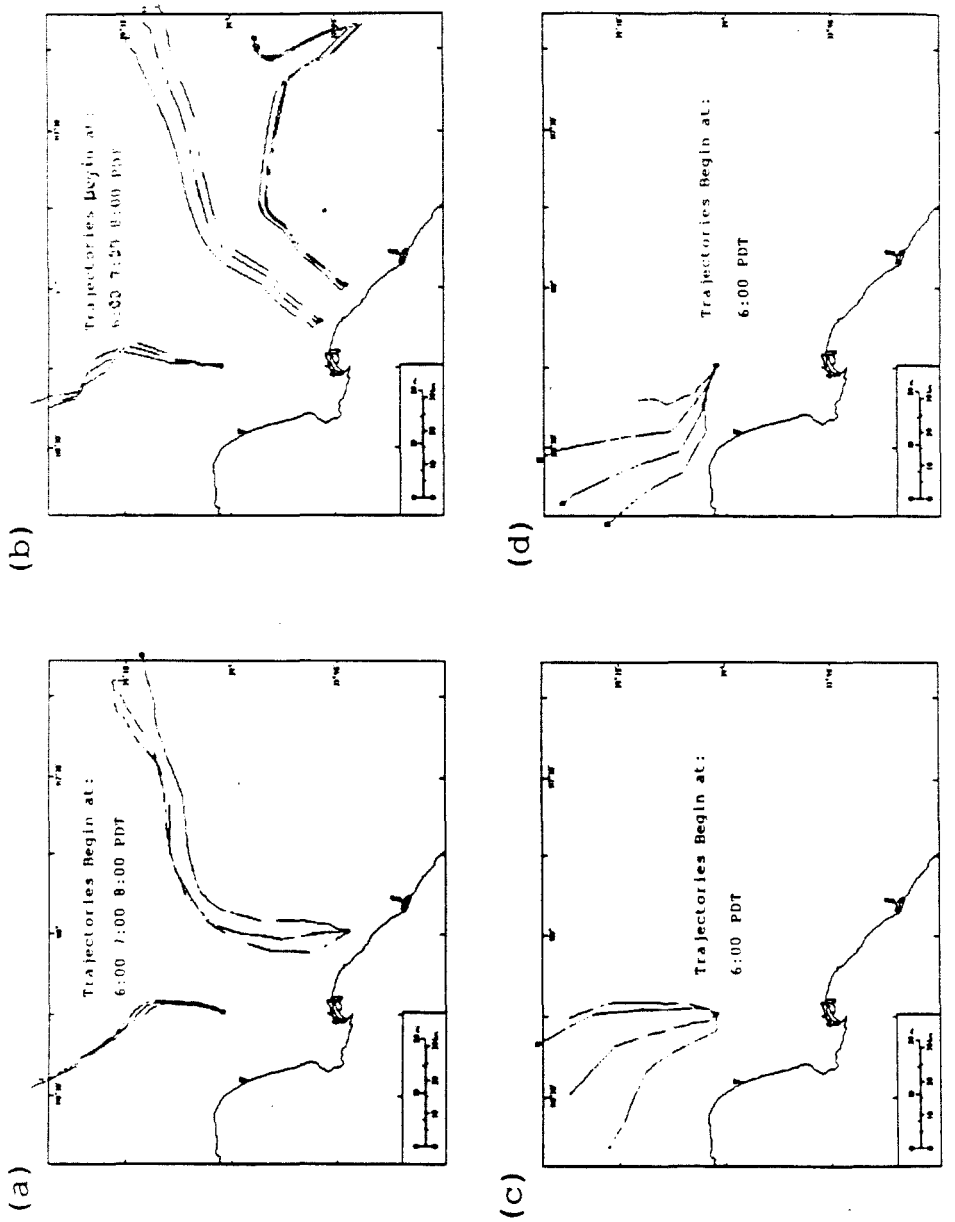

Figure 5. Surface wind trajectories from Vernon and other locations at 6, 7, and 8 PDT, and lasting 24 hours (a) July 15, 1987, (b) September 3, 1987, and upper air trajectories starting at 6 PDT for altitudes of 100, 200, 300, and 400 meters AGL going counter-clockwise about Vernon (c) July 15, 1987, and (d) September 3, 1987.

(a)

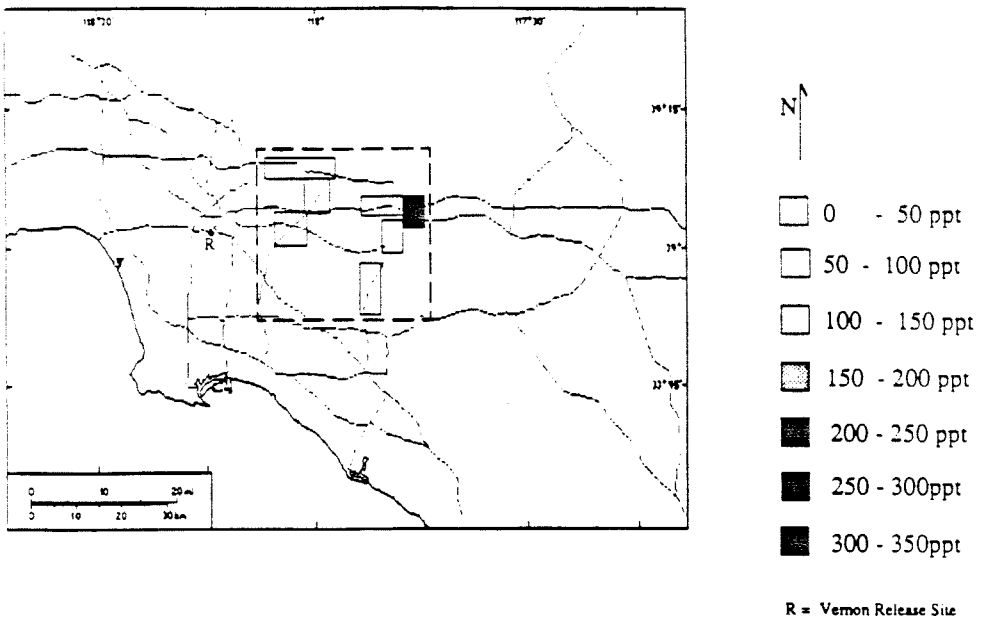

(b)

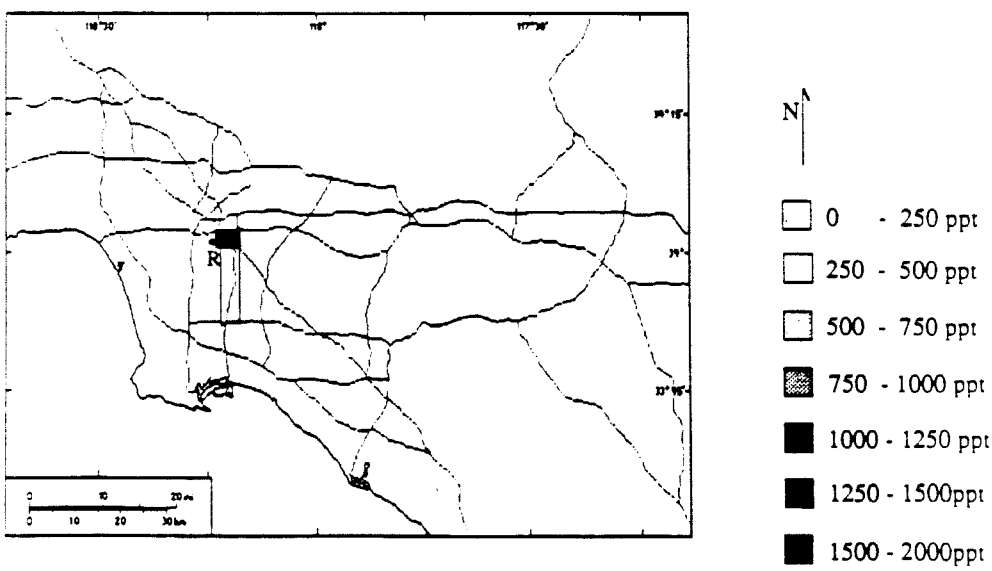

Figure 6, SF_6 tracer cloud as seen by auto traverses on (a) at 6:00 - 8:00 PST November 13, 1987, 24 hours after the release, (b) at 19:00 PST December 10, 1987, just after the evening release.

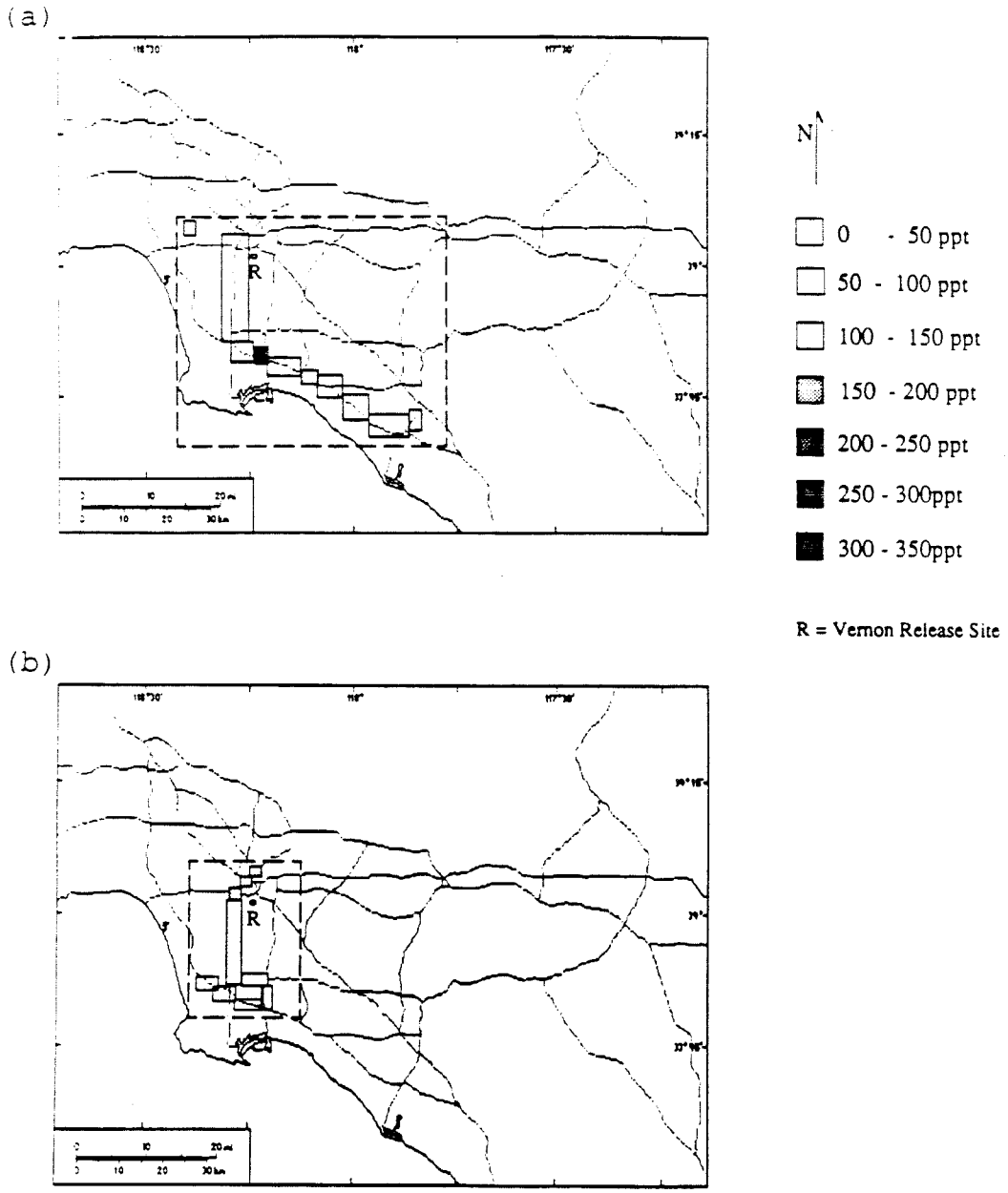

Figure 7. SF_6 tracer cloud as seen by auto traverses on December 11, 1987, the day after the release (a) at 7:35 PST, (b) at 14:00 PST.

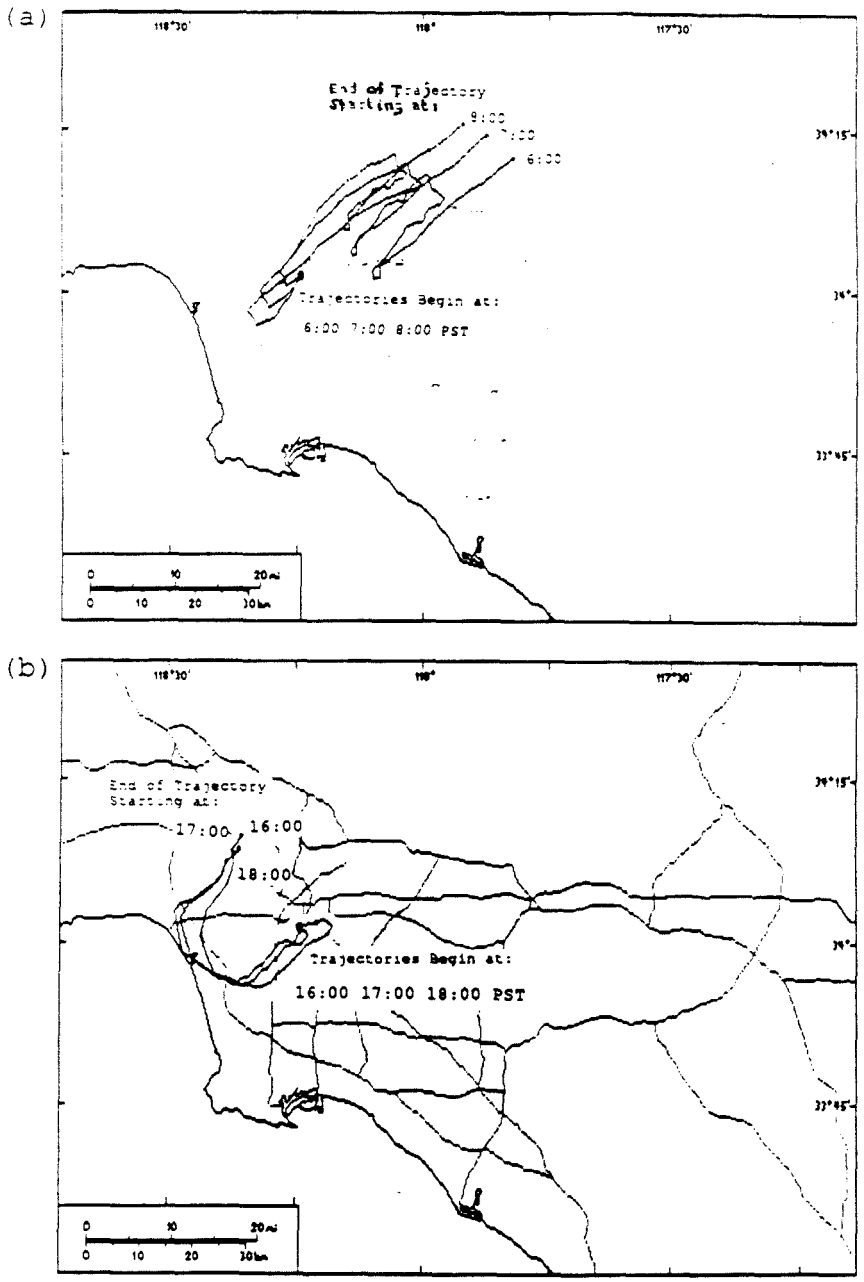

Figure 8. Surface wind trajectories from Vernon starting at (a) 6, 7, and 8 PST lasting 36 hours on November 12-13, 1987, and (b) 16, 17, and 18 PST lasting 24 hours on December 10-11, 1987.

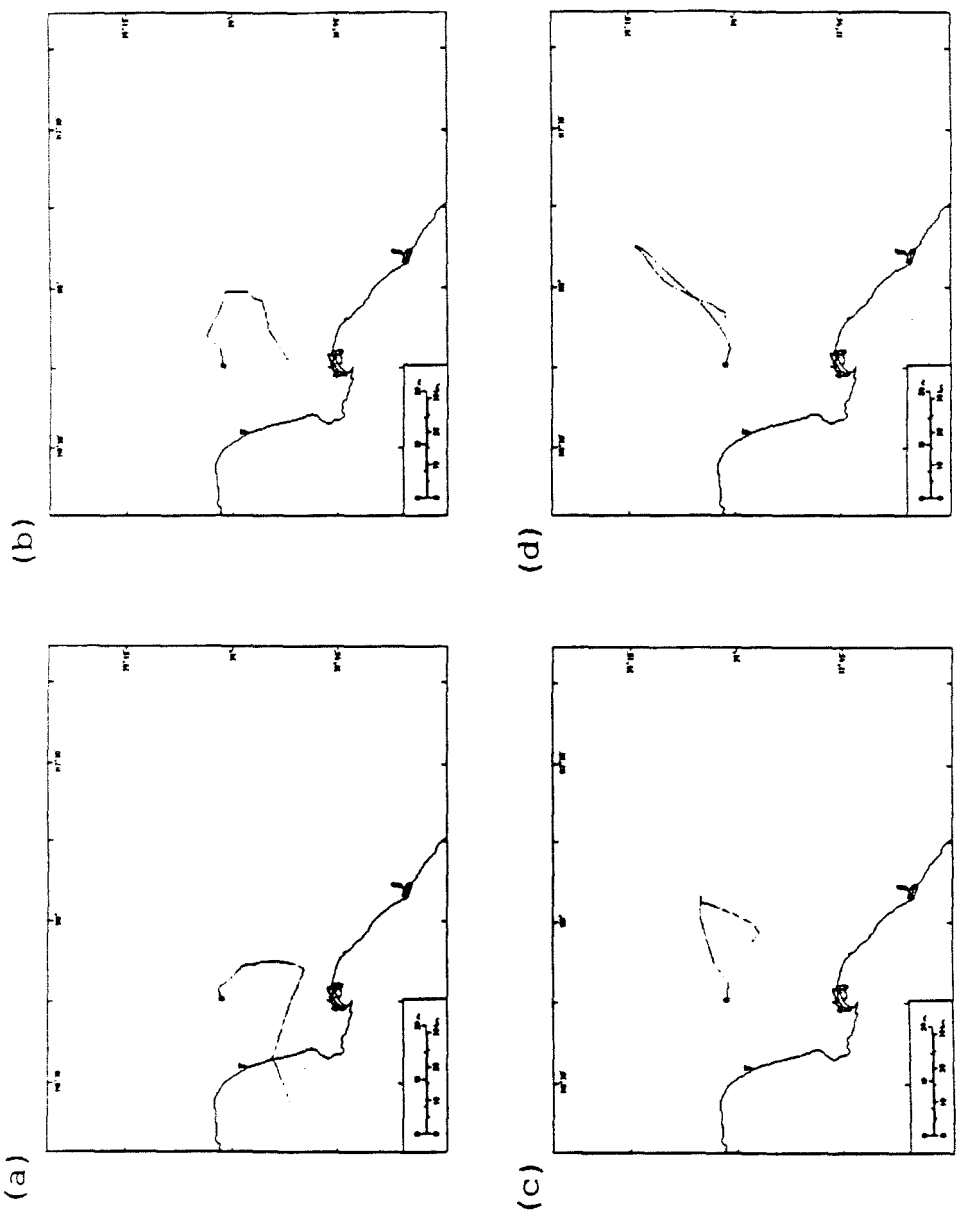

Figure 9. Upper air wind trajectories from Vernon starting on November 12, 1987, starting at 6:00 PST and lasting 18 hours at altitudes AGL of (a) 100 meters, (b) 200 meters, (c) 300 meters, (d) 400 meters.

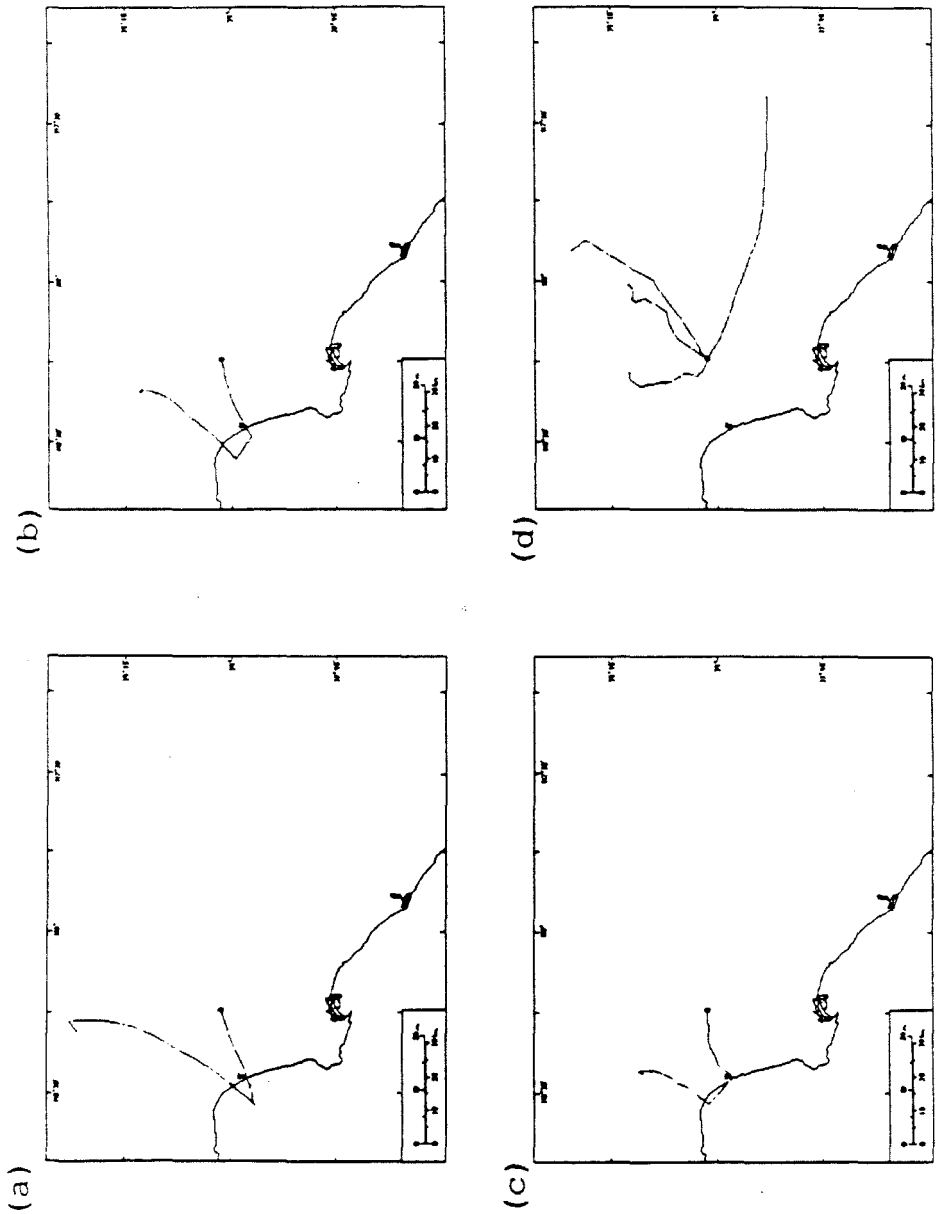

Figure 10. Upper air wind trajectories from Vernon starting on December 10, 1987, starting at 16:00 PST and lasting 18 hours at altitudes AGL of (a) 200 meters, (b) 300 meters, (c) 400 meters and (d) 600, 800, 1000, and 2000 meters going clockwise about Vernon.

2.2 Establishing Upper Bounds on Vertical SF_6 Tracer Transport During the 1987 SCAQS

Abstract

This document briefly describes how the commonly occurring temperature inversions in the Los Angeles Basin were used to establish upper bounds on the vertical tracer transport. Upper bounds on the transport of sulfur hexafluoride, SF_6, tracer during the Southern California Air Quality Study were obtained by examining the coinciding vertical atmospheric structure. Results are tabulated for the SF_6 experiments performed during July, November, and December, 1987.

Introduction

Within the Los Angeles Basin the vertical atmospheric structure is complex and varies with horizontal position as well as in time. The vertical transport and dispersion of surface-based emissions that results from the dynamic micro-meteorological conditions and winds within the basin has been studied extensively. For instance, Edinger (1959, 1973), Lea (1967), Stephens (1975), and Blumenthal et al. (1978) among others, have reported and used the vertical atmospheric structure of the Los Angeles Basin to explain some observations made during smog episodes.

Ground and near-ground released gaseous tracers, like other surface-based emissions, are influenced by the same transport mechanisms. Consequently, the closure of a tracer mass balance in the vertical direction can directly benefit from a quantitative description of the lower troposphere. This section describes how such descriptions gathered during the 1987 Southern California Air Quality Study enabled mass balancing on the SF_6 tracer data from the same period.

Typically, tracer mass balances are done to establish the fraction of tracer encountered at particular times and locations during a study. Reible (1982) has demonstrated that the fractional recovery can be determined within a 25 percent error given typical uncertainties for the pertinent data. Since tracer measurements are often obtained by ground based sampling, and airborne sampling techniques may be impractical for a variety of reasons, some method must be used to determine the vertical extent of tracer transport. In lieu of elevated tracer measurements, the extent of vertical tracer transport is infered from plots of the vertical atmospheric measurements. Once the extent of vertical transport is estimated, elevated concentrations are extrapolated from the tracer concentration measurements at the surface. This particular step is generally associated with a large uncertainty, possibly 40 percent or more. Minimization of this er-

ror is desirable and can be accomplished if a detailed hourly description of the lower troposphere's structure is available. To understand how the atmospheric structure is used in the analysis, it is important to be familiar with some practical aspects of doing the mass balance. For this reason some readers may find the next six paragraphs informative.

Two general methods of calculating atmospheric mass balances directly from measurements have been used. The first method is to measure the flux of material passing though a stationary point, line, or preferably a surface, and integrate the flux over time (Reible 1981, Shair 1982).

$$m_t = \rho \int \int C(x,y,z,t)\underline{\mathbf{v}}(x,y,z,t) \cdot \underline{\mathbf{n}}\, dA\, dt \qquad (2.2.1)$$

Equivalently, Equation 2.2.1 is applied to actual measurements in its differential form as Equation 2.2.2 below:

$$m_t = \rho \sum_{i=1}^{i=n} C_i(x,y,z,t)\underline{\mathbf{v}}_i(x,y,z,t) \cdot \underline{\mathbf{n}}_i\, \Delta A_i \Delta t. \qquad (2.2.2)$$

In Equations 2.2.1 and 2.2.2, m_t is the calculated total mass of tracer in kg, ρ is the tracer density in kg/m^3, and $C(x,y,z,t)$ in m^3 tracer/m^3 air is the time dependent tracer concentration in a fixed Cartesion coordinate system relative to the ground. For convenience, the directions x and y are in the horizontal plane of the ground, and z is the vertical direction. The unit vector $\underline{\mathbf{n}}$ is normal to the control surface, A. The vector velocity is denoted by $\underline{\mathbf{v}}$. In the differential form the i denotes an individual measurement. For typical measurements in the Los Angeles Basin, the principal component of the wind is horizontal, suggesting that ideally the control surface, A, should be perpendicular with the ground. Tracer measurements are then made at points along a line on the ground. Optimally, these points should also be perpendicular to the direction of flow.

The second method of conducting a mass balance is to simultaneously measure the concentration at many points in an enclosed volume, such as was done in the paper by Horrell et al. (1989). The total mass of tracer observed at time t is determined by Equation 2.2.3, below:

$$m_t = \rho \int \int \int C(x,y,z,t)\ dx\ dy\ dz. \tag{2.2.3}$$

Equivalently, Equation 2.2.3 is written in its differential form as Equation 2.2.4 below:

$$m_t = \rho \sum_{i=1}^{i=n} C_i(x,y,z,t)\ \Delta x_i\ \Delta y_i\ \Delta z_i. \tag{2.2.4}$$

The total mass is found by measuring the tracer concentration on a two-dimensional ground-level surface and making an estimate of the vertical concentration profile. The differential area, and volume of Equation 2.2.2 and 2.2.4 respectively, are calculated based on the physical spacing between the measurement sites.

The above two methods may be best suited to different circumstances. The first method is well suited to conditions where: (1) all the tracer is expected to cross a particular line some time after the release and (2) restrictions exist on the location of sampling sites. This first method was successfully applied to tracer which was advected offshore over the ocean by night, and then measured at the coastline as it returned onshore by day. The second method is probably best used under diagnositic conditions where (1) the direction of tracer transport is not anticipated *a priori*, and (2) the ground-level measurements can be taken on a two-dimensional surface.

Particularly relevant to determining the vertical extent of surface-based emission transport within the Los Angeles Basin is the airspace from ground level to roughly fifteen hundred meters. The mountains which bound the basin,

the sea breeze and a commonly occurring temperature inversion create conditions which may confine the surface based emissions below this height. The existence of a temperature inversion, the height at which it is first observed (its base), and the height at which the atmosphere returns to an adiabatic lapse rate (its top) all affect the ability of this interceding stable air mass to restrict vertical transport. The distance from the ground to the base of the inversion is referred to as the mixing depth or mixing height. Refer to Figure 1, reproduced from Fundamentals of Stack Gas Dispersion (Beychock 1979), to see an idealized rendition of the vertical atmospheric temperature structure. If an inversion exists it is likely to follow a diurnally rising and falling pattern. To identify the inversion and determine the mixing height, among other things, a number of quantities are measured. These include the state variables, temperature and pressure, the moisture content as dew point and relative humidity, and the wind speed and direction. By plotting these measurements and quantities calculated from them, the top and bottom height of the inversion and the approximate atmospheric stability can be determined by inspection.

Briefly, the stability of the atmosphere between the ground and the base of the temperature inversion determines the effective rate of turbulent transport of surface emissions up to that elevation. Beneath the inversion the air is likely to be neutral to very unstable. Beyond this elevation the strongly supressed mixing within the inversion acts to dampen turbulence and decrease the effective diffusive transport by orders of magnitude. Under these conditions the air is considered stable. Extensive research has been done to estimate vertical diffusivities from meteorological parameters under a wide range of stabilities. A summary of work on this subject which also includes extensive details on its application to air-shed modeling for the Los Angeles Basin was compiled by McRae, Goodin, and Seinfeld (see EQL, 1982). For the purposes of the

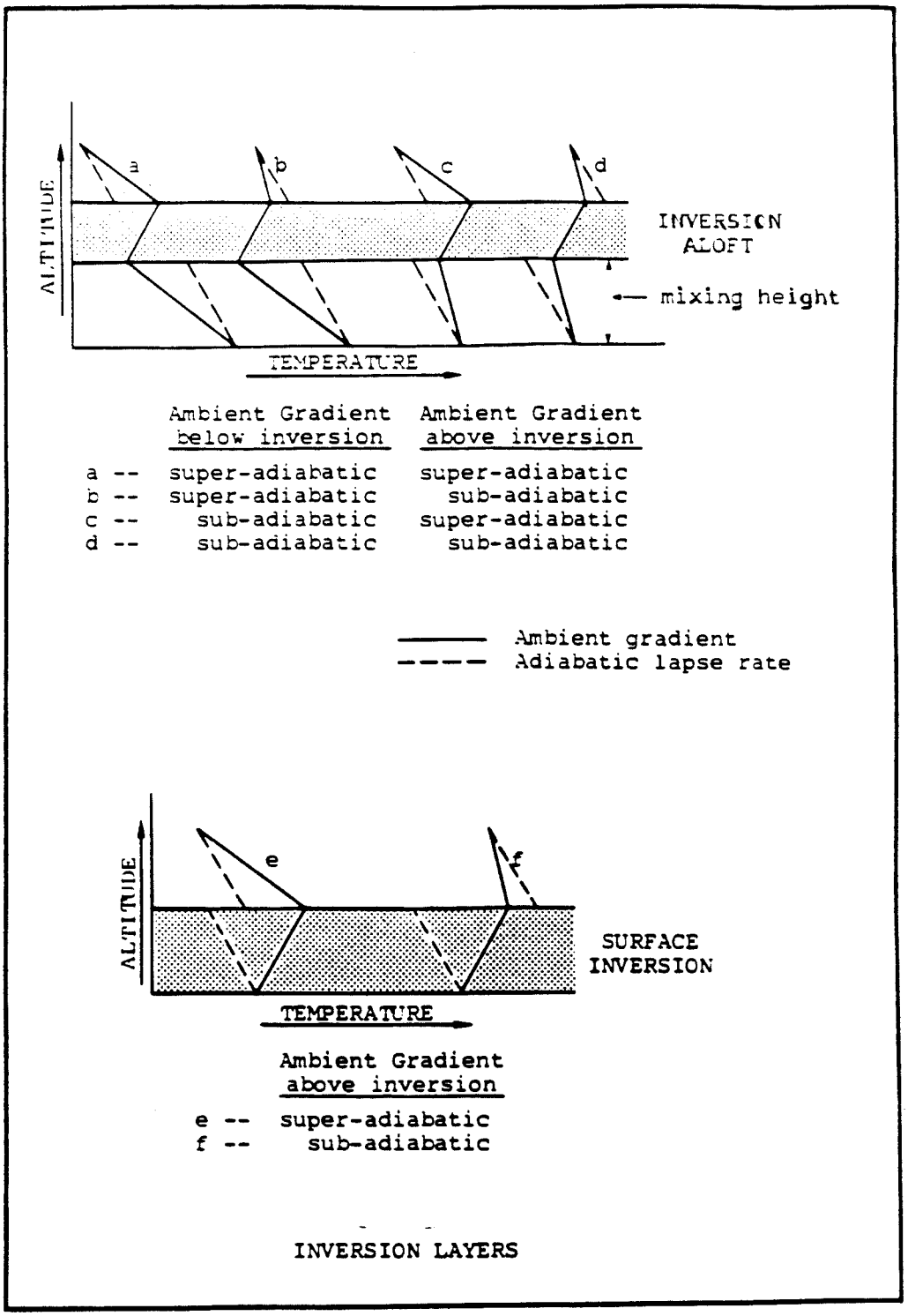

Figure 1. Idealized vertical temperature profiles (reproduced from Fundamentals of Stack Gas Dispersion, 1979).

preceeding paper's mass balances, a very simple assumption about the vertical mixing rates was used when an inversion existed. It is that vertical mixing is fast between the ground and the inversion base relative to horizontal tracer transport. This has the equivalent effect of assuming the tracer is constant in the z-direction at the measured ground-level concentration up to the base of the inversion.

For a given time, a reasonable upper bound on the extent of the tracer's vertical transport is the greatest height that the tracer could have been transported to at all previous times since its release. When a temperature inversion is present, the mixing height is the best upper bound. This is an especially good estimate when the inversion height has been constant or monotonically increasing since the tracer release. Under these conditions the air beneath the inversion is likely to be neutral to unstable, and tracer is being mixed readily upward from ground level. When the inversion height has been fluctuating or decreasing, the maximum height since the release is a more appropriate choice. First, the tracer may have been transported to a maximum height at an earlier time when the inversion base was higher. Finally, as the inversion base falls, it may be incorporating tracer-rich air from beneath it. By this mechanism tracer would become trapped in the inversion, and estimates of its maximum vertical dispersion would be too low, based on the current inversion height. This trapping phenomena has been observed with pollutants such as ozone (Edinger 1973). Alternatively, if the inversion base rises or the inversion is entirely destroyed by the eroding effect of unstable air from below (or other mechanisms), an upper bound on the transport may be harder to determine. In such cases the atmospheric stability can be used to compute an upper bound. Similarly, when the inversion begins at the surface and stays there throughout a tracer experiment, bounding the extent of vertical mixing is also done using the atmospheric

stability.

During the Southern California Air Quality Study, three of the four tracer releases began in the morning. Of these, two were done in the summer and on days where an elevated inversion existed. The third morning release was in the fall period, and the fourth release was a late afternoon fall release. Both were associated with neutral to stable conditions where the inversion bases were much lower than the summer releases.

The vertical measurements from the Southern California Air Quality Study will be presented below. The purpose of this section is to present the data which is available from the SCAQS, and at the time of this research had not been reported nor analyzed in the literature. It is not the purpose of this section to analyze this data in general, but simply to tablulate estimates of mixing heights, and clearly document how such estimates were obtained. These tabulated mixing heights and the preceding discussion are the basis for closing the mass balances described in the paper entitled "Ground Release SF_6 Tracer Experiments Used to Characterize Transport and Dispersion of Atmospheric Pollutants During the Southern California Air Quality Study of 1987" (Horrell et al. 1989). The extensive figure set in Appendix A2.2 is included because it is the best, most comprehensive simultaneous display of these data known to exist.

Method

The data set containing the vertical atmospheric measurements was obtained from the California Air Resources Board for the SCAQS days when sulfur hexafluoride tracer experiments were done. Recall, these days are July 15, September 3, November 12, and December 10-11, all of 1987. The measured quantities in the data set are temperature and dew point in degrees C, pressure in $mbars$, relative humidity, wind speed in m/s, and wind direction in *degrees off north.* Each data file consists of the measurements taken at one of six times during the day, generally around the hours 5, 8, 11, 14, 17, and 22 PST. Data was reported at 30 to 100 meter intervals sometimes to heights of 5000 meters above ground level (AGL).

Some data sets were lacking in entire categories, i.e., wind speed, or contained a large number of missing data. In such circumstances the mixing heights were reported but the plot was omitted from Appendix A2.2. Furthermore, to reduce the number of plots, only those locations that were impacted by tracer or surrounded impacted locations are presented. The diskette containing the data for November 13, a tracer sampling day, had failed at the time of plotting, but was used at an earlier time to compile the data.

The measured data was used to calculate the potential temperature, the gradient form of the Richardson number (Equation 2.2.6), and the change in wind direction with height at each vertical height that data was reported. The processing program, UPPR:UPPer air viewer (developed at California Institute of Technology by the author), then simultaneously generated plots for both measured and calculated variables. The potential temperature was calculated using the relationship:

$$\Theta = \Gamma T + T_0. \tag{2.2.5}$$

In Equation 2.2.5, Θ is the potential temperature, Γ is the atmospheric lapse rate, T is the measured temperature, and T_0 is the ground temperature. A constant value for Γ of 0.01 degrees C/m was used. This neglects the effect of water vapor on the lapse rate, but the effect is small (Seinfeld, 1975) and at no time did neglecting it prevent the inversion base from being located. The stability of the air below the inversion base was estimated from the slope of the vertical plot using Figure 2 as a guideline. In addition, a form of the gradient Richardson number and the change in wind speed with height was calculated in order to qualitatively, point-wise, compare their magnitude with the potential temperature and measured quantities. In theory the inversion base should coincide with a large gradient Richardson number because of the sharp temperature (density) change associated with the inversion. It was calculated based on the differential form of its definition.

$$Ri_g = \frac{\frac{g}{T}\frac{\partial \Theta}{\partial z}}{\left(\frac{\partial \overline{U}}{\partial z}\right)^2} \equiv \frac{\frac{g}{T}\frac{\Delta \Theta}{\Delta z}}{\left(\frac{\Delta \overline{U}}{\Delta z}\right)^2} = \frac{g}{T}\Delta\Theta\Delta z(\Delta\overline{U})^{-2} \qquad (2.2.6)$$

In Equation 2.2.6, g is the gravitational constant, and $\overline{U}$ is the time averaged speed as a function of z. The other variables have the same meaning as in Equation 2.2.5.

Limitations were imposed on the data and calculated values to ensure that the plots would be free of invalid data and easy to read. The Richardson number was limited to values below ten thousand. Negative values were permitted but seldom observed. Invalid speeds cause calculation of the Richardson number to be suppressed. The change in direction with height was limited to values of ± 18 degrees. Values which exceed these criteria were truncated.

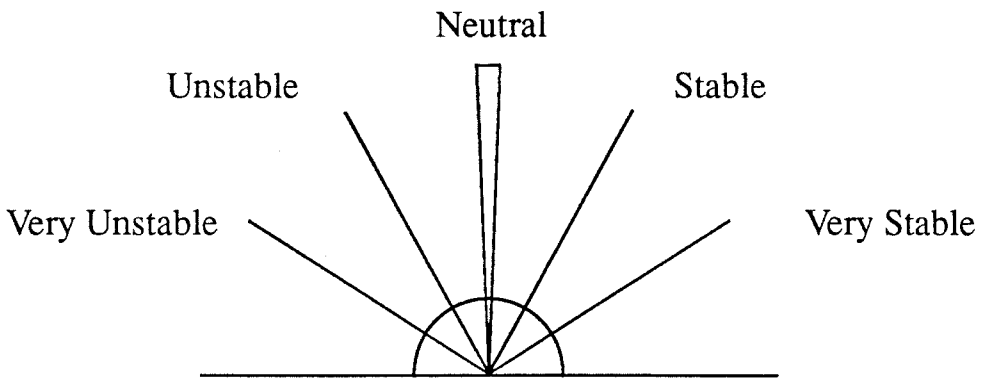

Figure 2. Slope of the potential temperature with increasing height versus range of atmospheric stability.

Results

The estimated mixing heights are presented in Tables 1-3. These values were obtained directly by interpreting Figures 1-68 of Appendix A2.2, and some additional plots not reproduced here, showing vertical data profiles upto 1500 meters. The estimated heights correspond with reasonable recovery rates for the mass balances.

Acknowledgements

I would like to thank Don Lehrman of Technical and Business Systems for providing me with some preliminary data and the data format just following the summertime SCAQS. This allowed me to develop the analysis tool UPPR for creating and manipulating the data well in advance of the release of the verified data by the California Air Resources Board in 1988. I would also like to thank Chuck Bennett of the California Air Resources Board for providing me with the verified data.

Date	Site Name	Hour of the Day	Inversion Base Height (meters)
July 15	Burbank	5	700
		8	450
		11	550
		15	500
		17	550
		22	500
	El Monte	5	550
		8	550
		11	375
		14	375
		18	550
September 3	Burbank	5	175
		8	175
		11	300
		14	300
		17	375
		22	600
	El Monte	8	175
		12	300
		14	750
		17	500

Table 1. Mixing Depths During the Summertime SCAQS 1987

Date	Site Name	Hour of the Day	Inversion Base Height (meters)
November 12	Burbank	4	0
		8	150
		11	150
		14	375
		17	0
		22	0
	El Monte	6	0
		11	375
		14	750
		17	0
	Long Beach	5	0
		8	0
		11	375
		14	200
		17	200
		22	0
	LMU	5	0
November 13	Burbank	5	275
		8	500
		11	450
		14	750
		18	750
		22	375
	El Monte	7	500
		8	500
		11	600
		14	750
	Long Beach	8	750
		11	750
		14	800
		17	800
	LMU	5	400
		8	700
		11	750
	Ontario	5	0
		9	0
		11	375

Table 2. Mixing Depths During the November SCAQS 1987

Date	Site Name	Hour of the Day	Inversion Base Height (meters)
December 10	Burbank	11	0
		14	375
		17	0
		22	0
	El Monte	5	0
		8	0
		11	100
		15	300
	Long Beach	11	200
		14	400
		17	200
		22	0
	LMU	0	0
		14	200
		17	0
December 11	Burbank	5	0
		8	0
		10	0
		14	200
	El Monte	8	0
		11	200
		17	0
	Long Beach	5	50
		8	50
		11	50
		14	200
	LMU	5	0
		8	0
		11	200
		14	200

Table 3. Mixing Depths During the December SCAQS 1987

A2.2 Appendix

The collection of 68 figures to follow were generated by the program UPPR in order to tabulate mixing layer heights and provide a qualitative picture for the atmospheric structure above the surface. The figures were reduced to the smallest size which allowed them to be of value for extracting quantitative data. For exact values of the measurements, consult the California Air Resources Board data sets described earlier.

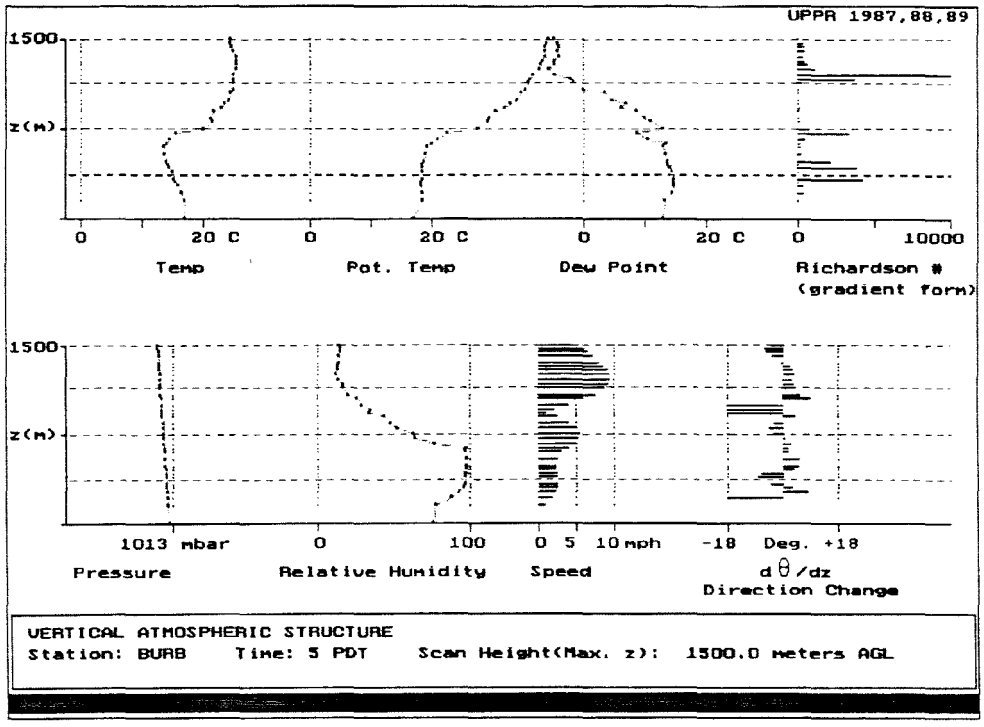

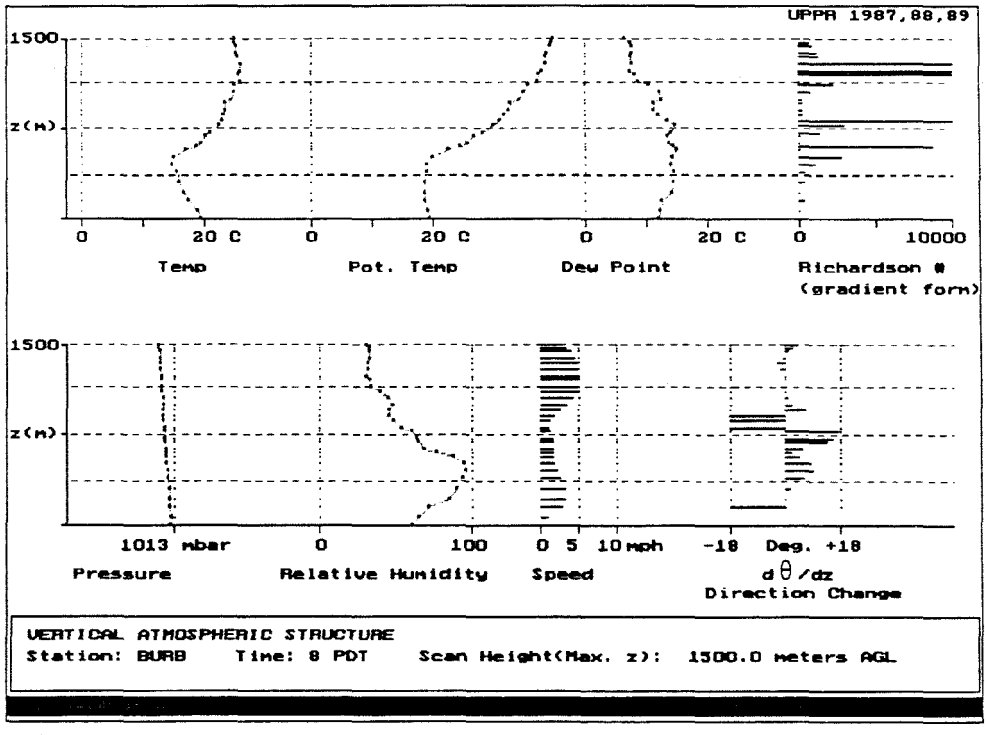

Figure 1. (Top) Vertical atmospheric structure at Burbank at 05:00 PDT, July 15, 1987.

Figure 2. (Bottom) Vertical atmospheric structure at Burbank at 08:00 PDT, July 15, 1987.

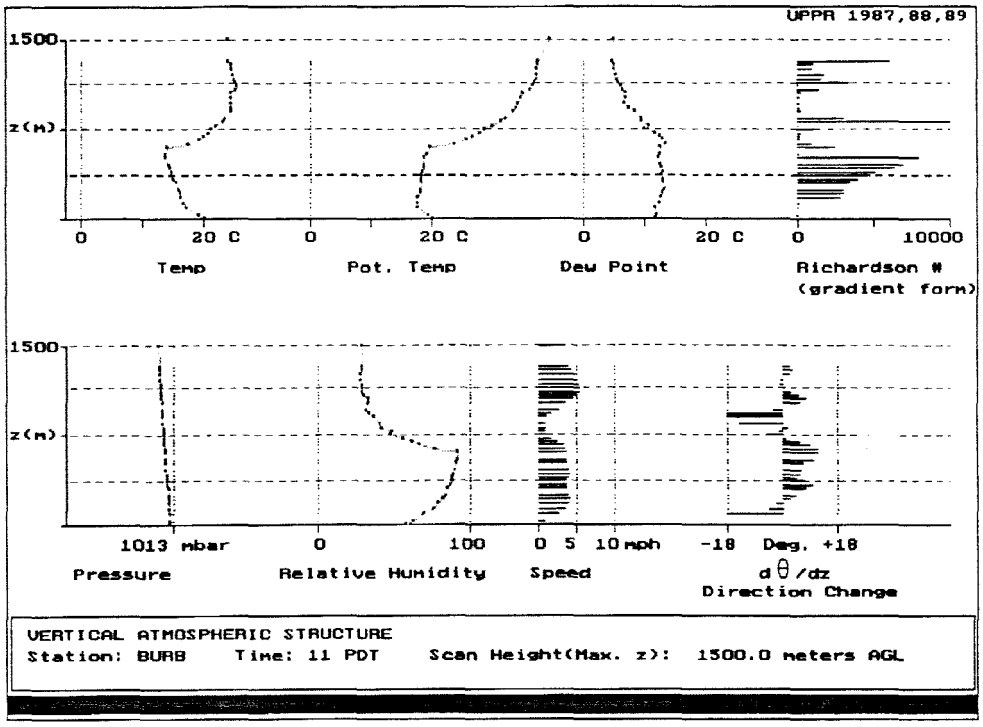

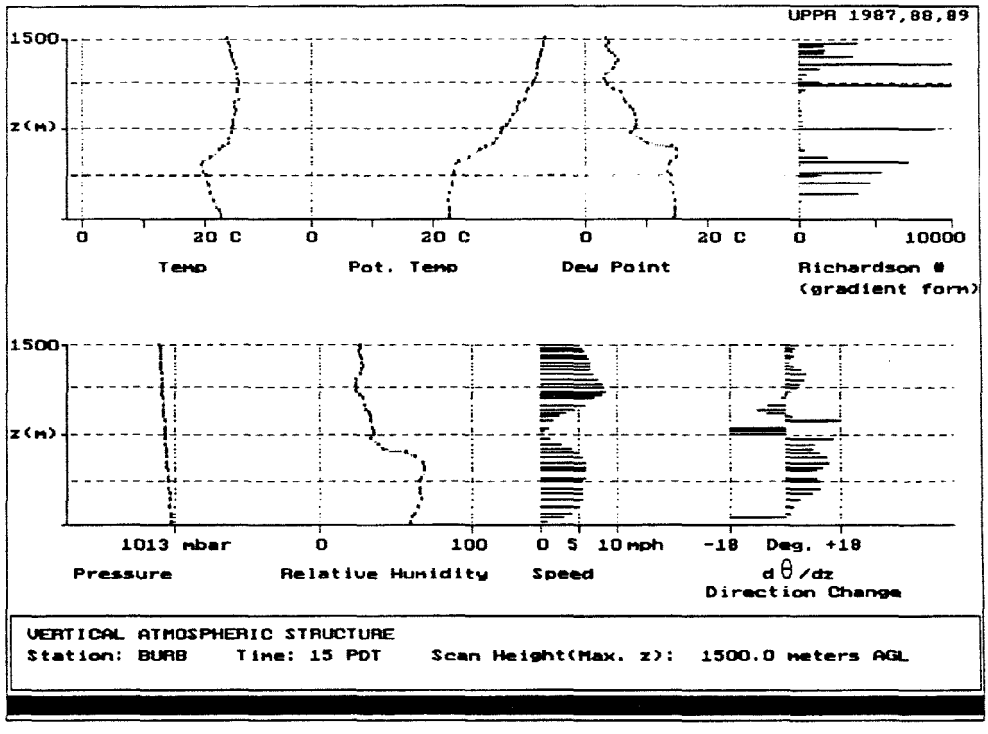

Figure 3. (Top) Vertical atmospheric structure at Burbank at 11:00 PDT, July 15, 1987.

Figure 4. (Bottom) Vertical atmospheric structure at Burbank at 15:00 PDT, July 15, 1987.

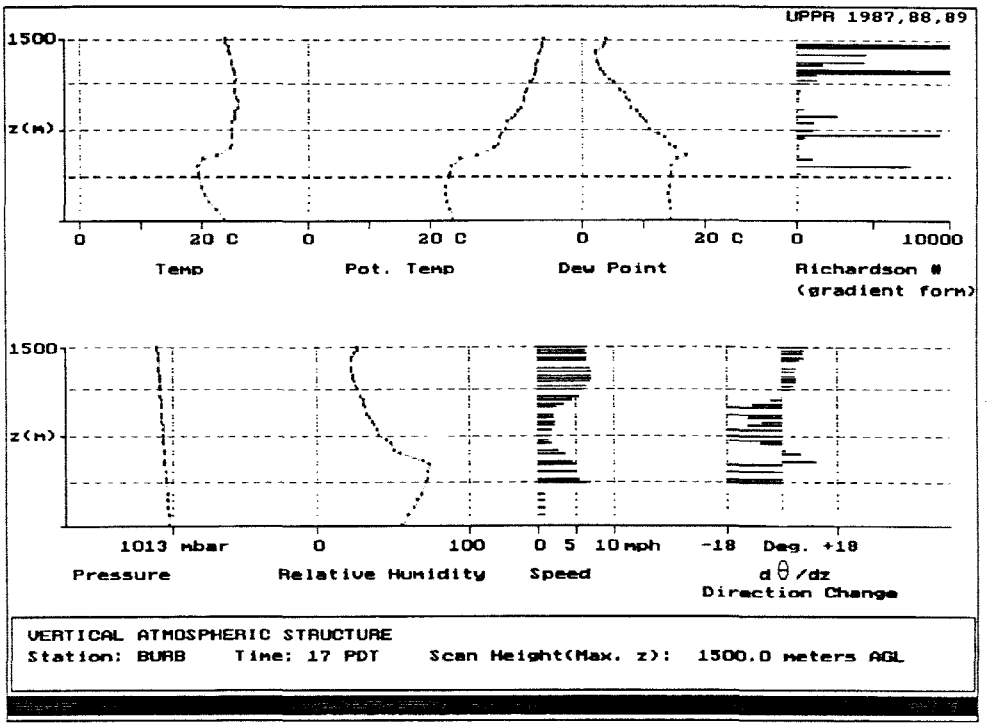

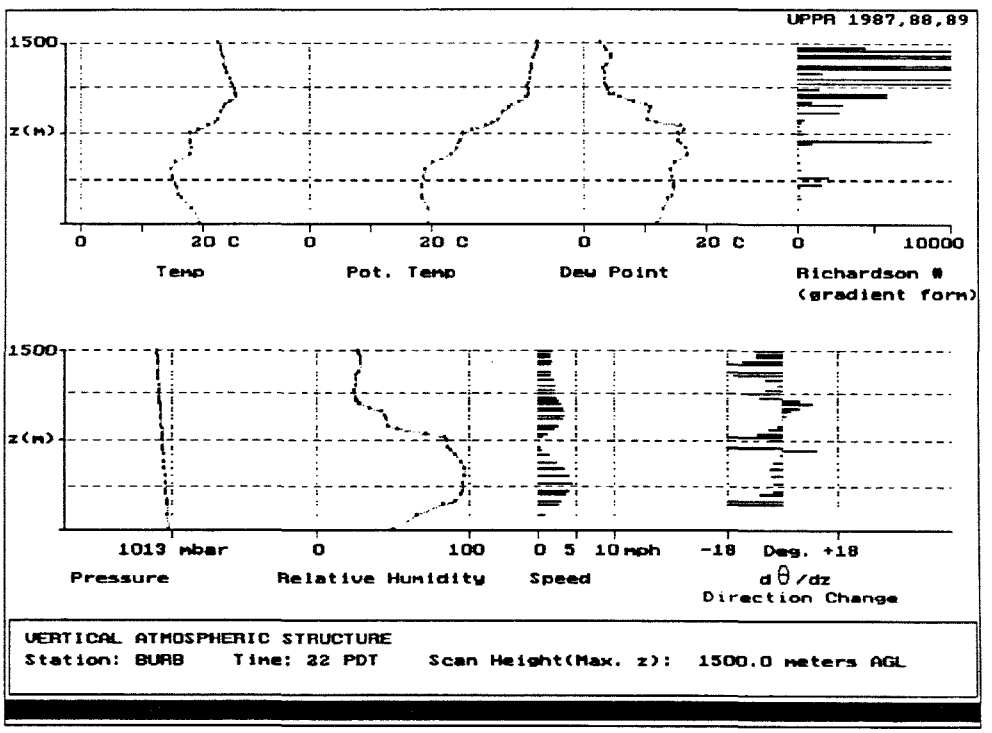

Figure 5. (Top) Vertical atmospheric structure at Burbank at 17:00 PDT, July 15, 1987.

Figure 6. (Bottom) Vertical atmospheric structure at Burbank at 22:00 PDT, July 15, 1987.

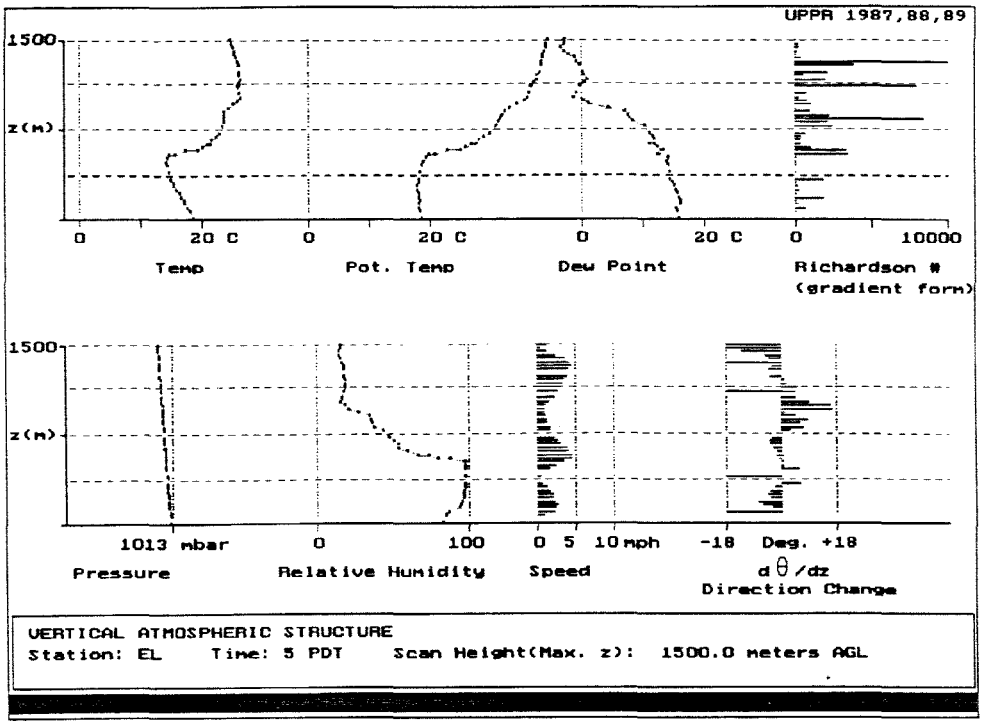

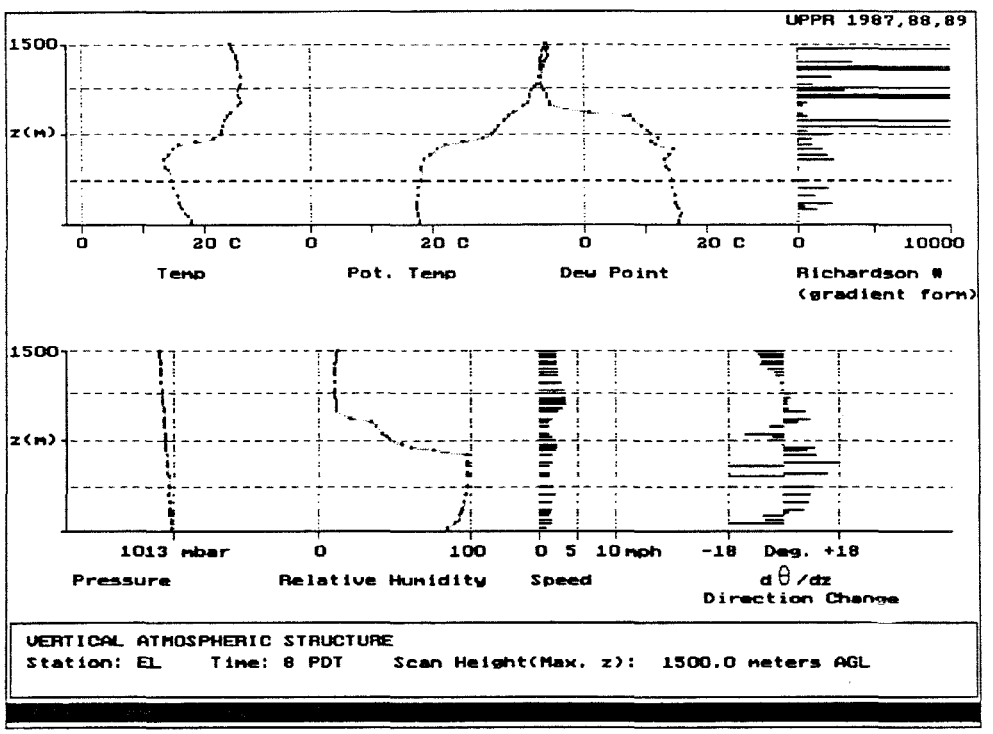

Figure 7. (Top) Vertical atmospheric structure at El Monte at 05:00 PDT, July 15, 1987.

Figure 8. (Bottom) Vertical atmospheric structure at El Monte at 08:00 PDT, July 15, 1987.

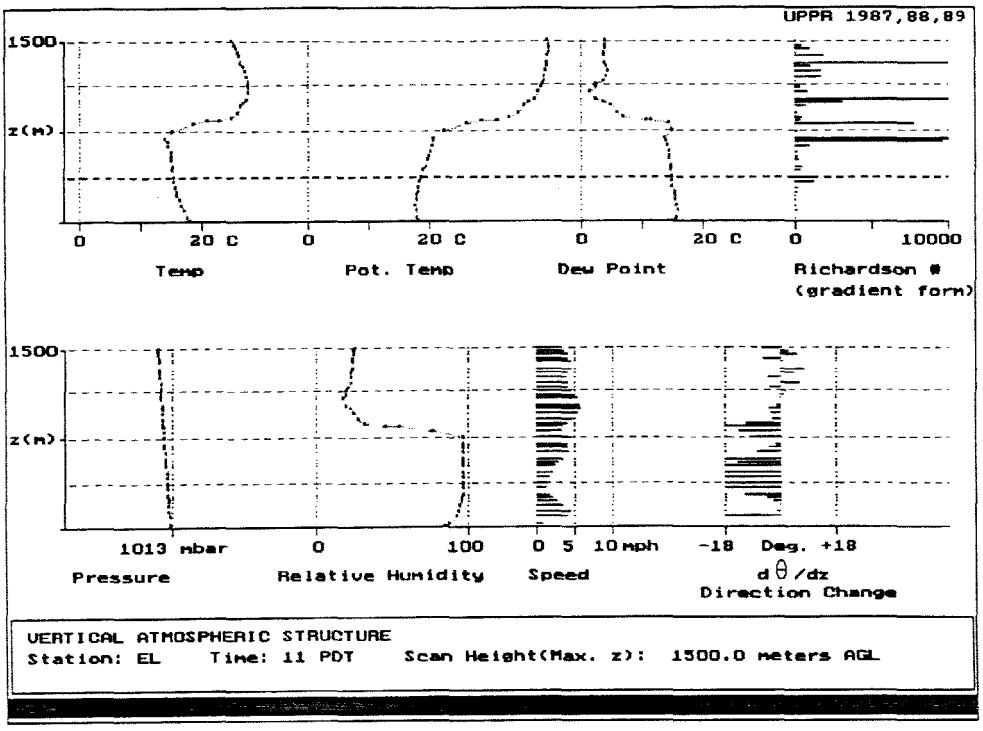

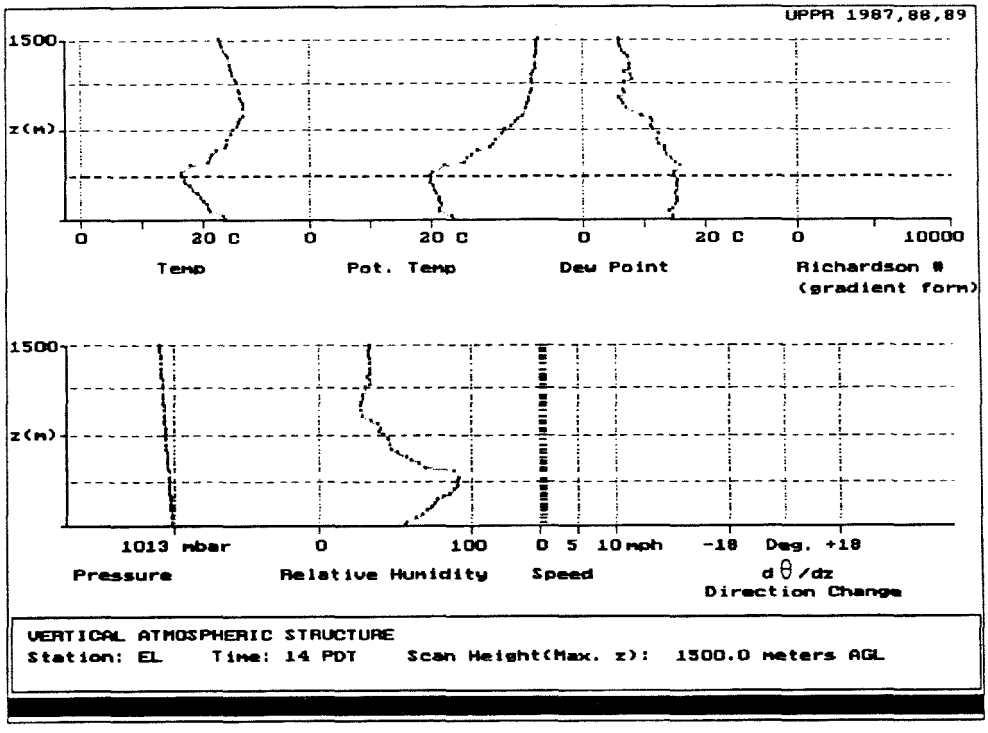

Figure 9. (Top) Vertical atmospheric structure at El Monte at 11:00 PDT, July 15, 1987.

Figure 10. (Bottom) Vertical atmospheric structure at El Monte at 14:00 PDT, July 15, 1987.

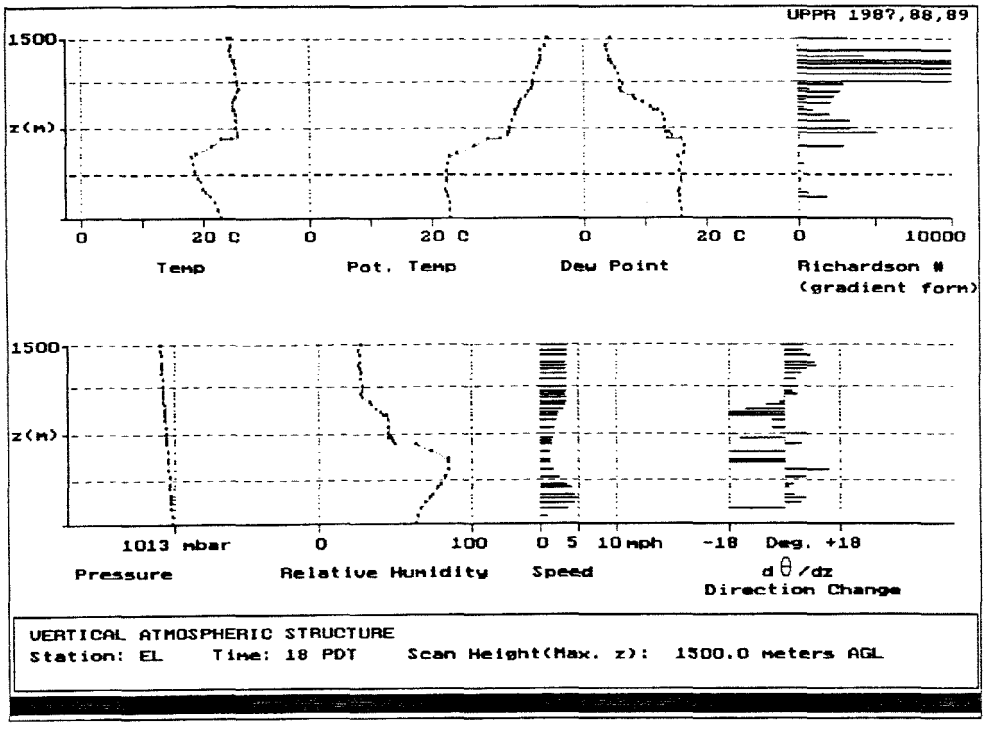

Figure 11. Vertical atmospheric structure at El Monte at 18:00 PDT, July 15, 1987.

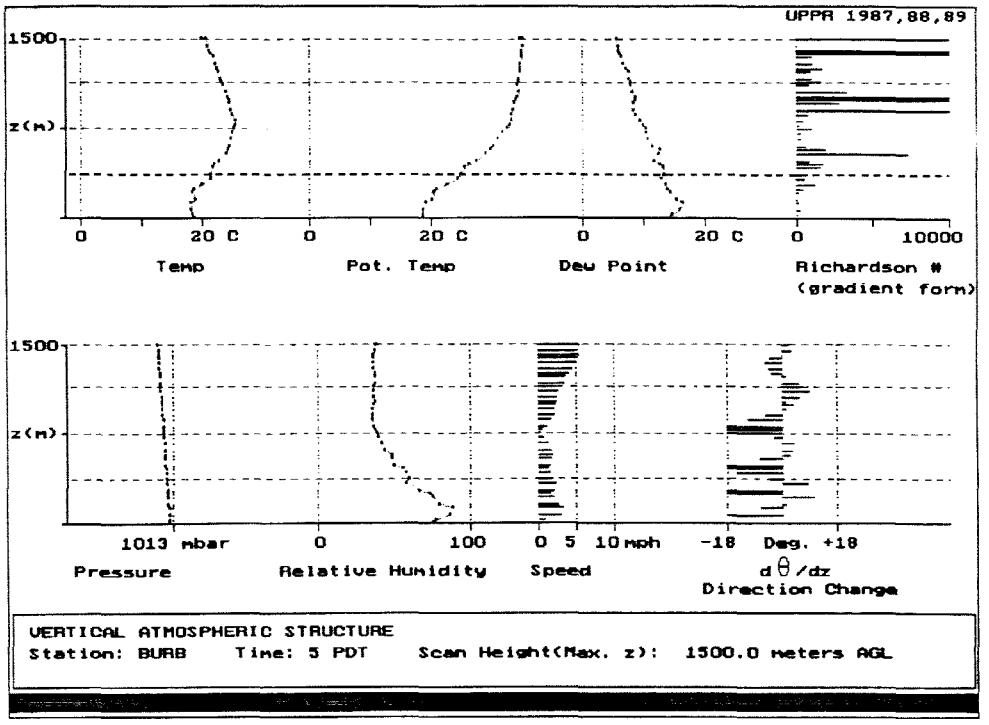

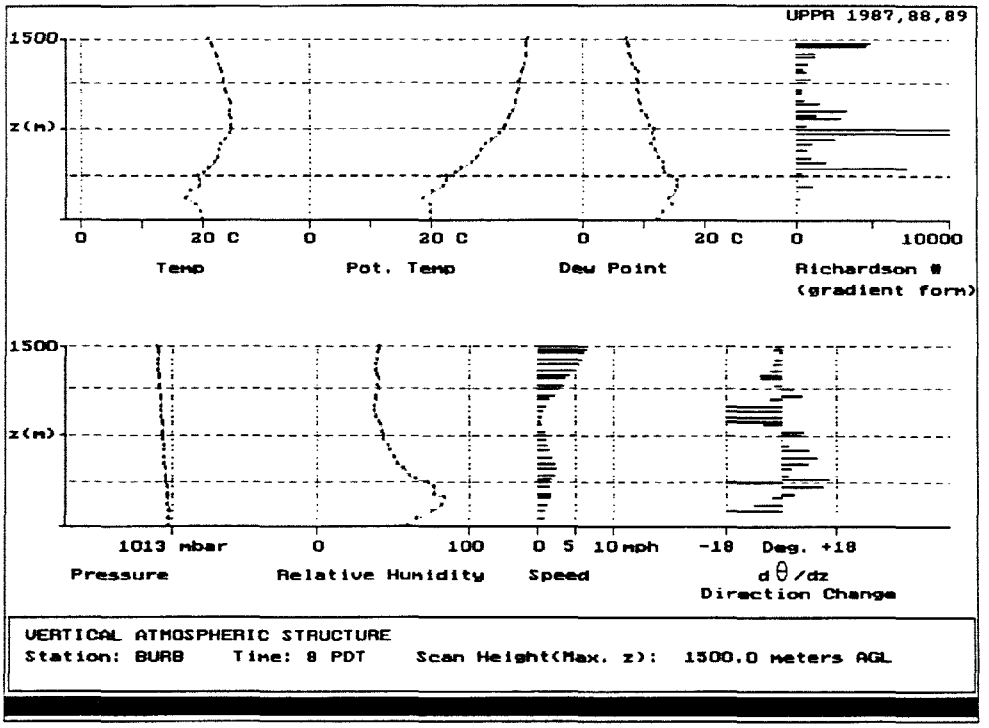

Figure 12. (Top) Vertical atmospheric structure at Burbank at 05:00 PDT, September 3, 1987.

Figure 13. (Bottom) Vertical atmospheric structure at Burbank at 08:00 PDT, September 3, 1987.

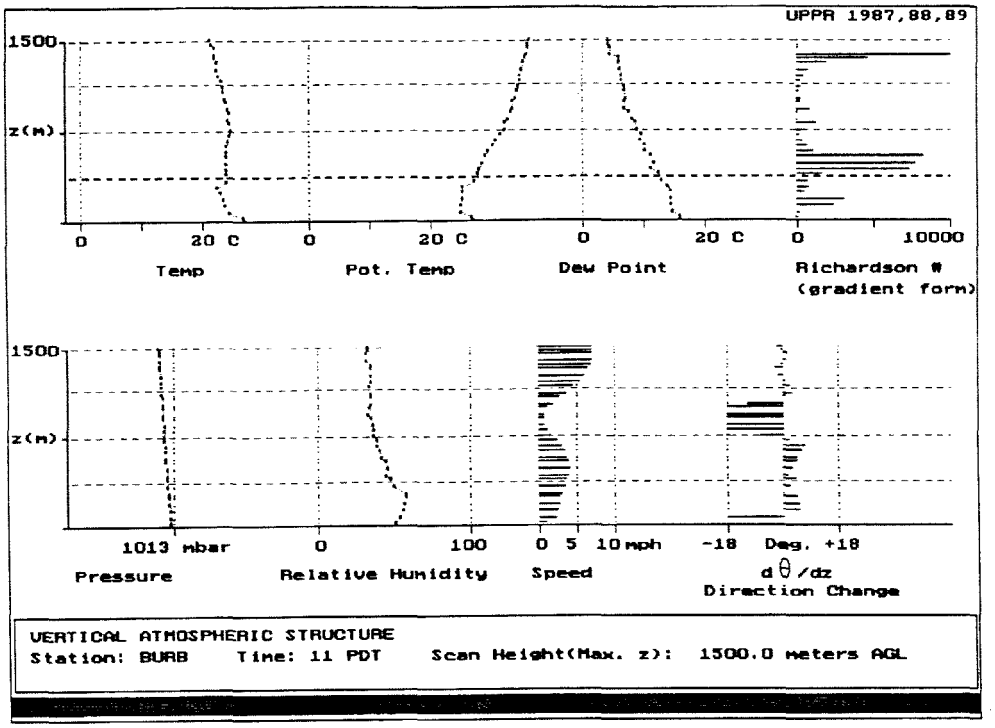

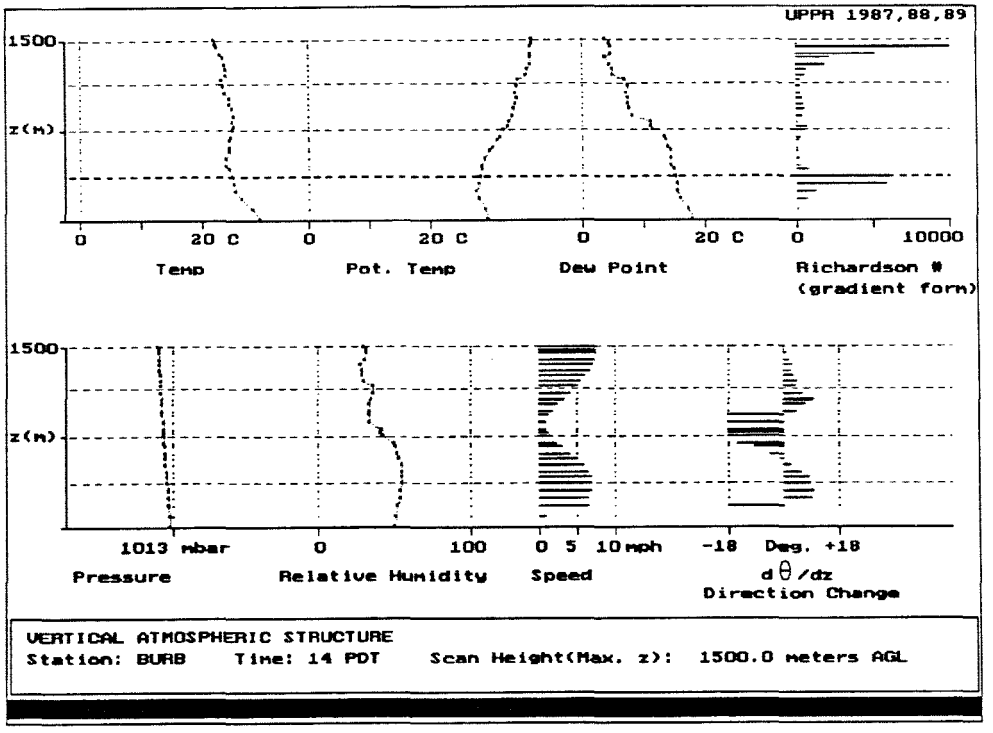

Figure 14. (Top) Vertical atmospheric structure at Burbank at 11:00 PDT, September 3, 1987.

Figure 15. (Bottom) Vertical atmospheric structure at Burbank at 14:00 PDT, September 3, 1987.

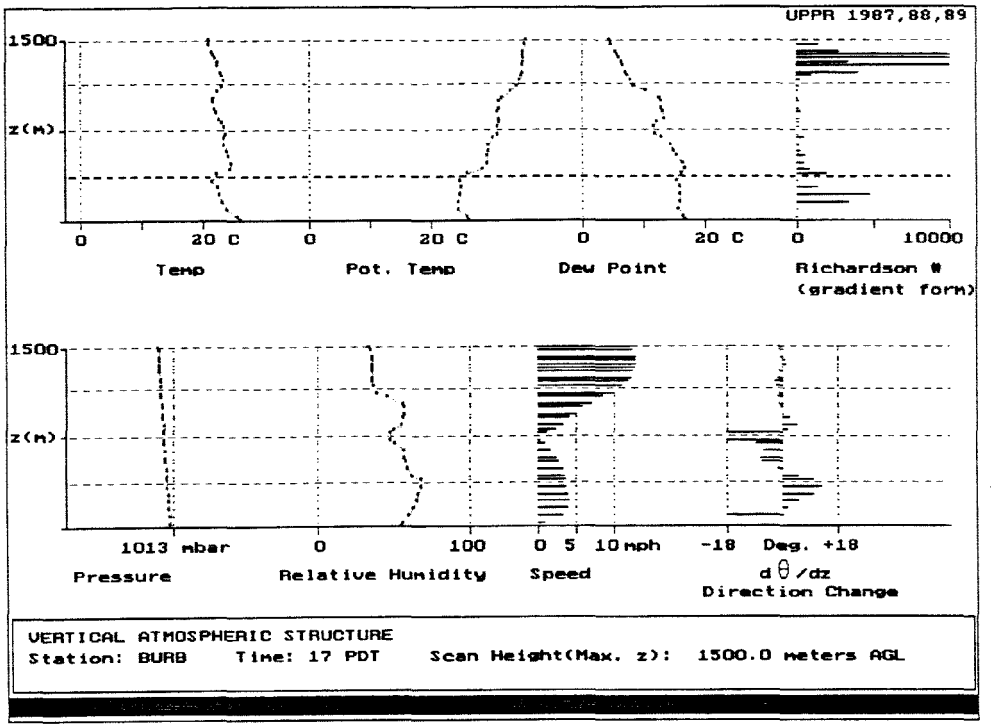

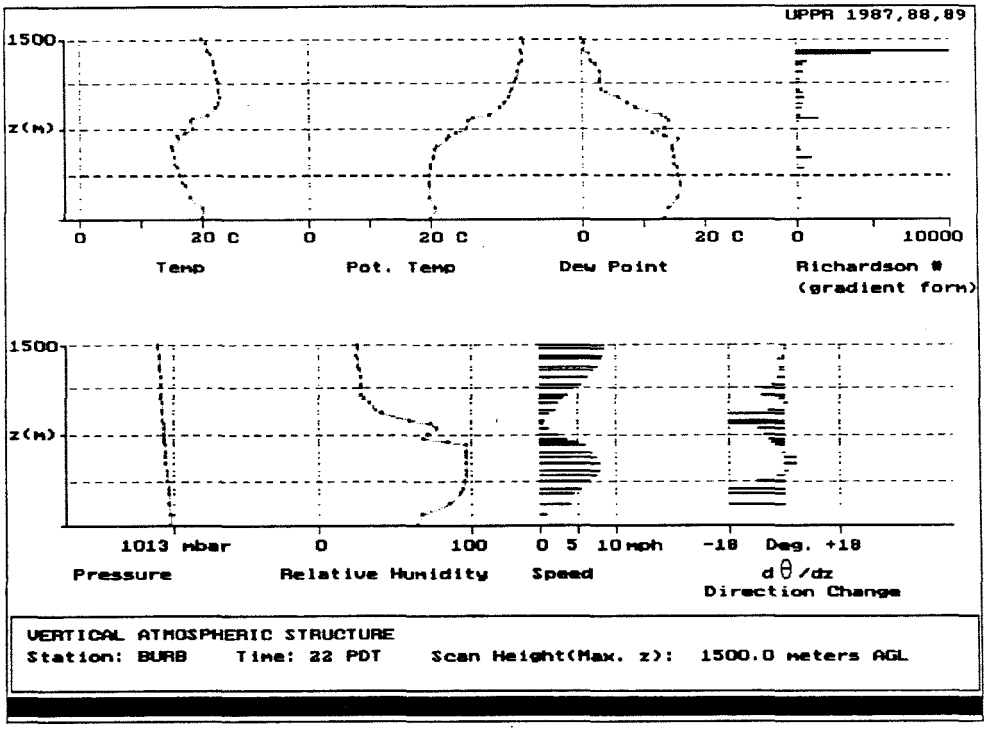

Figure 16. (Top) Vertical atmospheric structure at Burbank at 17:00 PDT, September 3, 1987.

Figure 17. (Bottom) Vertical atmospheric structure at Burbank at 22:00 PDT, September 3, 1987.

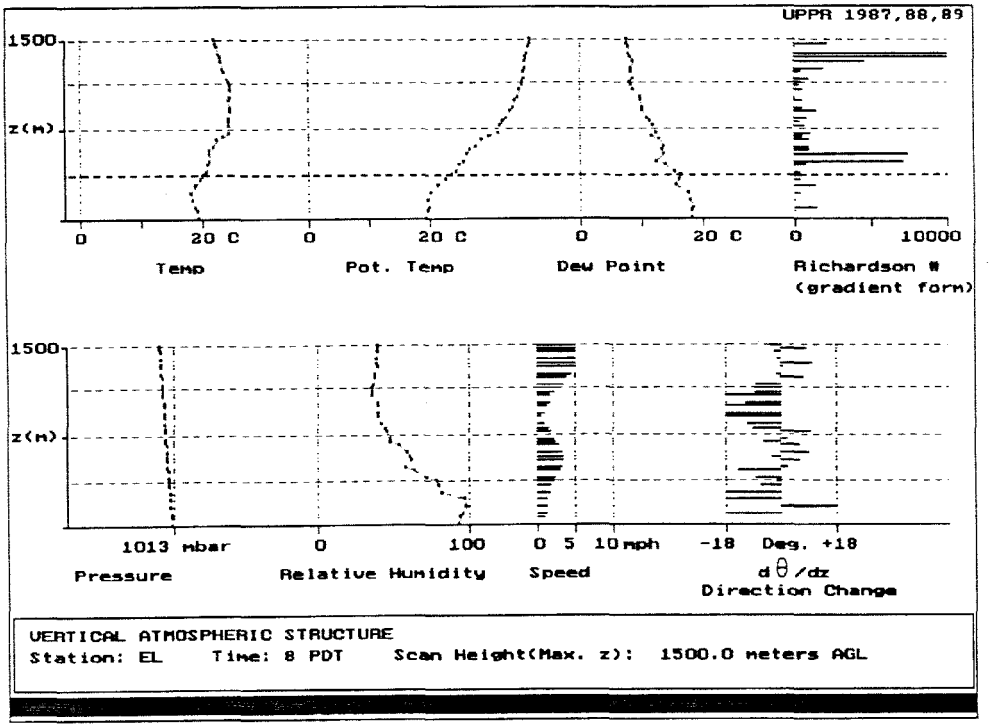

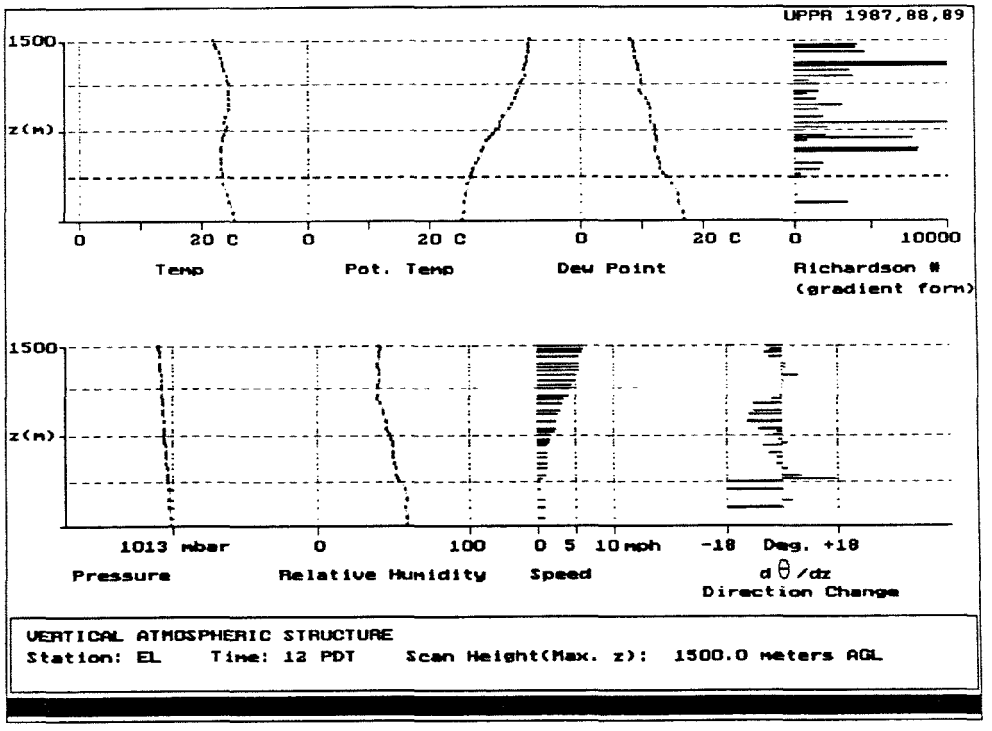

Figure 18. (Top) Vertical atmospheric structure at El Monte at 08:00 PDT, September 3, 1987.

Figure 19. (Bottom) Vertical atmospheric structure at El Monte at 12:00 PDT, September 3, 1987.

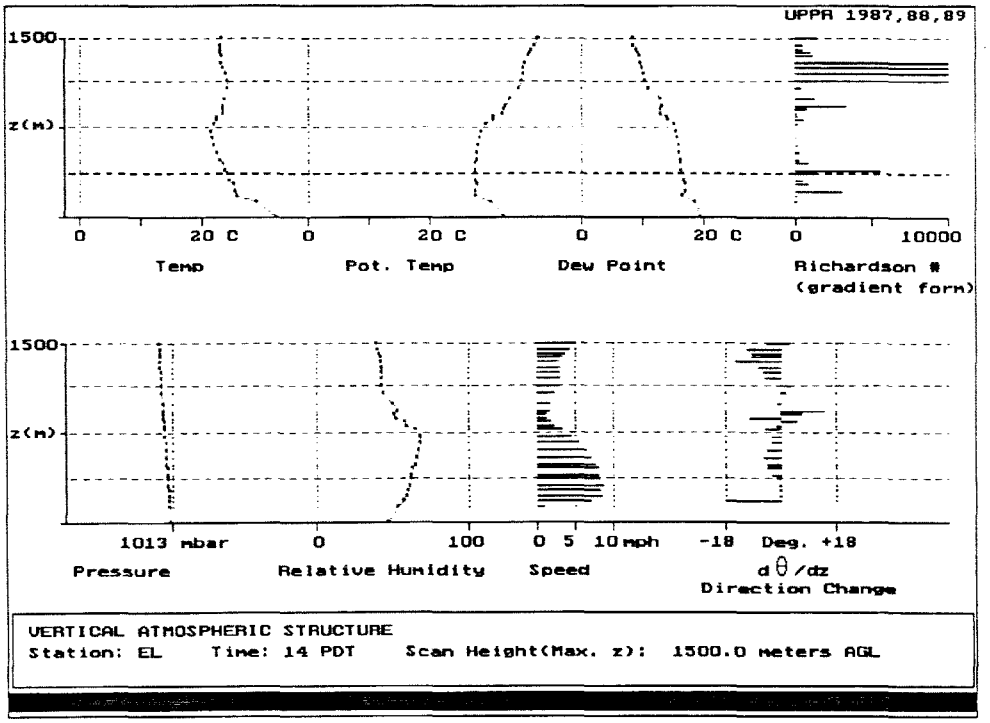

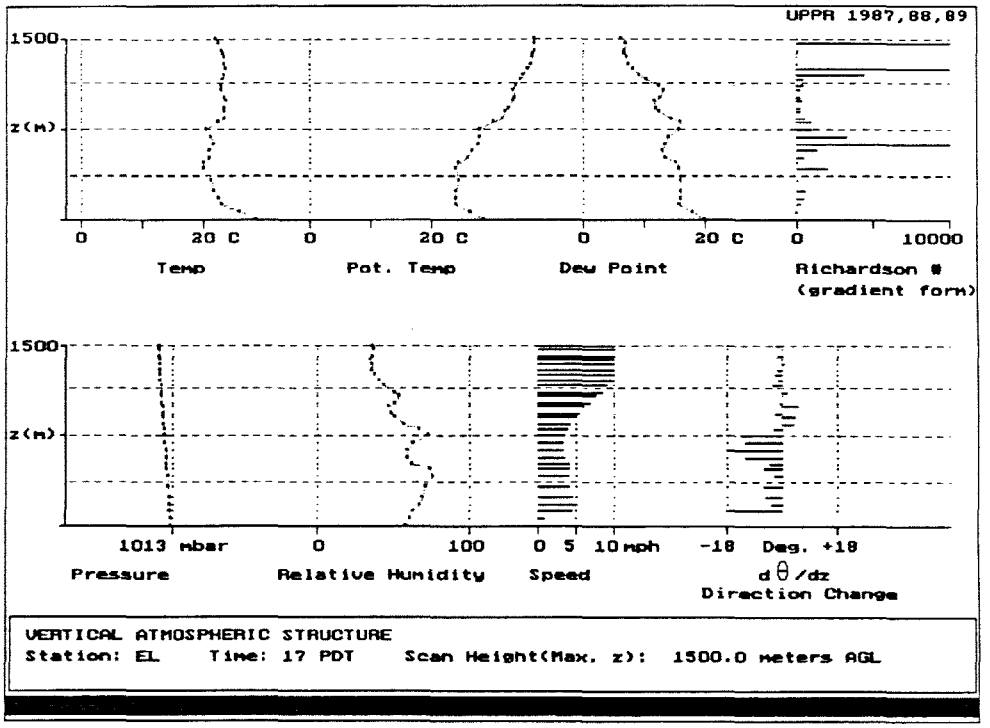

Figure 20. (Top) Vertical atmospheric structure at El Monte at 14:00 PDT, September 3, 1987.

Figure 21. (Bottom) Vertical atmospheric structure at El Monte at 17:00 PDT, September 3, 1987.

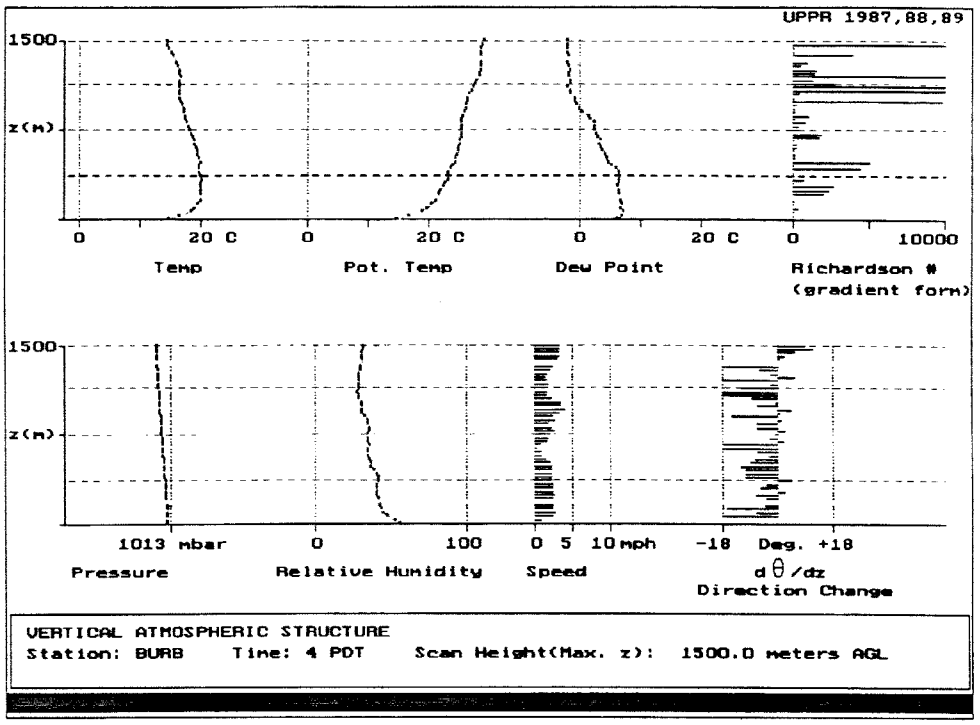

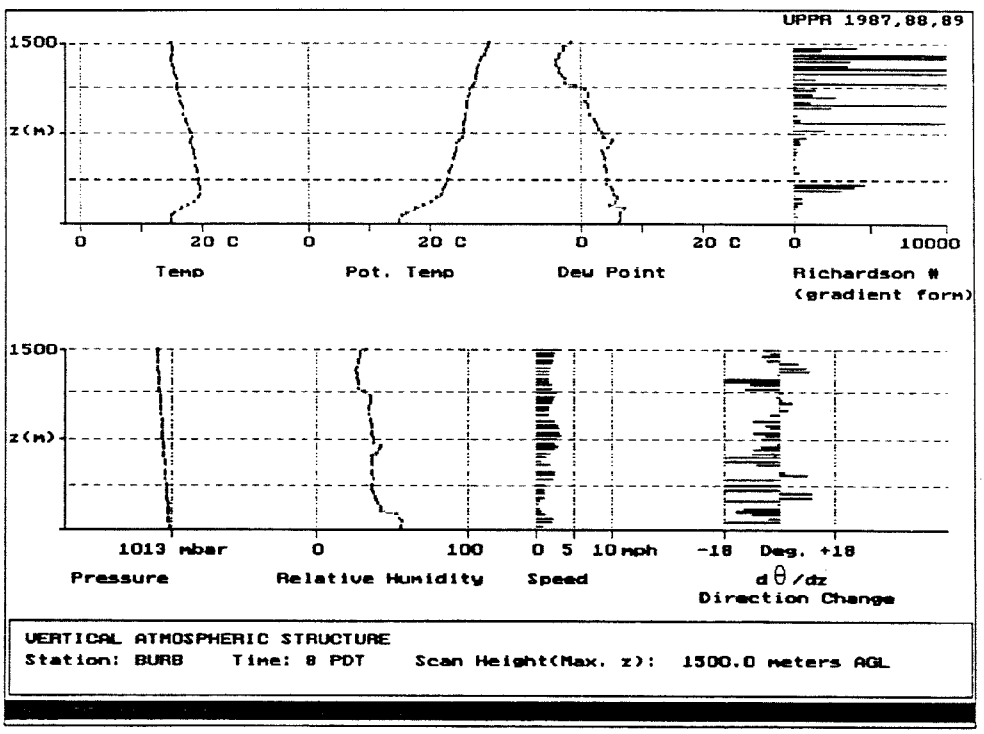

Figure 22. (Top) Vertical atmospheric structure at Burbank at 04:00 PDT, November 12, 1987.

Figure 23. (Bottom) Vertical atmospheric structure at Burbank at 08:00 PDT, November 12, 1987.

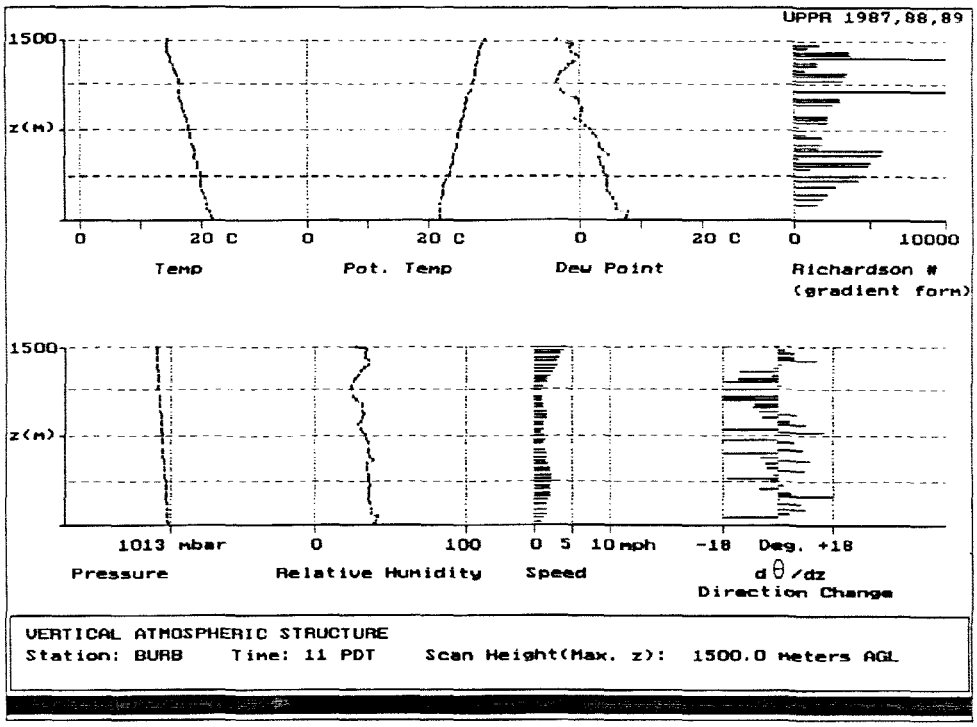

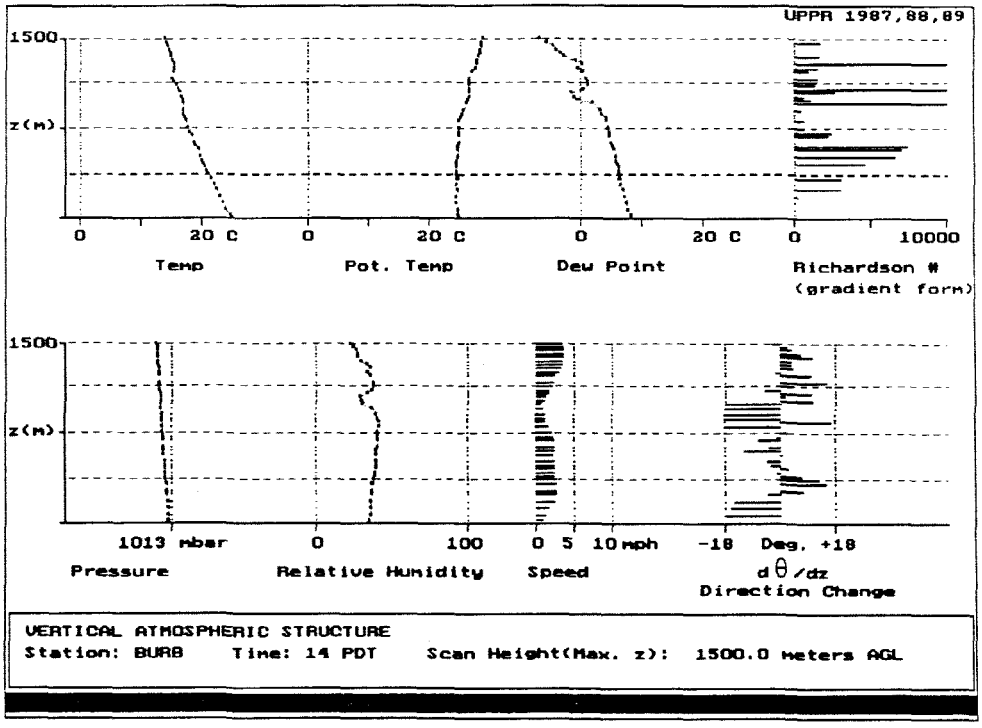

Figure 24. (Top) Vertical atmospheric structure at Burbank at 11:00 PDT, November 12, 1987.

Figure 25. (Bottom) Vertical atmospheric structure at Burbank at 14:00 PDT, November 12, 1987.

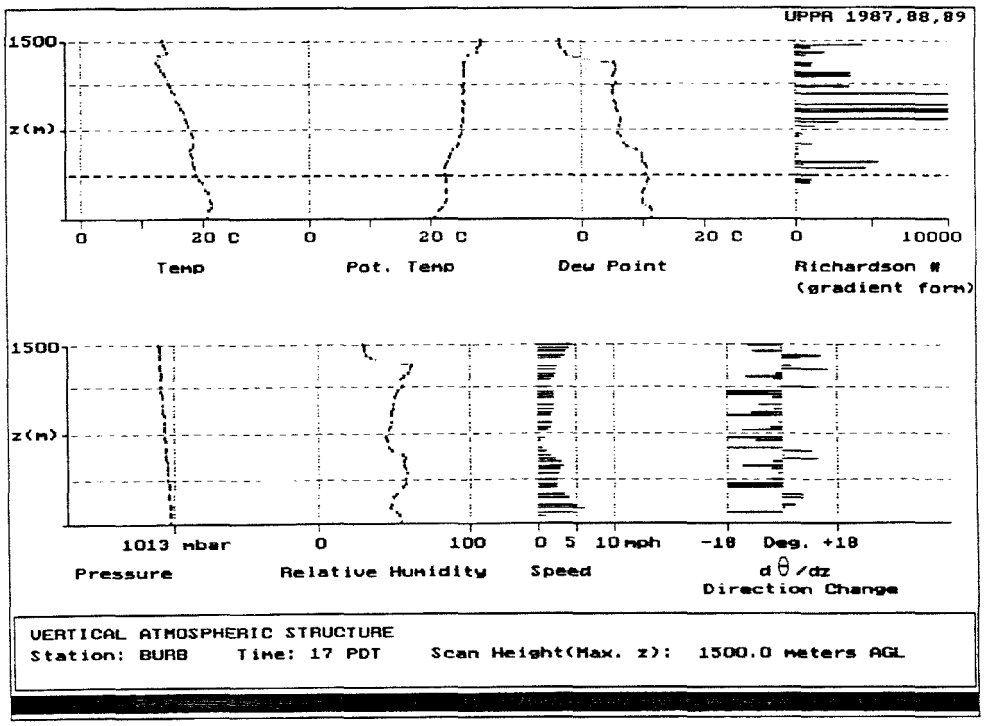

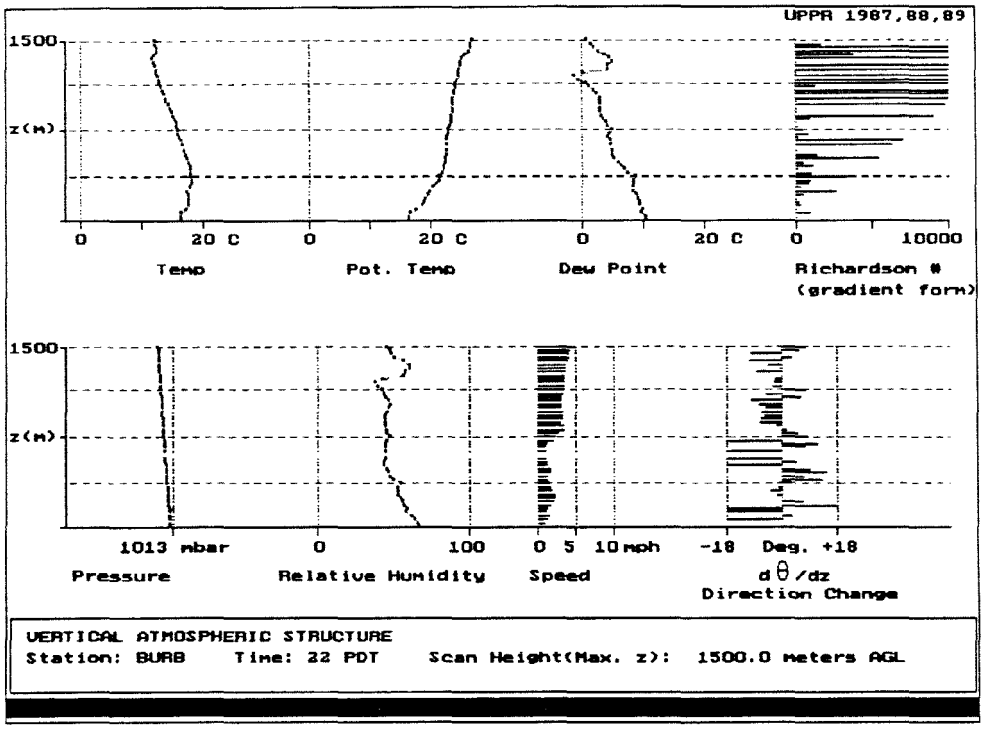

Figure 26. (Top) Vertical atmospheric structure at Burbank at 17:00 PDT, November 12, 1987.

Figure 27. (Bottom) Vertical atmospheric structure at Burbank at 22:00 PDT, November 12, 1987.

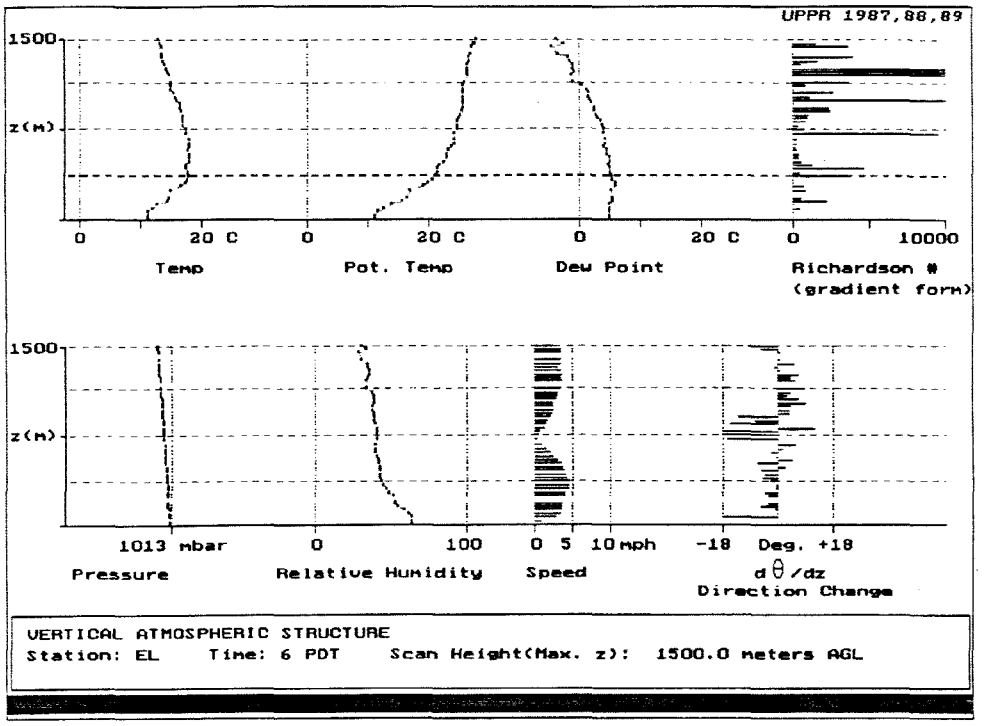

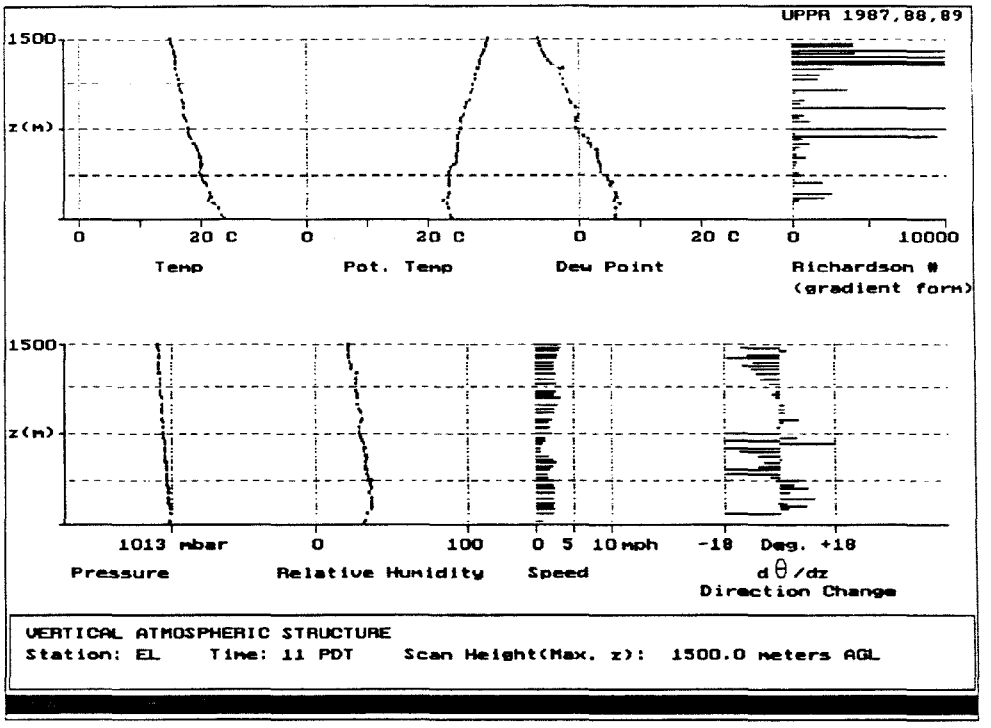

Figure 28. (Top) Vertical atmospheric structure at El Monte at 06:00 PDT, November 12, 1987.

Figure 29. (Bottom) Vertical atmospheric structure at El Monte at 11:00 PDT, November 12, 1987.

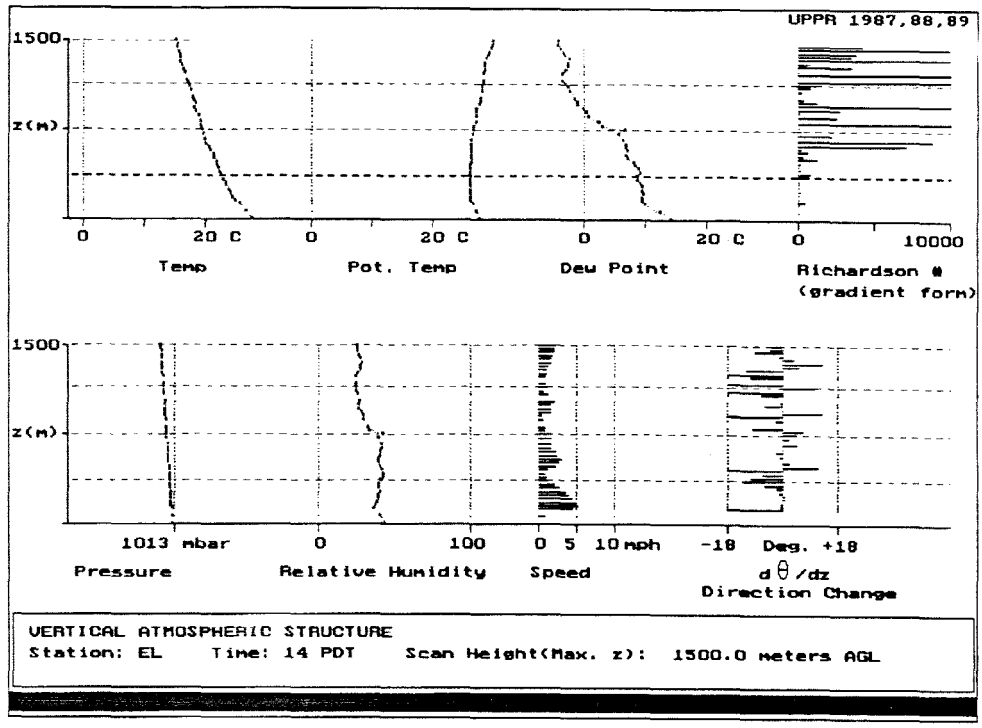

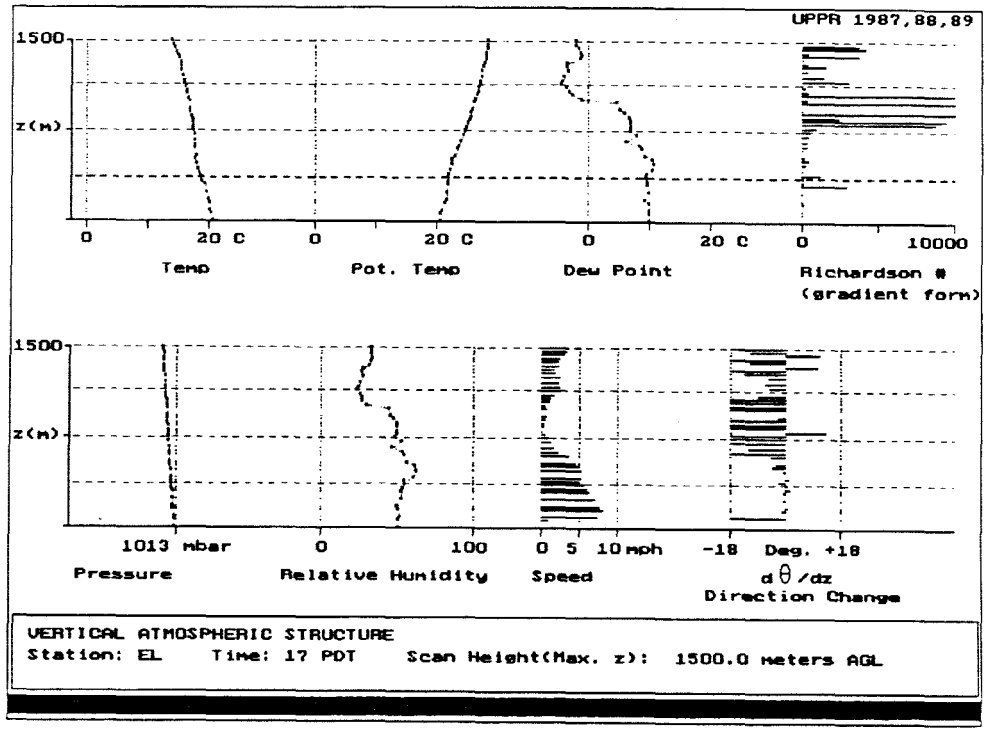

Figure 30. (Top) Vertical atmospheric structure at El Monte at 14:00 PDT, November 12, 1987.

Figure 31. (Bottom) Vertical atmospheric structure at El Monte at 17:00 PDT, November 12, 1987.

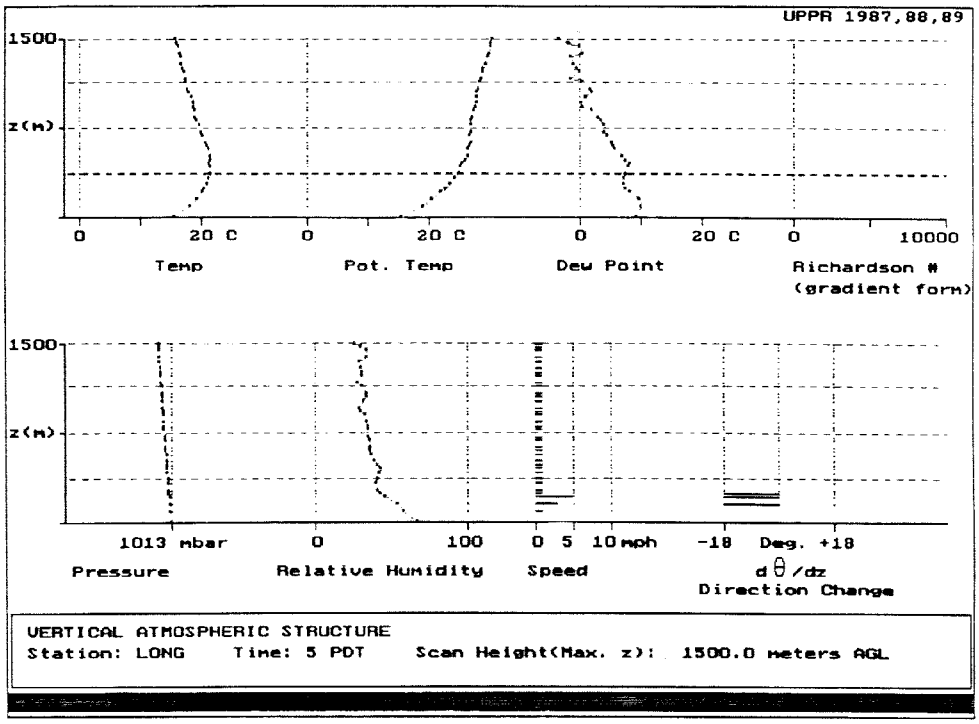

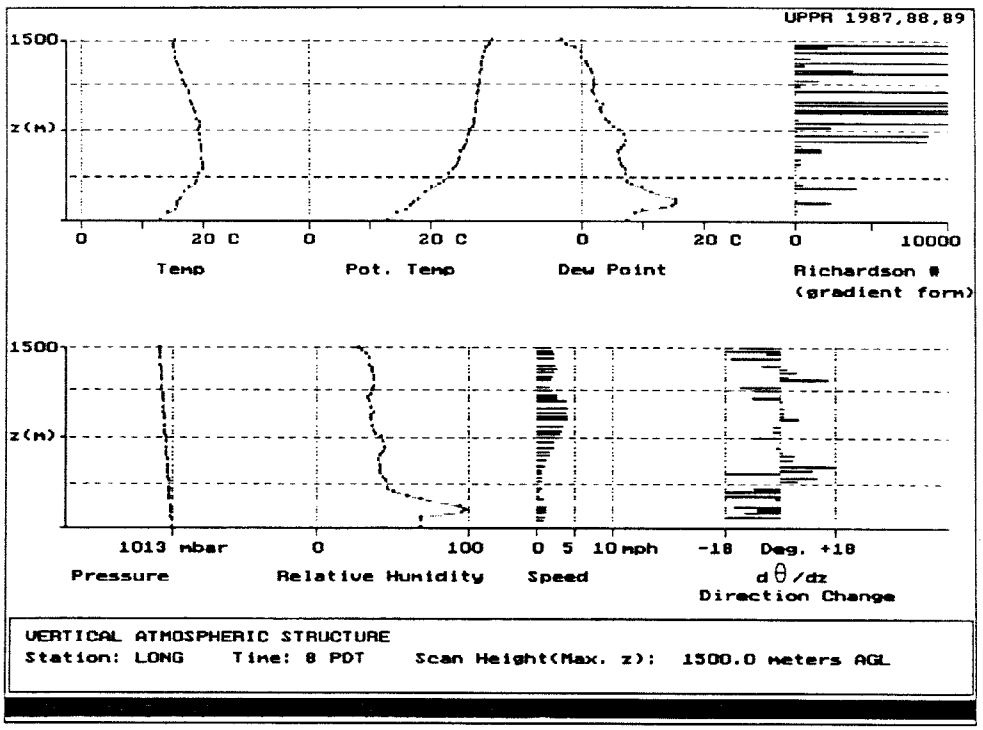

Figure 32. (Top) Vertical atmospheric structure at Long Beach at 05:00 PDT, November 12, 1987.

Figure 33. (Bottom) Vertical atmospheric structure at Long Beach at 08:00 PDT, November 12, 1987.

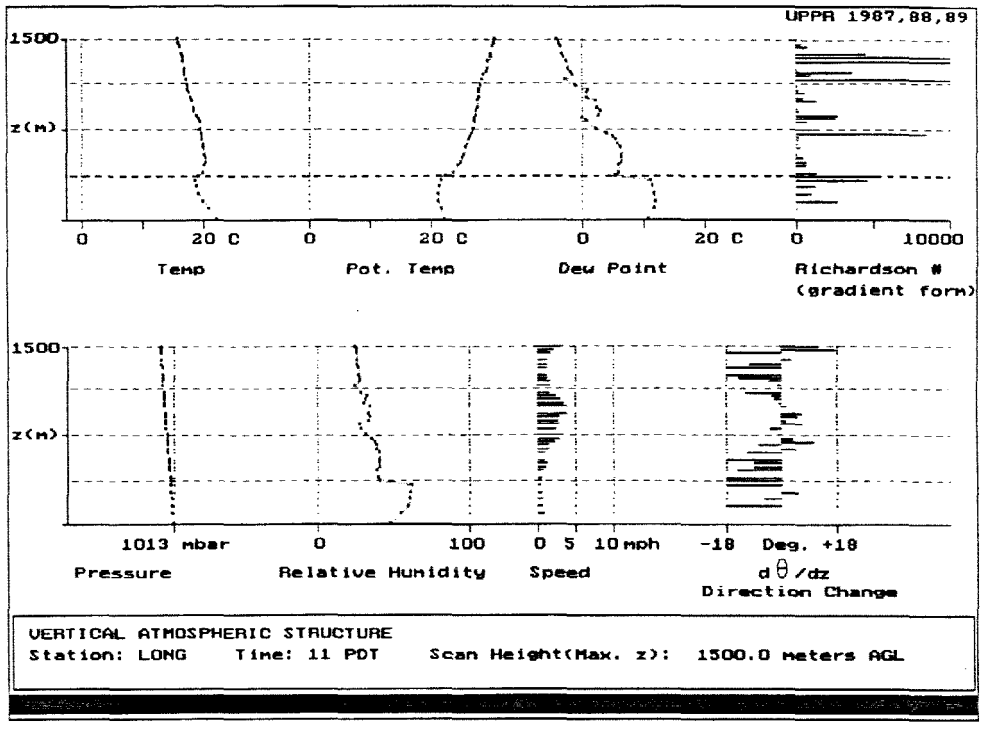

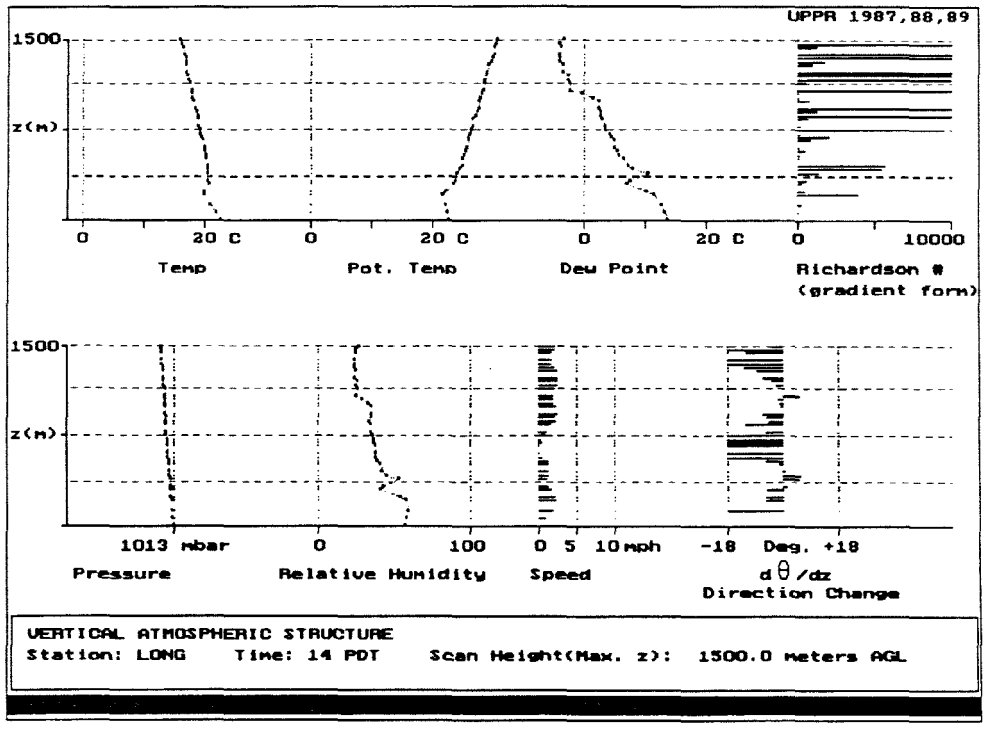

Figure 34. (Top) Vertical atmospheric structure at Long Beach at 11:00 PDT, November 12, 1987.

Figure 35. (Bottom) Vertical atmospheric structure at Long Beach at 14:00 PDT, November 12, 1987.

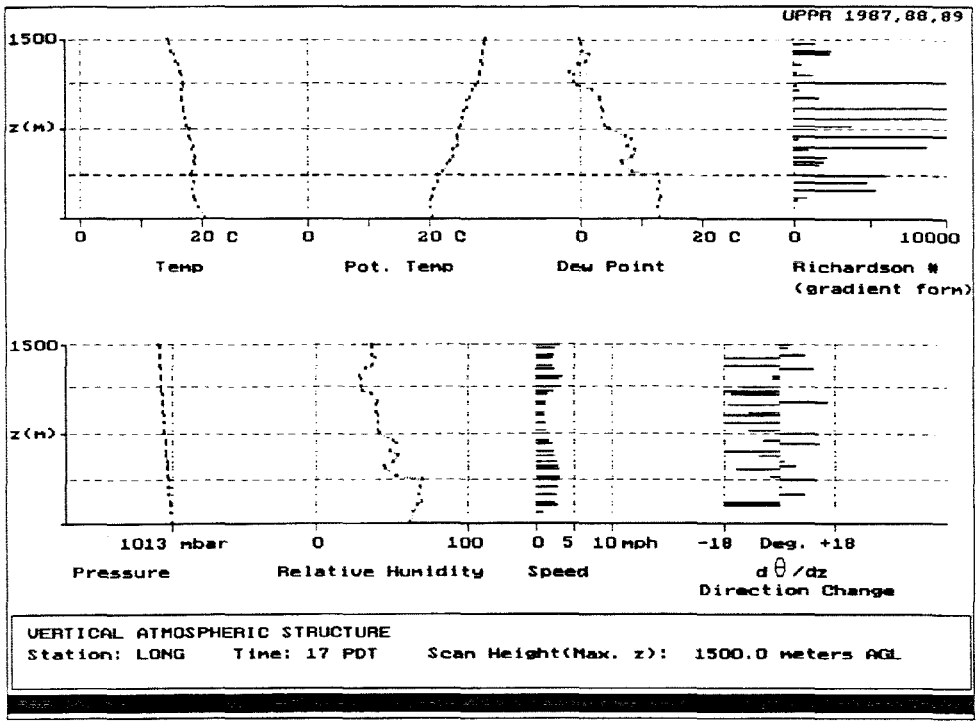

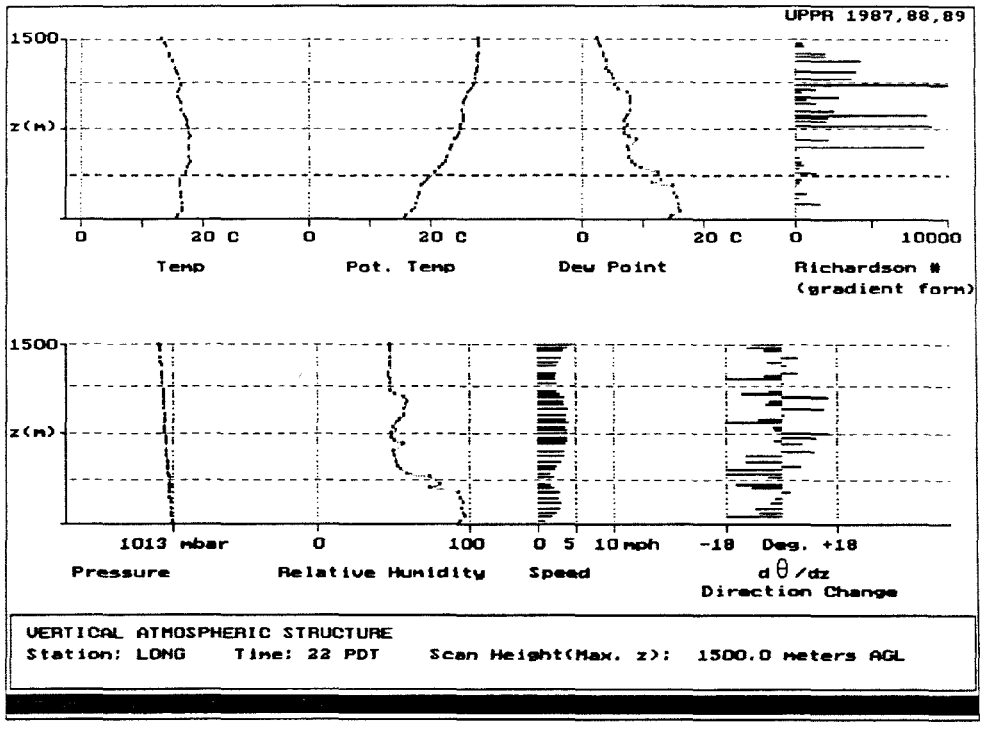

Figure 36. (Top) Vertical atmospheric structure at Long Beach at 17:00 PDT, November 12, 1987.

Figure 37. (Bottom) Vertical atmospheric structure at Long Beach at 22:00 PDT, November 12, 1987.

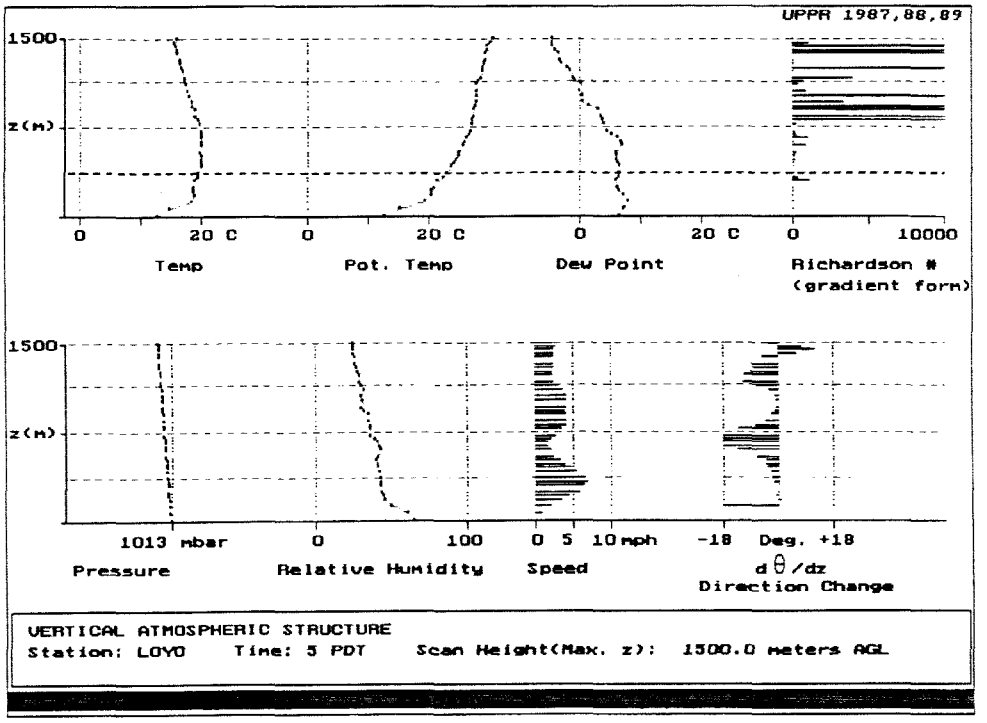

Figure 38. Vertical atmospheric structure at Loyola Marymount University at 05:00 PDT, November 12, 1987.

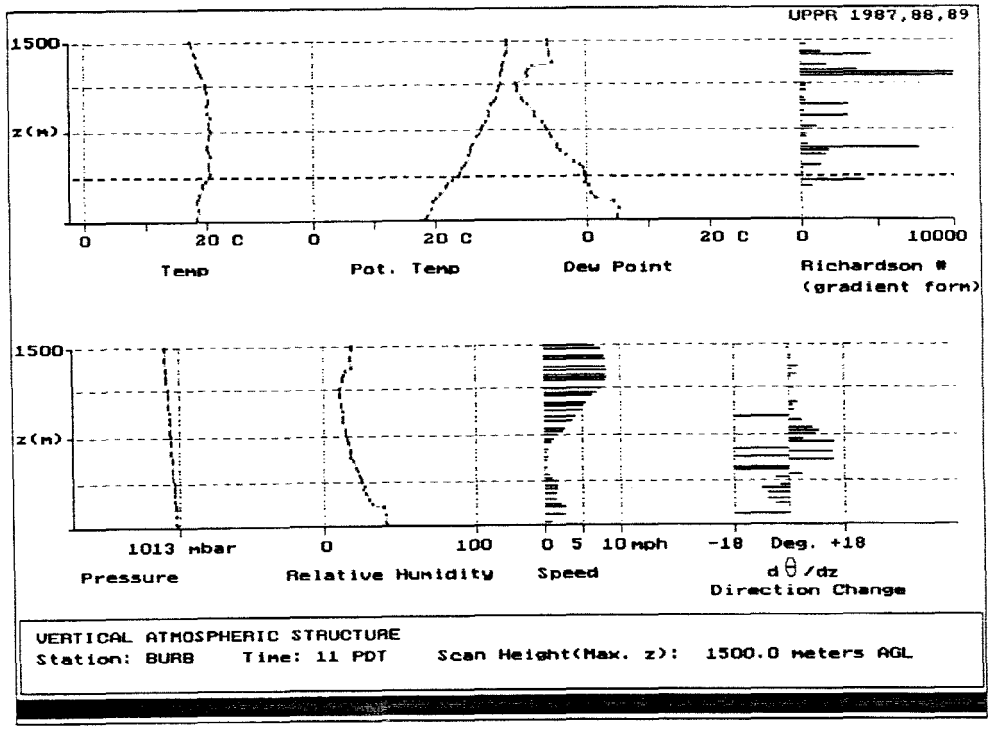

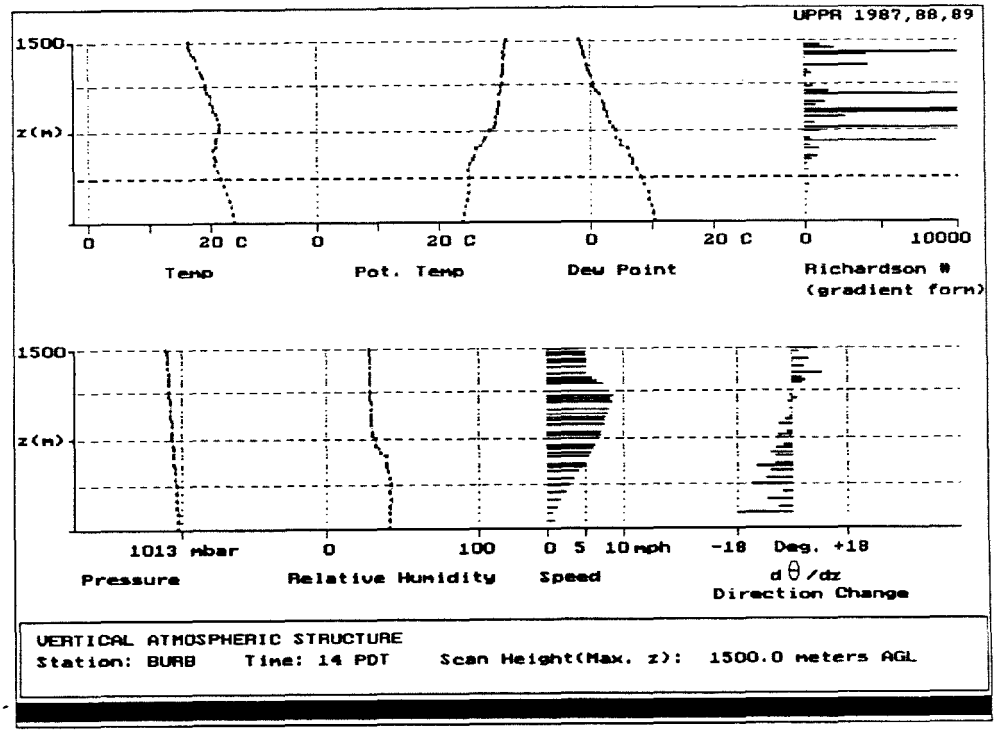

Figure 39. (Top) Vertical atmospheric structure at Burbank at 11:00 PDT, December 10, 1987.

Figure 40. (Bottom) Vertical atmospheric structure at Burbank at 14:00 PDT, December 10, 1987.

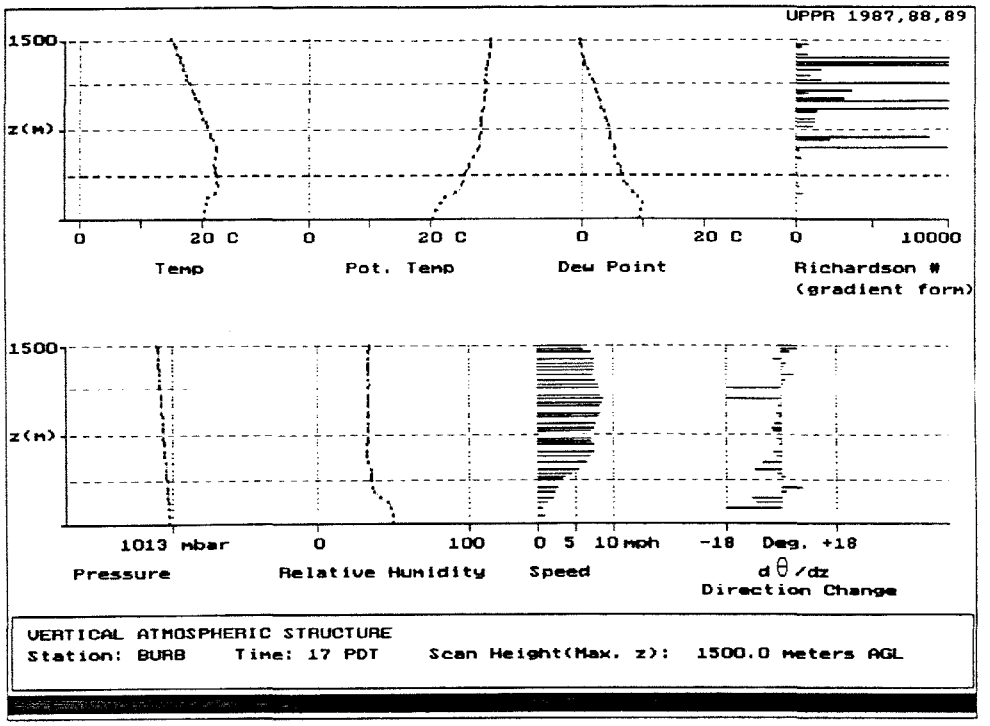

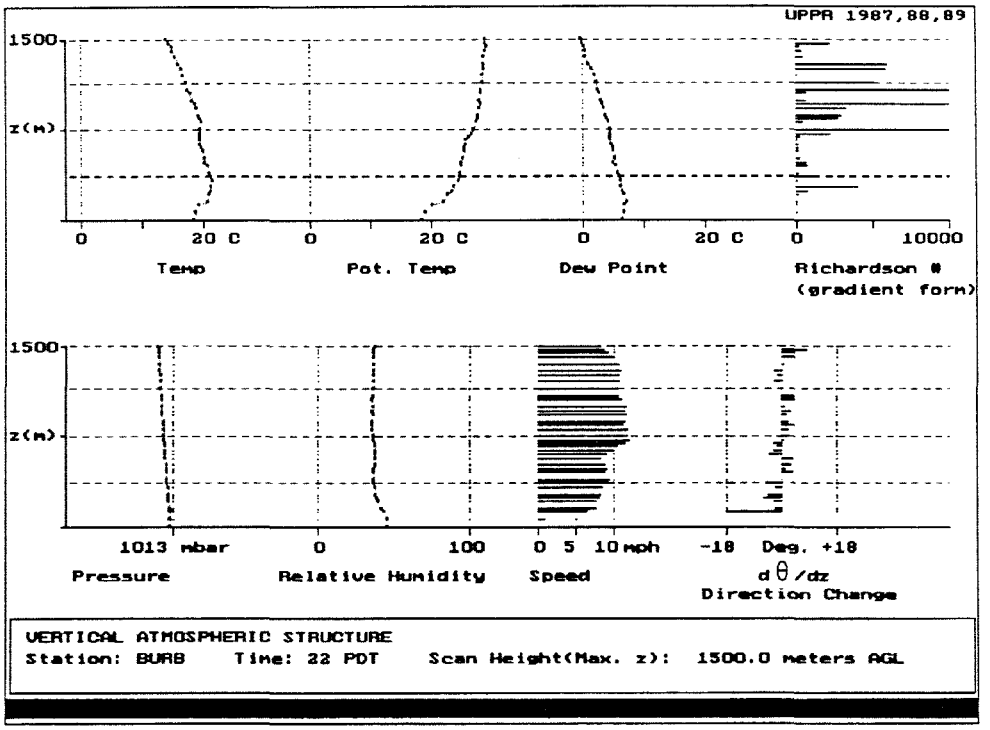

Figure 41. (Top) Vertical atmospheric structure at Burbank at 17:00 PDT, December 10, 1987.

Figure 42. (Bottom) Vertical atmospheric structure at Burbank at 22:00 PDT, December 10, 1987.

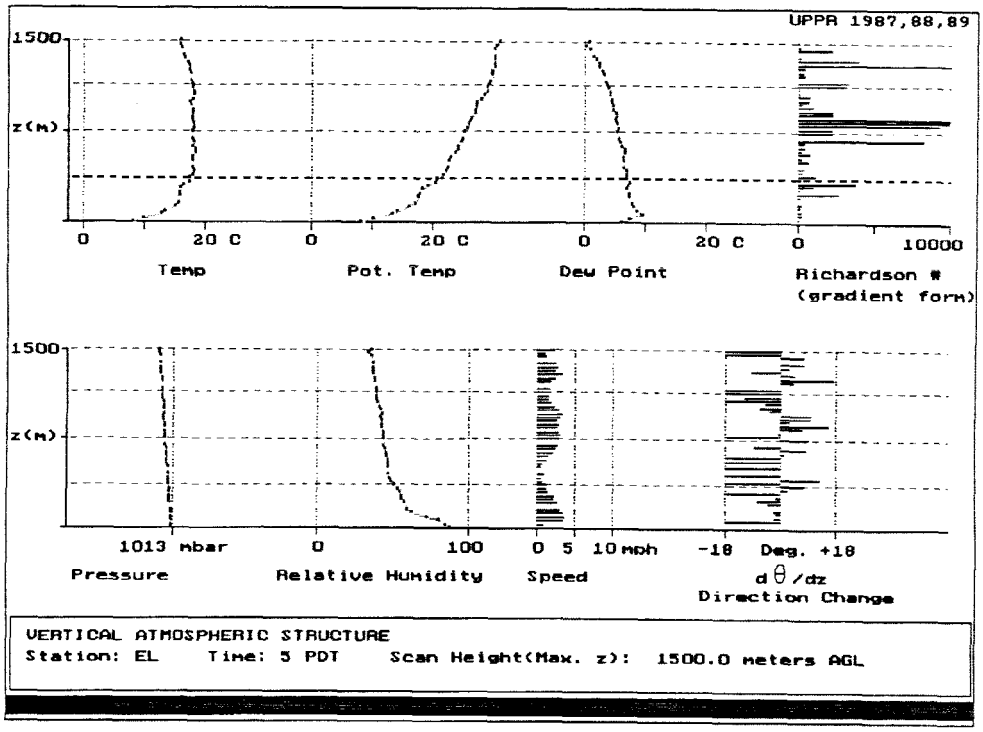

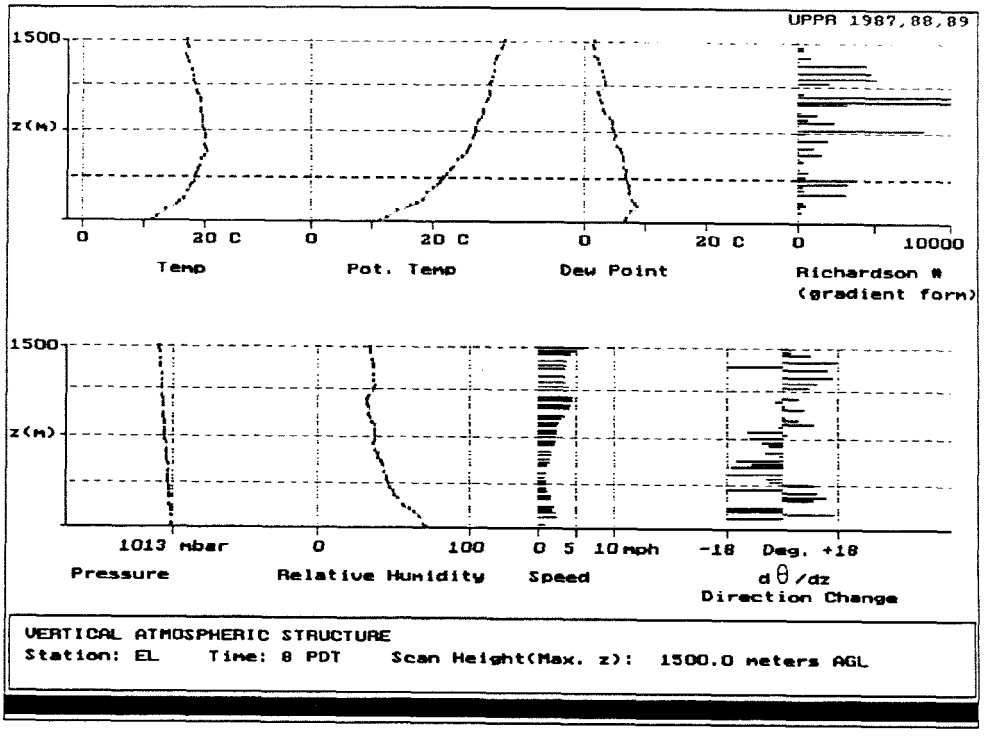

Figure 43. (Top) Vertical atmospheric structure at El Monte at 05:00 PDT, December 10, 1987.

Figure 44. (Bottom) Vertical atmospheric structure at El Monte at 08:00 PDT, December 10, 1987.

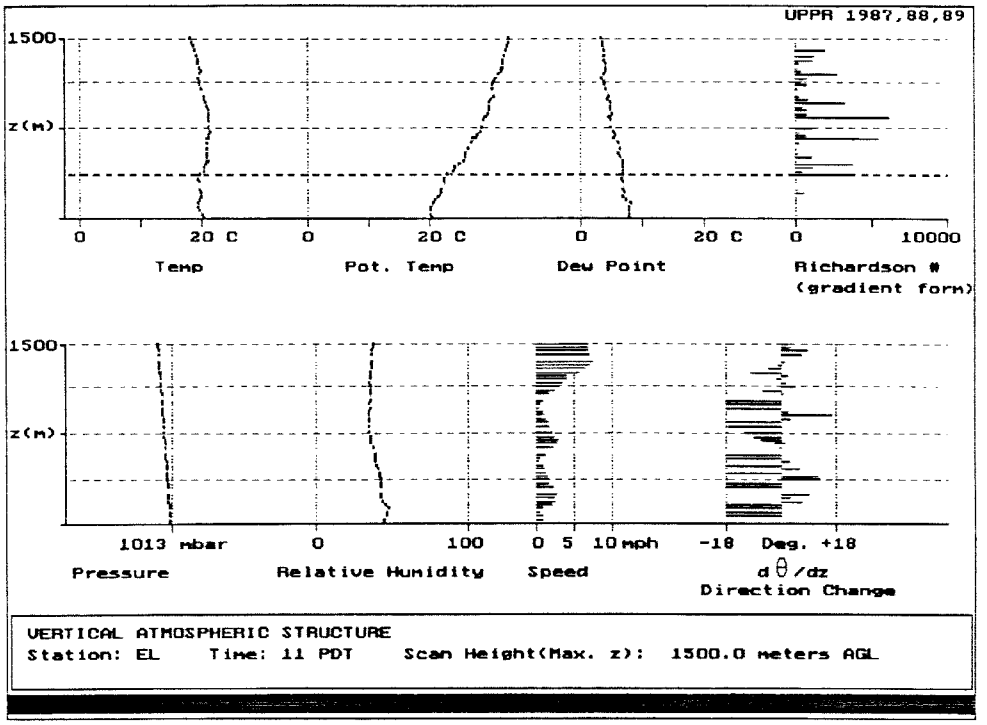

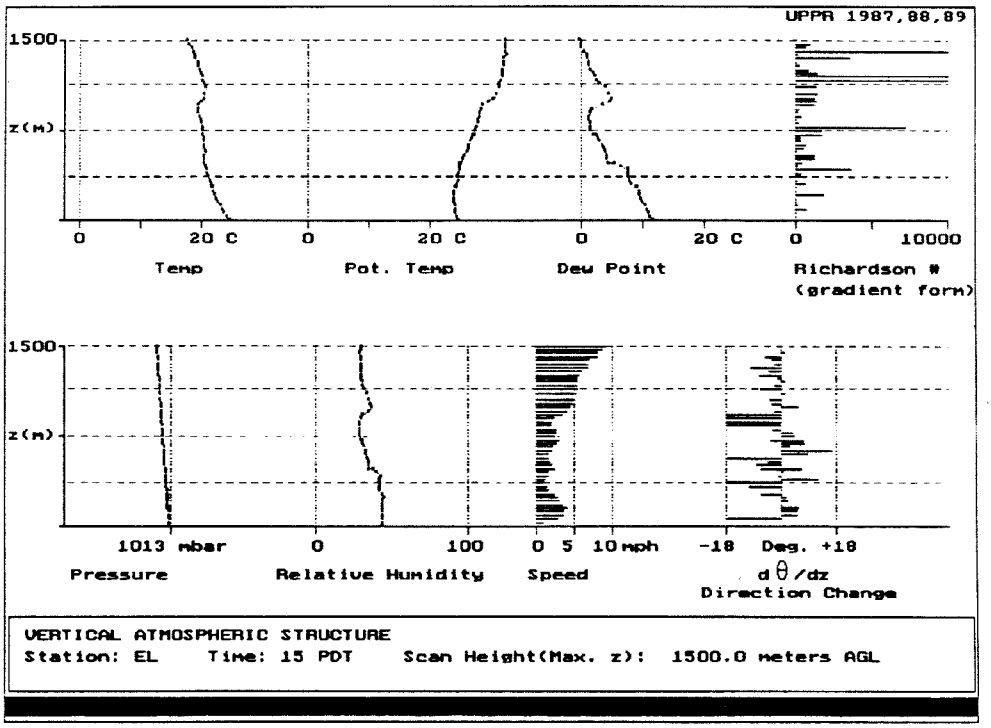

Figure 45. (Top) Vertical atmospheric structure at El Monte at 11:00 PDT, December 10, 1987.

Figure 46. (Bottom) Vertical atmospheric structure at El Monte at 15:00 PDT, December 10, 1987.

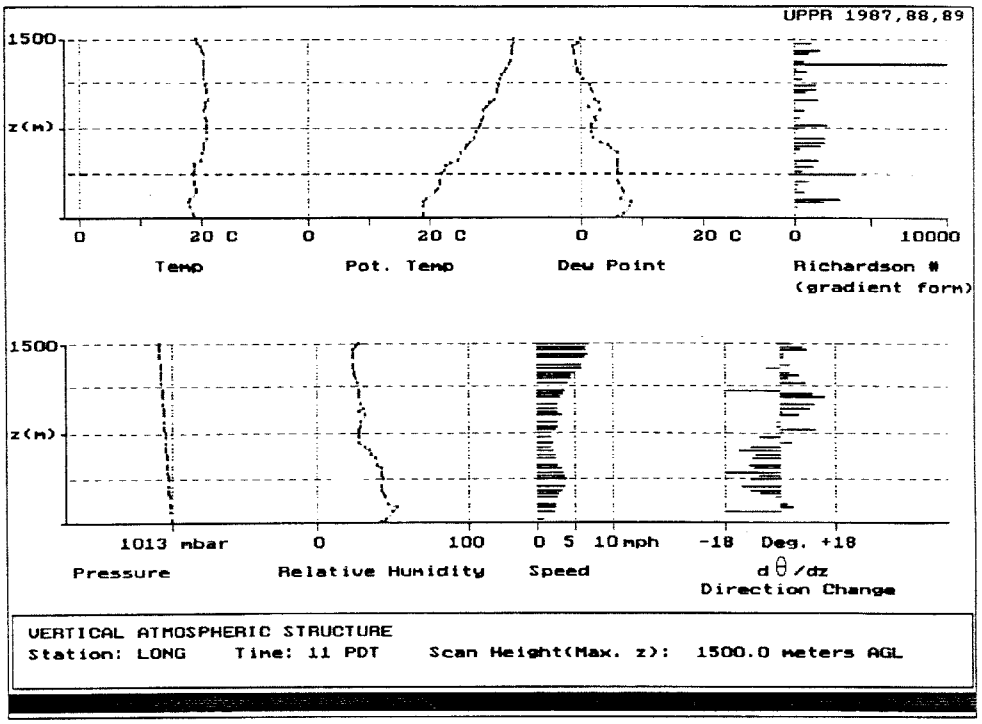

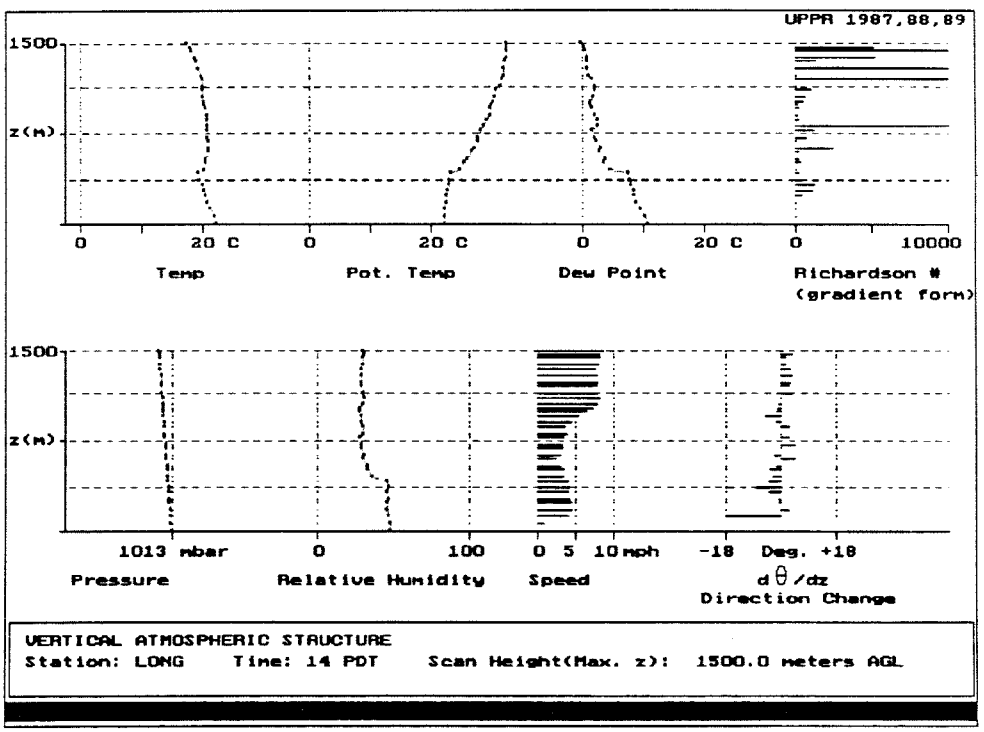

Figure 47. (Top) Vertical atmospheric structure at Long Beach at 11:00 PDT, December 10, 1987.

Figure 48. (Bottom) Vertical atmospheric structure at Long Beach at 14:00 PDT, December 10, 1987.

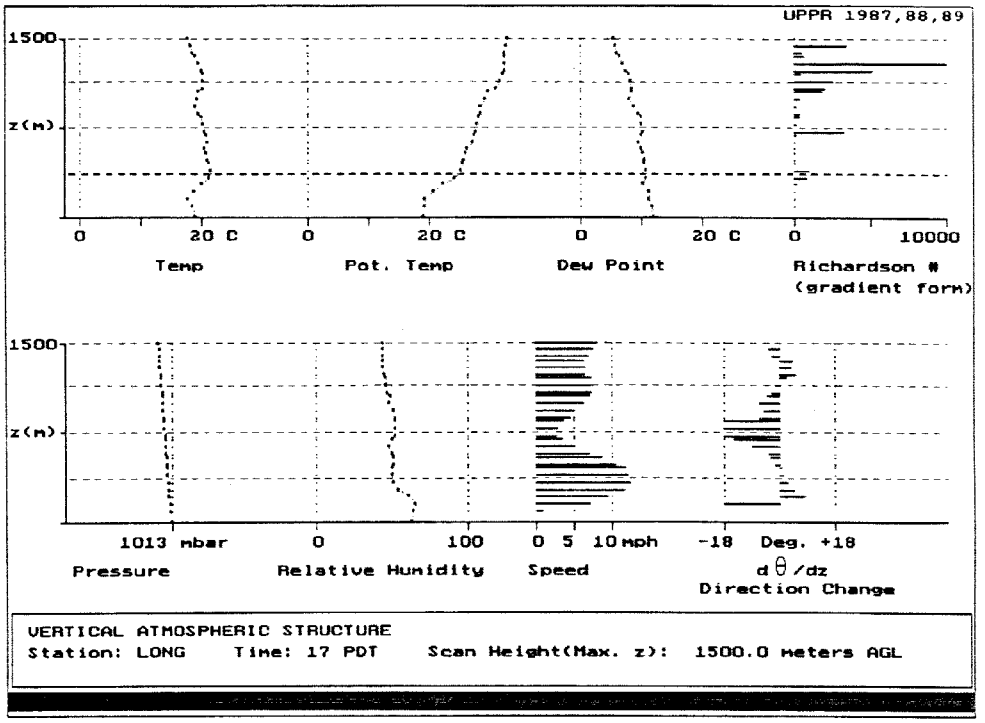

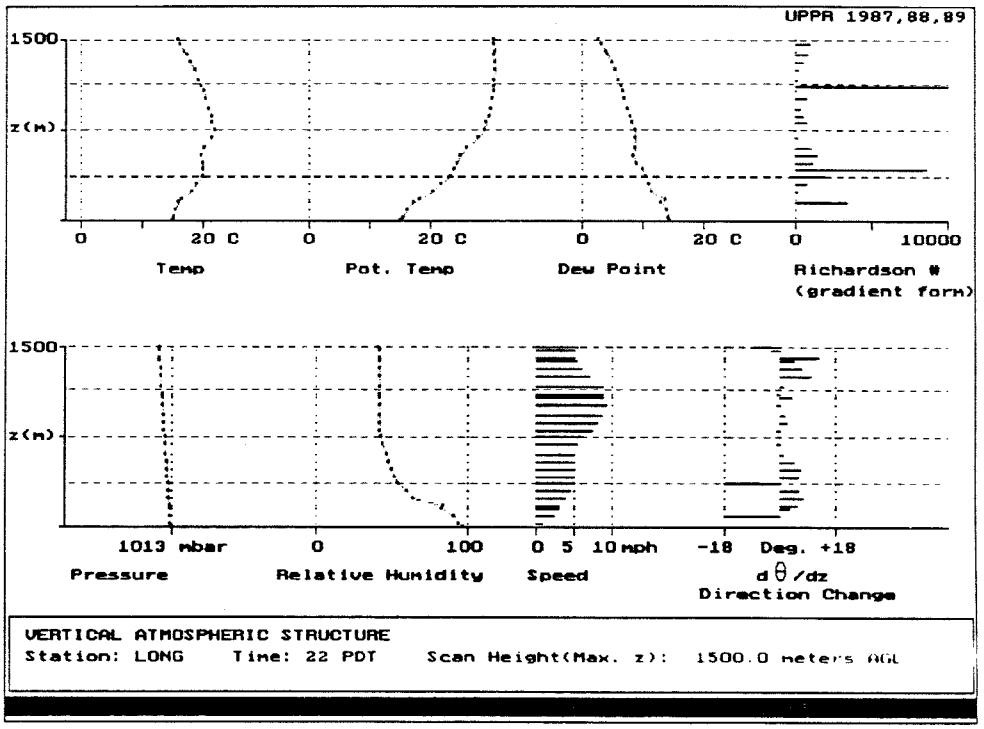

Figure 49. (Top) Vertical atmospheric structure at Long Beach at 17:00 PDT, December 10, 1987.

Figure 50. (Bottom) Vertical atmospheric structure at Long Beach at 22:00 PDT, December 10, 1987.

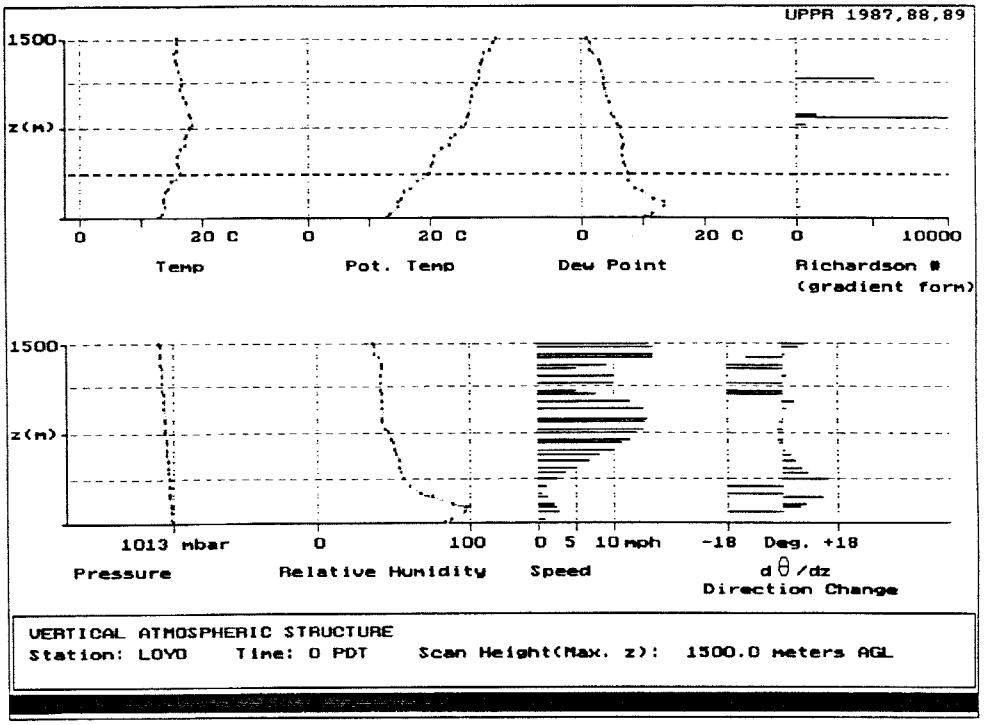

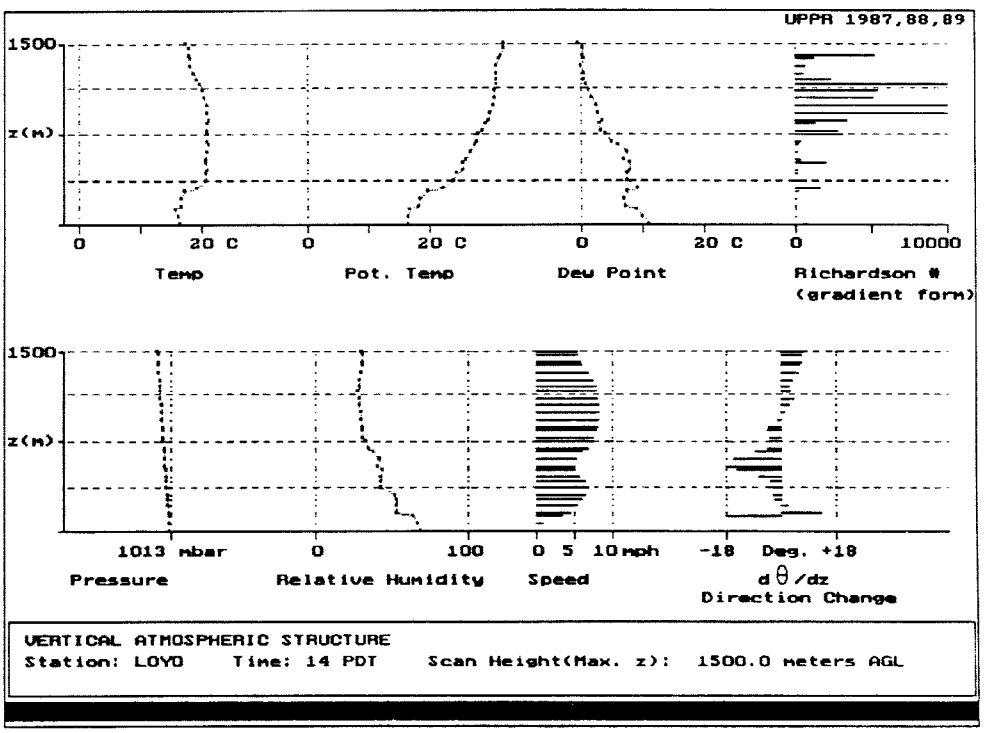

Figure 51. (Top) Vertical atmospheric structure at Loyola Marymount University at 00:00 PDT, December 10, 1987.

Figure 52. (Bottom) Vertical atmospheric structure at Loyola Marymount University at 14:00 PDT, December 10, 1987.

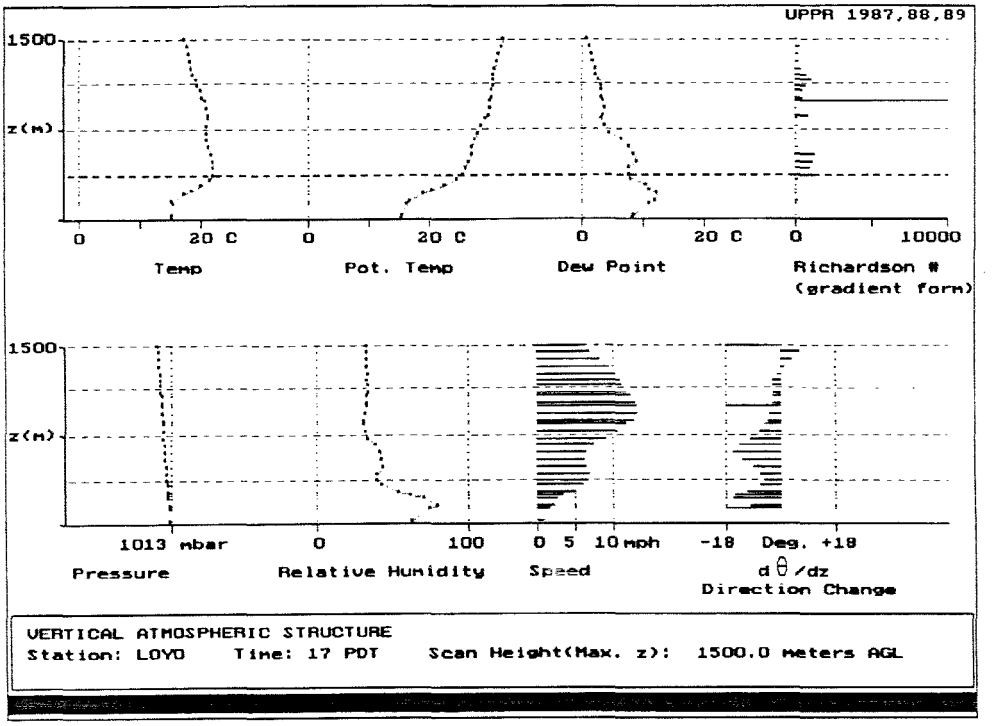

Figure 53. Vertical atmospheric structure at Loyola Marymount University at 17:00 PDT, December 10, 1987.

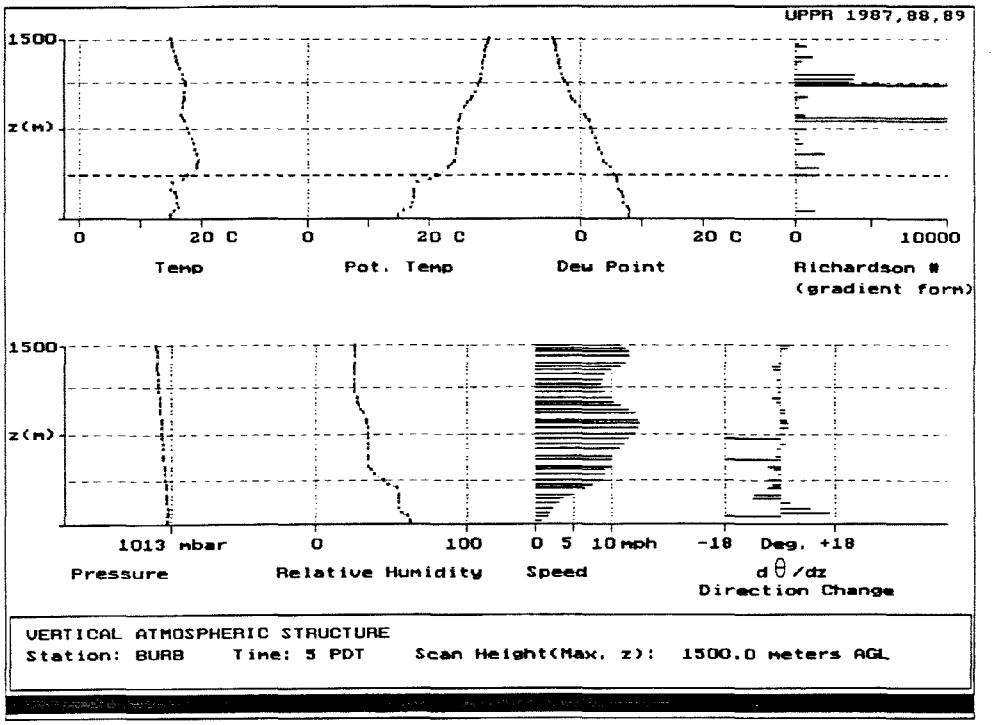

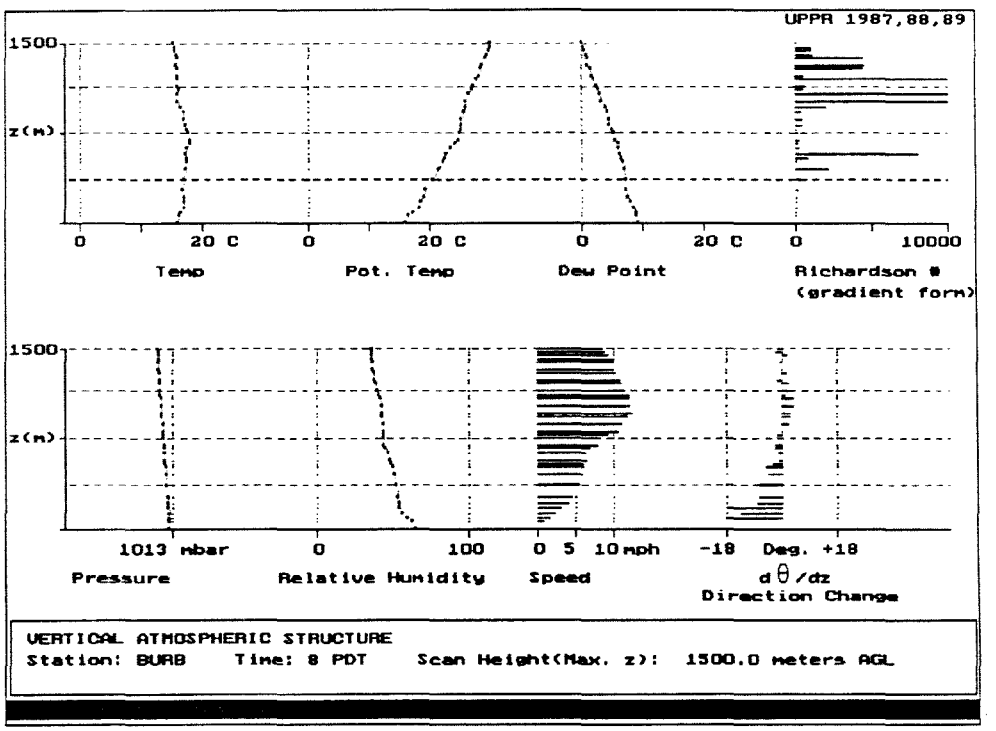

Figure 54. (Top) Vertical atmospheric structure at Burbank at 05:00 PDT, December 11, 1987.

Figure 55. (Bottom) Vertical atmospheric structure at Burbank at 08:00 PDT, December 11, 1987.

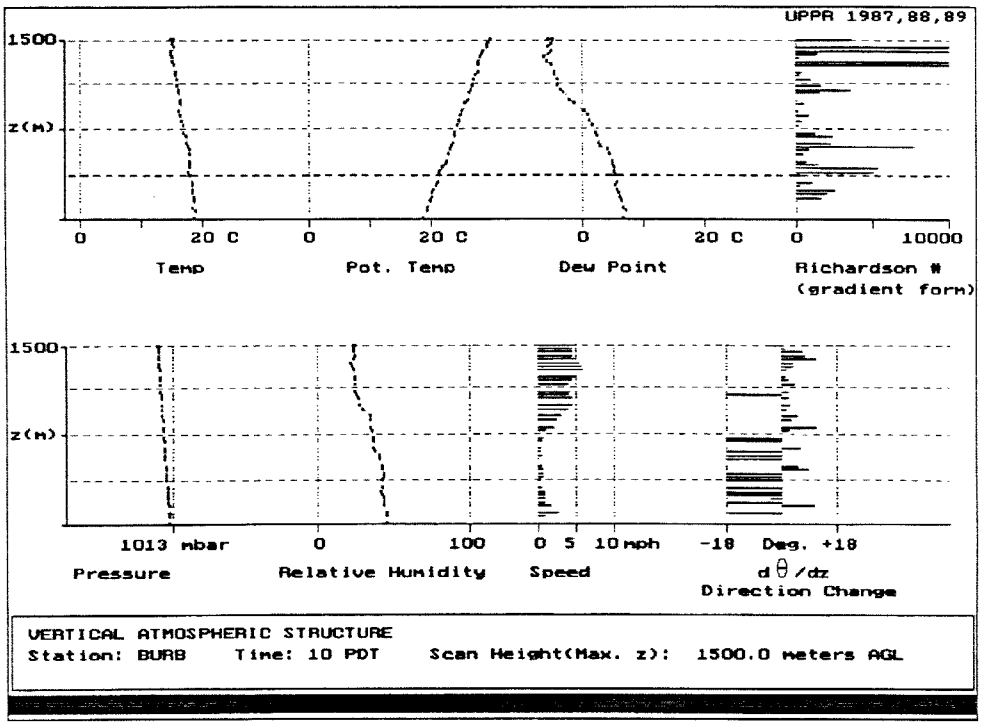

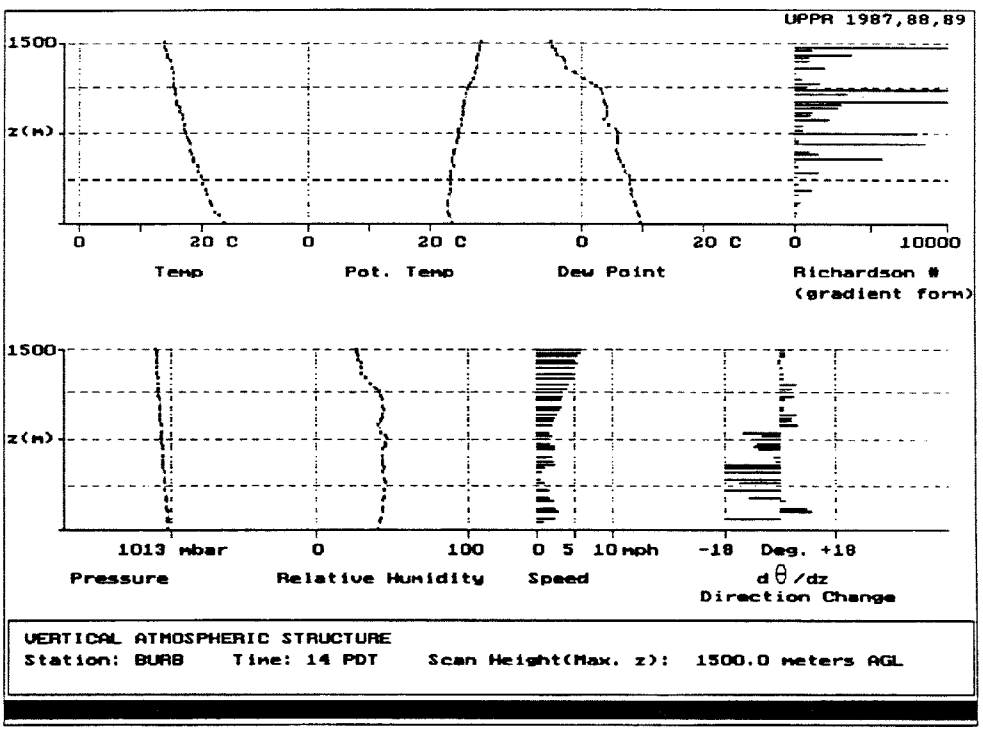

Figure 56. (Top) Vertical atmospheric structure at Burbank at 10:00 PDT, December 11, 1987.

Figure 57. (Bottom) Vertical atmospheric structure at Burbank at 14:00 PDT, December 11, 1987.

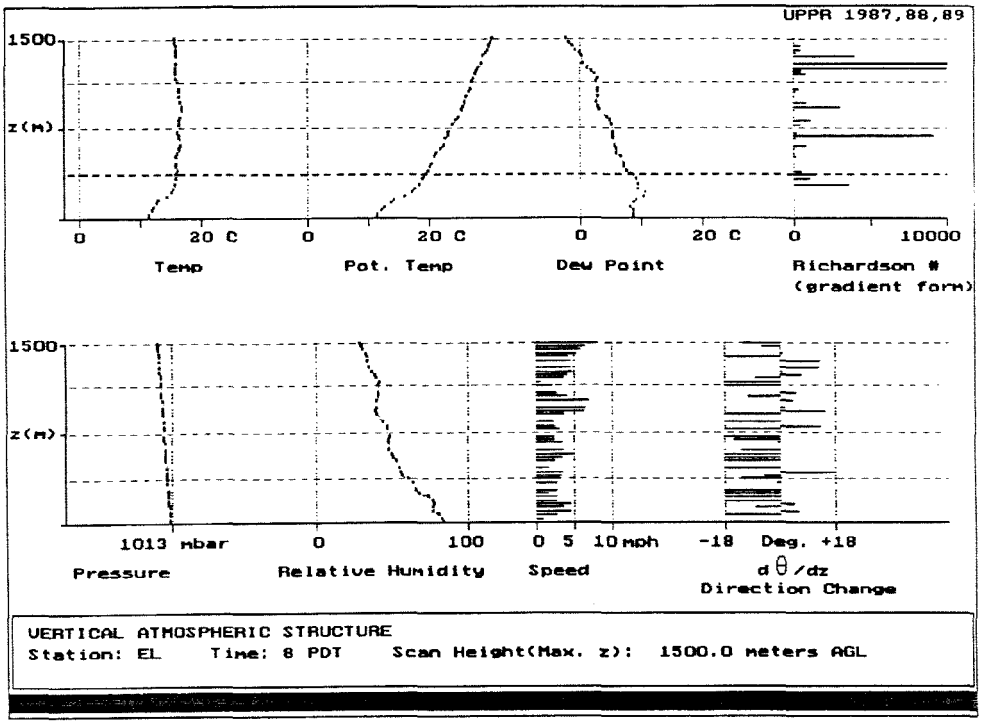

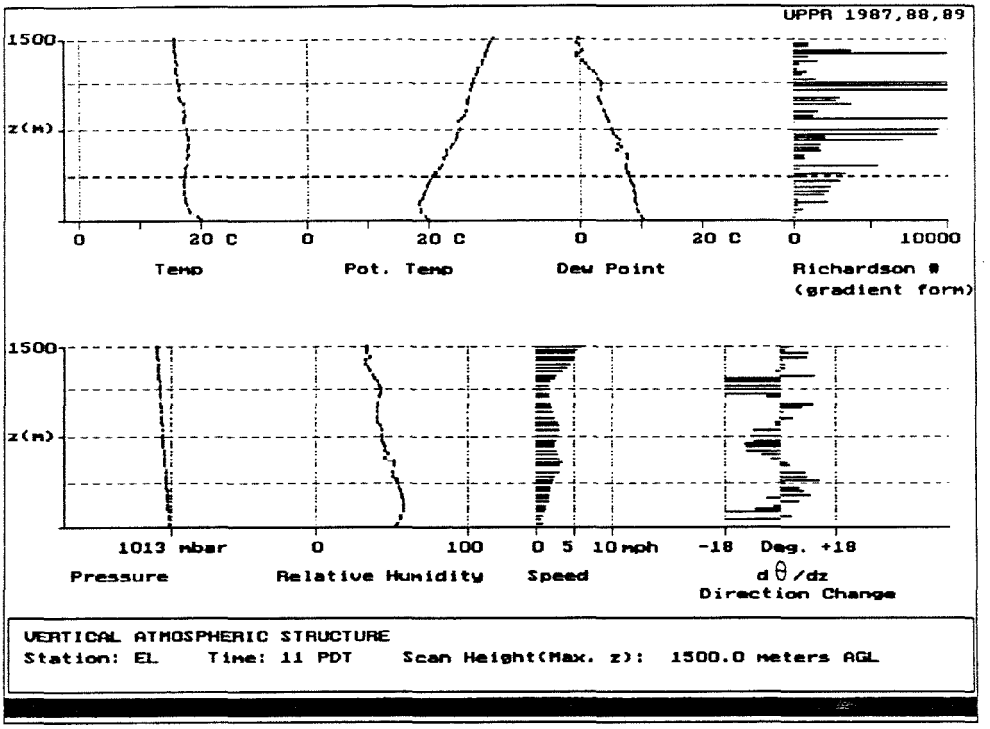

Figure 58. (Top) Vertical atmospheric structure at El Monte at 08:00 PDT, December 11, 1987.

Figure 59. (Bottom) Vertical atmospheric structure at El Monte at 11:00 PDT, December 11, 1987.

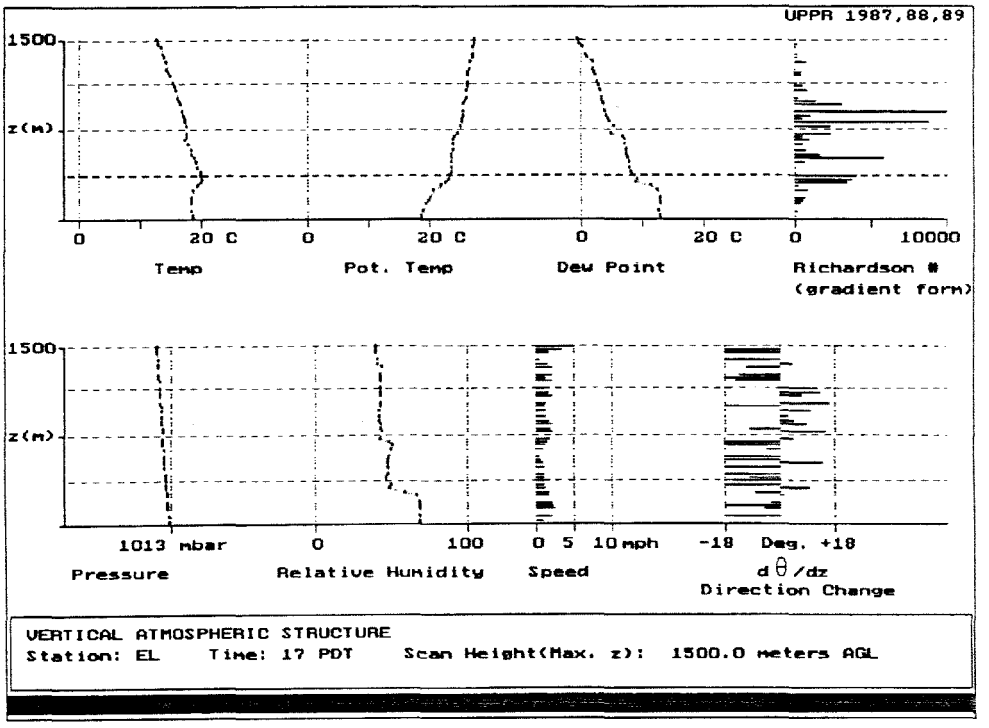

Figure 60. Vertical atmospheric structure at El Monte at 17:00 PDT, December 11, 1987.

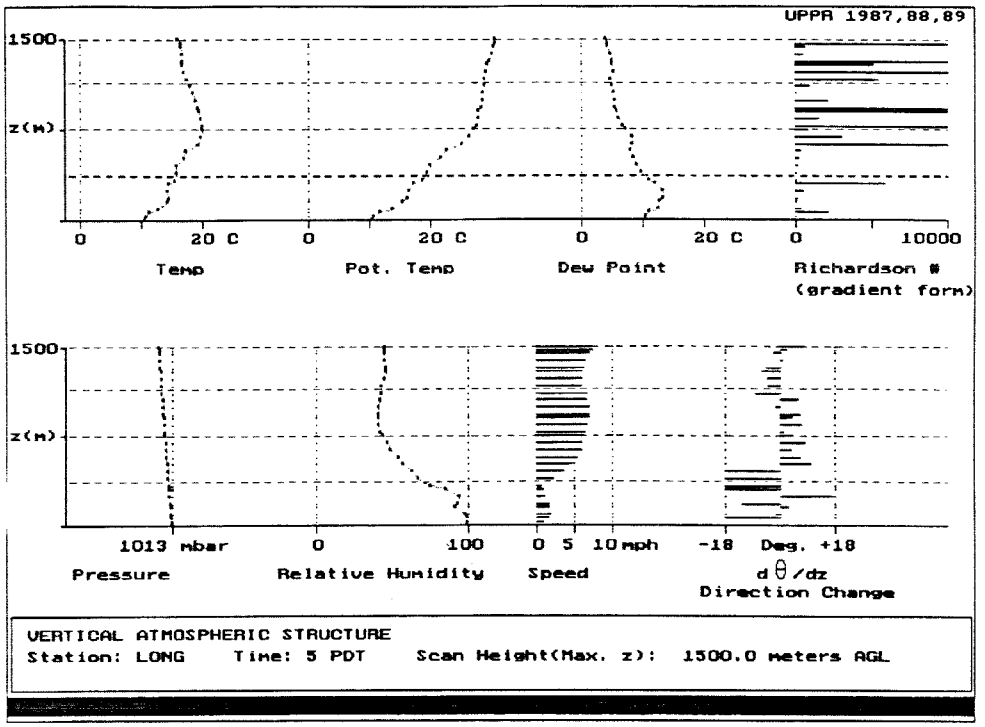

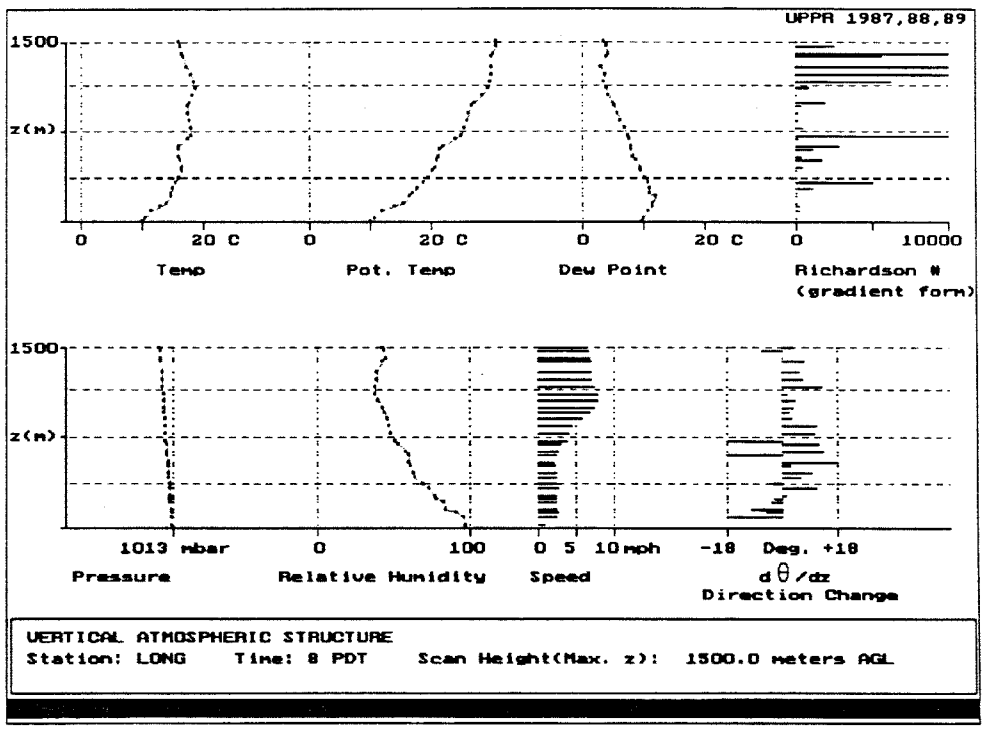

Figure 61. (Top) Vertical atmospheric structure at Long Beach at 05:00 PDT, December 11, 1987.

Figure 62. (Bottom) Vertical atmospheric structure at Long Beach at 08:00 PDT, December 11, 1987.

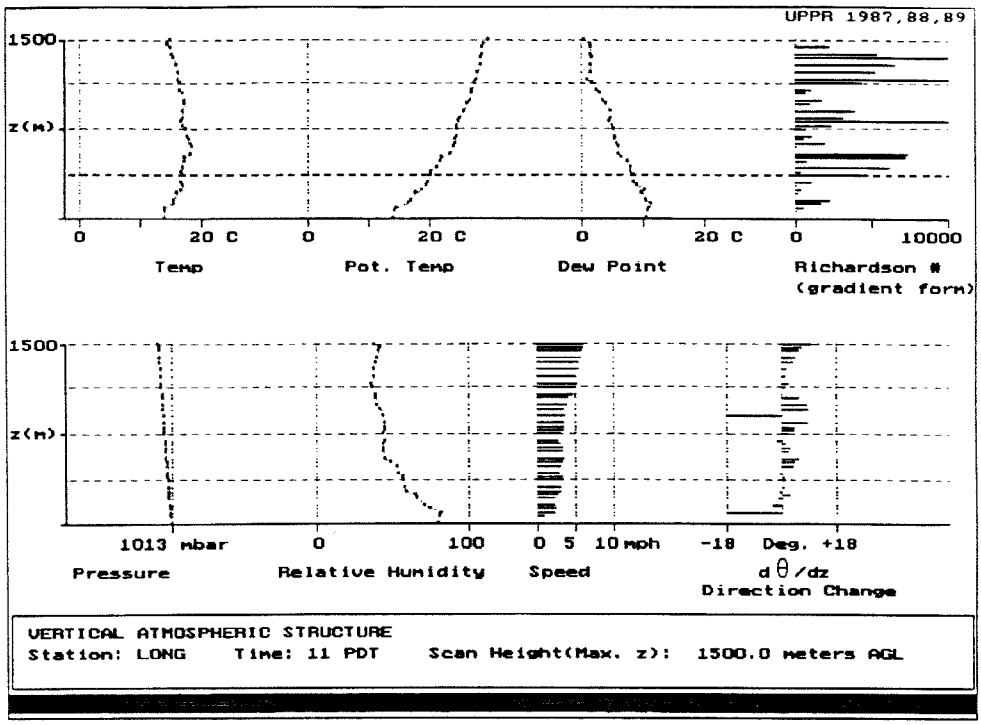

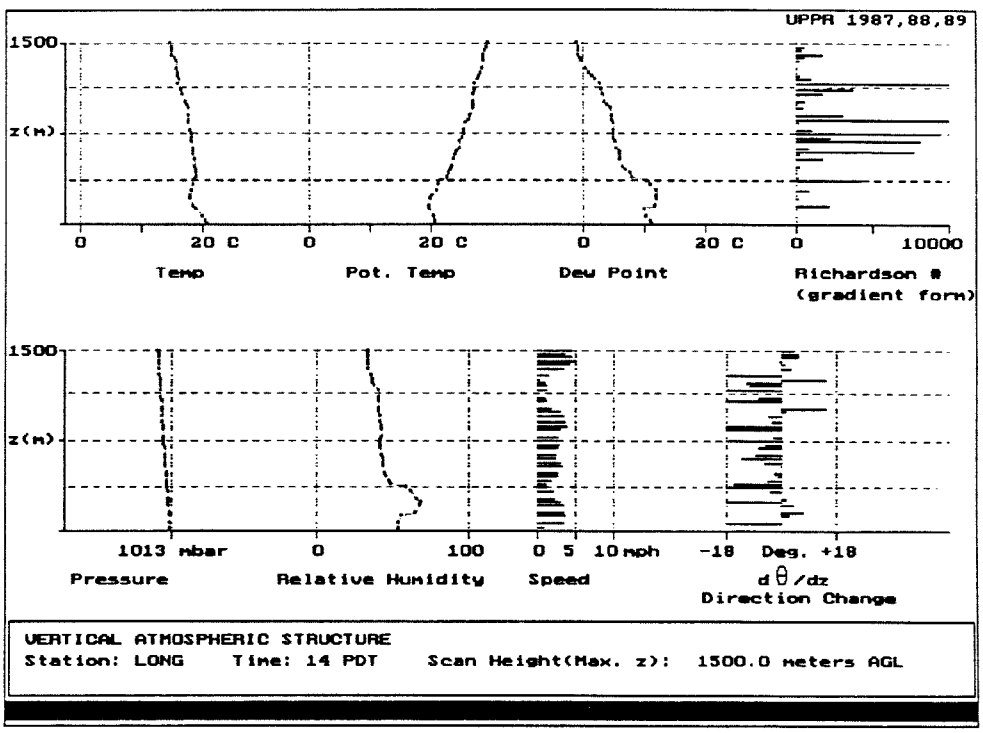

Figure 63. (Top) Vertical atmospheric structure at Long Beach at 11:00 PDT, December 11, 1987.

Figure 64. (Bottom) Vertical atmospheric structure at Long Beach at 14:00 PDT, December 11, 1987.

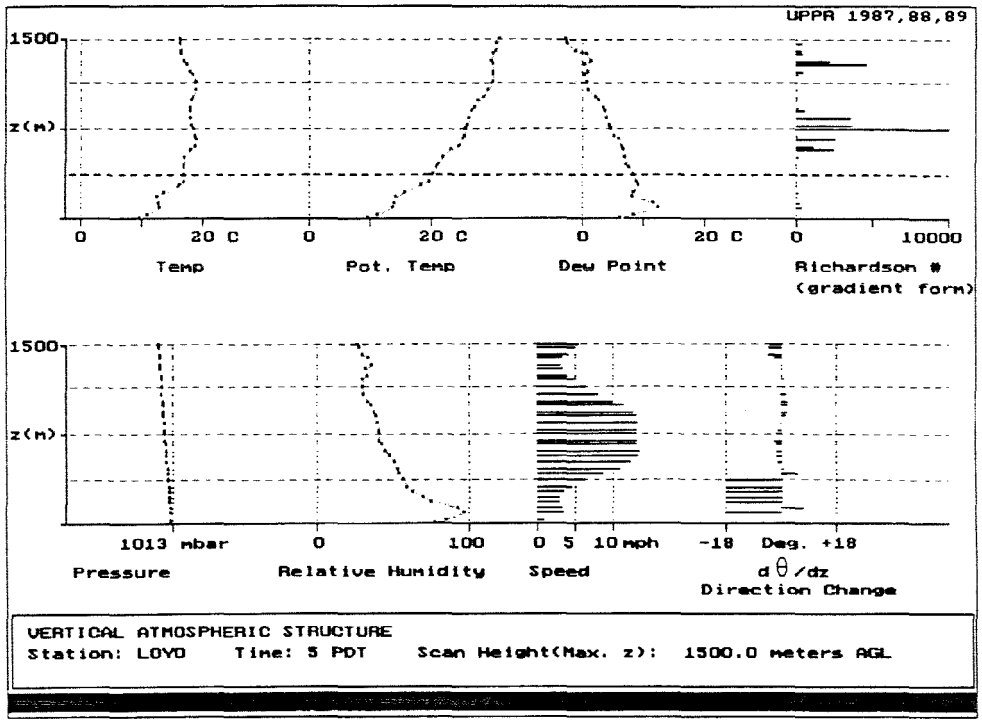

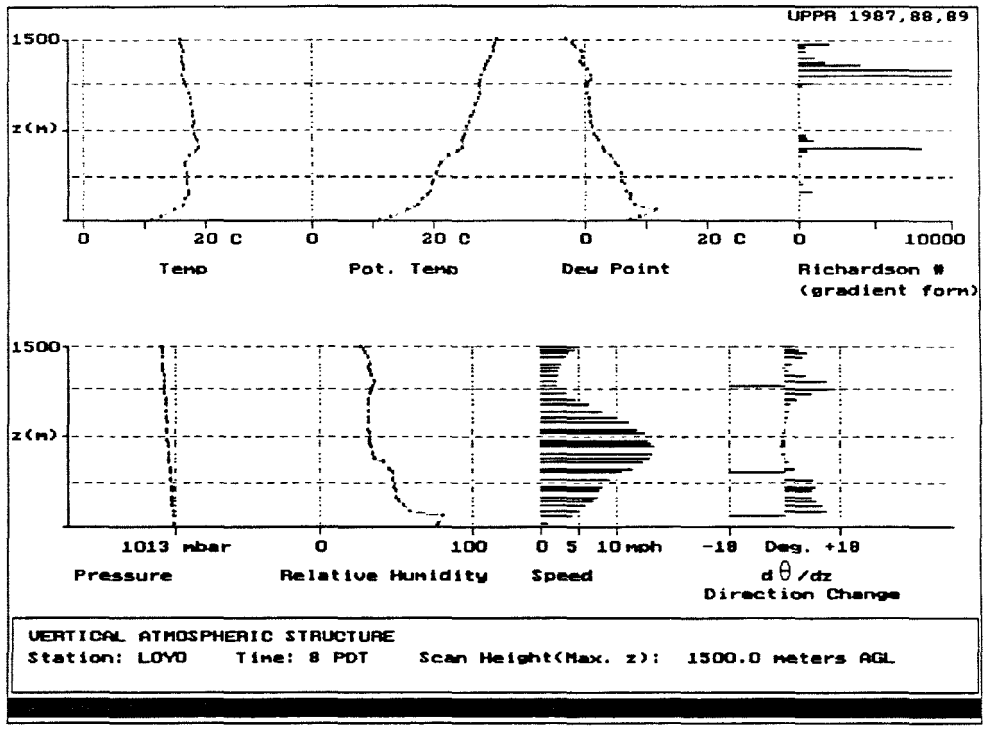

Figure 65. (Top) Vertical atmospheric structure at Loyola Marymount University at 05:00 PDT, December 11, 1987.

Figure 66. (Bottom) Vertical atmospheric structure at Loyola Marymount University at 08:00 PDT, December 11, 1987.

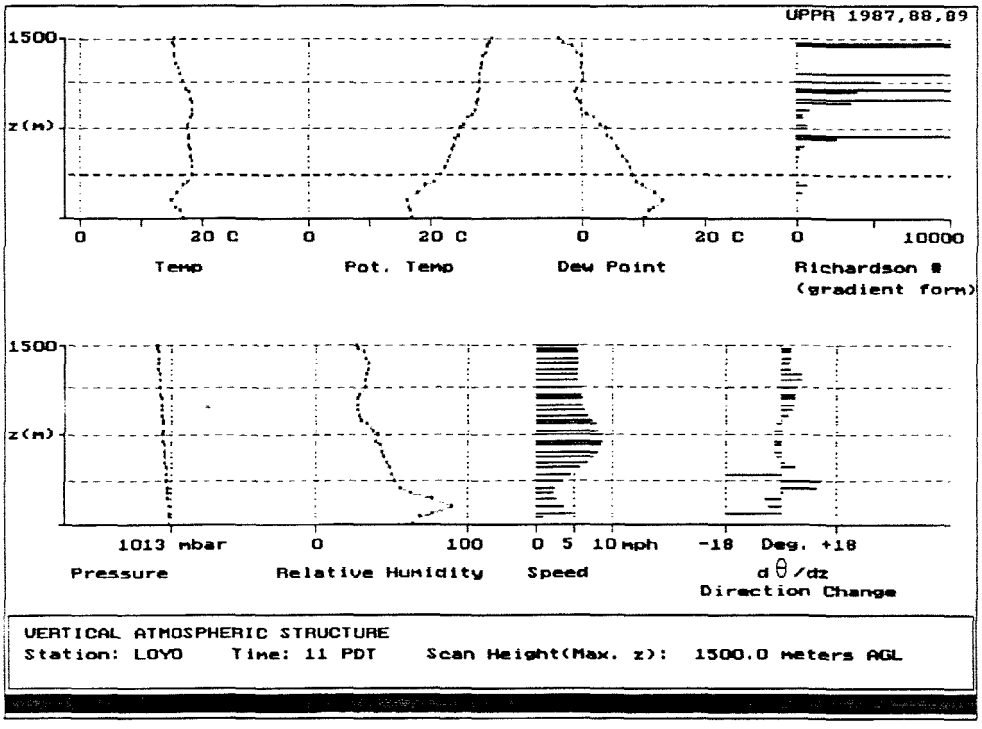

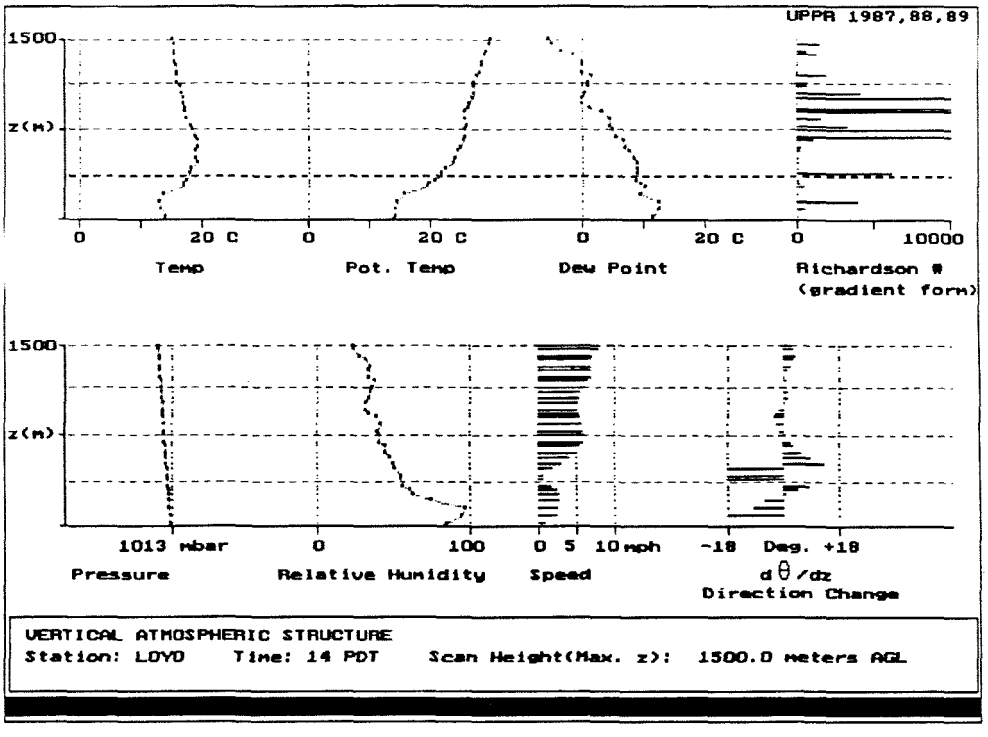

Figure 67. (Top) Vertical atmospheric structure at Loyola Marymount University at 11:00 PDT, December 11, 1987.

Figure 68. (Bottom) Vertical atmospheric structure at Loyola Marymount University at 14:00 PDT, December 11, 1987.

References

1. Beychock M. R. (1979), Fundamentals of Stack Gas Dispersion.

2. Blumenthal D. L. et al. (1978), Anatomy of a Los Angeles smog episode: pollutant transport in the daytime sea breeze regime, Atmos. Env., **12**, 893-907.

3. Edinger J. G. (1959), Changes in the depth of the marine layer over the Los Angeles Basin, J. of Met., **16** No. 3, 219-226.

4. Edinger J. G. (1973), Vertical distribution of Photochemical smog in Los Angeles Basin, **7** No. 7, 247-252.

5. EQL (1982), McRae G. J., Goodin W. R. and Seinfeld J. H., Environmental Quality Laboratory report 18, California Institute of Technology.

6. Horrell R. S., Deem M., Wyckoff P., Shair F. H. and Crawford N., (1989), Ground release SF_6 tracer experiments used to characterize transport and dispersion of atmospherice pollutants during the Southern California Air Quality Study of 1987, Air and Waste Annual Meeting paper 89-138.2.

7. Lea D.A. (1968), Vertical ozone distribution in the lower troposphere near an urban pollution complex, J. Appl. Met., **7** No. 2., 252-267.

8. Reible D. (1981), Thesis, California Institute of Technology.

9. Seinfeld J. H., 1975), Air Pollution Physical and Chemical Fundamentals, McGraw-Hill.

10. Shair et al. (1982), Transport and disperison of airborne pollutants associated with the land breeze-sea breeze system.

11. Stephens E. R. (1975), Chemistry and meteorology in an air pollution episode, J. of the Air Pollution Control Association, **25** No.5, 521-524.

Section 2.3

Submitted for Publication in Atmospheric Environment.

2.3 A Smog Season Examination of the LA – Glendale Divergence Zone

Abstract

The persistent smog season divergence zone which extends from north of the Pasadena/Glendale area through downtown Los Angeles and continues to the south west is examined by the use of surface wind data. The implications of this zone to emission transport from downtown Los Angeles and vicinity are explained in terms of trajectory analysis done for two days from the 1987 Southern California Air Quality Study (SCAQS) and for the entire smog season of 1988. The results of the trajectory analysis are used to give perspective to two summertime SF_6 tracer releases near the zone as part of SCAQS, and to clarify transport pathways starting from other locations in the western basin.

Introduction

A significant amount of the air quality research to study the Los Angeles Basin involves meteorology. The basin's complex terrain in concert with semi-permanent synoptic scale pressure gradients, and a strong tendency for a temperature inversion to exist in this area, creates wind fields which are complicated, yet in many respects similar from day to day. For the purpose of this paper, only patterns during the smog season, from May through September, will be considered. During this time, the synoptic pressure gradients resulting from the Pacific high pressure cell and the differential temperature between the ocean and land directs daytime air flow onshore (Edinger, 1967). The temperature inversion is often aloft during this time of year and exhibits a distinct diurnal variation in height (Edinger, 1959). On average, the base of the inversion ranges around one kilometer above ground level, creating a vertically restricted layer in which the winds must flow. Permanent obstructions such as hills, mountains, and valleys in this horizontal layer tend to redirect the flow horizontally and give the flow its characteristic features. Finally, the surface and upper air flow patterns, whether they be specific to a single day or summarized for an entire season, are of general interest because they describe the bulk transport within the basin.

Portrayal of the Los Angeles Basin's wind patterns has been done qualitatively by two major methods: (1) streamlines and vector maps, and (2) air parcel trajectories plots. Because the wind field is dynamic, (1) and (2) above are not the same. The flow streamlines over the basin at each hour of the day have been compiled for different circumstances from air monitoring stations within the basin. Examples are the Southern California Air Quality Management District's (see SCAQMD 1977) compilation of monthly patterns and the California Air Resources Board's (see CARB 1984) compilation of seasonal patterns in California. The trajectories of air parcels have been studied from two different perspectives: (1) indirect studies that computed trajectories from surface winds and winds

aloft, and (2) direct studies that determined air parcel movement by labeling. For example, a comparison of direct and indirect methods was done by Neiburger by using surface wind trajectories computed by several techniques and the actual transport of air parcels labeled with zinc-cadmium sulfide particles. Results were at best inconclusive because of the enormous loss of particles to unknown sinks, and the subsequent range limit (a few tens of km) to which transport could be tracked. A similar study by Calvert (1976) used radar tracked tetroons to follow air parcels in an attempt to test the theory of ozone generation in the basin. More recently, air parcels have deliberately been labeled by means of inert gaseous tracers, a technique which has proven to be superior to other labeling methods (Lamb, 1978). In the Los Angeles Basin, sulfur hexafluoride tracer experiments were done from the city of Anaheim by Drivas (1974) to examine both dispersion and transport for distances up to 100 km. More recently, the land breeze-sea breeze system of Los Angeles was studied using sulfur hexafluoride by Shair (1982). These tracer experiments are very effective for determining the actual transport trajectories for particular days, but the large amount of time and man power required to do such experiments prevents them from being done in large numbers.

Investigators have been concerned with individual recurring features of the basin's wind field that were identified by the previously discussed methods. The intra-basin divergence and convergence zones are of particular interest. As mentioned above, Edinger examined the changes in the marine layer depth over the Los Angeles Basin during the summer of 1957. Within this paper, he noted the following three basic factors that produce changes in the marine layer: (1) horizontal convergence or divergence of the wind, (2) dilution of the marine layer from above by mixing superadjacent dry (inversion) air with the marine air, and (3) advection of deeper or shallower layers of marine air into the area. It is specifically the first factor that is to be examined further in this paper. Edinger

and Helvey (1961) quantified the San Fernando Convergence Zone and examined the impact it had on channeling smog generated from downtown Los Angeles for 75 days in the summers of 1956-57. They observed the zone and compiled statistics about its location throughout the summer. In addition, Edinger provided an idealized map of the known areas of convergence and divergence within the basin. His map labels the Elsinor convergence zone southeast of the Los Angeles Basin, and notes three divergence zones located approximately near the cities of Newhall, Glendale, and San Bernardino. More recently, in an effort to suggest ways for improving air pollution simulation models, Unger (1986) suggested that the influence of divergence and convergence zones on observed pollution levels may not have been adequately investigated. This paper presents evidence to support this suggestion and presents motivation to undertake future studies of intra-basin divergence and convergence zones.

The Glendale divergence zone is particularly interesting because it apparently divides the substantial emissions from downtown Los Angeles between to the two major downwind exits from the basin to the east and northwest. Appendix A shows the hydrocarbon emission distribution of mobile sources, and the population distribution of the basin (SCAQMD,1987). The hypothesis that the trajectory of emissions from the downtown area is determined by the location of this zone is partially supported by tracer experiments done near downtown. In a recent study, as part of the 1987 Southern California Air Quality Study, four sulfur hexafluoride tracer experiments were conducted just south of downtown Los Angeles, in Vernon during the summer and fall. A detailed summary of the results prepared by Horrell et al. (1989) describes the transport of the summertime tracer out of the basin to the north and northwest. These findings conflicted with the expectations of the authors and other persons designing the SCAQS studies. At the time of the SCAQS studies, it was anticipated that the tracer would exit primarily from the eastern outlet of the basin. This study was undertaken

to place into context the unanticipated findings of the two summertime SCAQS SF_6 tracer studies, and to quantify the dynamics of the LA-Glendale divergence zone during a 24-hour cycle.

Method

The WIND simulation package described by Horrell et al. (1989) was used as the primary research tool in this study. Briefly, this package of programs provides an interactive environment for the performance of simulated tracer experiments with the measured surface winds, and to monitor simultaneously the measured surface air quality data from a randomly distributed set of reporting stations. The advanced interface of this program allows simulated tracer releases to be performed quickly, making it practical to examine data from an entire month in only a few hours. For this study, the package has been set up to look at the Los Angeles Basin from 33 degrees 26 minutes to 34 degrees 29 minutes in latitude and from 117 degrees 6 minutes to 118 degrees 42 minutes in longitude (See Figure 1). Six sets of simulations and/or data compilations were done: (1) to determine the percentage of days the LA-Glendale divergence zone was present at 6 a.m. and 3 p.m., (2) to identify the average location of the LA-Glendale zone, (3) to determine the trajectories initiated from the nine western basin sites for the average smog season day, (4) to determine the trajectories from the nine western basin sites and compile statistics on their exit route from the basin for every day in the 1988 smog season, (5) same as (4), except using the two 1987 SCAQS days, and (6) to create contour maps of the average surface values for ozone and to explain features in these maps with regard to the location of the LA-Glendale divergence zone. The source of the data and method for preparing it for input into WIND are discussed below.

Surface wind data came from the AQMD data telemetry system for: (1) the two days of the summer SCAQS period of 1987 (July 15 and September 3) and (2) all days during the months of May through September 1988. Of the 153 days in the 1988 smog season, 151 were used; June 3 and July 8 were missing from the data set. The surface wind data is received as hourly averaged data and is reported as a speed in miles per hour and a direction in degrees off north. The

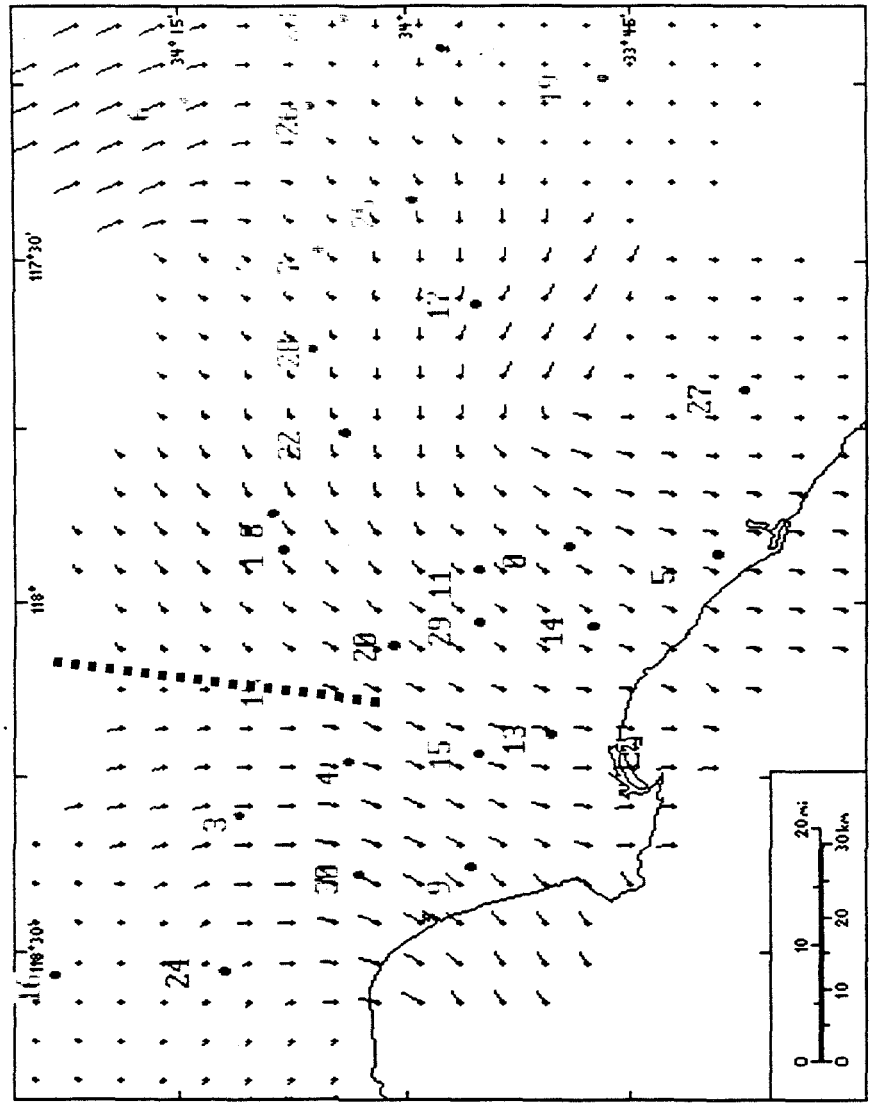

Figure 1. Hourly averaged wind vectors for the 1988 composite average day during the smog season at 8:00 a.m. Vectors are shown 5 km apart, their length proportional to the wind speed, and their direction away from their origin is the direction of flow. The bold dashed line through Pasadena (site 18) and east of downtown LA (site 4) shows the location of the divergence zone at this time.

data is grouped as single days, one value for each of the 24 hours at each of the reporting stations. Thirty-one data reporting sites were operational during this study (see Table 1 for a detailed list of the site names and their location). In addition to the surface wind data, hourly averaged ozone data was obtained from the AQMD for all 31 stations in a similar format.

The surface wind data was then prepared as input data for the WIND simulator. The data was converted from its raw text format into binary files each containing a block of data for a single month. From the wind data, one additional data set was generated containing the vector-averaged hourly winds for the entire period from May through September of 1988 and the scalar averaged ozone for the same period. This created a composite day (31 sites by 24 hours, where each hour is the average for that hour for all 1988 smog season days). In this study, the composite day was used to do preliminary assessments of the data set, to look for patterns and trends in the wind fields and simulated tracer releases, and to compare with individual days from 1988 and other years. The WIND program treats this composite day just like any other day.

Trajectories and Vector Maps

WIND was set up to use a linear interpolation between reporting stations to develop the wind field as described in Horrell (1989). Though inverse square law relationships have been recommended by other authors (Seinfeld et al., 1982) for interpolating wind data, testing with various power laws for the set of simulations failed to establish additional accuracy for any particular power. Consequently, a linear interpolation was chosen because of the associated ease of calculation and interpretation. These experiments were conducted from nine points distributed in the western basin (see Table 2). These sites were chosen for two reasons. First, they surround the sulfur hexafluoride tracer release site. Second, they bound the major emission region associated with the downtown Los Angeles area. Simulated releases were conducted at 6 a.m. and 3 p.m. Pacific Daylight

Station Number	Abbrev.	Station Name	Latitude	Longitude
0	ANAH	Anaheim	33.818	117.919
1	AZUS	Azusa	34.133	117.923
2	BANN	Banning	33.9	116.83
3	BURK	Burbank	34.184	118.304
4	CELA	Central LA	34.063	118.228
5	COST	Costa Mesa	33.652	117.929
6	CRES	Crestline	34.243	117.274
7	FONT	Fontana	34.096	117.491
8	GLEN	Glendora	34.186	117.936
9	HAWT	Hawthorne	33.926	118.376
10	HEME	Hemet	33.733	116.950
11	LAHB	La Habra	33.919	117.951
12	LANC	Lancaster	34.667	118.133
13	LGBH	Long Beach	33.837	118.205
14	LSAL	Los Alamitos	33.792	118.033
15	LYNN	Lynwood	33.917	118.215
16	NEWL	Newhall	34.388	118.533
17	NORC	Norco	33.921	117.570
18	PASA	Pasadena	34.132	118.126
19	PERI	Perris	33.778	117.244
20	PICO	Pico Rivera	34.013	118.059
21	PLSP	Palm Springs	33.8	116.60
22	POMA	Pomona	34.066	117.754
23	RDLD	Redlands	34.066	117.159
24	RESE	Reseda	34.199	118.528
25	RIVR	Riverside	33.993	117.418
26	SNBO	San Bernardino	34.104	117.283
27	TORO	El Toro	33.621	117.691
28	UPLA	Upland	34.103	117.634
29	WHIT	Whittier	33.918	118.026
30	WSLA	West LA	34.051	118.389

Table 1. Air Quality and Meteorological Reporting Stations

Time	Percent
8 a.m.	50
3 p.m.	88

Table 2. Percentage of Days where the LA – Glendale Divergence Zone is Identifiable at a Particular Time

Time (PDT). These times were chosen to label emissions from the morning and evening rush hours.

The trajectory simulations all had the same protocol. At each site, tracer was released for three hours. This means one trajectory was started at each hour, and it steps ahead in time at one hour intervals. The trajectory away from the release site was plotted as a non-diffusing point carried by the resultant winds for a period of 12 hours. Twelve hours was chosen because a subset of test experiments showed that the residence time of morning emissions from this region was on the order of 12 hours, and a similar value of 10 hours was obtained from the actual SF_6 tracer experiments. Trajectories were computed using the recursive trajectory method described in Horrell et al. (1989) and carried out via its implementation in the WIND program.

Visualization Method for Locating Divergence Zones

The WIND package computes and displays maps that highlight regions of angular spreading in the surface wind fields and assist in identifying divergence zones. The method for this will be discussed in this chapter. The method was developed to provide a quick, objective, visual way of identifying regions of angular spreading in the surface wind vector field.

For the maps to be displayed below, the region of interest was divided into grid squares 2.5 km on a side. A value was computed for every grid square by using the following rule. The angular spreading associated with a particular grid square was determined by computing the dot product of the velocity vectors from the four corners of that grid square. Six combinations of vectors result when all corners are dotted with their neighbors and diagonals (see below).

$$a \cdot \quad \cdot b$$

$$c \cdot \quad \cdot d$$

The angle between the two vectors was determined by using Equation (1).

$$\theta = cos^{-1}\left[\frac{\mathbf{A}\cdot\mathbf{B}}{|A||B|}\right] \tag{2.3.1}$$

The pair yielding the largest angle was chosen to be the value for a given grid square. The relative direction of the two vectors was determined geometrically, i.e., whether the vectors pointed towards, away, or parallel to one another. The sign of the angle was assigned negative if the two vectors pointed away from one another or were parallel and was assigned positive if they pointed towards one another. The positive angle differences indicate the presence and location of divergence zones. WIND graphically displays the results of these calculations by dividing each individual grid square's value by the maximum observed in the entire region. Then, a false color image of those values that are larger than the fractions 0.08, 0.11, 0.14, and 0.17 is created. These fractions were found to highlight most clearly the divergence zones in the basin when the method was developed.

Unfortunately, some of the visual contrast of the images is lost when they are converted to black and white. The darkest squares are experiencing the strongest divergence, whereas the lightest squares show the domain of the calculation. Those shades of gray in between are lower levels of divergence. The divergence maps should be compared with the vector maps to assist in reading them.

One alternative method for identifying regions of high angular spread in the surface wind field was considered. This method is based on the fact that locations of divergence would have negative accumulation when a line integration was performed around them. When first considered, this approach seemed promising since large regions (10 km edge squares) where the surface winds diverged nominally showed negative accumulation. However, when attempted on smaller scale grid squares, 2.5 km edges, this approach was unsuccessful for two main reasons. First, negative accumulation occurs more commonly where the flow accelerates in the direction of flow than where it diverges. Second, the flow

decelerates near stagnation regions, which gives positive accumulation even in regions of angular spreading. Both problems tend to obscure the identification of the actual divergence zones.

Results

Wind Fields

The first use of the WIND program was to create and display the wind fields at each hour from the 1988 composite average day for the purpose of locating the divergence zone (Simulation 1). Two hours from the composite day, 8 a.m. and 3 p.m., are shown in Figures 1 and 2, respectively. Figures 1 and 2 show the LA-Glendale divergence zone marked with a bold dashed line.

Divergence

As part of this preliminary investigation into the location of the LA-Glendale divergence zone, the two-dimensional angular divergence in the surface winds was computed at each hour over the region of interest. Similar to the wind vectors, the computation was done for the entire region under consideration and at each of the 24 hours. These images were converted into the pictures, examples of which are seen in Figures 3 and 4. These figures correspond to the same times as the vector maps in Figures 1 and 2.

Observed Frequency of the LA-Glendale Divergence Zone

The percentage of time the LA-Glendale divergence zone was present at 8 a.m. and at 3 p.m. for the 151 days of the 1988 data set was determined from WIND generated wind vector maps. (See Table 2.) The wind vector maps were studied visually to determine if the zone was present. In cases where the zone barely appeared, the angular divergence was computed, displayed as discussed previously, and used as an objective means of deciding whether the zone should be counted. If the zone appeared on the map as clear line, several grid squares thick, it was counted as being present. If it did not appear clearly, or if it appeared as a scattered pattern of grid squares, it was counted as absent. The presence or absence of a zone was clarified in all marginal cases using this technique.

Simulation 2 revealed that the zone was much more likely to be identified in

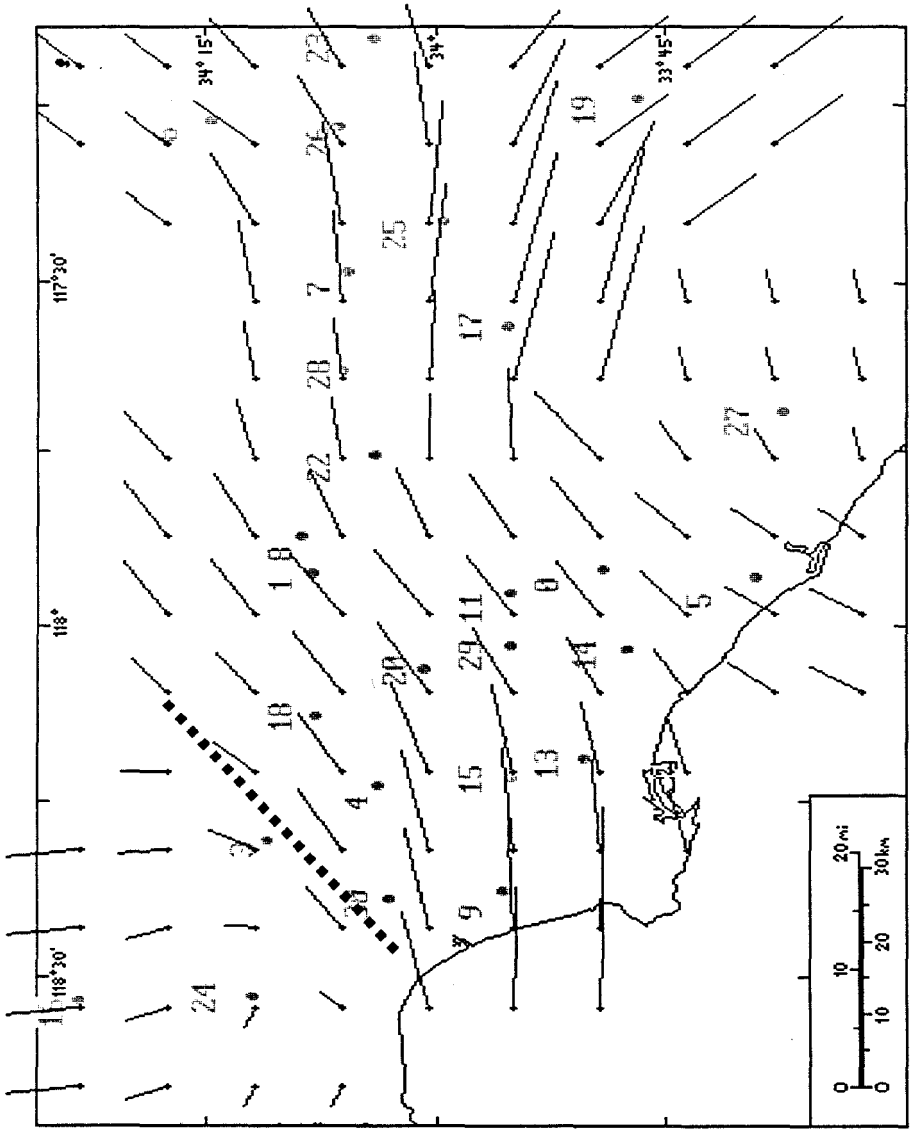

Figure 2. Hourly averaged wind vectors for the 1988 composite average day during the smog season at 3:00 p.m. Vectors are shown 10 km apart, their length proportional to the wind speed, and their direction away from their origin is the direction of flow. The bold dashed line to the west of Pasadena (site 18) and downtown LA (site 4) shows the location of the divergence zone at this time.

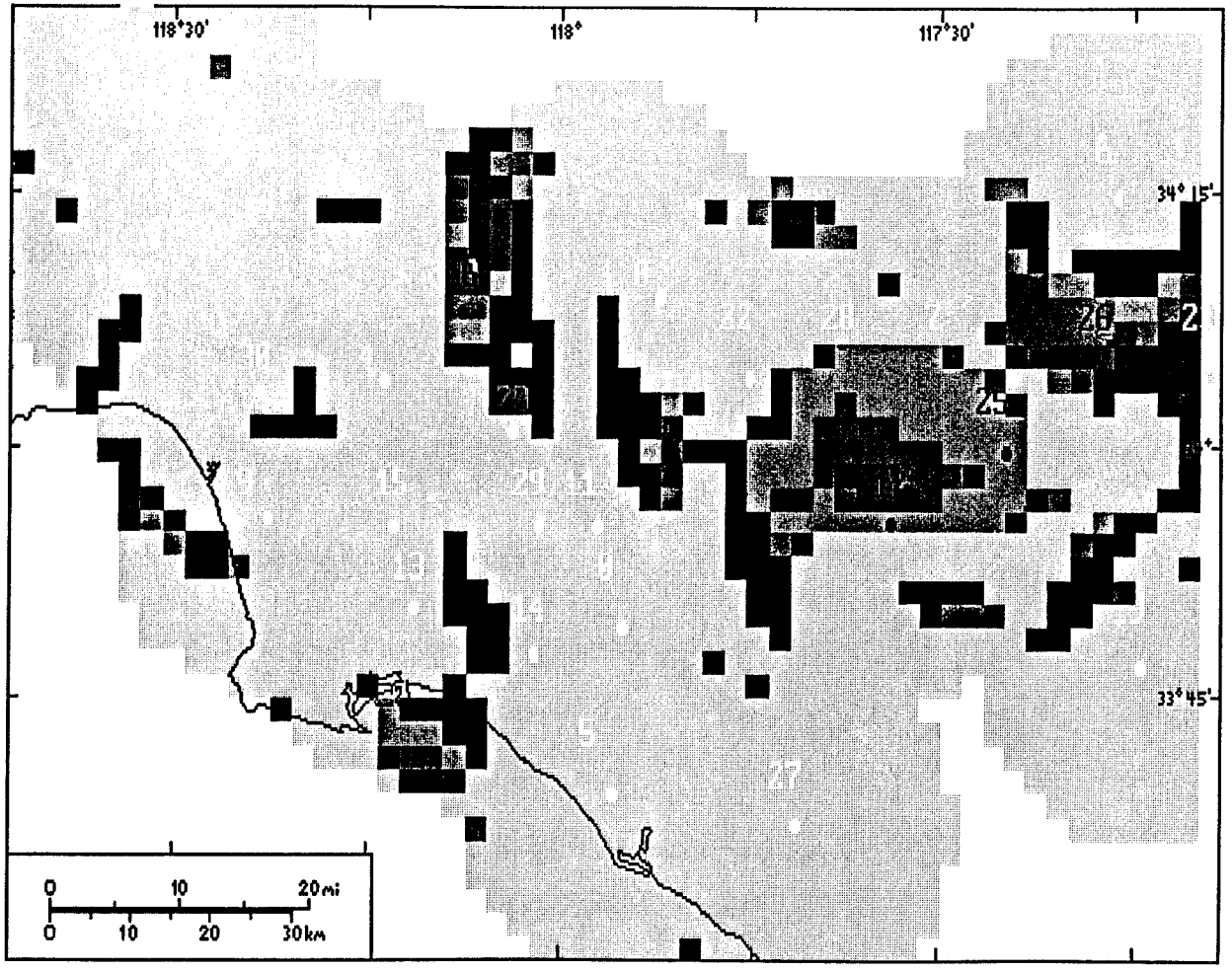

Figure 3. Angular divergence map of the western Los Angeles Basin for the 1988 composite average day during the smog season of 1988 at 8:00 a.m. Grid size is 2.5 km on an edge. The black regions represent locations of maximum angular divergence, the lightest shading indicates the total region in which angular divergence is calculated, shades in between the lightest shading and the black indicate areas of slight angular divergence.

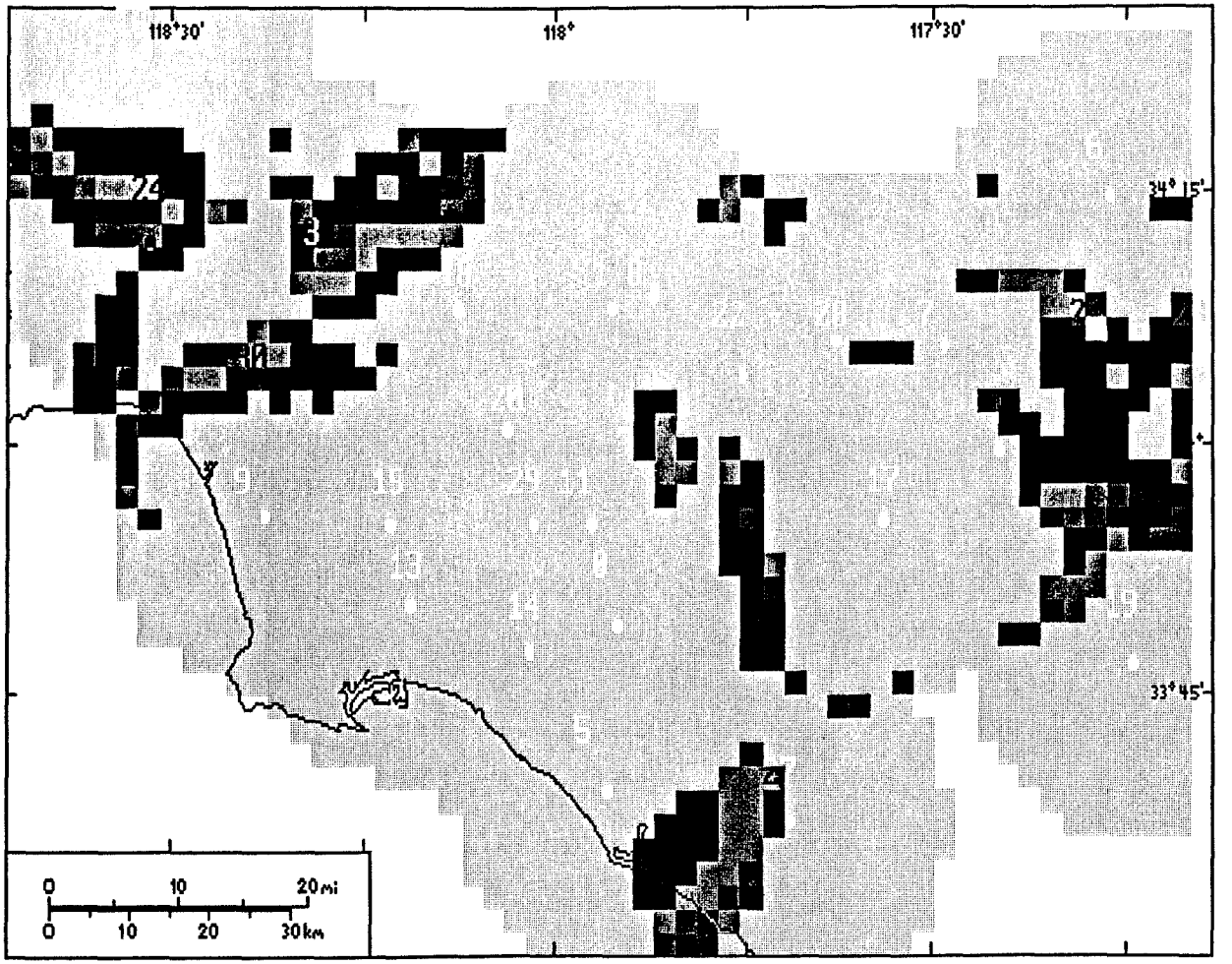

Figure 4: Angular divergence map of the western Los Angeles Basin for the 1988 composite average day during the smog season of 1988 at 3:00 pm. Grid size is 2.5 km on an edge. The black regions represent locations of maximum angular divergence, the lightest shading indicates the total region in which angular divergence is calculated, shades in between the lightest shading and the black indicate areas of slight angular divergence.

the afternoon than in the morning. The zone was identifiable around 50 percent of the time at 8 a.m., but was seen clearly 90 percent of the time by 3 p.m. At 3 p.m., the zone had often moved to be centered over station 3 or even to be between station 24 and 3 (and from there extended down to station 30). In contrast, if the zone was observed during the morning, it was most often located over station 18. An occasional day put the zone to the east of station 18, but the zone was never identified west of station 4 in the morning. The information provided by these statistics explains why the observed SF_6 transport might have been unexpected. Prior to the SCAQS, the morning period near downtown was relatively uncharacterized, while the afternoon period was more well understood. If the flow patterns for the afternoon were used as a guideline, one would conclude tracer would flow to the eastern basin.

Surface Trajectories

Average 1988 Day

For comparison, simulated tracer experiments to elucidate source-receptor relationships were performed using the average 1988 day (Simulation 3). As mentioned, two sets of releases were done, the first began at 6 a.m. and the second at 3 p.m.. The resulting trajectories are shown in Figures 5 (a)-(d) and 6 (a)-(d) for 6 a.m. starts and Figures 7 (a)-(d) and 8 (a)-(d) for the 3 p.m. starts.

Individual Days of 1988 and 1987

To understand how the dynamics of the LA-Glendale divergence zone's movement affects the trajectory of downtown LA emission on individual days, a set of simulated tracer experiments was done on each day of the 1988 smog season (Simulation 4) and on all of the 1987 days (Simulation 5) mentioned above. Four sites were selected that created a square region that both surrounded the average mid-morning location of the divergence zone and encompassed the region of massive morning emissions associated with downtown LA. These are a subset of the sites shown in Table 3 and correspond roughly with data reporting stations 4, 30, 9, and 15.

Statistics were then compiled for these 151 days by performing a simple data reduction. Each simulated release was assigned to 1 of 16 bins according to the direction, relative to the release point, the trajectory exited from the basin. The 16 bins correspond to the 16 points of the compass centered in the 16 equipartioned pie slices of a circle. Ambigous cases were resolved on the basis of the direction of the tracer at its last hour or two. It should be noted that less than one percent of the cases were ambigous, and that not a single trajectory failed to exhibit a strong directional sense by which it could be characterized. From the three releases associated with each site, a composite bin value was determined for that site by averaging.

Further processing of the binned data was done to assist in interpreting the

Release Point Description	SiteCode	Latitude	Longitude
Near Site 30	s1	34 4'	118 23'
Site 4	s2	34 4'	118 14'
N of Site 20	s3	34 4'	118 4'
Near Site 9	s4	33 57'	118 23'
Near Site 15	s5	33 57'	118 14'
NW of Site 29	s6	33 57'	118 4'
Coast Line	s7	33 48'	118 23'
SW of Site 13	s8	33 48'	118 14'
W of Site 14	s9	33 48'	118 4'

Table 3. Release Sites in the Western Los Angeles Basin

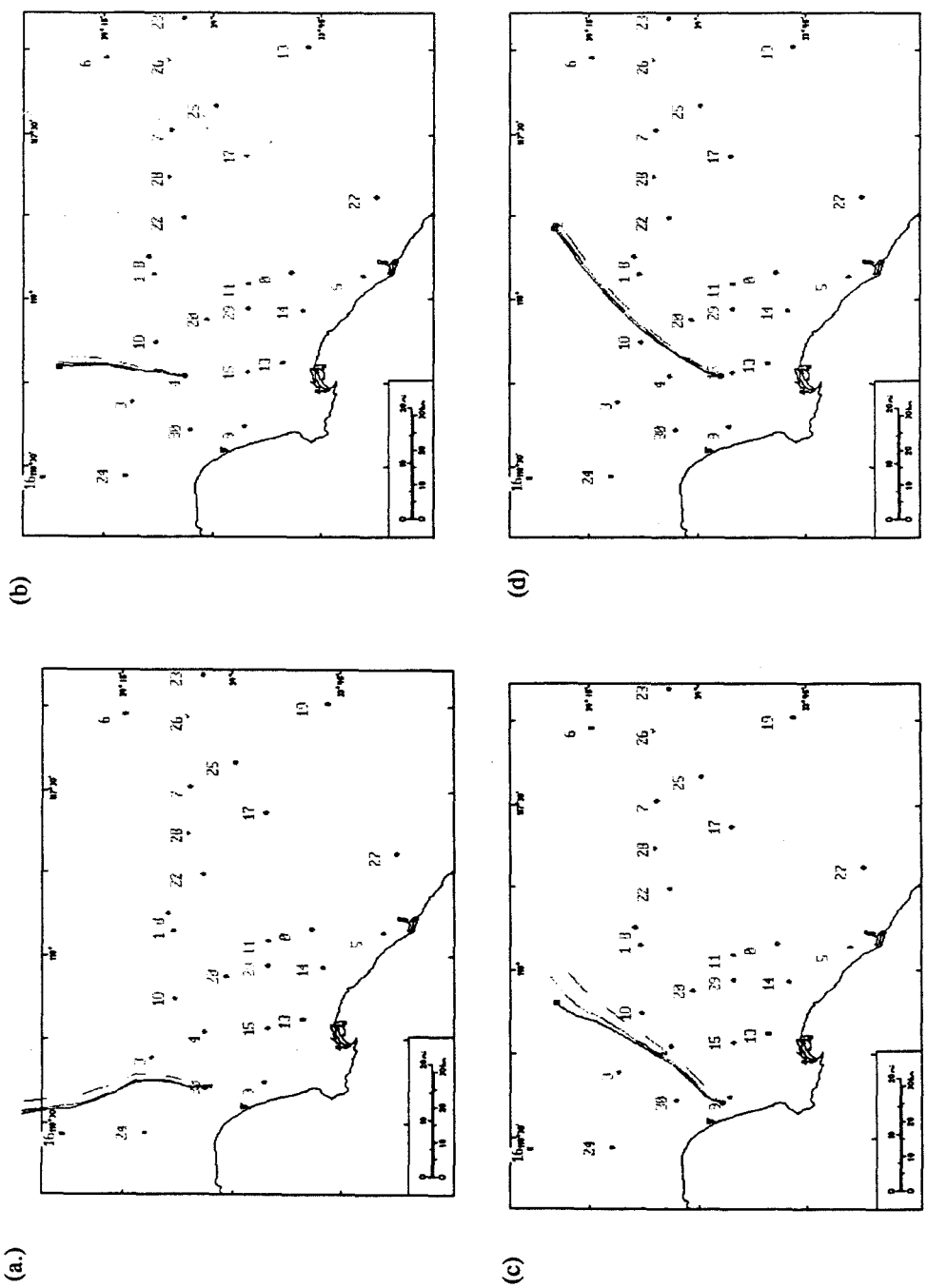

Figure 5. Simulated 12 hour tracer releases initiated at 6,7, and 8 a.m. for 4 sites in the western Los Angeles Basin using the 1988 average smog season winds, (a) West Los Angeles near site 30, (b) downtown LA site 4, (c) Hawthorne near site 9, and (d) Lynwood near site 15. Only the trajectory lines are depicted.

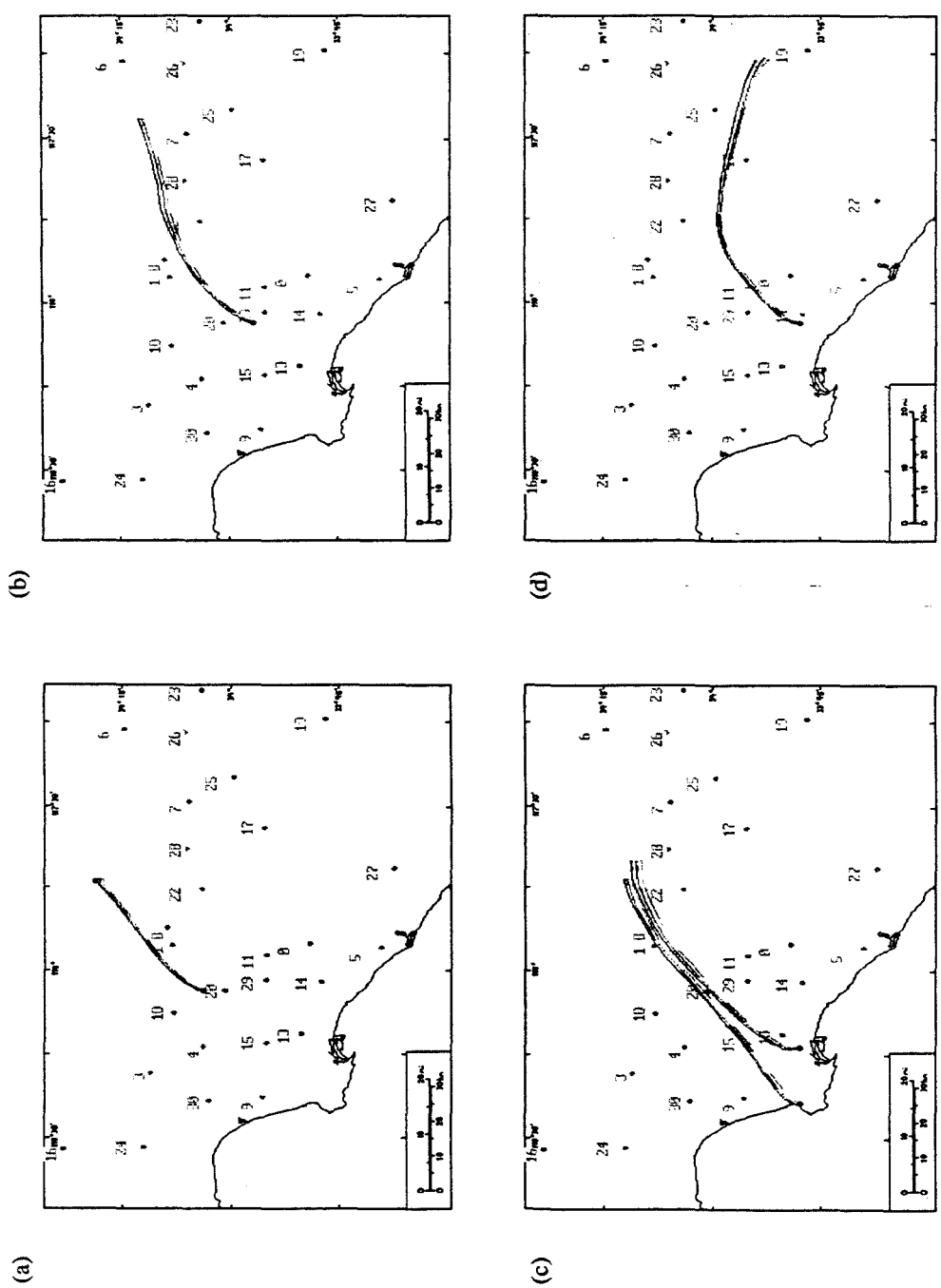

Figure 6. Simulated 12 hour tracer releases initiated at 6, 7, and 8 p.m. for 5 sites in the western Los Angeles Basin using the 1988 average smog season winds, (a) Pico Rivera near site 20, (b) Whittier near site 29, (c) southwest coastline and Long Beach near site 13, and (d) Los Alamitos near site 14. Only the trajectory lines are depicted.

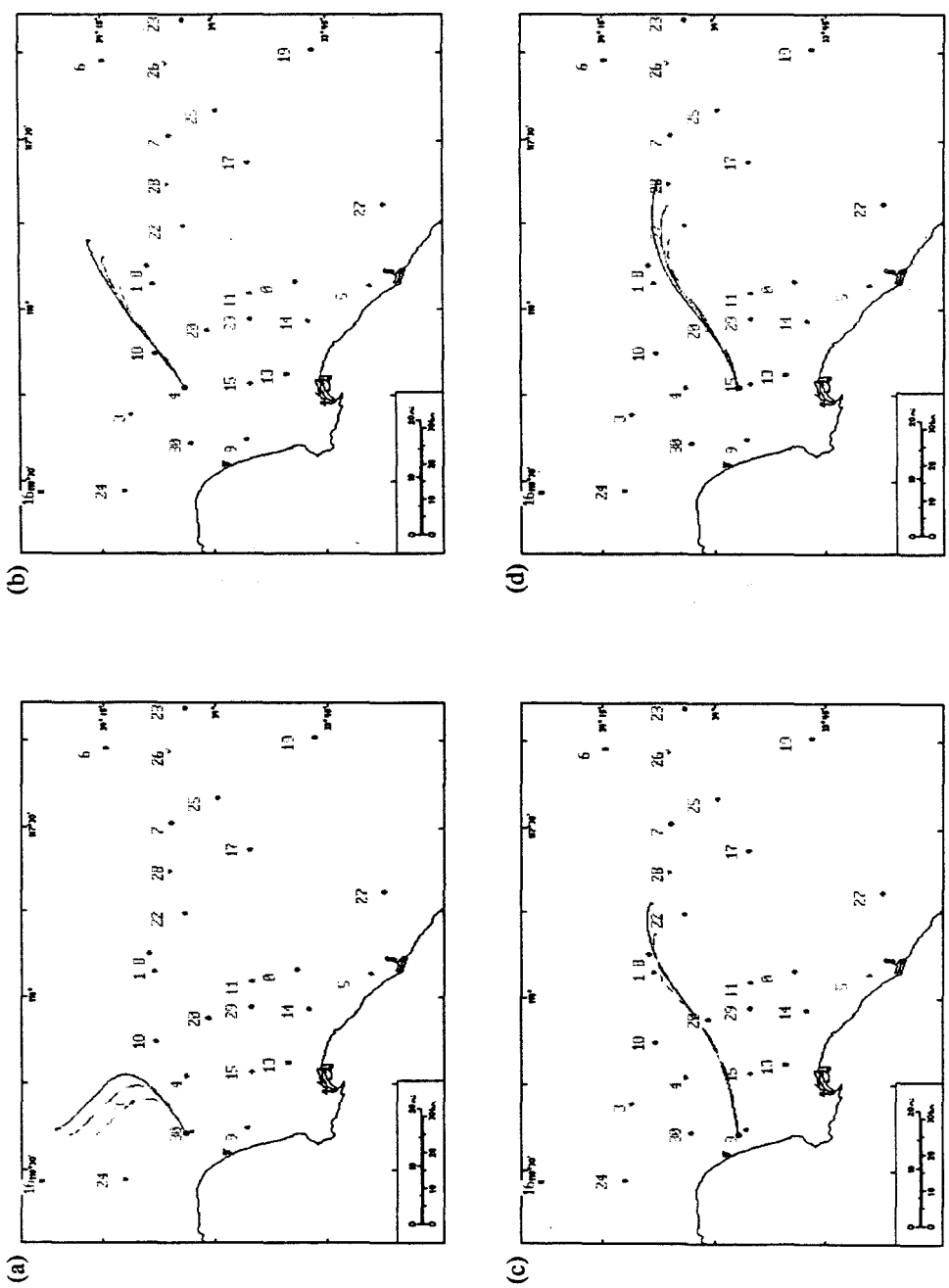

Figure7. Simulated 12 hour tracer releases initiated at 3,4, and 5 p.m. for 4 sites in the western Los Angeles Basin using the average smog season winds, (a) West Los Angeles near site 30, (b) downtown LA site 4, (c) Hawthorne near site 9, (d) Lynwood near site 15. Only the trajectory lines are depicted.

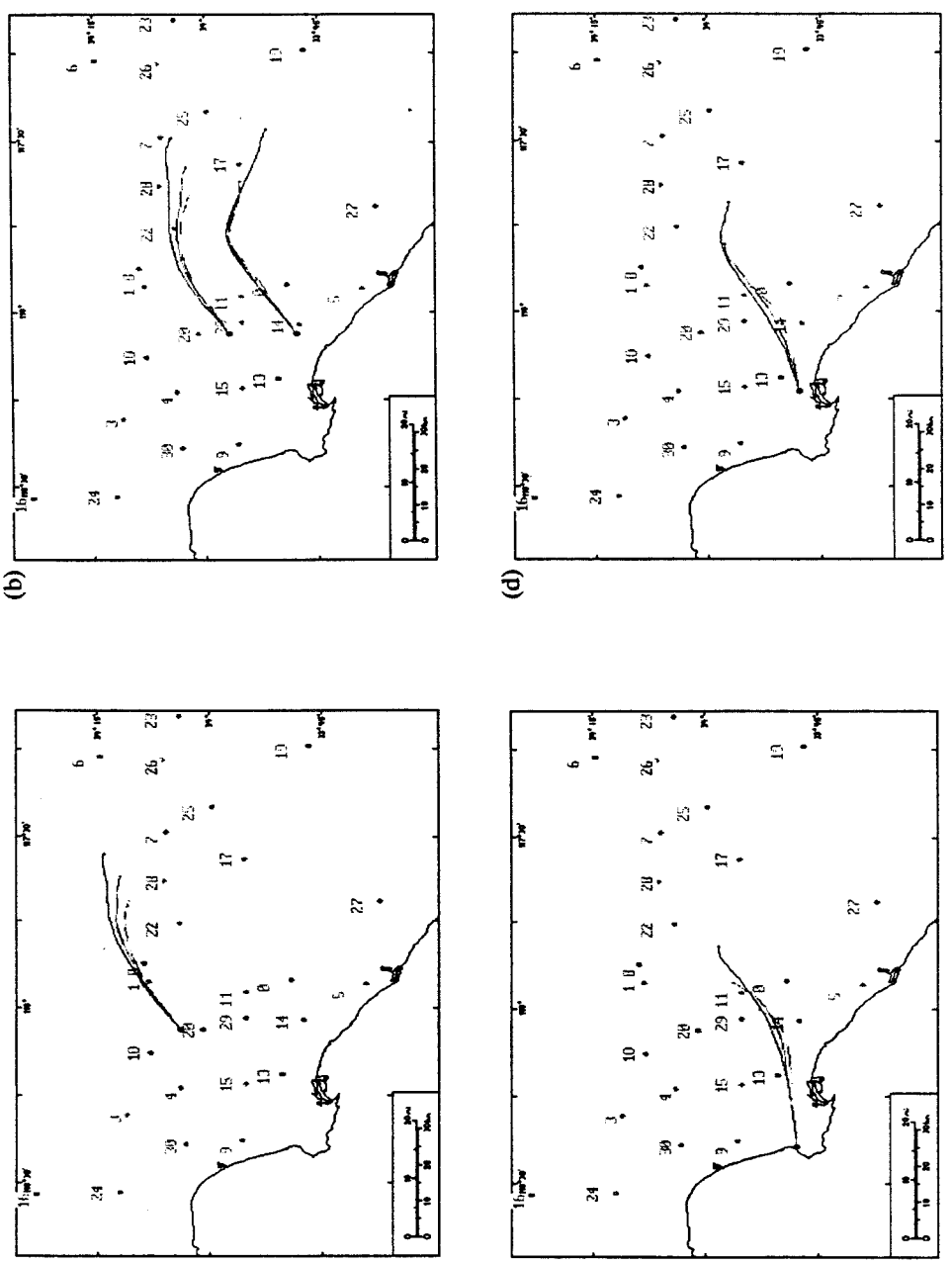

Figure 8. Simulated 12 hour tracer releases initiated at 3,4, and 5 p.m. for 5 sites in the western Los Angeles Basin using the 1988 average smog season winds, (a) Pico Rivera near site 20, (b) Los Alamitos near site 14 and Whittier near site 29, (c) southwest coastline, and (d) Long Beach near site 13. Only the trajectory lines are depicted.

results. The composite bin value for each site was aggregated into six groups, which reflect the distribution of the four corners in the sixteen bins on a single day. One category is the days when zero of the four corners are transported to the NE, E/NE, or E. The second category is the days when one of the four corners are transported to NE, E/NE, or E, and that one corner is one of the two southernmost sites, 9 or 15. The third category is the days when the two southernmost corners (sites 9 and 15) are transported NE, E/NE, or E. The fourth category is the days when three corners (except site 30) are transported to the NE, E/NE, or E. The fifth category is the days when all four corners are transported to the NE, E/NE, or E. The sixth category is comprised of all the days that do not fit in any of the above categories. Figure 9 shows the the results from simulation 4 as a percentage of the 151 1988 days examined.

In Simulation 5, the two days of the 1987 SCAQS had trajectories simulated for them in the same fashion as was done for the individual days of 1988. Both days were found to be in category one above, where none of the four corners was transported into the eastern basin.

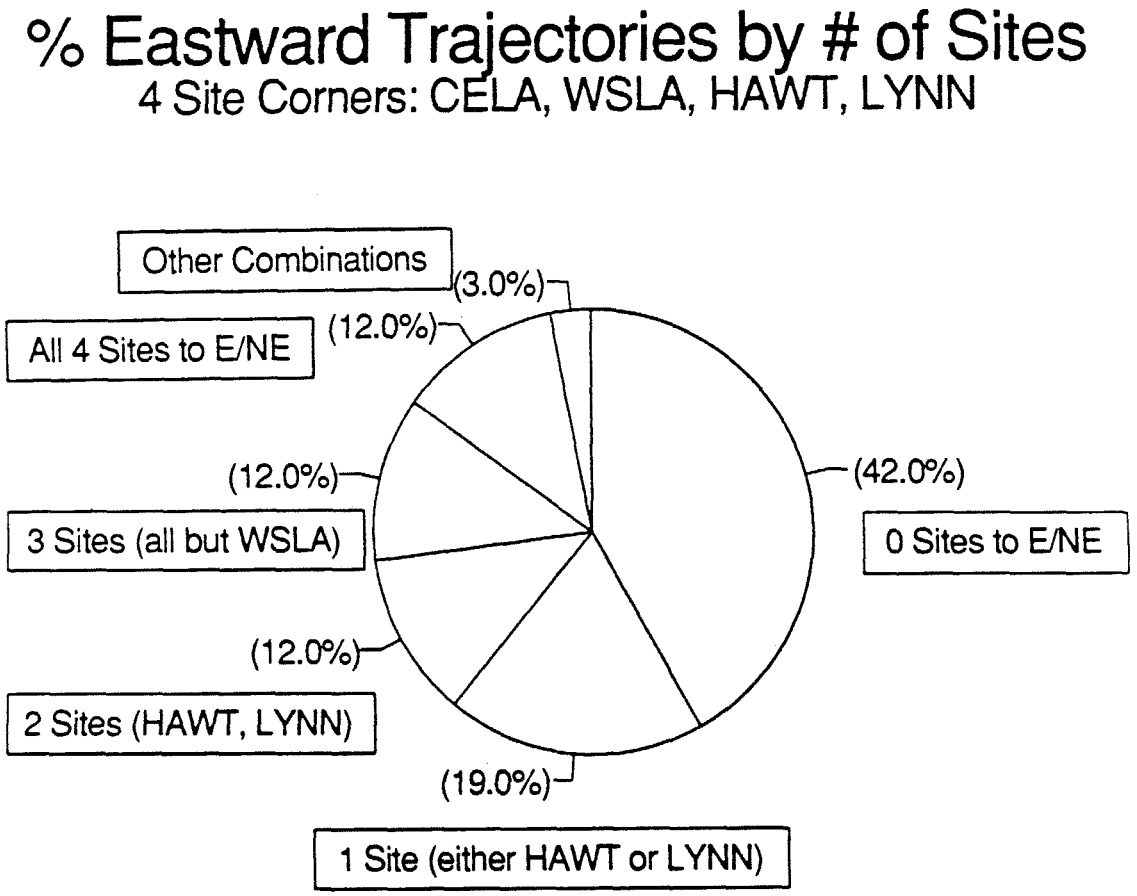

Figure 9. Percentage of simulated western Los Angeles Basin trajectories exiting the basin to the E/NE from 4 selected sites (downtown Los Angeles, West Los Angeles, Hawthorne, and Lynwood). Each trajectory started at 6 a.m. The 4 sites are grouped by the number of sites which produce trajectories that exit the basin to the E\NE. The data is 151 days of the 1988 smog season from May to September.

Dynamics of the LA-Glendale Divergence Zone

Based on examination of the divergence maps created from the composite average smog season day of 1988 (Simulation 1), it can be said that LA-Glendale divergence zone is a feature of the basin's wind field for about 21 hours in a day. The zone is also dynamic, moving 30 km east to west and back over the course of the composite day.

Figure 10 depicts the dynamics of the zone and labels various positions the zone occupies. In the average day the zone showed the following pattern of movement. It appeared at 7 a.m., at which time it lay along a nearly perfect north-south line originating between station 4 and station 20, position (a). The zone remains at this location until around 10 a.m.. At this time, the zone begins to elongate to the southwest stretching from station 4 towards stations 9 and 30 passing through positions (b) and (c) to position (d). At 11 a.m. the zone extends from the coast around station 9 inland to station 18 (Pasadena) and then north beyond Pasadena stabalizing in position (d). At around 1 p.m., the zone begins to migrate west at all locations so that it extends from the coast north of station 30 to north of station 18, position (e). Between 2 and 3 p.m., the zone moves to a new location which lies north of station 30 and extends through station 3 through to a point about 10 km north of station 18, position (f). A broad double peak occurs in the divergence map from between station 24 and station 18, indicating the zone is equally likely in any number of places between station 3 and station 18. The zone remains in this position until 6 p.m. when it starts to drift back eastward at all points about 5 km, between position (e) and (f). The length of the zone begins to shorten at this time also, as it recedes from the coastline. At 8 p.m., the zone extends from station 30 south of station 3, north of station 4 to a point north of station 18, between position (e) and (d). The zone slowly moves eastward, at about 1 to 2 km an hour until 3 a.m. at which time it spans from station 30 to station 4 then to station 18. At 4 a.m.

the zone begins to disappear and from 5-6 a.m., the zone is gone entirely.

Analogy

A simple analogy for the basin is proposed. Under this proposition, the western basin is considered analogous to a Y-shaped pipe which has a hinged door at the branch of the Y. Offshore flow comes up the base of the Y, gathers emissions, and is split by the divergence zone into either of the northwestern or eastern outlet branches. Tracer experiments have demonstrated that transport is restricted across the zone, suggesting that the hinged door be considered a solid door, not a screen door. The fractional splitting of the downtown emissions into the two outlet streams is sensitive to the position of the hinged door. Subsequent smog development later in the day results, at least in part, from the fractional splitting. To complete the analogy, the position of the hinged door must be described. Its most likely position is due to factors such as the pressure gradients across the basin that result from the synoptic scale weather and differential heating at the outlets. Thus, the zone's position at any time represents the relative difference between the pressure at both outlets and the inlet.

The mechanism by which the LA-Glendale zone partitions the massive western basin emissions has a distinct influence on receptor locations for these emissions. On the average day, the LA-Glendale divergence zone sweeps across an area of approximately 800 square kilometers. On particular days, the zone appears to be able to sweep across as much as twice this area as shown by the demarcation lines for the extremes in the observed locations of the zone, Figure 10 positions (a') and (f'). This means that emissions may be routed to the northwestern basin in the morning while the zone occupies position (a) of Figure 10, but as the day proceeds the zone moves into position (f) and emissions are routed into the eastern basin. Because the zone directs a large portion of the western basin's emissions into two vastly different directions, a complete understanding of the zone is necessary to describe accurately the source-receptor relationships

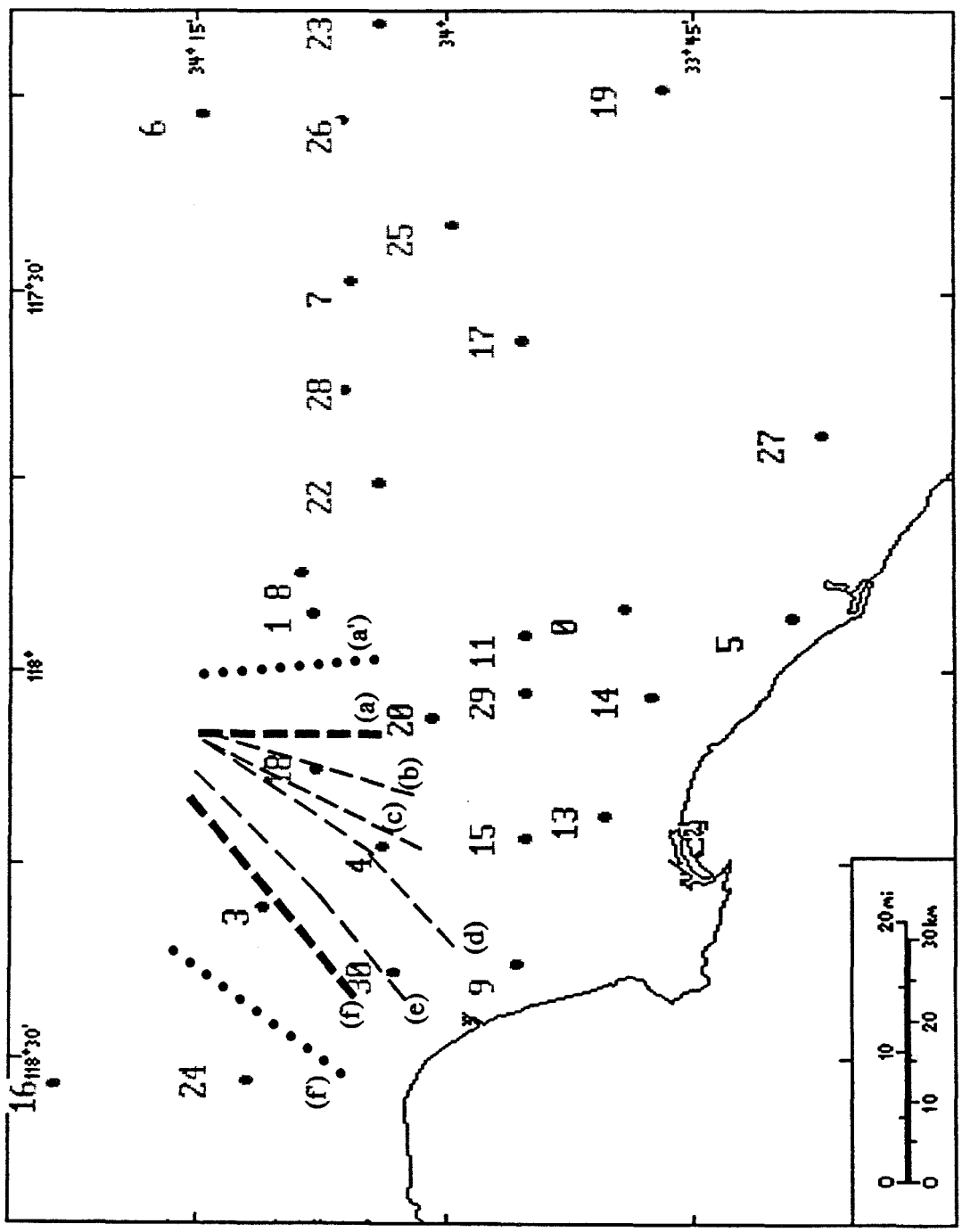

Figure 10. Positions of the LA-Glendale divergence zone based on observations made using the 1988 composite average day, sites (a) through (f), and total range of the zone's movement based on individual days (a') through (f').

between the western basin and the northwestern and eastern portions of the basin.

Two plausible conclusions can be drawn based on the above analogy and the trajectory analysis of the 1988 average smog season day. On average the higher observed ozone levels in the eastern portion of the Los Angeles Basin result from emissions made during the evening of the previous day. These are present when the emissions from the current morning are produced and then the mixture undergoes reaction. Elevated afternoon ozone levels in the San Fernando Valley (sites 3, 16, and 24) depend in part on the position of the divergence zone. Evening rush hour emissions are not generally directed to the northwest into the San Fernando Valley, and therefore do not impact morning ozone levels in that locale.

The trajectories generated in simulation 3 provide practical evidence of how the LA-Glendale divergence zone affects emission trajectories from sources in the western basin on average. Trajectories in Figures 5(b) and 6(a) demonstrate that on average the zone lies between the two release points depicted in these figures at 8 a.m.. This is seen by comparing the different directions the trajectories take away from the two sites. Examination of the same two sites in Figures 7(a) and 7(b), and the site depicted in Figure 8(a), shows that by 3 p.m. the LA-Glendale divergence zone has moved westward, and is now routing a majority of western basin emissions into the eastern basin. The results of simulation 4 where individual days are examined in the proximity of the zone will complement these results.

The results from simulation 4 show just how infrequently the emissions from the entire area encompassed by the four points in the northwestern basin had no impact on the eastern basin. Figure 9 summarizes the findings for the simulated morning releases. Forty-two percent of the time four corners fit the first category above. The second category accounted for 19 percent of the observations. In

contrast to the first category, only 12 percent of the time did the four corners fit the third, fourth, and fifth category. It should be noted that only three percent of the observations did not fit any of the categories.

It is interesting to note the route the trajectories took when they did not exit the basin through the E to NE directions. In excess of 95 percent of the trajectories went out the NNE, N, NNW and NW. This route sends the air parcels into the San Gabriel Mountains or into the San Fernando Valley, exactly where the SF_6 was observed in the 1987 studies.

Simulation 5 clearly demonstrated the observations of the summer SCAQS SF_6 tracer experiments were, in fact, not anomalous but representative of most smog season days. Both days fell into category one, which represents 42 percent of the total days. Furthermore, from the Vernon release site, a day could fall into categories two or three and still have a trajectory like those actually observed. This means up to 73 percent of the time emissions from the Vernon tracer release site are destined to exit the basin to the ENE, N, NNW, or NW.

Association Between Observed Ozone Levels and the LA-Glendale Divergence Zone

The ozone contour maps produced as part of simulation 6 clearly depict the geometrical relationship between the LA-Glendale divergence zone and the ambient ozone levels. These maps were generated using the 1988 smog season average ozone levels described previously. Twenty-four maps were generated, one for each hour of the average day, and two are presented here. At 8 a.m., the only region of the basin that is below the 0.1 pphm ozone level is the region right around site 3 (See Figure 11). This is approximately 15 km east of the divergence zone. At 3 p.m., a minimum band in the ozone lies along the line formed by the sites 9, 30, and 3. (See Figure 12.) This also corresponds to the location of the divergence zone. The position of this depressed ozone band and the divergence zone are both the result of the geography, but the minimum ozone band seems

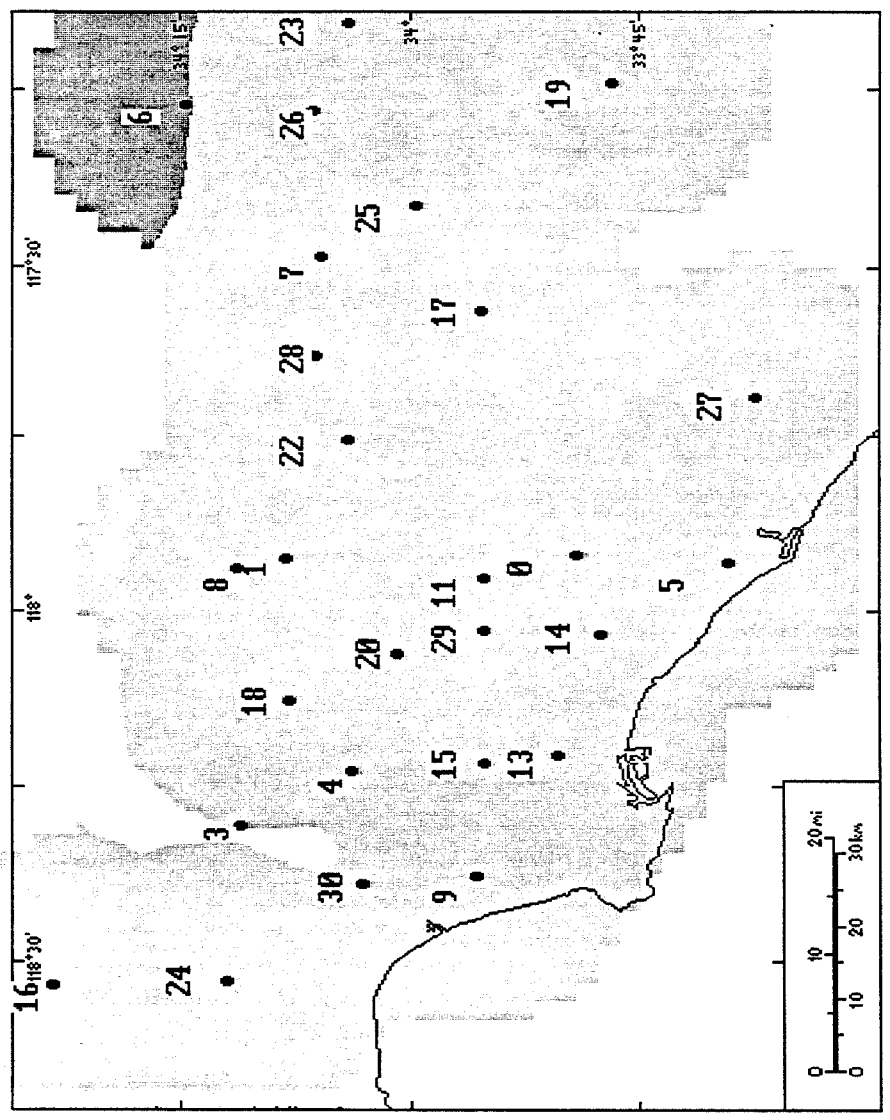

Figure 11. Hourly averaged ozone contour map for the 1988 composite averaged day during the smog season at 8 a.m. The contoured regions are, from lightest shading to darkest: (i) 0.1 -4.1 pphm, (ii) 4.1-8.1 pphm, (iii) 8.1-12.1 pphm, and (iv) 12.1-16.1 pphm. As a reference station 5 is in (i), and station 6 is in (ii). No higher levels are reported. Note the position of the ozone minimum just west of the location of the Los Angeles-Glendale divergence zone.

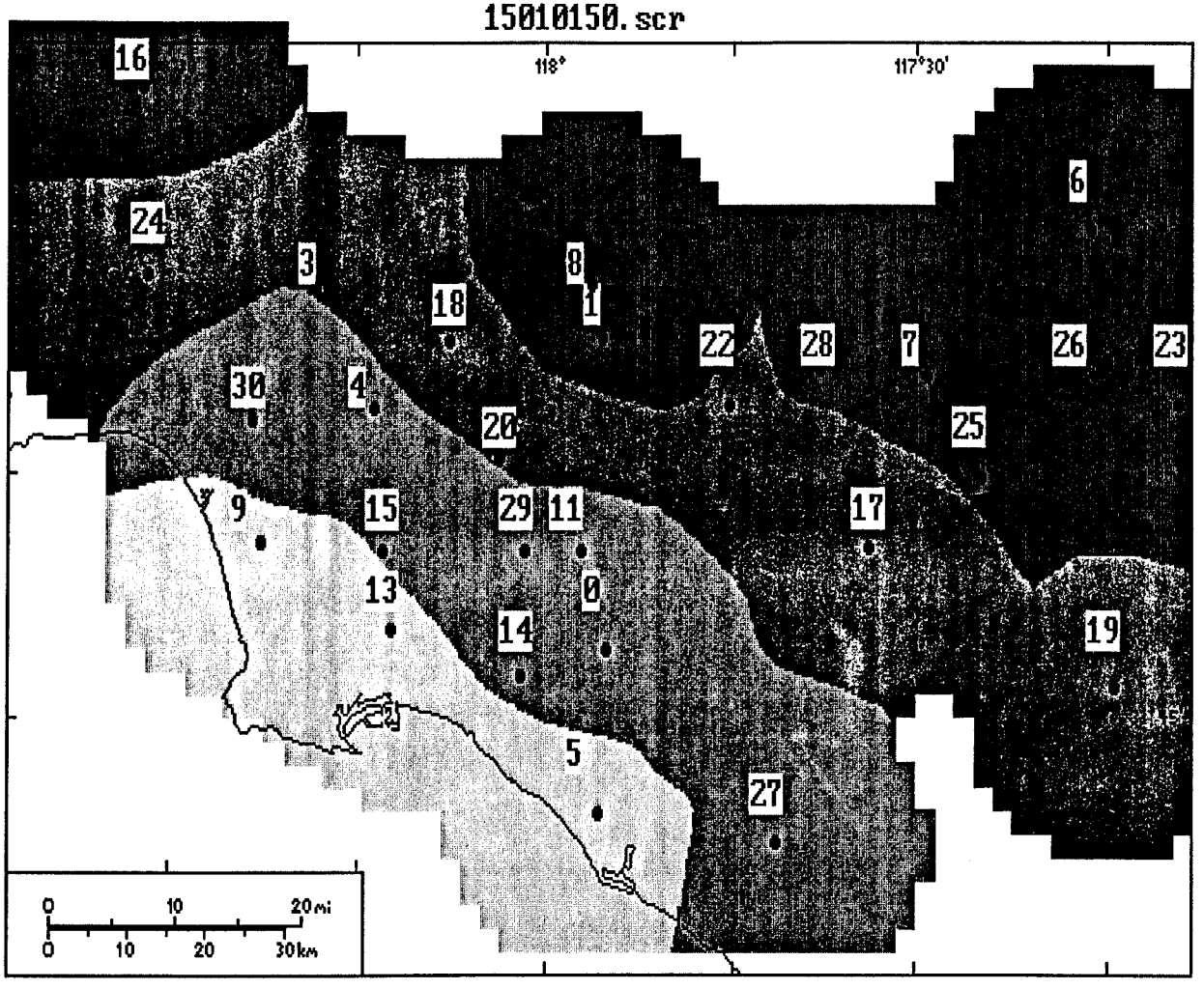

Figure 12. Hourly averaged ozone contour map for the 1988 composite averaged day during the smog season at 3 p.m. The contoured regions are, from lightest shading to darkest: (i) 0.1 -4.1 pphm, (ii) 4.1-8.1 pphm, (iii) 8.1-12.1 pphm, and (iv) 12.1-16.1 pphm. As a reference station 5 is in (i), station 27 is in (ii), station 19 is in (iii), and station 7 is in (iv). No higher levels are reported. Note the position of the ozone minimum just west of the location of the Los Angeles-Glendale divergence zone.

to be stationary and does not follow the divergence zone. This has been verified using the contour and wind field maps for the rest of the hours of the average day which were not depicted. Notice that the diminished ozone band is roughly at the same place on both maps independent of the location of the LA-Glendale divergence zone. Possibly the geography around site 3 and the lower population density of this area are responsible for these observations.

One additional observation that can be made from the ozone contour map of Figure 12, and from other maps not depicted, is the presence of an ozone maximum peak to the east of the divergence zone. This maximum is a persistent feature of the 1988 average ozone map for the hours of 10 a.m. to 6 p.m., and is located near sites 1 and 8 on the maps. One hypothesis that explains the presence of this maximum peak is that the three-dimensional structure of the eastern side of the divergence zone is a wake, or recycling cell, that is trapping emissions along the mountains that bound that portion of the basin to the north. Surface wind data alone is not sufficient to resolve definitively whether the above hypothesis is correct. The apparent association between the location of the divergence zone and the location of this maximum ozone peak is intriguing. Currently, insufficient data exists to confirm the observations, but perhaps future investigations will unravel any connection between them.

Summary

The six sets of simulations and compilations performed using the 1987 and 1988 wind and ozone data have elucidated the dynamic nature of the LA-Glendale divergence zone and established its persistence. Simulations 4 and 5 clarify that the transport observed during the two summer SCAQS studies were not anomalous observations, but in fact the norm for the smog season. The comparison of ozone data with the location of the zone in simulation 6 suggests a link between the ozone peaks around sites 1 and 8 and the eastern edge of the zone. The physics of the area around sites 1 and 8 has not been adequately studied so as to clarify the interaction between the divergence zone, the mountains, ozone precursors, and any other unknown factors.

This more complete understanding of the dynamics of the LA-Glendale divergence zone is likely to improve the overall understanding of the source-receptor relationship that exists the western basin and the receptors to the east and northwest. Finally, the exact location of this zone can be used as a sensitive diagnostic for confirming wind field models, because any model that does not accurately position the LA-Glendale zone is not correctly capturing the physics of the western Los Angeles Basin.

Acknowledgements

The authors wish to express their thanks to the technical staff of the California Air Resources Board, especially Chuck Bennet. Thanks are also made to the technical staff of the South Coast Air Quality Management District (SCAQMD) for supplying the data used in this analysis. Special thanks are made to Joseph Casmassi and Dr. Julia Lester, both of the SCAQMD, for their insightful suggestions. Partial Funding for this project came from the California Air Resources Contract A932-051.

A2.3 Appendix

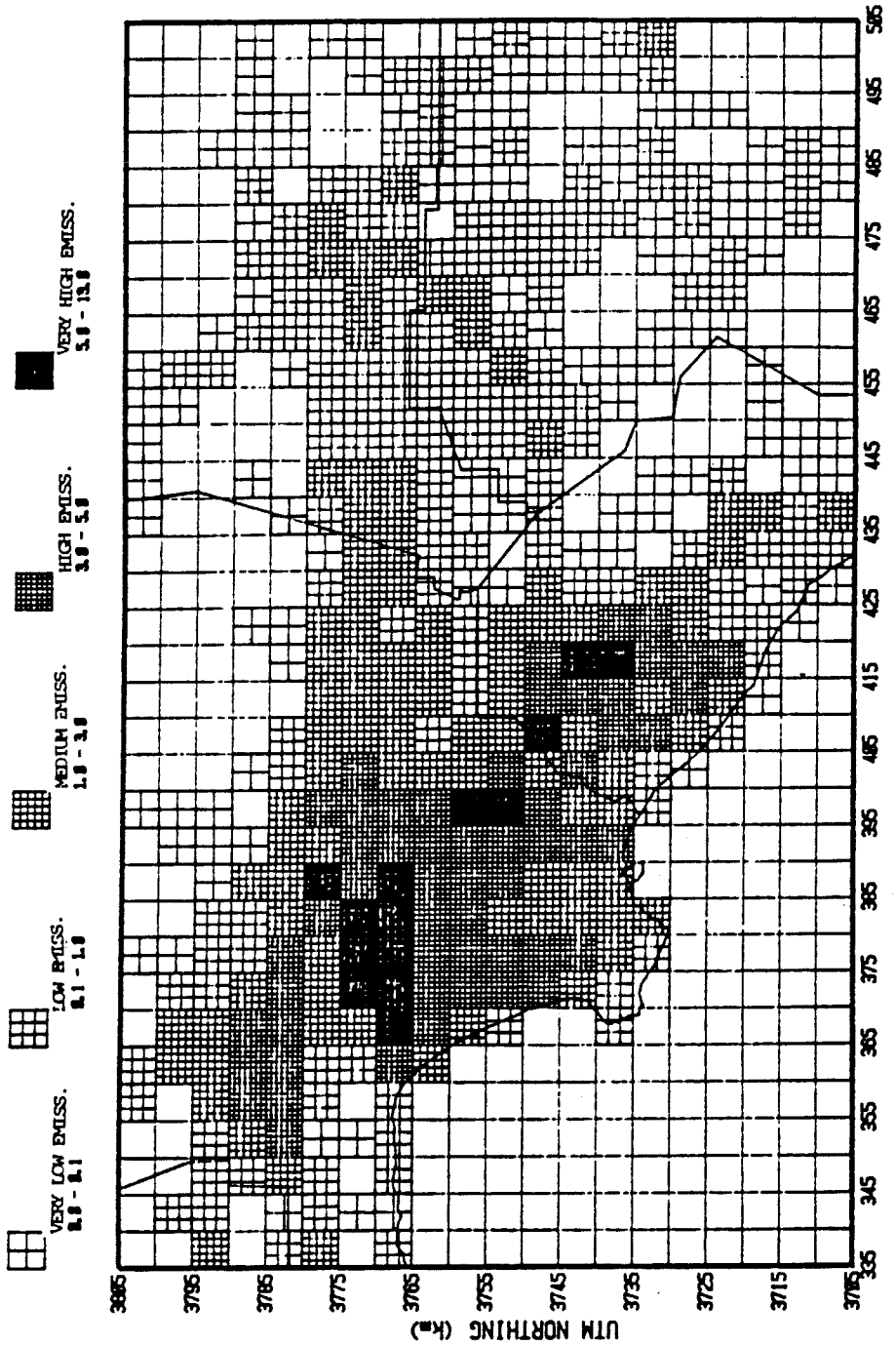

DISTRIBUTION OF MOBILE SOURCE EMISSIONS OF REACTIVE ORGANIC GASES

Figure A.1. Taken from: The Magnitude of Ambient Air Toxics Impacts from Existing Sources in the South Coast Air Basin (SCAQMD 1987).

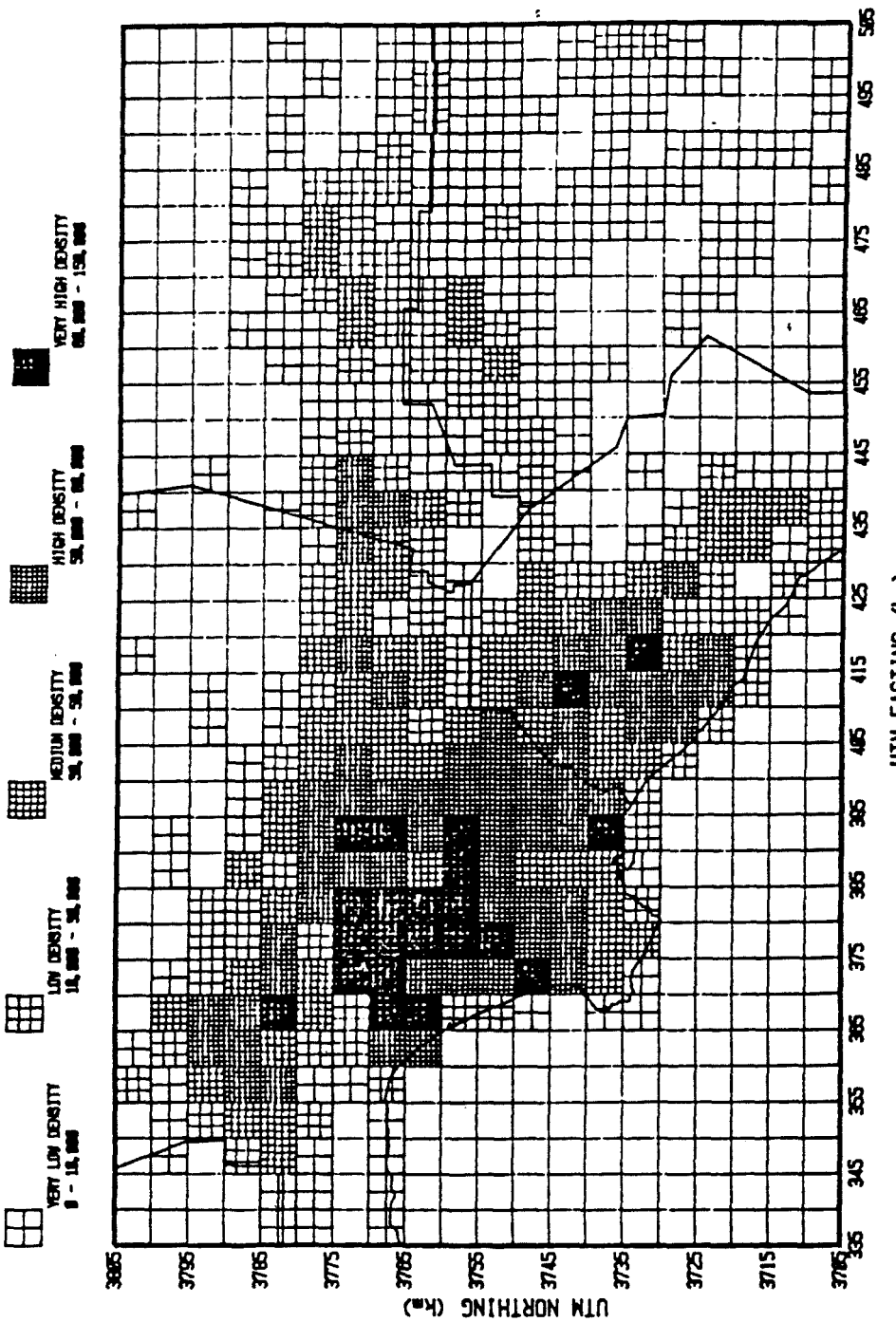

SPATIAL DISTRIBUTION OF POPULATION DENSITY

Figure A.2. Taken from: The Magnitude of Ambient Air Toxics Impacts from Existing Sources in the South Coast Air Basin (SCAQMD 1987).

References

1. Calvert J. G. (1976), "Test of the Theory of Ozone Generation in Los Angeles Atmosphere," Env. Sci. and Tech., **10** (3), pp. 248-255.
2. CARB (1984), *California Surface Wind Climatology*, State of California Air Resources Board Aerometric Data Division.
3. Edinger J. G. (1959), "Changes in the Depth of the Marine Layer over Los Angeles Basin," J. of Met., **16** (3), p. 219.
4. Edinger J. G. and Helvey R. A. (1961), "The San Fernando Convergence Zone," Bull. Am. Met. Soc., **42** (9), p. 626.
5. Edinger J.G. (1967) , Watching for the Wind, Doubleday and Company, Inc., NY.
6. Horrell R. S., Deem M., Wyckoff P., Shair F. and Crawford N. (1989), "Ground Release SF_6 Tracer Experiments Used to Characterize Transport and Dispersion of Atmospheric Pollutants During the Southern California Air Quality Study of 1987," Air and Waste Association 82nd Annual Meeting, paper 89-138.2.
7. Lamb B.K. (1978), Development and Application of Dual Atmospheric Tracer Techniques for the Characterization of Pollutant Transport and Dispersion, Doctoral Thesis, California Institute of Technology, Pasadena, CA 91125.
8. McRae G. J., Goodin W. R. and Seinfeld J. H. (1982), EQL Report Number 8, California Institute of Technology, Environmental Air Quality Laboratory.
9. Neiburger M. (1955), "Tracer Tests of the Accuracy of Trajectories Computed from the Observed Winds in the Los Angeles Area," Air Pollution Foundation,.
10. SCAQMD (1977), "California South Coast Air Basin Hourly Wind Flow Patterns," South Coast Air Quality Management District, El Monte, CA.
11. SCAQMD (1987), "The Magnitude of Ambient Air Toxics Impacts from Existing Sources in the South Coast Air Basin," South Coast Air Quality

Management District, El Monte, CA.

12. Shair et al. (1982), "Transport and Dispersion of Airborne Pollutants Associated with the Land Breeze-Sea Breeze System," Atmospheric Environment, **16** (9), pp. 2043-2053.

13. Unger C. D. (1986), "Meteorological Factors Which Affect Pollution Concentration," Research Division Draft Report, California Air Resources Board, Sacramento, CA 95812.

2.4 Examination of Wind Field Dynamics Using Cross Differencing

Abstract

A new visualization technique for rapidly assessing the dynamics in the wind flow at a single location is presented. This method is useful for making comparisons of the horizontal wind speed and direction of one day with (1) another day at the same location, (2) an average day (monthly, seasonally, yearly, etc.) at the same location, (3) the same day at different locations, and (4) the same day at the same location where each set of data comes from different sources such as raw, smoothed, and computer generated. The technique highlights similarities in the dynamics of different days which might otherwise be overlooked when analyzed on the basis of static wind fields alone. It can also be used to compare (rapidly and concisely) the accuracy of results generated by numerical models with field data. The technique is implemented to show a single day's winds which were collected in 24 one hour averaging periods from wind reporting sites in Los Angeles. The method is used to quantitatively examine wind direction transitions at 31 sites in Los Angeles and its surroundings during the smog season from May through September 1988.

Introduction

The wind field dynamics can be as important as the static features of the flow in determining transport patterns and source-receptor relationships. While this may seem evident, methods for studying wind flow fields are firmly rooted in visualization techniques which emphasize static conditions. This stems primarily from the fact that surface wind data is commonly and easily visualized by means of a two-dimensional vector map, an example of which is shown in Figure 1. This method of presentation places its emphasis on describing what the state of the wind flow field is at a specific time at all positions in the region of interest.

At least one additional step is required to go from the static vector map to the dynamics of the wind flow field. For many investigators, this additional step may not be an attractive option. For instance, a cumbersome option is the manual examination of a time series of vector maps such as those in California Surface Wind Climatology generated by the California Air Resources Board, (CARB,1984). However, where computing resources are available, it is common to plot air-parcel trajectories by advancing the parcel in accordance with a set of interpolation rules in position and time. This approach is instructive when considering the fate of a given parcel of air, but precludes the possibility of examining the dynamics at a specific location in the wind field. An additional problem with using trajectories is the steady accumulation of errors in position along the trajectory at each time step. These are only mitigated when the flow field is known to a high spatial and temporal resolution. Animation of the maps is very demonstrative, but it directly translates into the need for more sophisticated computer equipment.

However, an alternative method for visualizing wind dynamics exists which is derived directly from the time dependent variations in the flow. The technique is based on computing a signed difference between a given time series and a reference time series between all hours, and at a single location in the flow

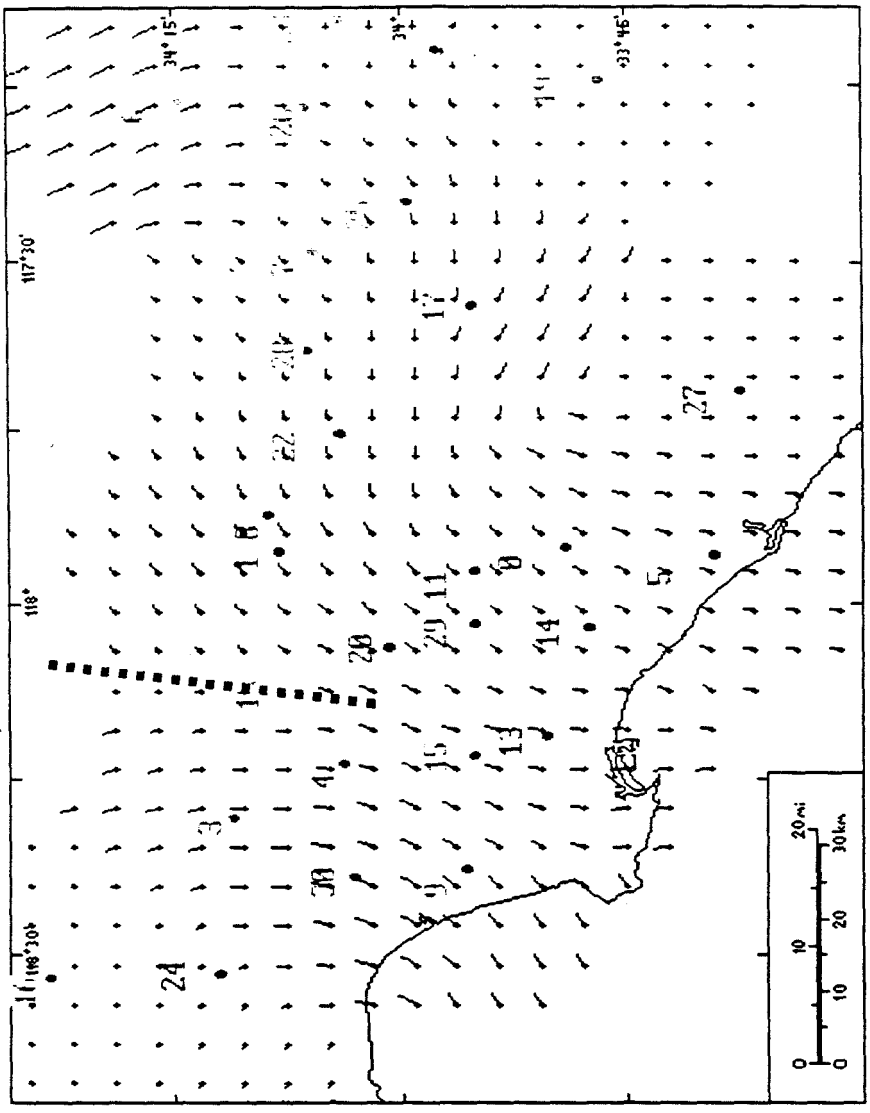

Figure 1. Hourly averaged wind vectors for the 1988 composite average day during the smog season at 8:00 a.m. Vectors are shown 5 km apart, their length proportional to the wind speed, and their direction away from their origin is the direction of flow. The bold dashed line through Pasadena (site 18) and east of downtown LA (site 4) shows the location of the divergence zone at this time.

field. The two types of times series which are considered are wind speed and direction. Graphically displaying the two-dimensional array which is created provides a geometrical way to quickly interpret the wind dynamics at that single location. From here on, this technique will be referred to as cross differencing. Cross differencing has the advantage that the location being examined can be a place where data is actually being taken, thus minimizing errors to those which correspond to the data acquisition methods. Cross differencing requires minimal calculation and can be implemented in any number of ways using general purpose computer equipment which is likely to be available, such as a PC or a workstation. The details of performing and displaying results from a cross differencing are the subject of the first part of this paper.

The second part of this paper focuses on using the cross differencing method to study the average smog season dynamics of 31 sites in the Los Angeles Basin, including the San Fernando Valley and the eastern desert in locations as distant from the coastline as Palm Springs. A detailed study of downtown Los Angeles' dynamics is required to clarify the complex interaction between emissions released during the morning rush hour and the timing of sharp wind direction changes that generally occur during the summertime morning hours and at some sites in the afternoon and evening. Such sharp directional changes are attributed to the interactions between the macroscale synoptic scale pressure differences which result from the earth's spin and differential heating of the earth's surface and mesoscale phenomena due to local geography and energy transport. The mesoscale phenomena include the well-studied land breeze-sea breeze system, e.g., Defant (1951), Scorer (1978), Shair (1982), the mountain valley system e.g., Schroeder (1960), and Blumen (1984), slope wind e.g., Banta (1981), Doran (1983), Horrell (1987, 1990), Kondo (1988), and the less well-studied convergence and divergence zones Edinger (1959) and Horrell (1990). These mesoscale systems are a persistent feature in the coastal regions of California and exhibit

considerable influence over the wind flows during certain times of the day. This is due in part to the orientation and close proximity of the coastal mountain ranges to the ocean.

The third portion of this paper focuses on identifying the unique features of the surface flow at three locations in the basin (Downtown Los Angeles, Burbank, and Upland) on two days of the 1987 Southern California Air Quality Study (July 15, and September 3). These were days on which the authors released sulfur hexafluoride tracer. The two sulfur hexafluoride tracer experiments performed from the downtown area (Horrell 1989) provided quantitative evidence on how the low speed morning transition winds disperse and route rush hour emissions from this release site out of the basin. The results from these two experiments provide supporting evidence for the theory that the time when the daily flow field establishes itself in the downtown area is as important as the specific features of the wind field in determining source-receptor relationships on certain days. The reason for studying the detailed dynamics of downtown Los Angeles, Burbank, and Upland is to further validate this theory and refine current understanding of the mechanism by which transport and dispersion occur within this area of the basin.

Method

Prior to mathematically describing the cross differencing technique, a simple intuitive discussion of the method is provided. The starting point is a time series, having 24 elements, each element representing the one hour averaged wind speed or direction at every hour of the day. A second time series having the same number of elements as the first is used as a reference. The question is how do these two time series compare to one another on the basis of shifts in time, the difference in magnitudes of individual elements at identical times, and the similarity of elements at different times. A simple method to establish the answers to all these questions simultaneously is to subtract one element of the first time series from each element of the reference time series. Thus, from two time series a two-dimensional array is created, in which each element is the difference described above. The diagonal elements of the matrix are a measure of the difference between the two series at identical times, and the rest of the elements describe the difference between a single series element and all the other elements in the reference series. If one examines the matrix, regions of similarity have the lowest absolute magnitude, whereas regions of high absolute difference are dissimilar. The orientation of these regions of small and large difference provides information about the relative timing of particular features between the two series. Finally, to avoid the generally undesirable task of examining a matrix of numbers, a graphical technique is used to display the results. The rest of this section will be used to explain mathematically how to take the difference, normalize the differences for plotting, graphically present the results, and interpret various patterns in the plots. This combination of tasks is referred to as cross differencing.

Mathematical Description

Cross differencing is described mathematically by the following relationship.

$$\Delta V[q(t1),r(t_2)] \;=\; (Vq(t_1) \;\triangle\; Vr(t_2) \;=\; \frac{[Vq(t_1) - Vr(t_2)]}{\mathrm{Max}|\mathrm{V[q,r]}|}\Bigg|_{t_1=0\;\;t_2=0}^{t_1=n\;\;t_2=n} \tag{2.4.1}$$

Where $\Delta V[q(t_1),r(t_2)]$ is the n by n element cross difference matrix, $Vq(t_1)$ is the time series being compared, and $Vr(t_2)$ is the reference series. Cross differencing between two time series will be denoted by the operator $\triangle$, and will be written in the above format. The series being compared will always appear first (left of the operator) and the reference series will appear second (right of the operator). The index variables t_1 and t_2 will independently range from some initial time, generally $t_1 \;=\; t_2 \;= 0$ to some final time in distinct intervals of seconds, minutes, hours, etc. The largest absolute difference between any element in $V[q(t_1),r(t_2)]$ is denoted by

$$\mathrm{Max\ V[q,r]} \;=\; \mathrm{Max\ Vq(t_1) - Vr(t_2)}\Big|_{t_1=0\;\;t_2=0}^{t_1=n\;\;t_2=n}. \tag{2.4.2}$$

Normalizing the raw difference between series elements by the absolute maximum guarantees all elements of the cross difference are in the interval [-1,1]. This rescaling provides an invariant size range when presenting the data in graphical form.

Several other definitions are made which will be used later. The maximum diagonal difference for a pair of variables $Vq(t_1)$ and $Vr(t_2)$ is defined as:

$$\mathrm{DiaMax\ V[q,r]} \;=\; \mathrm{Max\,|Vq(t_1) - Vr(t_2)|}\Big|_{t_1=t_2=0}^{t_1=t_2=n} \tag{2.4.3}$$

Similarly, the average diagonal difference for a pair of variables $Vq(t_1)$ and $Vr(t_2)$ is defined as:

$$\overline{\mathrm{Dia\ V[q,r]}} \;=\; \sum_{t_1=t_2=0}^{t_1=t_2=n} \frac{\mathrm{Max\,|Vq(t_1) - Vr(t_2)|}}{n} \tag{2.4.4}$$

Cross differencing for hourly averaged data, for a single day, using wind speed S and angle from the north T takes on the following form:

$$(Sq\ \Delta\ Sr) = \frac{[Sq(t_1) - Sr(t_2)]}{\text{Max S[q,r]}} \quad \begin{matrix} t_1=23 & t_2=23 \\ t_1=0 & t_2=0 \end{matrix} \tag{2.4.5}$$

$$(Tq\ \Delta\ Tr) = \frac{[Tq(t_1) - Tr(t_2)]}{\text{Max T[q,r]}} \quad \begin{matrix} t_1=23 & t_2=23 \\ t_1=0 & t_2=0 \end{matrix} \tag{2.4.6}$$

Note that $(Sq\ \Delta\ Sr)$ and $(Tq\ \Delta\ Tr)$ are 24 by 24 matrices. For the examples which follow, it is assumed that the series consist of hourly averaged data. The averaging process was done forward in time such that the index $t_1 = 0$ signifies the average from midnight to 1 a.m. taken at one minute intervals, $t_1 = 1$ the average from 1 to 2 a.m., and so forth all the way up to $t_1 = 23$. The same holds true for t_2.

Two time constants are defined and will be used below. The first is the duration time constant, t_d. It is the length of time over which a series remains at a constant value. The second is the transient time constant, t_t. It is the length of time over which a series exhibits change and falls between two sub-series of constant value. Typically, every element of the wind speed and direction time series to be examined below can be assigned to a t_d or t_t sub-sequence of the main sequence. The cross diffferencing plots highlight the boundaries between the constant and transient sub-sequences.

Examples of Cross Differencing

At this point in the discussion, the best way to become familiar with cross differencing and the selection process for references relevant to a particular task is by example. The examples will build in complexity, starting with some very idealized conditions, and will end with more complex cases which are analogous to the real cases to be encountered further in this paper. The examples are designed to educate the reader about how to spot the salient features which occur in cross difference plots involving wind speed and direction. The features which are presented may help the reader to perceive the following relationships between series: when the series (1) are identical, (2) are the same at certain times, (3) are similar but shifted in time from one another, (4) are similar in dilated or compressed time, (5) consist of similar discrete regions of constant value and transients between them, and (6) the series have coinciding extrema.

It is necessary to keep in mind, while going through these examples, how a sensible choice of a reference is really the key to obtaining useful information. In particular, a sensible reference has the property of selectively highlighting the information being searched for in the comparison series. In this respect, cross differencing acts as a selective filter, and the examples will be referred to by the type of filtering which they perform. At the same time, the reference must be simple enough for the information which is highlighted to be identified.

Method of Data Presentation

Before proceeding, it should be noted that the graphs are presented in pairs; the left one is the speed cross difference and the right one the direction (angle) cross difference. The magnitude of each element of the cross difference array is displayed as a circle; the bigger the size of the element, the larger the size of the circle. There are six circle sizes, each one represents one sixth of the range between zero and one. Six is not a special number, but it was chosen because of graphical display constraints. Recall large array elements mean a big

difference exists between the two series elements being compared. Conversely, the small elements are regions of small difference. A very noteworthy observation within the following plots is the case where the diagonal contains small elements. This means the two sequences are the same. The method of plotting means the diagonal runs from the lower left corner of the axis to the upper right corner. More will be said about this below.

This method has several inherent advantages for graphically displaying the magnitude of each element. First, this type of plot conveys information clearly when limited only to black print and single color page reproduction. It is also possible to represent magnitude using a uniform sized region by varying the shade and/or color of the region. However, in this case it is currently difficult to have the color images published and, even supposing that they were, future reproduction of the pictures with conventional copying techniques leads to pictures with indiscernable shades. Finally, the graphical method has precedent in current literature. Analogs of this method are being used in the scientific literature in fields such as neurocomputing and electrical engineering to represent system states.

Opened and filled circles are used in the plots to denote the sign of the difference. For the plots presented herein, only the speeds are signed. The angle differences are given as an absolute value. Positive differences are denoted with black. Thus, the angle differences and the positive speed differences are all black. Negative values are denoted by white, which has a black rim to distinguish it from the background. (The key on each plot says blue, again a remnant of the computer screen image from which these pictures are taken.) Finally, the diagonal is denoted by a gray edge in speed plots and a solid gray image in angle plots. (On copying this may tend toward black, which presents no risk of information loss.)

In these plots, the axis is always oriented the same way with the reference series time along the abscissa and the comparison series along the ordinate. This

provides a simple rule for analyzing the series being compared. For a given hour m of the ordinate, one reads the plot horizontally along a line of circles. If the circle at a particular abscissa location n is large, then the comparison series differs from the reference series at the time found by vertically scanning down to the abscissa. Similarly, a small circle at (m,n) means the comparison series at time m is like the reference at time n. For the purpose of this paper, moving from left to right and down to up on the axis corresponds to going from early morning to late evening.

Visually, the method provides only relative information about the two data sets being compared. Thus, it is useful to display simultaneously absolute numbers along with the plots. In order to gauge the size of the largest circles, the maximum difference between any two elements in the matrix is displayed (as defined by Equation 2.4.2). This value is also a measure of the dynamic range for that variable. The maximum diagonal difference, Equation 2.4.3, and the average diagonal difference, Equation 2.4.4, are also displayed. These provide a measure of the difference between the two series. Each of these three numbers is reported below the plots.

Filtering for Constant Flow Speed and Direction

The first example, Figure 2, is a cross difference performed between two series which have uniform properties in time. Refer to Table 2a (wind speed) and 2b (wind direction) which show the numerical values for each of the examples. The simplest cross reference is a uniform data set with itself, in this case two wind speeds, ($S1 \triangle S1$). Similarly, a cross difference between two different but constant in time data sets produces a uniform but non-zero matrix; in this case it is two wind directions, ($T1 \triangle T2$). The results are shown on the right half of Figure 2. These two cases demonstrate the two extremes in the cross differencing

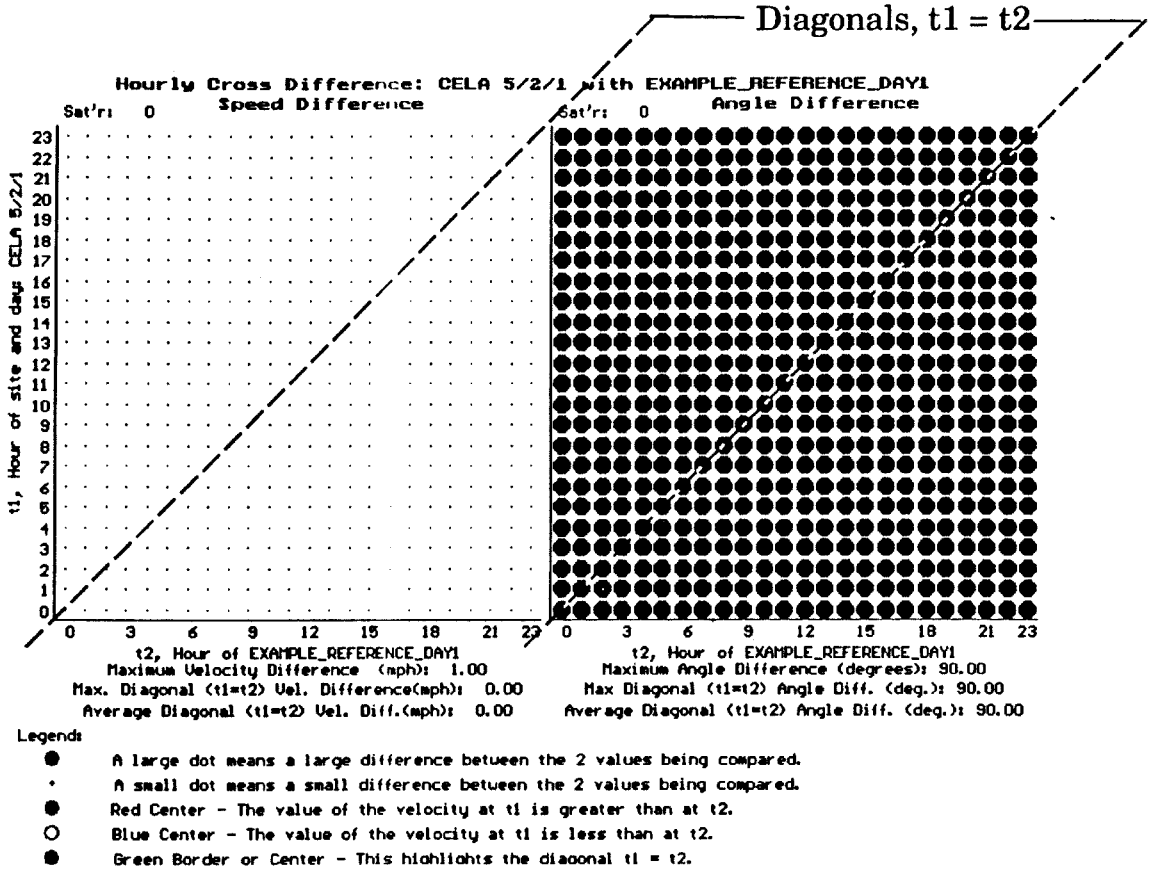

Figure 2. Cross differencing example 1, (left) speed: uniform for all 24 hours [S1 table 2] cross differenced with itself [S1 table 2] as a reference, (right) direction: uniform for all 24 hours at 180 degrees [T2 table 2] cross differenced with a uniform direction at 90 degrees [T1 table 2] at all 24 hours as a reference. (Note: CELA 5/2/1 is the label given to the comparison day consisting of speed S1 and direction T2. EXAMPLE_REFERENCE_DAY1 is speed S1 and direction T1.)

Station Number	Abbrev.	Station Name	Latitude	Longitude
0	ANAH	Anaheim	33.818	117.919
1	AZUS	Azusa	34.133	117.923
2	BANN	Banning	33.9	116.83
3	BURK	Burbank	34.184	118.304
4	CELA	Central LA	34.063	118.228
5	COST	Costa Mesa	33.652	117.929
6	CRES	Crestline	34.243	117.274
7	FONT	Fontana	34.096	117.491
8	GLEN	Glendora	34.186	117.936
9	HAWT	Hawthorne	33.926	118.376
10	HEME	Hemet	33.733	116.950
11	LAHB	La Habra	33.919	117.951
12	LANC	Lancaster	34.667	118.133
13	LGBH	Long Beach	33.837	118.205
14	LSAL	Los Alamitos	33.792	118.033
15	LYNN	Lynwood	33.917	118.215
16	NEWL	Newhall	34.388	118.533
17	NORC	Norco	33.921	117.570
18	PASA	Pasadena	34.132	118.126
19	PERI	Perris	33.778	117.244
20	PICO	Pico Rivera	34.013	118.059
21	PLSP	Palm Springs	33.8	116.60
22	POMA	Pomona	34.066	117.754
23	RDLD	Redlands	34.066	117.159
24	RESE	Reseda	34.199	118.528
25	RIVR	Riverside	33.993	117.418
26	SNBO	San Bernardino	34.104	117.283
27	TORO	El Toro	33.621	117.691
28	UPLA	Upland	34.103	117.634
29	WHIT	Whittier	33.918	118.026
30	WSLA	West LA	34.051	118.389

Table 1. Air Quality and Meteorological Reporting Stations

(a) SPEED [S]

Example: #	Site	Time: Hour 0	1	2	3	4	5	6	7	8	9	10	11
S1	CELA	7	7	7	7	7	7	7	7	7	7	7	7
S2	CELA	0	1	2	3	4	5	6	7	8	9	10	11
S3	CELA	0	1	2	3	4	5	6	7	8	9	10	11
S4	CELA	0	1	2	3	4	5	6	7	8	9	10	10
S5	CELA	0	2	4	6	8	10	12	10	8	6	4	2
S6	CELA	0	1	2	3	4	5	6	7	7	7	7	7
S7	CELA	4	5	6	7	8	9	10	11	12	11	10	9

#	Site	Hour 12	13	14	15	16	17	18	19	20	21	22	23
S1	CELA	7	7	7	7	7	7	7	7	7	7	7	7
S2	CELA	12	13	14	15	16	17	18	19	20	21	22	23
S3	CELA	12	11	10	9	8	7	6	5	4	3	2	1
S4	CELA	10	10	10	9	8	7	6	5	4	3	2	1
S5	CELA	1	1	1	1	1	1	1	1	1	1	1	0
S6	CELA	7	7	7	7	7	7	6	5	4	3	2	1
S7	CELA	8	7	6	5	4	3	2	1	1	1	1	1

(b) DIRECTION [T]

Example: #	Site	Time: Hour 0	1	2	3	4	5	6	7	8	9	10	11
T1	CELA	90	90	90	90	90	90	90	90	90	90	90	90
T2	CELA	180	180	180	180	180	180	180	180	180	180	180	180
T3	CELA	90	90	90	90	90	90	90	90	90	90	90	90
T4	CELA	90	90	90	90	90	90	90	90	180	180	180	180
T5	CELA	90	90	90	90	90	180	180	180	180	180	180	180
T6	CELA	90	90	90	90	90	90	90	90	90	90	90	180
T7	CELA	0	15	30	45	60	75	90	105	120	135	150	165
T8	CELA	90	90	90	90	90	90	105	120	160	180	180	180

#	Site	Hour 12	13	14	15	16	17	18	19	20	21	22	23
T1	CELA	90	90	90	90	90	90	90	90	90	90	90	90
T2	CELA	180	180	180	180	180	180	180	180	180	180	180	180
T3	CELA	180	180	180	180	180	180	180	180	180	180	180	180
T4	CELA	180	180	180	180	90	90	90	90	90	90	90	90
T5	CELA	180	90	90	90	90	90	90	90	90	90	90	90
T6	CELA	180	180	180	180	180	180	180	90	90	90	90	90
T7	CELA	180	195	210	225	240	255	270	285	300	315	330	345
T8	CELA	180	180	180	160	120	105	90	90	90	90	90	90

Table 2. Example 24 element sequences which are used to create a number of possible features in the cross differencing plots in Appendix A 2.4. Site CELA is simply a label; this data was created to provide idealized instances: (a) speed as hourly averages, in miles per hour and (b) direction as hourly averages, in degrees.

method. In the first case,

$$(S1 \triangle S1) = \begin{matrix} 0.0 & \ldots & 0.0 \\ \vdots & 0.0 & \vdots \\ 0.0 & \ldots & 0.0 \end{matrix}$$

wind speeds are identical at all hours, thus all elements of $(S1 \triangle S1)$ are 0.0. In the second case,

$$(T1 \triangle T2) = \begin{matrix} 1.0 & \ldots & 1.0 \\ \vdots & 1.0 & \vdots \\ 1.0 & \ldots & 1.0 \end{matrix}$$

wind directions are uniformly different at all hours, thus all elements of $(T1 \triangle T2)$ are 1.0. This says the directions between the two series are at a maximum difference at all hours.

Example 2, Figure 3, is an idealized, but realistic speed profile. (See Table 2a example number S3). Similar profiles are observed in regions with light nighttime winds and strenghtening wind flow observed until midday at which time it slowly diminishes. In this case, the flow ramps from 0 mph to 12 mph between midnight and noon then ramps down to zero from noon to the following midnight. For this example day, the direction changes are a very idealized version of the wind turning through all 360 degrees starting from the north at midnight and returning to the north on the following midnight, T7 of Table 2b. The example task is to show at what times the wind speed was at or near 7 mph, and at what times was the direction near 90 degrees. The natural reference for speed filtering is then the uniform 7 mph sequence, S1, and similarly for direction the uniform 90 degrees sequence, T1 is chosen. Figure 3 shows the results of $(S3 \triangle S1)$ and $(T7 \triangle T1)$. To find the times when series $S3$ was around 7 mph and series $T7$ was around 90 degrees, look for the regions of small circles on the plots. Because of the choice of filters, these are seen as horizontal regions centered at 7 and 17 hours for speed and centered at 6 hours for direction.

Further interpretation of the speed is possible by examining the diagonal. Starting at time 0, the diagonal is made up of opened circles indicating the wind

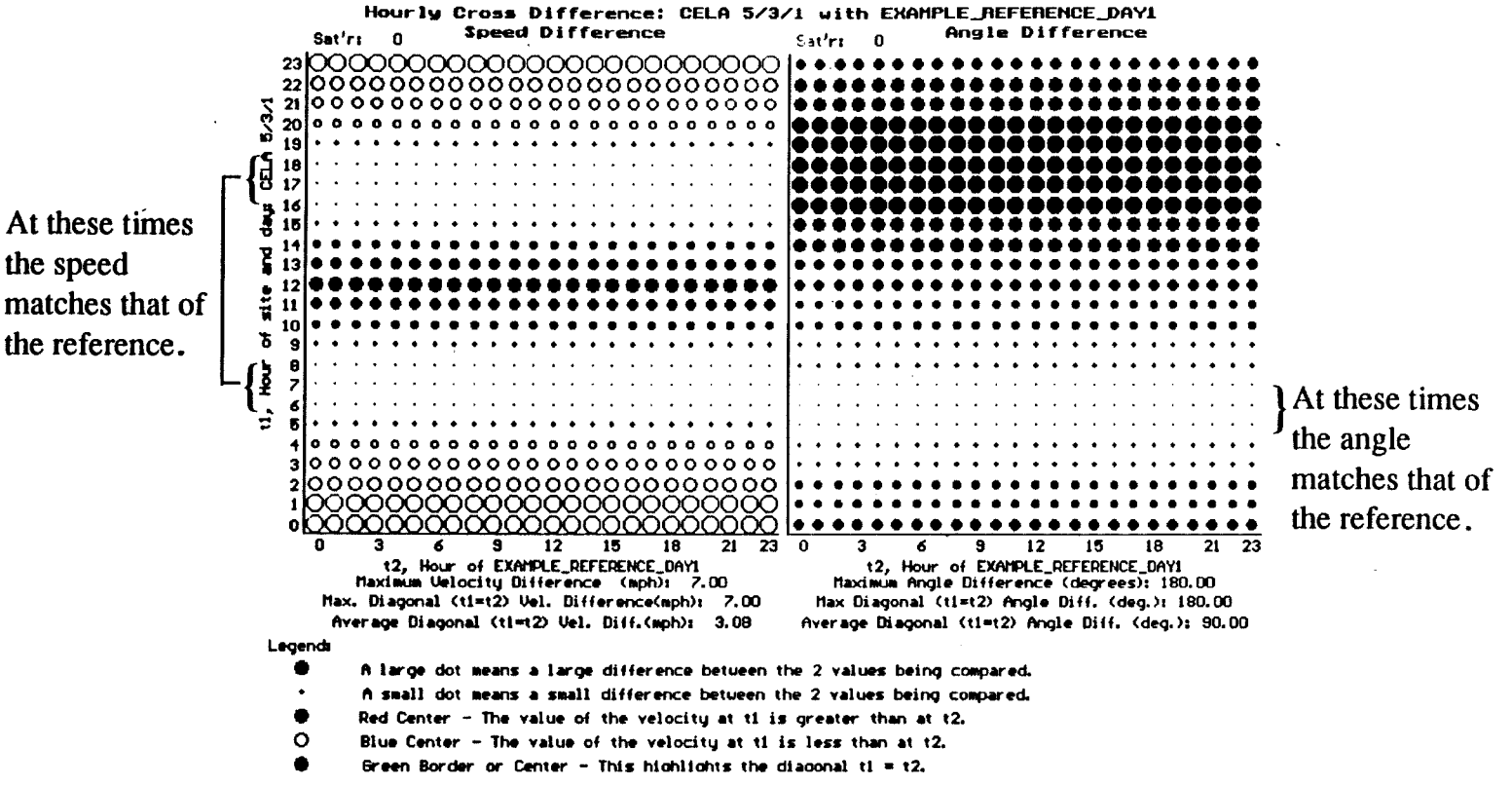

At these times the speed matches that of the reference.

At these times the angle matches that of the reference.

Figure 3. Cross differencing example 2, (left) speed: ramps from 0 mph at hour 0 to 12 mph at hour 12 then back down to 0 mph at hour 23 [S3 table 2] cross differenced with a uniform speed of 7 mph [S1 table2] as a reference, (right) direction: starts at 0 degrees at hour 0 and increases by 15 degrees at each hour to 345 degrees at hour 23 [T7 table 2] cross differenced with a uniform direction of 90 degrees [T1 table 2] at all 24 hours as a reference. (Note: CELA 5/3/1 is the label given to the comparison day consisting of speed S3 and direction T7. EXAMPLE_REFERENCE_DAY1 is speed S1 and direction T1.)

speed of S3 is smaller than the reference $S1$. These opened circles become smaller and pass through a minimum around a time of 7 hours. Between 7 hours and 17 hours, $S3$ is greater than $S1$, passing through a maximum difference at a time of 12 hours, as seen by the filled gray circles. As the wind speed on day $S3$ diminishes, it again passes through a minimum difference and becomes less than $S1$ in the hours from 19 to 23. A similar description of the direction diagonal places the maximum angular difference between $T7$ and $T1$ at around a time of 18 hours.

Time Shifts and Time Dilation and Compression using Diagonal Symmetry and Asymmetry

Until now, only comparisons between a dynamic series and uniform or static series have been made. The real power of this method lies in comparing two dynamic series. In particular, it will be seen that the method works very well when comparing two series which are likely to be similar because they are of similar origins. The similarity of wind flows from day to day (i.e. 24 hour blocks) at a particular site provides an ideal set of series on which to do comparisons. For instance, comparing one day's flow at a site to that of the next day's is a perfectly reasonable endeavor to undertake using this method. Because the days are expected to be similar in their bulk features, the times when they are different is highlighted by the method. The examples presented below all involve comparing two similar series which differ in carefully orchestrated ways. By creating these idealized, but realistic examples, it is hoped that the reader will be able to develop the skills to interpret the real cases presented later in this paper.

Example 3 shown in Figure 4 is a comparison which highlights similarity. It depicts the dynamic series for wind speed and direction compared to themselves, $(S2 \triangle S2)$ and $(T3 \triangle T3)$. The resulting matrices have the distinct property of creating symmetric plots about the 45 degree diagonal line $t_1 = t_2$. When

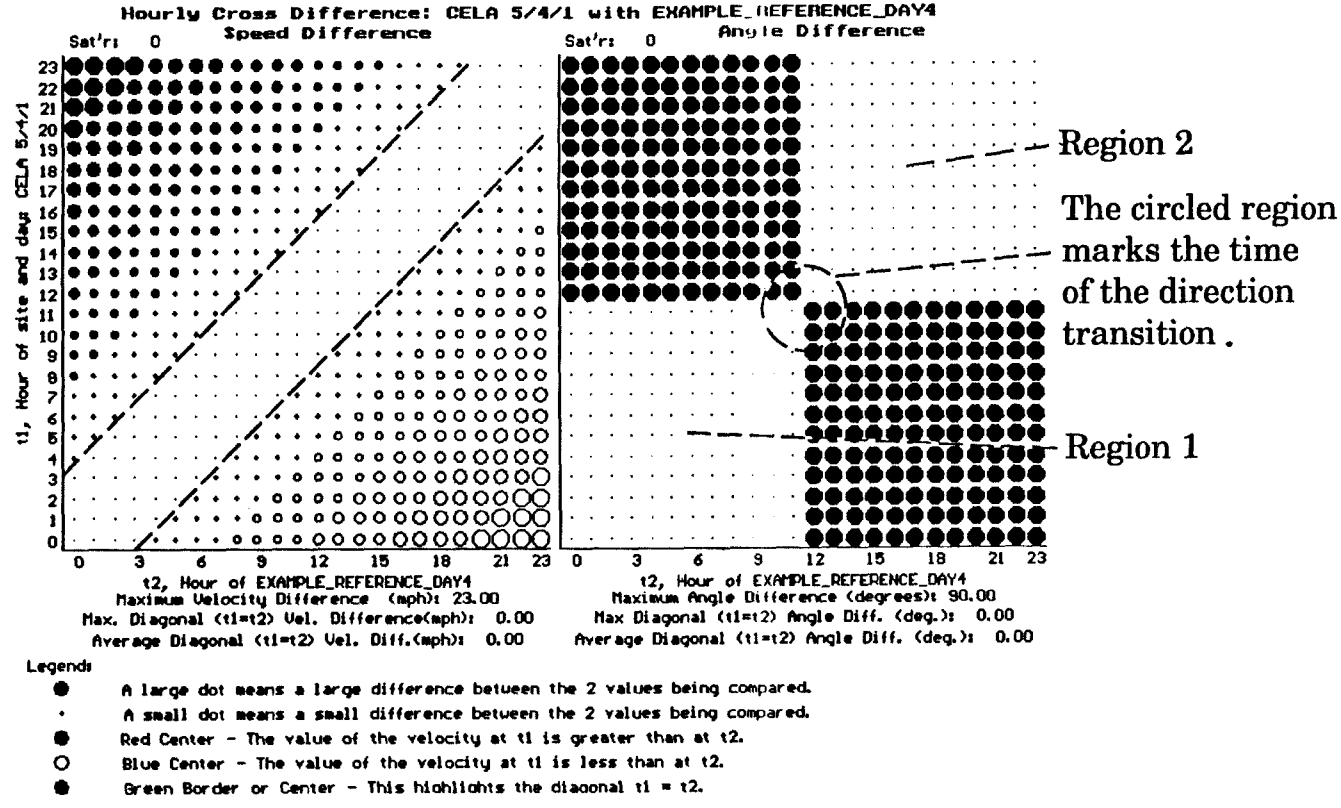

Dashed lines bound region of minimum difference.

Figure 4. Cross differencing example 3, (left) speed: ramps from 0 mph at hour 0 to 23 mph at hour 23 [S2 table 2] cross differenced with itself [S2 table 2] as a reference, (right) direction: uniform at 90 degrees from hour 0 to hour 11 then abruptly changes to 180 degrees at hour 12 then remains constant until hour 23 [T3 table 2] cross differenced with itself [T3 table 2] as a reference. (Note: CELA 5/4/1 is the label given to the comparison day consisting of speed S2 and direction T3. EXAMPLE_REFERENCE_DAY4 is speed S2 and direction T3.)

reflected across the diagonal, the circle sizes are the same, except the sign of the wind speed circles is different. This is seen as opened circles on one side and closed circles on the other. The diagonal of the wind speed plot is seen as a route of minimum difference, bounded in the plot by dashed lines.

It is constructive to consider the analogy which can be drawn between the cross difference plots of two dynamic series and an elevation contour map. To start the analogy, suppose each circle of the plot corresponds to a mountain peak. The size of each circle is proportional to the height of the mountain peak. Opened cirles are cold snow covered mountains corresponding to the cross difference being negative. Closed cirles are hot arid high desert mountains corresponding to the cross difference being positive. Groups of big circles are mountain ranges, whereas smaller circles at the edge of the mountains are foothills. Lines of small circles are valleys, and patches of small circles are low elevation basins. Edges between small circles and large circles are sharp cliffs. The reader, a potential user of this method, is like a pioneer who wishes to scout out the best path from the lower left corner to the upper right corner of the map. If the diagonal line from these corners is filled with mountainous obstacles, the user knows the two series being compared are dissimilar. However, a valley or basin along the diagonal means the series compare well for that range of times. Beneath each plot is a legend which tells the pioneer the height of the tallest mountain, the height of the tallest pass and the average elevation along the diagonal route in this section of map. Finally, the pioneer may discover there is a route which is not necessarily the diagonal route but has the lowest elevation in going from near the lower left corner to near the upper right corner. This route may cause the pioneer to travel extra distance, but this is offset the reduced travel time involved in taking the easier route. If such a route is found in the cross difference plot, it means the series are similar in elements but offset in time, or similar to one another in expanded or compressed time frames. When the pioneer encounters

a new map, the first step in the process would be to map out the low elevation route across the plot. In each of the remaining example cross difference plots, the reader should endeavor to map out this route of lowest elevation. Once found, the guidelines given below explain how to interpret the route in terms of the differences which exist between the series.

With the above analogy in mind, reexamine example 3. On the speed map, the pioneer is going to go right along the valley running along the diagonal since the minimum travel distance and minimum travel elevation are one and the same. This is equivalent to saying that the two series are exactly alike. The direction map would be traversed along the diagonal also, but it is worth noting the scenery which the pioneer would see. On entering the map at location (0,0), the pioneer would be in region 1, a flat basin with cliffs in the distance both to the right, left and front. Based on taking the shortest path alone, the pioneer would stick to the diagonal. At noon, the pioneer would pass through the very narrow gorge which joins regions 1 and 2 between locations (11,11) and (12,12). This narrow gorge corresponds to a sharp directional change in both series simultaneously. The pioneer would stick to the diagonal in region 2 based only on minimizing travel distance. Future examples will have valleys and narrow gorges off of the diagonal.

Example 4 which is an idealized version of a typical day at one of the Los Angeles Basin sites, $(S3 \triangle S3)$ and $(T4 \triangle T4)$ shown in Figure 5. The diagonal symmetry and a minimum valley along the diagonal are again characteristics of both the wind speed and direction plots. Both of these plots have distinct characteristics which appear in the real plots, though the features have been accentuated to make reading them unambiguous. The distinct fingerprint of the speed pattern for this day is the large X made up of two intersecting lines of small circles (see annotations on the figure). The intersection point of these two lines is either a maximum or minimum. For this day, this point is a maximum,

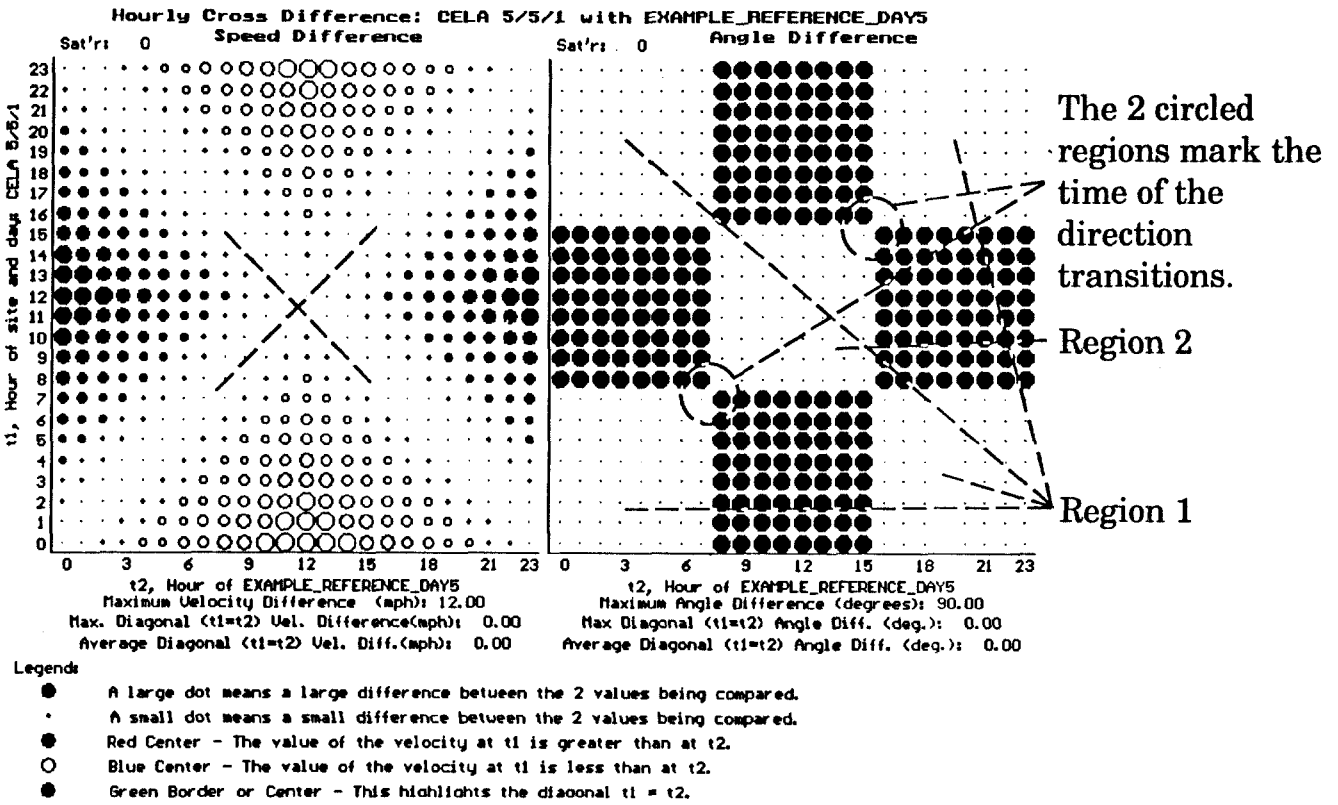

Dashed "X" marks the time when the velocity is at a maximum.

The 2 circled regions mark the time of the direction transitions.

Region 2

Region 1

Figure 5. Cross differencing example 4, (left) speed: ramps from 0 mph at hour 0 to 12 mph at hour 12 then back down to 0 mph at hour 23 [S3 table 2] cross differenced with itself [S3 table 2] as a reference, (right) direction: uniform at 90 degrees from hour 0 to hour 7 then abruptly changes to 180 degrees from hour 8 to hour 15 at which time the direction returns to 90 degrees from hour 16 to hour 23 [T4 table 2] cross differenced with itself [T4 table 2] as a reference. (Note: CELA 5/5/1 is the label given to the comparison day consisting of speed S3 and direction T4. EXAMPLE_REFERENCE_DAY5 is speed S3 and direction T4.)

which can be reasoned out by noting the relationship between the positive and negative circles elsewhere on the plot relative to the X. A common variation of the X pattern is seen by jumping ahead to example 6, Figure 7. The variation arises from the comparison day's speed either being smaller or exceeding the maximum speed of the reference day, but otherwise the two speed series are identical. This leads to a separated X; the point of separation is seen by the annotations on the wind speed plot of Figure 7.

The direction pattern of example 4 also has a distinct fingerprint which commonly appears. This is the checker-board pattern, characteristic of two sharp direction changes. In this case annotations mark the sharp changes occurring between 7 and 8 (am) and between 15 and 16 (or 3 and 4 p.m.). Pairs of sharp direction changes (especially one pair) are commonly observed in cross difference plots from actual applications. This observation has a simple physical explanation resulting from the persistent cyclic nature of the diurnal wind flows being considered. If the angle changes on average, it must on average change back to its original position. If a strong angle change occurs once, it is likely that some geographical feature at the site or in its surroundings is creating cause for the change. Consequently, a sharp change back to the first direction is often observed to maintain the true cyclic nature of the wind patterns.

Time series which are similar to one another in element size and order, but are shifted in time, have a different 45 degree symmetry line $t_1 = t_2 + n$ where n is plus (the comparison series lags the reference series in time) or minus (the comparion series leads the reference). To demonstrate a series leading the reference, the speed time series $S3$ is shifted four hours ahead in time to make $S7$ and the direction time series $T4$ is shifted three hours ahead to make $S5$. In example 5, the two new series are cross differenced with the series from which they were derived as $(S7 \triangle S3)$ and $(T5 \triangle T4)$ and are shown in Figure 6. The characteristic X marking the wind speed maximum has moved down four hours,

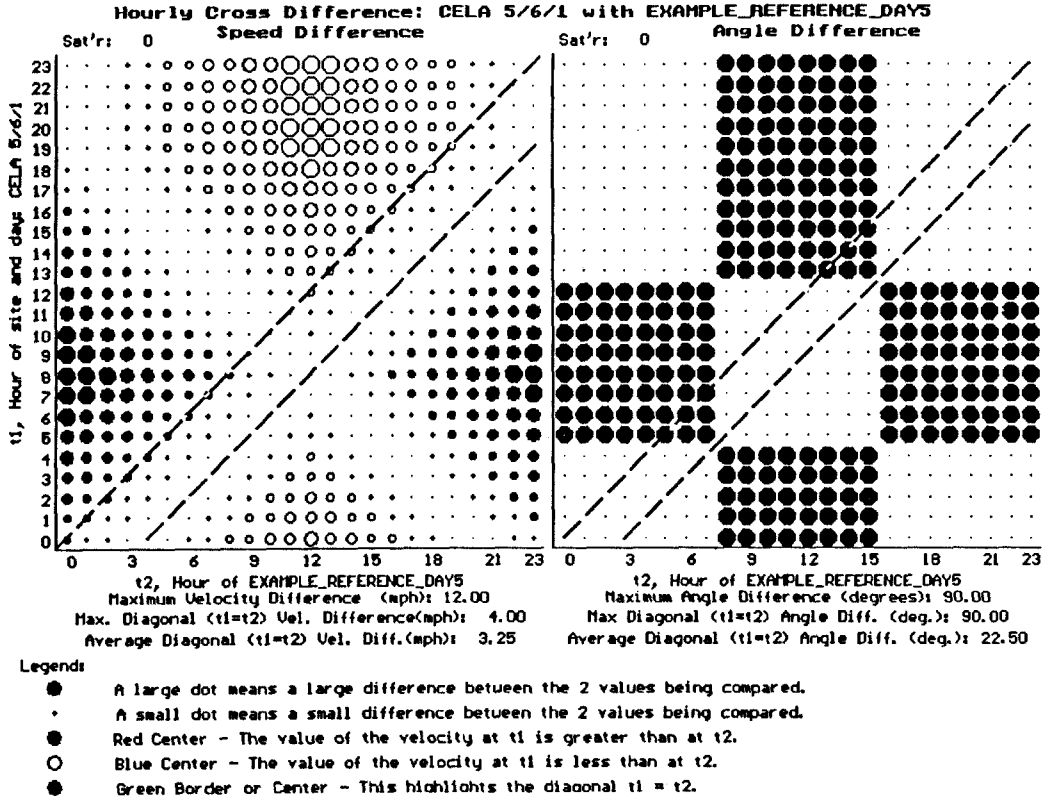

Dashed lines are the diagonal and the minimum difference. Speed is a 4 hour time shift, direction is a 3 hour shift.

Figure 6. Cross differencing example 5, (left) speed: ramps from 4 mph to 12 mph from hour 0 to hour 8 then back down to 1 mph at hour 19 [S7 table 2] cross differenced with a similar ramp starting at 0 mph and reaching a maximum of 12 mph at hour 12 [S3 table 2] as a reference, (right) direction: 2 transitions occur 3 hours earlier [T5 table 2] than the reference [T4 table 2]. Both the speed and direction examples demonstrate how a time shift looks. (Note: CELA 5/6/1 is the label given to the comparison day consisting of speed S7 and direction T5. EXAMPLE_REFERENCE_DAY5 is speed S3 and direction T4.)

The circled region shows the times when the comparision day has speeds lower than the reference day.

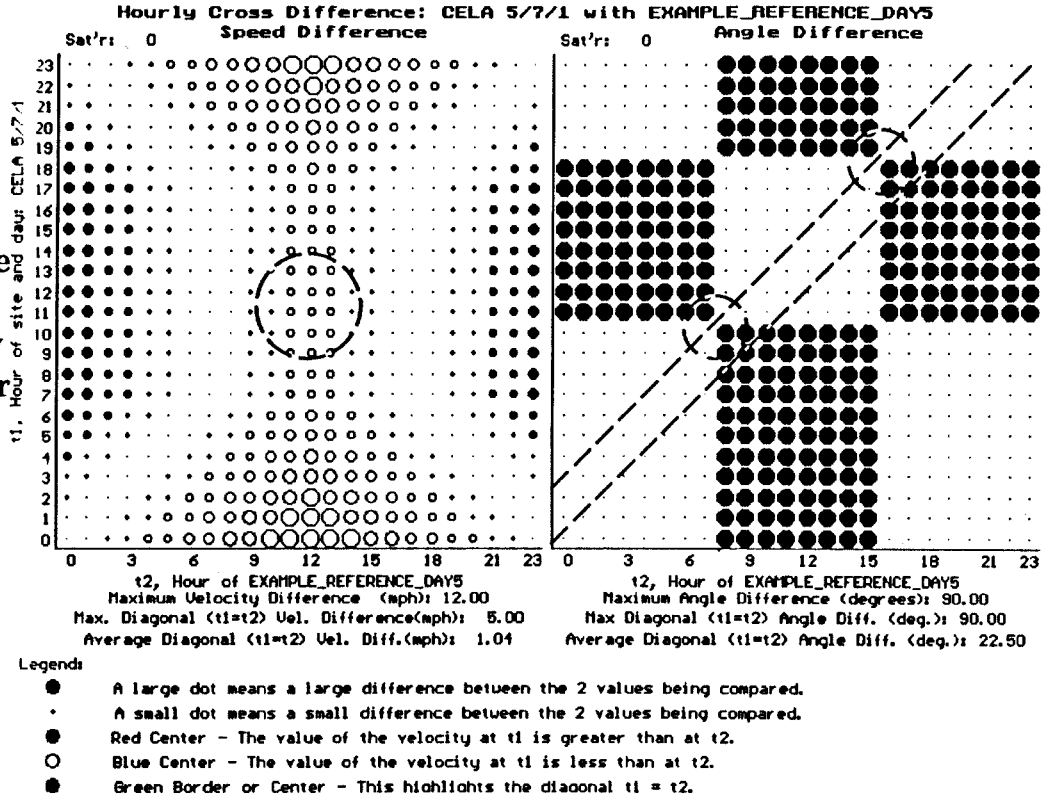

The 2 circled regions mark the time of the delayed direction transitions.

Figure 7. Cross differencing example 6, (left) speed: ramps from 0 mph at hour 0 to 7mph at hour 7 remains at 7 mph until hour 17 and then ramps back down to 1 mph by hour 23 [S6 table 2] cross differenced with with speed ramping from 0 to 12 mph from hour 0 to hour 12 then back to 1 mph by hour 23 [S3 table 2] as a reference, (right) direction: 2 transitions occur 3 hours later [T6 table 2] than the reference [T4 table 2]. This speed example is commonly observed when an average day is compared to a single day. (Note: CELA 5/7/1 is the label given to the comparison day consisting of speed S6 and direction T6. EXAMPLE_REFERENCE DAY5 is speed S3 and direction T4.)

placing it at 8 a.m., while the checker board pattern of the wind direction is shifted three hours the same way. The wind direction difference plot on the right side of Figure 5, example 6, is a case of the comparison series lagging the reference by three hours. A simple rule to follow is this: when a minimum valley in a plot is observed to the right of $t_1 = t_2$, the events of the comparison series happened earlier in the day than in the reference. A similar shift to the left in a minimum valley means the events happened later.

The comparison of a time series which is a time dilation or compression of the reference series shows a symmetry line $t_1 = Nt_2$ where N is a positive fraction less than unity for time dilation and N is greater than unity for a time compression. In example 7, the wind speed $S3$ was exaggeratedly compressed into half its normal period ($N = 2$) to give $S5$ then ($S5 \triangle S3$) was done and shown on left half of Figure 8. Notice the X has been compressed, and the line of symmetry has been changed to an angle of 22.5 degrees. A time dilation would give angles greater than 45 degrees.

Obtaining Time Constants of Change from the Plots

Cross differencing is useful in identifying characteristic times associated with wind speeds and wind directions. The two times which are relevant to the investigations made later in this paper are as follows: (1) the length of time a series remains at a (nearly) constant value t_d and (2) the length of time it takes a series to change from one constant value to another t_t. When analyzing a time series pair of wind speed and direction, two questions can be quickly answered by examining the cross difference plot: (1) what is the duration of time with like wind speeds and/or like directions, (2) what length of time is required for a particular directional change? This information is contained in all of the examples Figures 2 - 8 and will be discussed in terms of the vertical width rule.

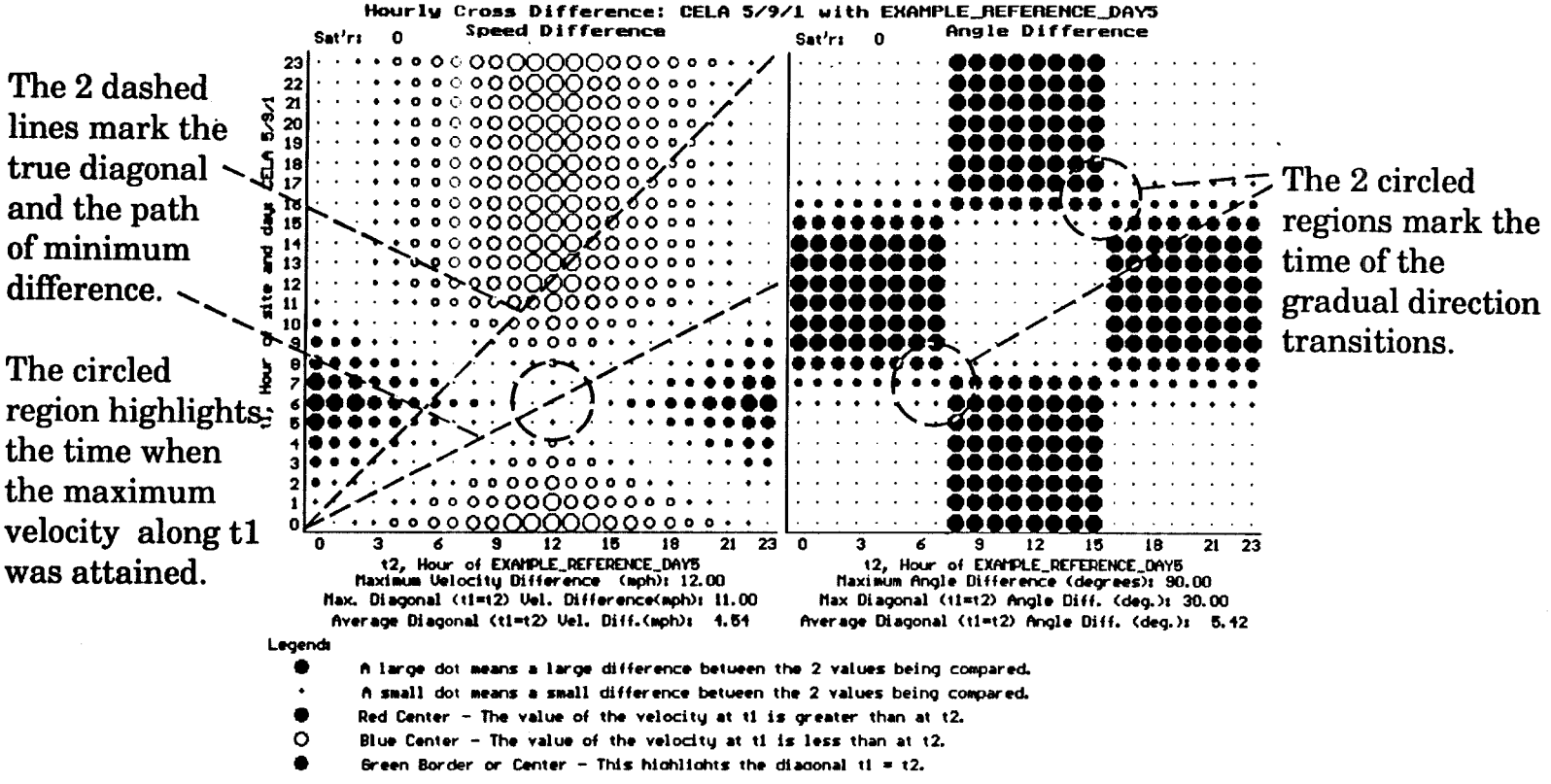

Figure 8. Cross differencing example 7, (left) speed: ramps from 0 mph to 12 mph from hour 0 to hour 6 then ramps back down to 0 mph by hour 12 and stays there until hour 23 [S5 table 2] cross differenced with the same ramp occuring over twice the time [S3 table 2] as a reference, (right) direction: 2 gradual transitions occuring over a period of 3 hours [T8 table 2] cross differenced with the identical transitions occuring over a single hour [T4 table 2] as a reference. (Note: CELA 5/9/1 is the label given to the comparison day consisting of speed S5 and direction T8. EXAMPLE_REFERENCE_DAY5 is speed S3 and direction T4.)

The Vertical Width Rule

The rule is this: to find the duration time constant, t_d, for an element of the comparison series, count the number of like vertical circles which are in a contiguous strand with the element in question. The duration time constant is the number of circles counted (in hours for the series being looked at herein).

A corollary is as follows: to find the t_d for an element of the reference series, count the number of like horizontal circles which are contiguous with the element in question.

The rule also applies to finding the transient time constant, t_t, for an element of the comparison (or reference) series, except that instead of counting like circles around an element, contiguous strands of monotonically increasing or decreasing sized elements are counted. Such strands of changing circles are looked for between strands of uniform circles. Categorically, every element falls into one or the other type of strand.

This rule will be used to answer the above two questions. First, to answer the question of how long the speed remains relatively constant, consult the speed plot of Figure 5 for an example. From any element along the diagonal $t1 = t2$, count the number of the smallest circles up and down from it; in this case there are 3 or 5 depending on which diagonal element. Stop when the circle changes size. At a glance, one knows that the wind speed at any time during the day is within one circle size (one sixth) of the maximum speed difference of 12 mph, or 2 mph of its neighbor's wind speed. Depending on which diagonal element was chosen, this is between 3 and 5 hours. An equivalent procedure is used to determine the duration of constant angle difference. (See the annotations made on Figure 5.) The annotations designate two regions in the plots. Region 1 covers a time period of 16 continuous hours for both the comparison and reference series. It appears as four pieces, but by using the plot itself one can infer that the four regions must all be the same direction. Region 2 covers a time period of eight

hours.

To determine the period of time over which a particular directional change occurs, the second issue in question, examples will be used. Locate the directional change in Figure 5 between 7 and 8 a.m.. Do this by going to the diagonal at hour 8, now step back to hour 7 vertically. Notice that the circle size changes full scale. Remember each change in circle size represents a 16.7 percent increment on the maximum observed difference scale. For the above example, the change is from smallest to largest in one step. This means 100 percent of the maximum observed direction change for this comparison is observed across the hours from 7 to 8. Noted below the plot is Max's value of 90 degrees. Then, for this case, $t_t \leq 1$ hour and a 90 degree change occurs over this time. In the case of a gradual angle change, the circles would grow larger gradually when moving downward in the vertical direction. Under such conditions, the sharp checkerboard pattern of the entire plot has usually been replaced by one with less pronounced edges. In these cases, $t_t \geq 1$ hour. An example of this is shown in the angle difference of Figure 8, $(T8 \triangle T4)$ where the directional change occurring between 5 and 8 a.m. gives $t_t = 4$ hours. To understand this, go to $(t_1 = 0, t_2 = 4)$ and move vertically along the small circles until they begin to get larger. Count the number of time steps where the circles increase. Stop when the circles become constant at the new large size. This is four hour steps.

Developing a Seasonal Average as a Reference

A reference for speed and direction cross differencing was created for each of the 31 wind reporting stations located in the Los Angeles Basin (Appendix A1.9). The reference was created by vector averaging the wind vectors for every day from May through September of 1988, at each hour and at each site. These results are reported in Section 1.9. The composite vector average was then converted back into the 31 speed and direction time series, 24 hours long, one pair of series for each site. The 1988 smog season wind data was chosen as the reference because it best satisfied a number of criteria which were desirable. Recapitulating from Appendix A1.9, the desired criteria are (1) the year was not exceptionally low or high, statistically, in observed levels of ozone, and (2) the year was as close in time to the year 1987 as possible (unfortunately, 1987 ozone levels were too low and therefore that year was rejected).

The persistent diurnal patterns at each site justify using a composite average series as a reference. Appendix A1.9 provides a detailed examination of the statistics of the day to day variation in the wind patterns at each site.

Two topological properties arise when using a seasonal average as the reference in a cross difference. The first relationship is that hour 0 and hour 23 are connected to one another in time. Conceptually, this is the equivalent of taking the plot and connecting columns 0 and 23 so that they are side by side to form a cylinder. The second relationship arises when both the reference and the comparison series are composed of averages. As described above, the sheet is first folded into a cylinder. Then the cylinder is connected by bending one end to meet the other, matching like times, into a torus. Practically, this means regions with similar sized circles are the same across the 23 to 0 hour boundary. This fact may be useful in interpreting the plots done for the section Individual Days Compared to Seasonal Averages below. When comparing a particular day to an average day, the cylinder topography is the rule to use. This applies to the

plots derived from one or two average days.

Results

Average Summertime Dynamics

The cross difference is computed for 31 sites in the Los Angeles Basin from the composite average 1988 smog season day at each site and compiled into Figures 12 - 27 in Appendix A2.4. From these plots, the following data is obtained at each site: (1) the average number of transition periods, (2) the average time the transition periods occur, (3) the average duration of transition periods, (4) the average angle change on transition, (5) the maximum angle difference between any two hours on the average day, and (6) the time of the extremum in the wind speed. Numbers (1), (2), (3), and (5) are reported in Table 3. (It is assumed that the reader having read to this point has enough skill to interpret the plots in Appendix A2.4.) In interpreting the plots, recall regions across the boundary from 23 to 0 hours of both the reference and comparison edges are topologically connected because both are average days.

The wind speed plots of an average day cross differenced with itself are straightforward to read and contain information that could be obtained by a simple time series plot, so only a brief mention of them will be made. On each day, a distinct extremum in the wind speed is seen via the characteristic X, which occurs atop of the time when the extremum is observed. In this respect, all of the sites are identical except that Palm Springs is at a minimum wind speed at midday, while the other 30 sites are approaching a maximum.

The angle difference plots for each site generally have more features than the wind speed plots and are able to provide a considerable amount of information about the average behavior of the summertime winds at that location in a way which is more difficult to convey in simple time series plots. Again, consult Figures 12 - 27 in Appendix A2.4. The cross differencing plots provide an excellent method for determining the length of time a site remains in both the macroscale and mesoscale systems. The method also provides a way to examine the struc-

Station Name	Angle Changes	Hour of Changes	Max. Degree Change	Transition Period in Hrs.
ANAH	1		72.8	3
AZUS	2	4-5,6-7	113.6	2
BANN	0		40.6	0
BURK	2	9-10,16-17	44.5	0
CELA	2	2-4,5-6	178.5	3
COST	2	2-3,6-7	96.2	4
CRES	3	5-6,10-11 20-21	76.3	5
FONT	2	2-3,6-7	179.5	4
GLEN	2	23-0,6-7	179.8	7
HAWT	2	3-4,6-7	87.5	4
HEME	1	6-7	107.6	1
LAHB	2	3-4,7-8	59.9	4
LANC	0		32	0
LGBH	0		156.8	0
LSAL	4	1-2,5-6 7-8,17-18	70.1	2
LYNN	2	4-5,10-11	57.0	6
NEWL	2	4-5,6-7	138.0	2
NORC	2	4-5,5-6	109.7	1
PASA	2	3-4,5-6	177.5	2
PERI	5	1-2,2-3, 4-5 10-11,20-21	167.5	4
PICO	2	2-3,7-8	53.7	4
PLSP	2	8-10,13-14	179	4
POMA	1	7-8	41.9	0
RDLD	2	6-7,22-23	179.9	7
RESE	3	6-7,17-18 20-21	177.3	2
RIVR	2	5-6,10-11	179.9	3
SNBO	2	5-6,7-8	71.0	2
TORO	2	7-10,20-22	142.1	7
UPLA	1	7-8	126.9	1
WHIT	2	3-4,6-7	179.2	3
WSLA	2	1-2,5-6	178.3	4

Table 3. Features of the Average Angle Difference Plots at 31 Sites

ture of the transition periods both on average and on specific days. The cross difference plots alone do not provide unique identification of the specific flow system category to which a site belongs. Thus, this chapter is complemented by the subject matter of Appendix A1.9 which discusses the specific types of flows exhibited by each of the 31 sites and the standard deviation of the wind speed and direction at each site and hour taken over the 151 1988 smog season days. Information presented in Section 2.3 may be helpful in understanding some aspects of the following results.

Qualitatively, each of the sites exhibit the same features. For instance, of the 31 sites 28 show at least two distinct flow regimes on a single day. Additionally, 3 of the 28 show more than two distinct flow regimes. For these 28 sites, 75 to 90 percent of the smog season day is spent in a single flow pattern. This period of a single pattern represents the macroscale flow regime. During the remaining 10 to 25 percent of the time, the site is in a transitional or mesoscale flow which is identified in the plots by a flow direction different from the macroscale. The ratio of the time spent in the macroscale flow versus the time spent in the mesoscale flow is a measure of the relative strengths of the two flows. Though there is no direct evidence to substantiate this hypothesis, the ratio is potentially an indicator of the probability of observing the mesoscale flow on any particular day.

The similarity between the different sites and the common features observed in many of the plots can be used to refine the conceptual model of the transition period. First, notice 20 sites on average have a pair of large angle changes separating a one to six hour period with a uniform flow direction. Second, the timing and duration of each of the transition periods is different for each site, with 19 out of 31 sites having a pair of direction changes between 0 and 12 a.m. Of the four sites with only one transition, the transition occurs between 6 and 8 a.m.

Though 22 out of 31 of the sites examined have an even number of pairs of wind direction changes, it is possible to observe an odd number of changes or no distinct angle changes at all. The sites which exhibited no change had one or both of the following characteristics: (1) it was surrounded by relatively level terrain or, (2) it was surrounded by highly channeling terrain. These environmental features create conditions which minimize mesoscale forcing, making it difficult to observe such effects even under conditions of very mild synoptic scale pressure forcing. Relatively flat terrain does not generate slope wind, and the absence of nearby mountains excludes mountain valley drainage winds. The flat terrain does not confine the wind to any one direction, making gradual directional changes possible. The presence of channeling terrain provides a guide for the wind and under normal conditions restricts the wind flow to the two directions parallel to the channel. Mild, but persistent synoptic scale pressure gradients which exist between the two air basins joined by a channel creates a steady uni-directional wind flow capable of suppressing mesoscale effects. Of the four stations exhibiting gradual or no change, three (ANAH, LANC, and LGBH) were surrounded by flat terrain. The fourth station was Banning (BANN) which is located in the valley channel (San Gorgonio Pass) linking the LA basin to Palm Springs. The six sites which exhibited an odd number of direction changes are accounted for by the explanation that a sharp change was paired with a gradual change which returned the wind to the original direction.

The definition of the term *transition period* is refined for sites in the Los Angeles Basin in light of the above findings. The transition period is actually the time between two generally sharp directional changes which surround the period when mesoscale effects dominate the local wind field. Because the winds during this period are light, often below 1.0 ms^{-1}, their importance to transport has usually been overlooked. However, when one realizes that these winds are light, but directionally not variable, they could be responsible for relocating emissions

on the order of 3 - 15 kilometers from the original release point during the 1 - 5 hours of a typical transition period. Finally, the dispersion which has usually been noted during these transition periods is probably attributable to the two sharp directional changes which bracket both ends, and not necessarily to variable winds occuring all during the transition period itself.

Individual Days Compared to Seasonal Averages: SCAQS 1987 SF_6 Tracer Days

To complement the conclusions drawn in previous chapters, the wind flow dynamics of the two summertime 1987 sulfur hexafluoride tracer studies done as part of the Southern California Air Quality Study are studied using the cross differencing technique. The dynamics of three sites were examined, including one near the release site (Downtown Los Angeles, CELA), a site in the northwestern basin where the tracer was observed (Burbank,BURK), and a site in the eastern desert (Upland, UPLA) where ozone was observed but tracer. These sites represent a source region (CELA) and two potential receptor sites (BURK,UPLA). The goal of this section is to provide additional evidence that the morning dynamics of the release site were largely responsible for the location of the late morning and afternoon observations of tracer in the basin. Six pairs of speed-direction cross differences were computed and put into Figures 9 - 11, the plots from the same site from July 15 and September 3 both being put on the same page. The cross differences were computed comparing the specific day to the average smog season day of 1988.

It is immediately evident from the plots for CELA, Figure 9, that the wind speed near the release site was below the seasonal average in the afternoon on both of the tracer days. At CELA, the maximum wind speed difference on July 15 was 5.9 mph below average at 4 p.m. The maximum wind speed on September 3 is 4 mph below average at 4 p.m. The standard deviation, σ, in the speed for this time at CELA based on the seasonal average for 1988 is 3.2 mph. Both days have values greater than the standard deviation. The angle difference on July 15 indicates the transition period began later and ended earlier than average. On September 3, there was no transition period at all. On both days, this indicates that there was little or no time between the surface flow pattern from the previous day and the onset of the flow on the tracer day. On the same days, the other

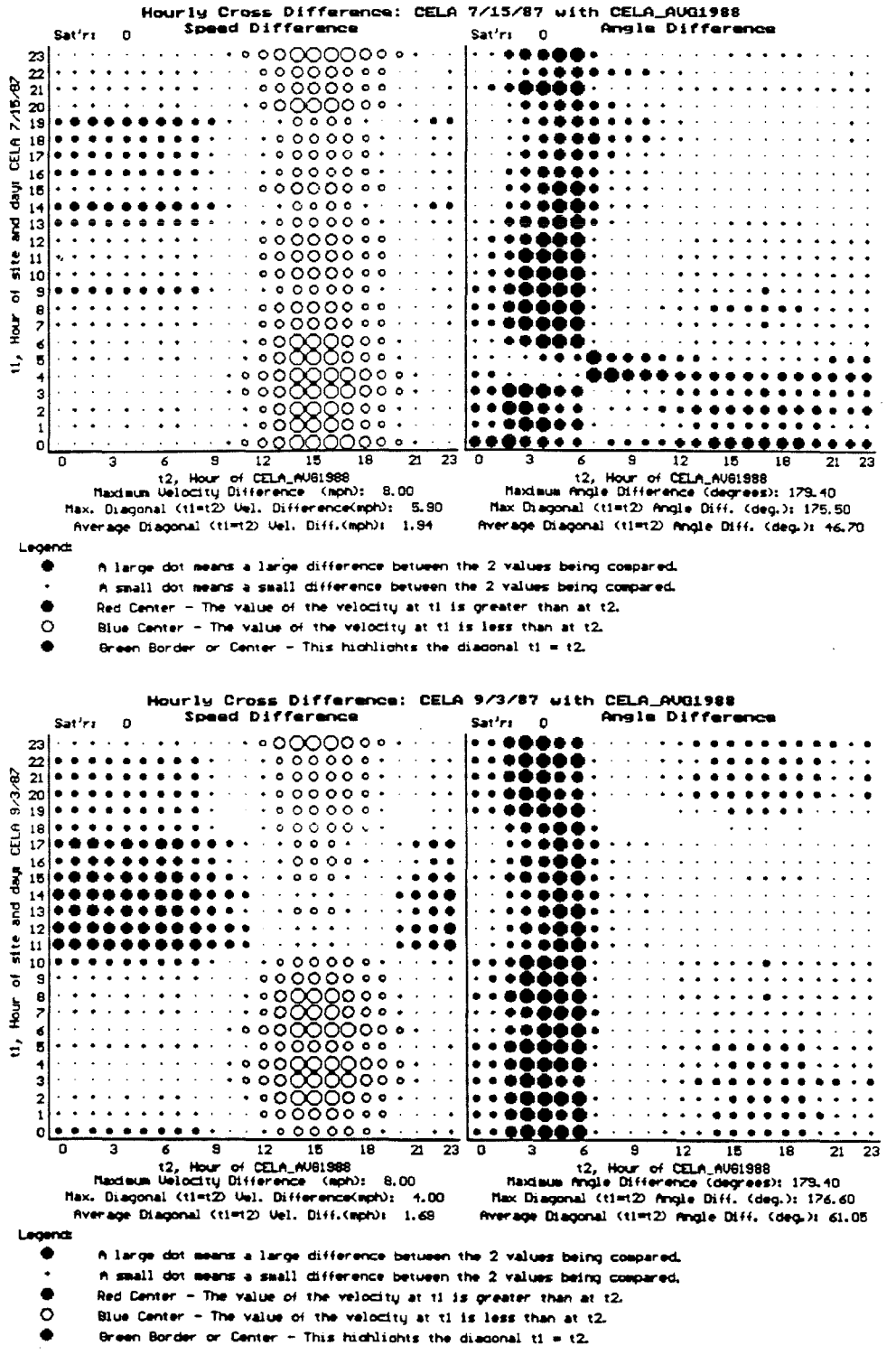

Figure 9. Speed and angle cross difference at Downtown LA (CELA) (top) July 15, 1987,(bottom) September 3, 1987. In both cases the reference for comparison is the average smog season day 1988 at CELA. Note the similarity between both days.

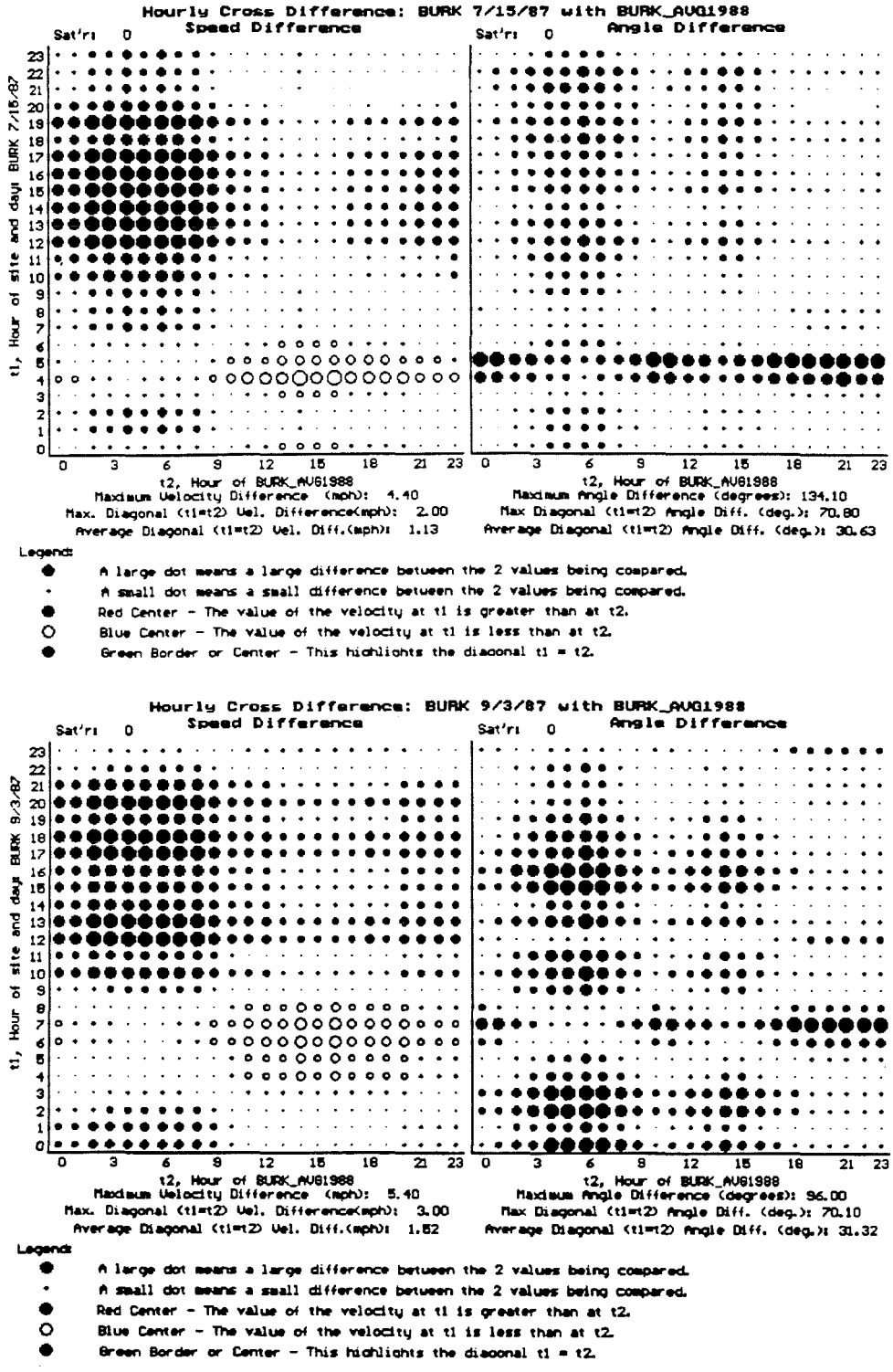

Figure 10. Speed and angle cross difference at Burbank (BURK) (top) July 15, 1987, (bottom) September 3, 1987. In both cases the reference for comparison is the average smog season day 1988 at BURK. Note the similarity between both days.

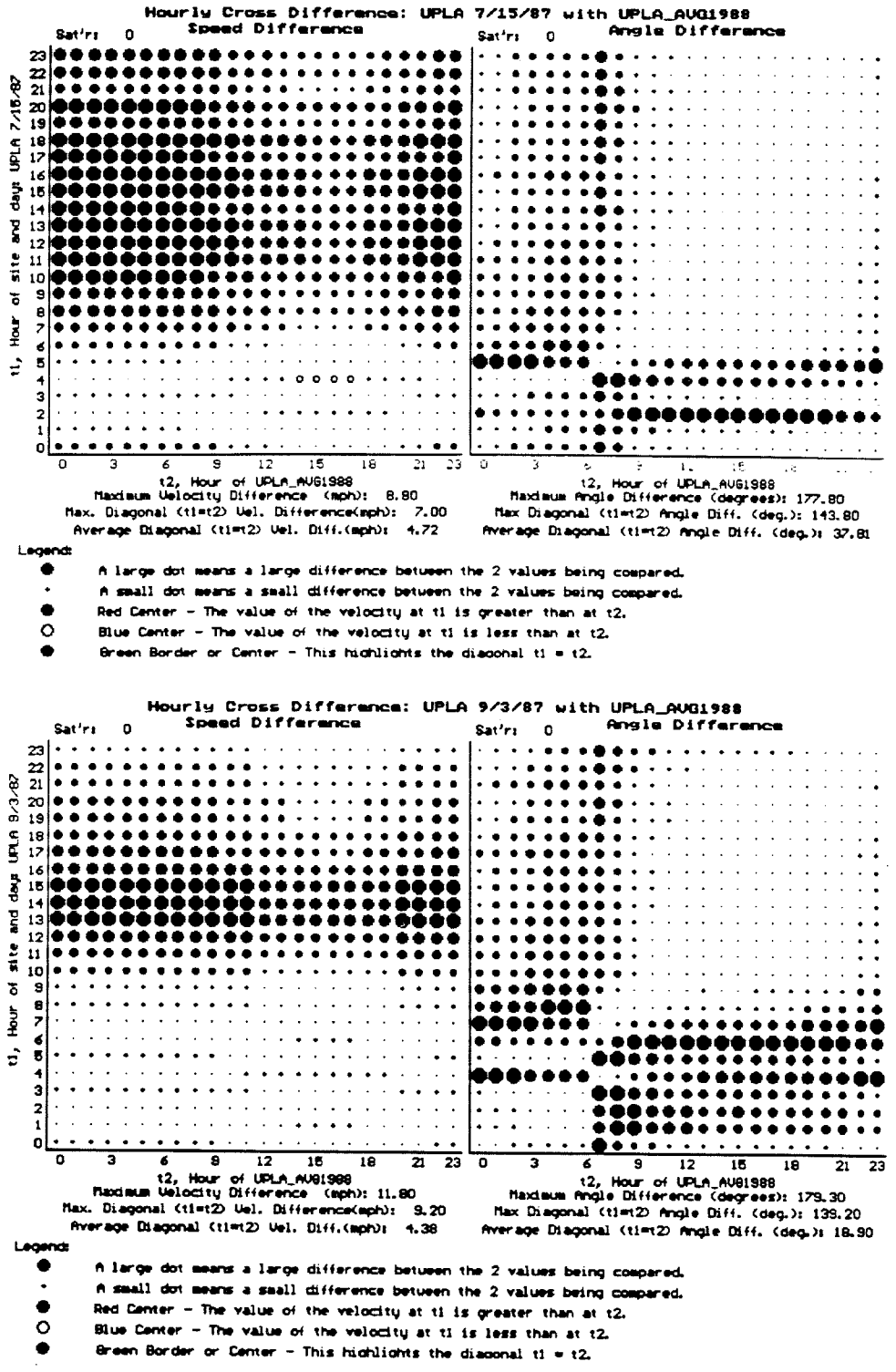

Figure 11. Speed and angle cross difference at Upland (UPLA) (top) July 15, 1987, (bottom) September 3, 1987. In both cases the reference for comparison is the average smog season day 1988 at UPLA. Note the similarity between both days.

two sites, Burbank (BURK, Figure 10) and Upland (UPLA, Figure 11), have wind speeds which are higher than the average. For BURK, maximum wind speed difference on July 15 was 2 mph (σ = 3.2) above average at 5 p.m. On September 3, the wind speed is 3 mph above average (σ = 2.6) at 6 p.m. For UPLA, maximum wind speed difference on July 15 was 7 mph (σ = 1.2) above average at 6 p.m. On September 3, the wind speed is 9.2 mph above average (σ = 1.3) at 3 p.m. The morning transition at Burbank is weak on July 15, and occurs two hours later than average on September 3. On the afternoon of both days, the angle plot does not exhibit the typical strong direction change. The directional change is seen in Figure 10 as the black region between hours 12 and 15 of the reference day, and extending roughly from hour 10 to hour 20 of the comparison days. The angle difference plot at Upland has a simple interpretation: on July 15, the morning transition period comes to an end two hours early; on September 3 the angle profile is a close match to the average day (with the exception of an abrupt 139 degree angle difference recorded at hour 4).

Taken collectively, the results from these three stations describe the following circumstances. The two major outlets from the basin are experiencing higher than normal outflow rates. Downtown Los Angeles, the branch point between the two outlets, is experiencing a strongly suppressed wind flow speed because of the sharper than average divergence which resides in the air space above this location. The consequence of this sharper than average divergence region is the creation of a sharp division between which emissions from the downtown area are routed out of each outlet. For the two tracer experiments, all of the tracer was routed via the route which passes by Burbank to the northeast of the release point. Less than one percent of the tracer was observed to head towards Upland or any other location in the eastern basin.

Conclusions

The Cross Differencing Method

1. The cross differencing method is easy to implement, requires commonly available computing hardware, and is fast to use once reading the plots is mastered.
2. The method has been successfully demonstrated using wind fields from both seasonal average days and individual days.
3. A natural application of the method, but one not examined in this paper, is the comparison of two wind fields for the same site. This approach is likely to be very useful in visually identifying times when numerical models succeed and fail at a particular location. Furthermore, the comparison of the results of different numerical models can be accomplished by this method.

Transition Periods in the Los Angeles Basin

1. The transition periods primarily have an effect on the morning rush hour. On average, strong direction change occurs within the morning rush hour at 27 of the 31 sites, while only 2 of the 31 sites (Burbank, Reseda) have direction changes during the evening rush hour.
2. On average, the transitions are characterized by two sharp directional changes; one occurring at the end of the previous day's wind flow and the other at the start of the new day's flow. The wind direction often changes on the order of 100 or more degrees on transition.
3. Transport during a one to five hour transition period may relocate emissions from between 3 - 15 kilometers from the source because of the directional nature of the flows during these periods.

SCAQS SF_6 Days

1. The two days examined show similar dynamics both near the downtown Los Angeles release site and at two sites situated near basin air flow exits. Both days had strongly suppressed wind speeds near the downtown area and higher than average speeds at the exits.

Accountability Modeling needs to accurately account for the timing of the transitions, and their flow direction and speed. Mesoscale effects are observed primarily after dark, and most commonly in the early morning hours.

A2.4 Appendix

Cross Difference Plots for Average Smog Season Days at 31 Sites in Los Angeles

The following 16 pages contain cross difference plots for the 31 sites listed in Table 1. Each plot is generated by performing the cross differencing method on the seasonal average for that site with itself. Certain observations which can be made from the plots are summarized in Table 2 and discussed within the text.

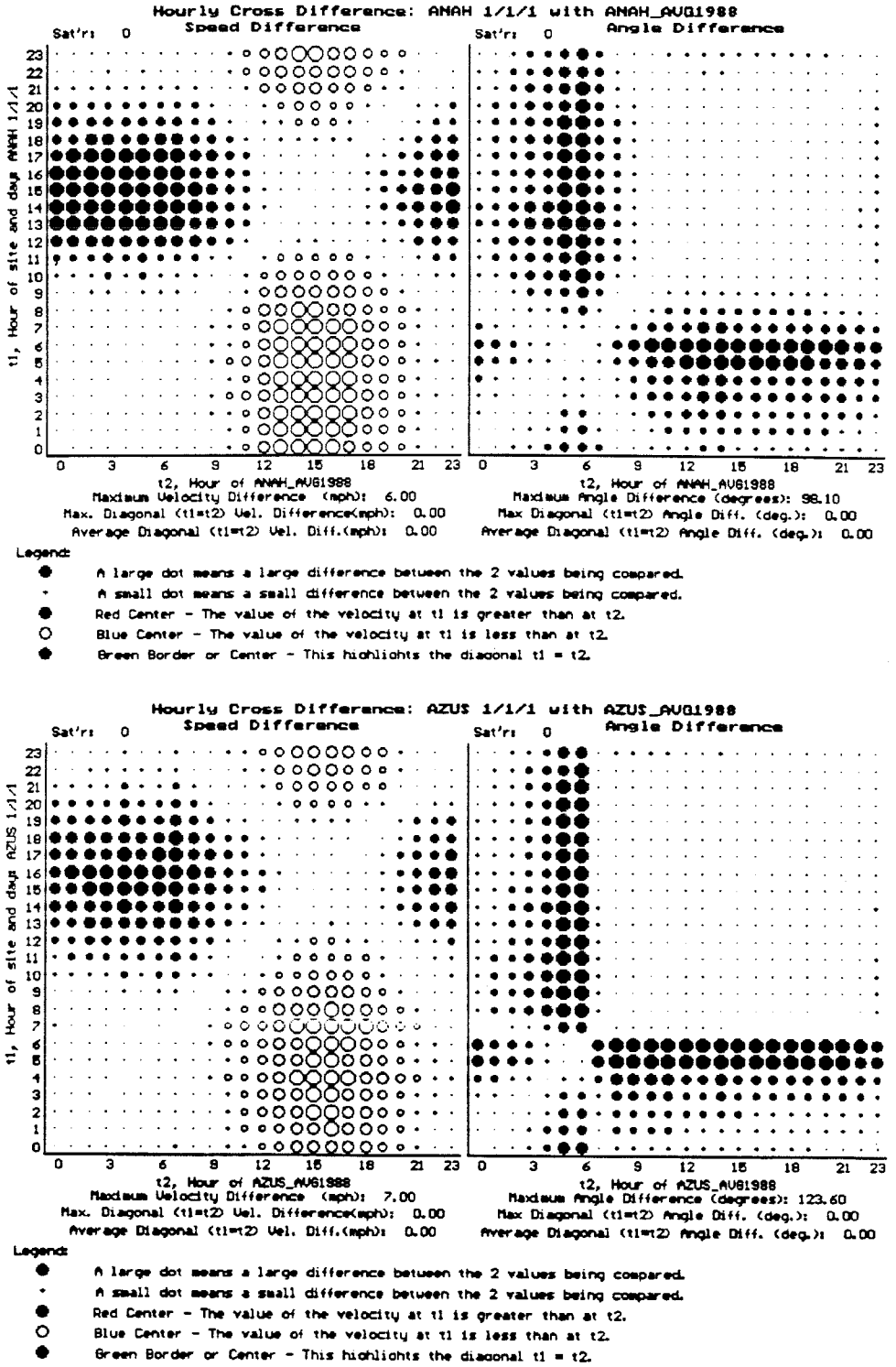

Figure 12. Speed and angle cross difference (top) Anaheim (ANAH) average smog season day 1988 compared to itself, (bottom) Azusa (AZUS) average smog season day 1988 compared to itself.

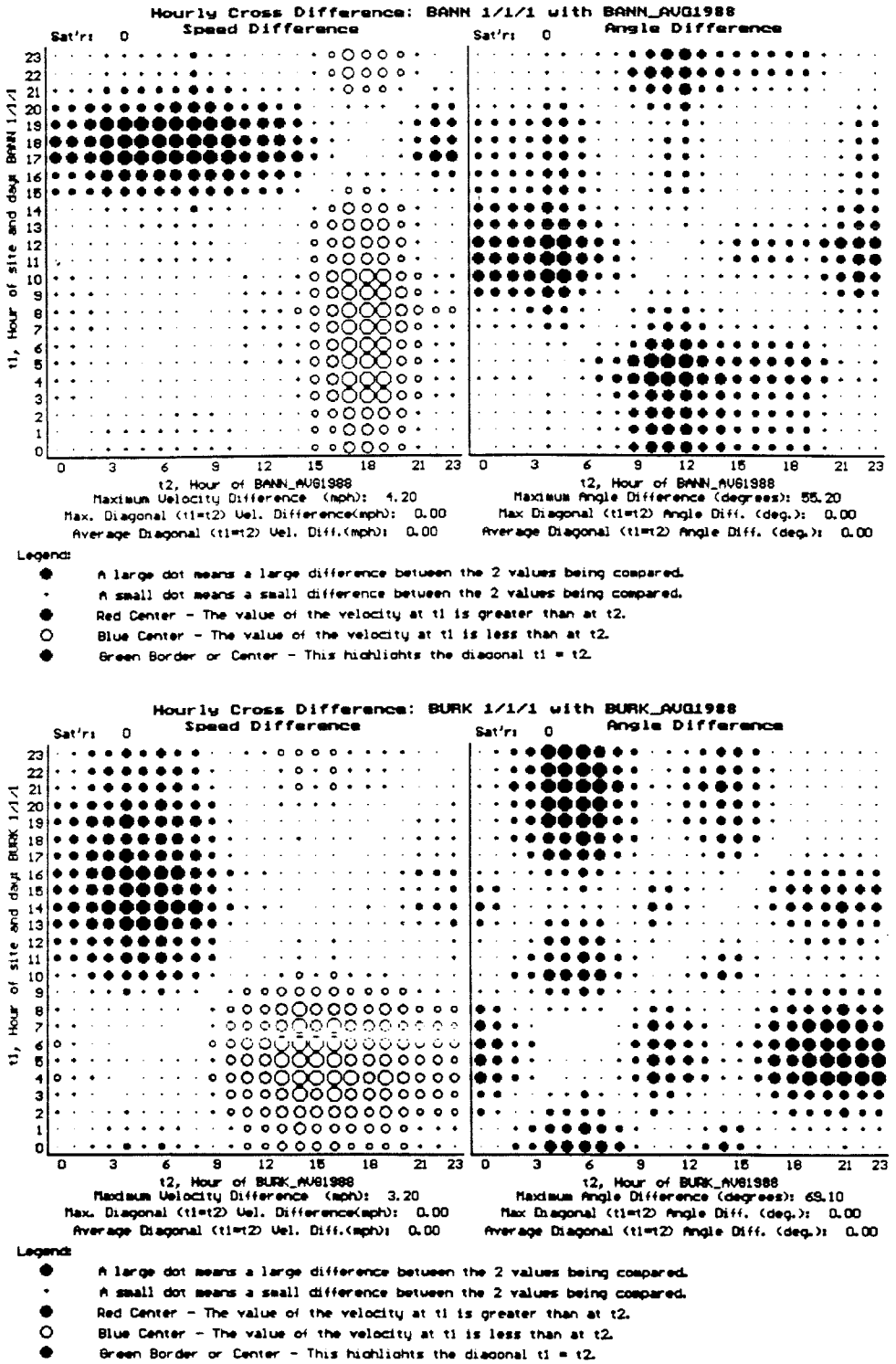

Figure 13. Speed and angle cross difference (top) Banning (BANN) average smog season day 1988 compared to itself, (bottom) Burbank (BURK) average smog season day 1988 compared to itself.

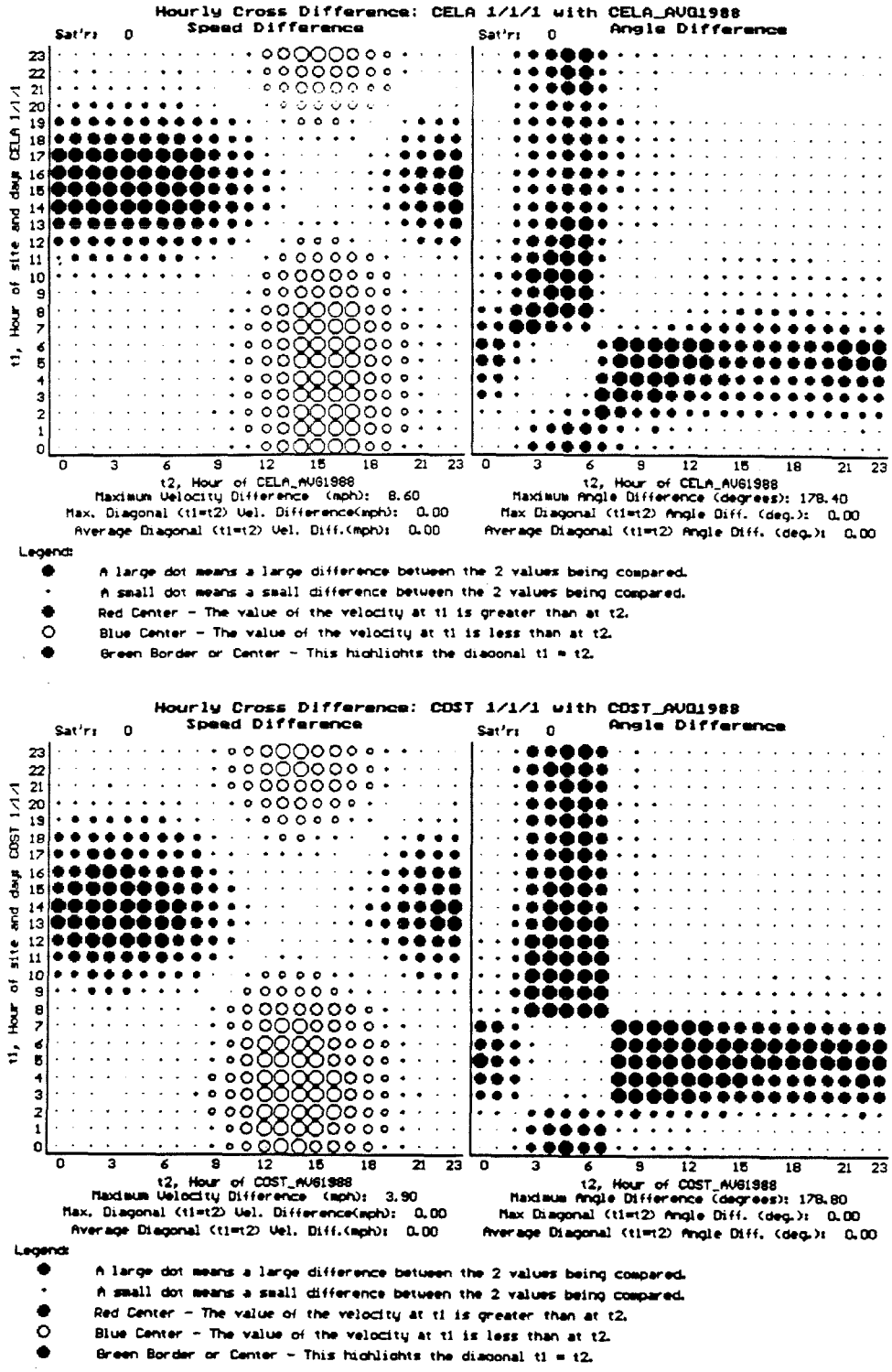

Figure 14. Speed and angle cross difference (top) Central Los Angeles (CELA) average smog season day 1988 compared to itself, (bottom) Costa Mesa (COST) average smog season day 1988 compared to itself.

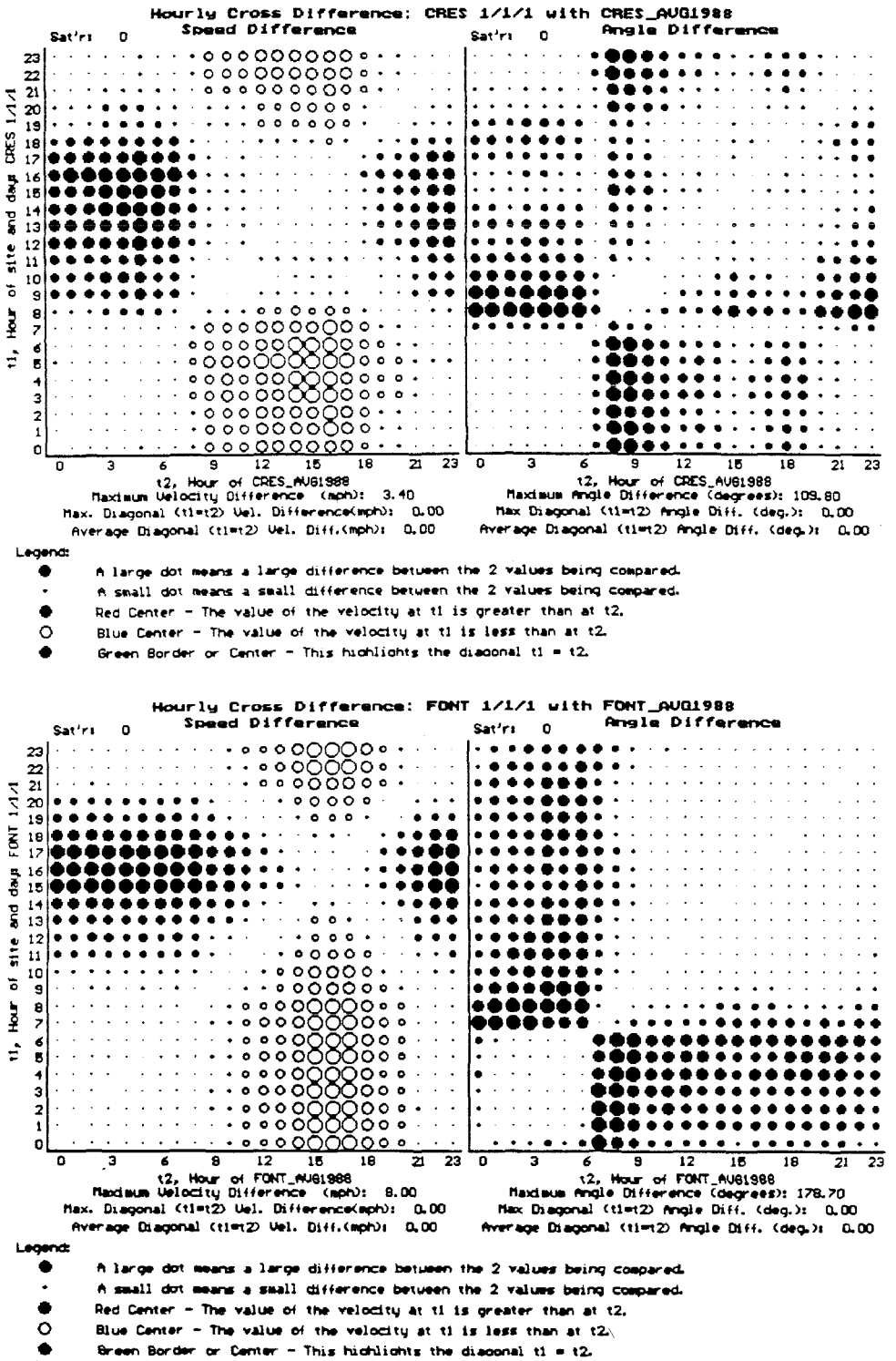

Figure 15. Speed and angle cross difference (top) Crestline (CRES) average smog season day 1988 compared to itself, (bottom) Fontana (FONT) average smog season day 1988 compared to itself.

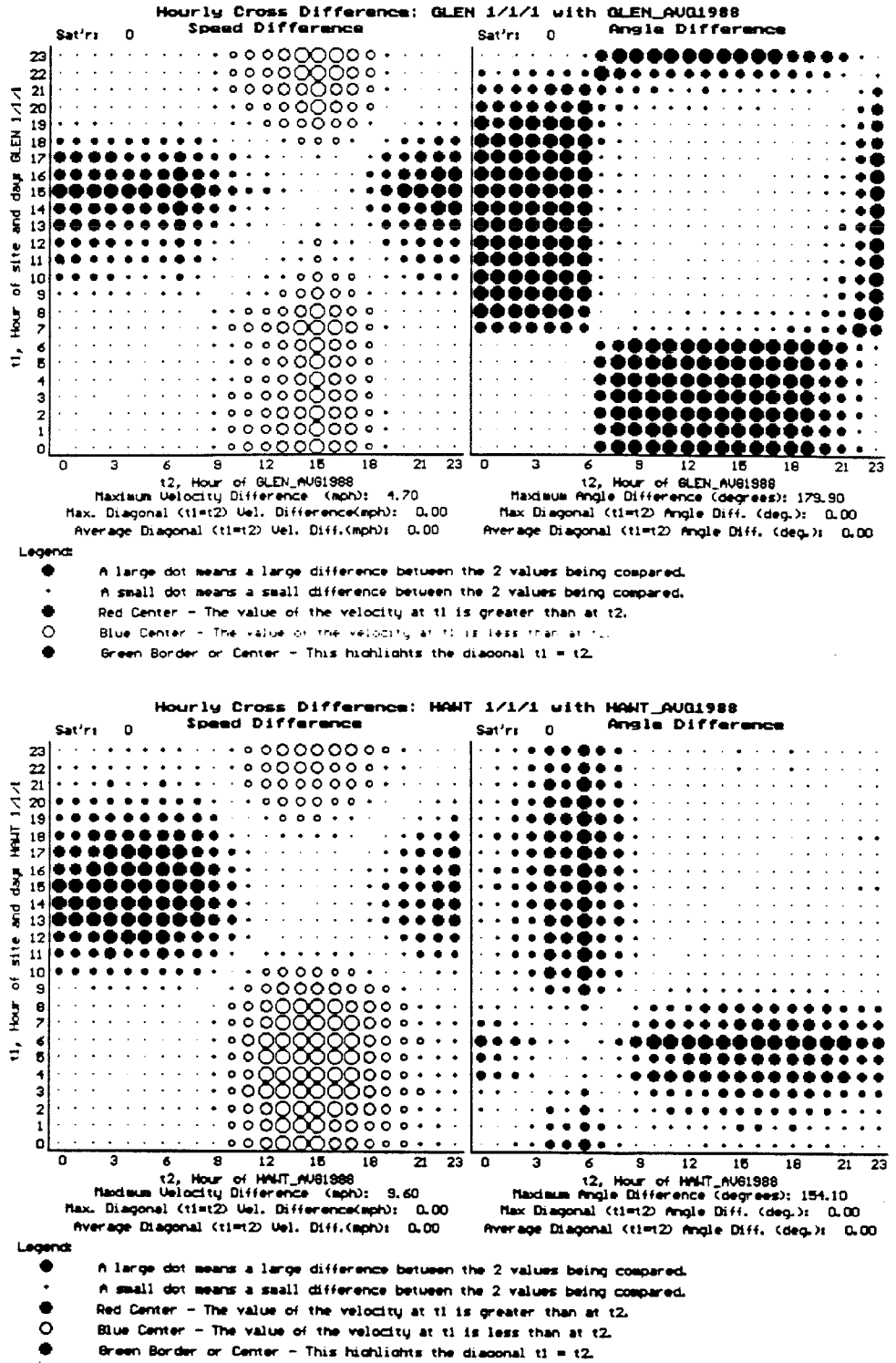

Figure 16. Speed and angle cross difference (top) Glendora (GLEN) average smog season day 1988 compared to itself, (bottom) Hawthorne (HAWT) average smog season day 1988 compared to itself.

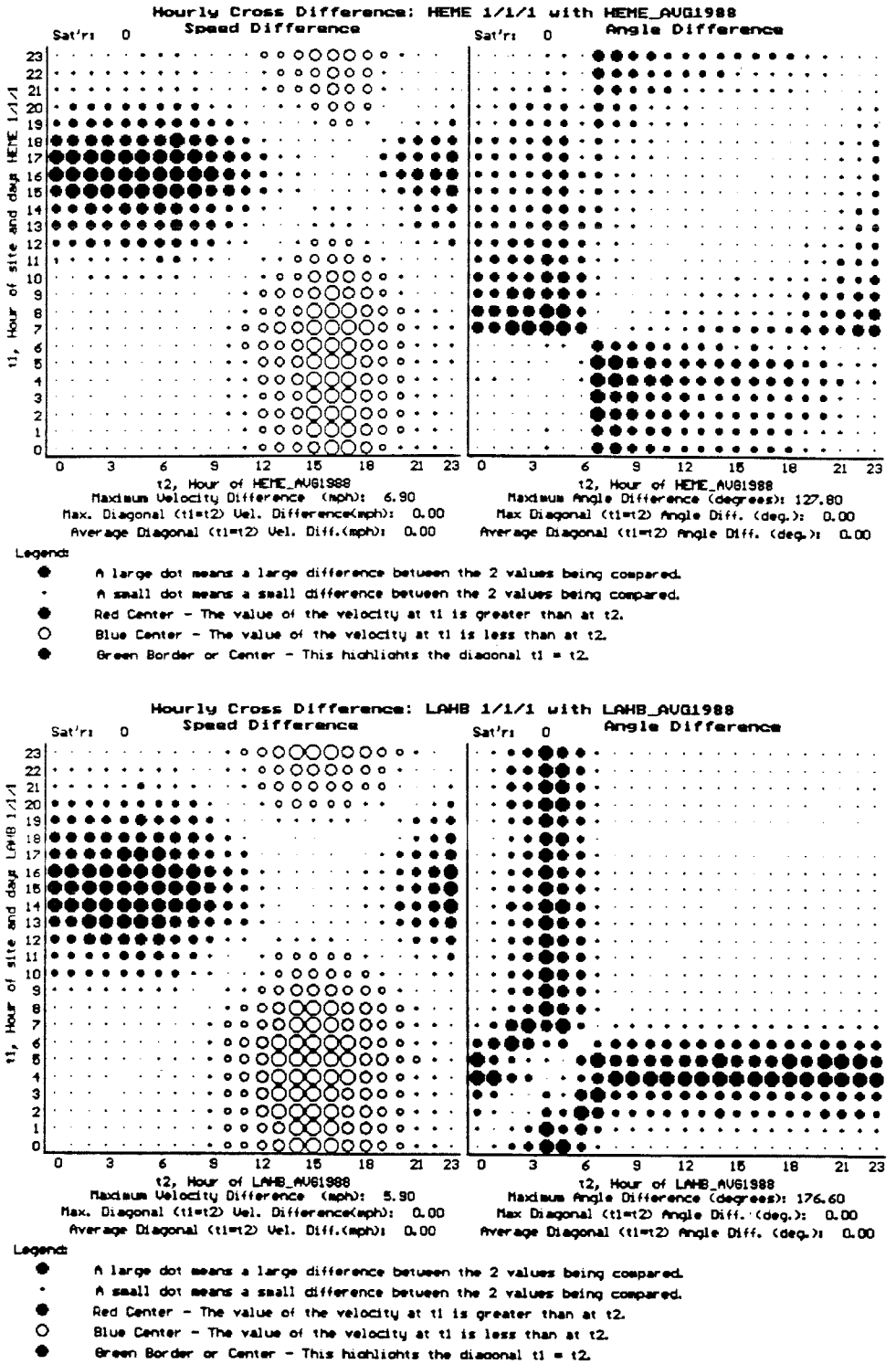

Figure 17. Speed and angle cross difference (top) Hemet (HEME) average smog season day 1988 compared to itself, (bottom) La Habra (LAHB) average smog season day 1988 compared to itself.

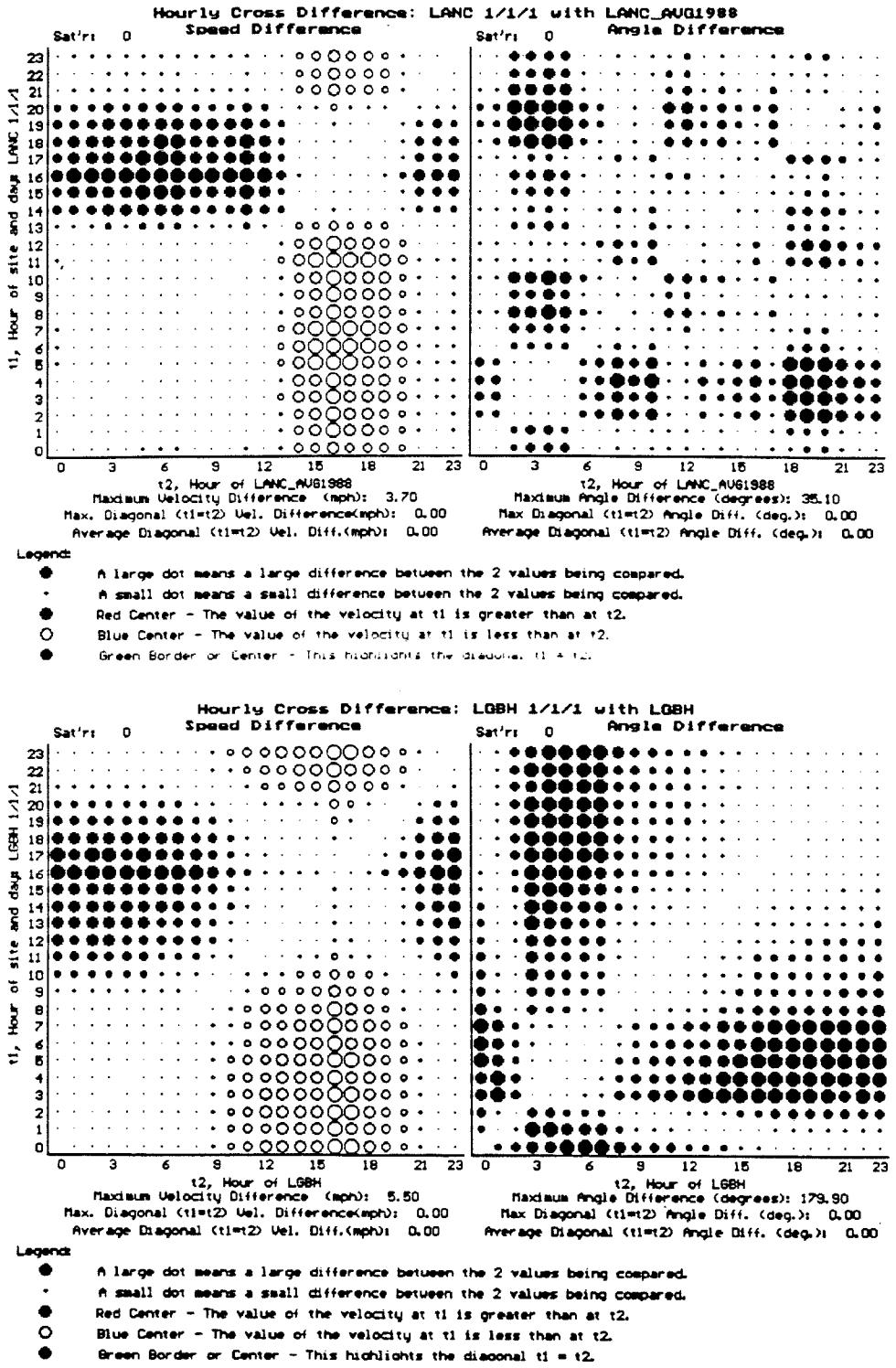

Figure 18. Speed and angle cross difference (top) Lancaster (LANC) average smog season day 1988 compared to itself, (bottom) Long Beach (LGBH) average smog season day 1988 compared to itself.

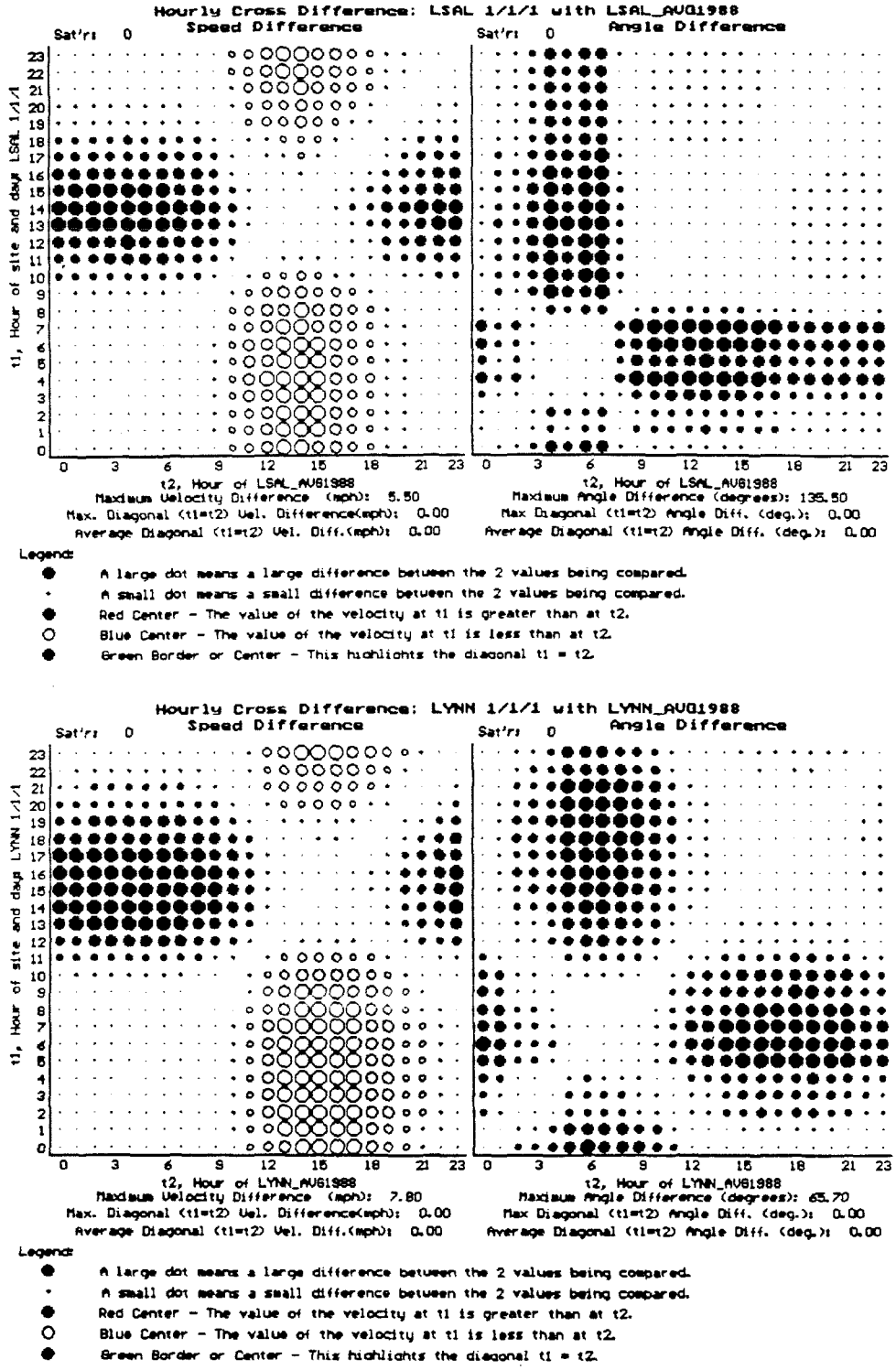

Figure 19. Speed and angle cross difference (top) Los Alamitos (LSAL) average smog season day 1988 compared to itself, (bottom) Lynwood (LYNN) average smog season day 1988 compared to itself.

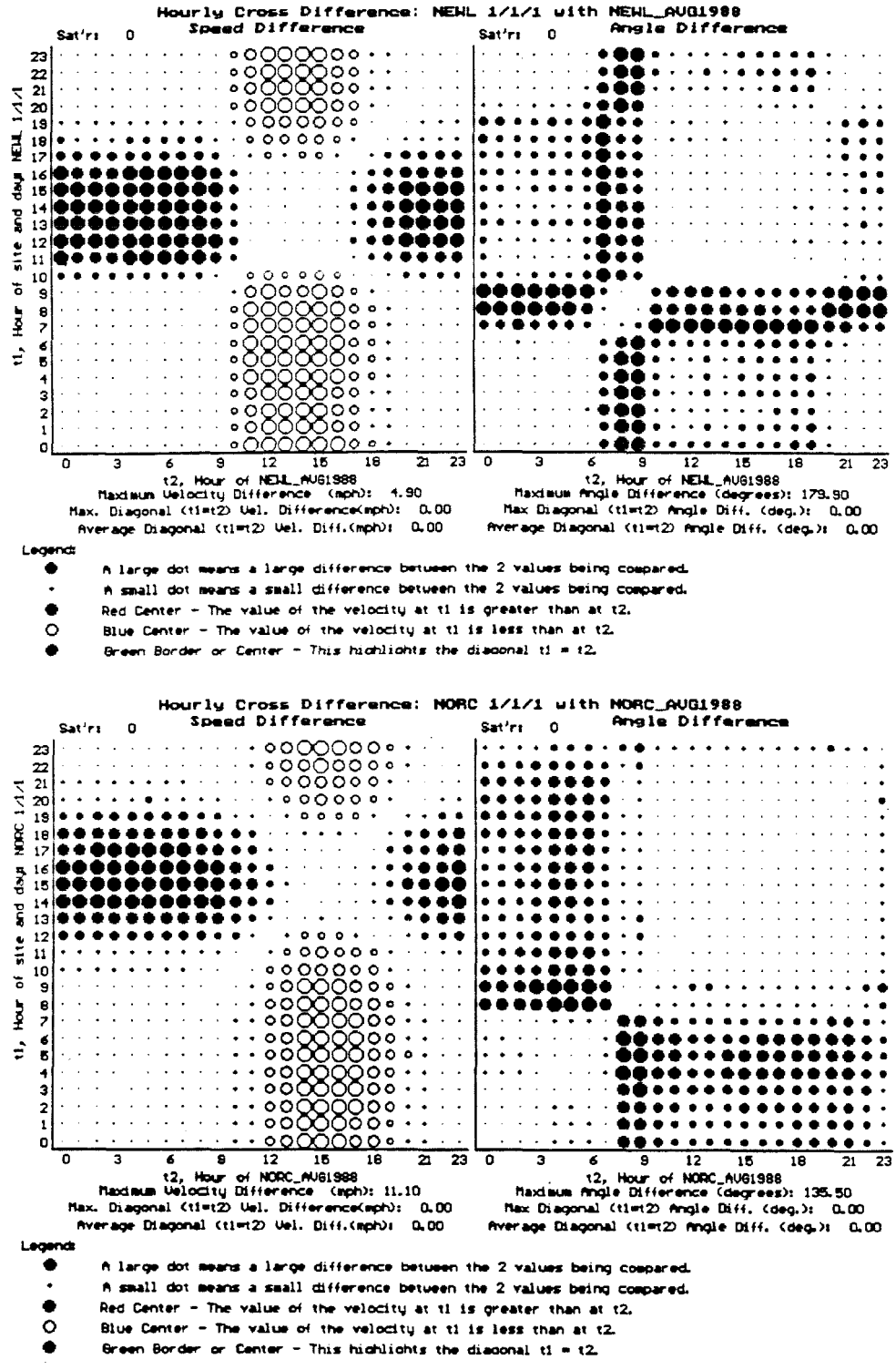

Figure 20. Speed and angle cross difference (top) Newhall (NEWL) average smog season day 1988 compared to itself, (bottom) Norco (NORC) average smog season day 1988 compared to itself.

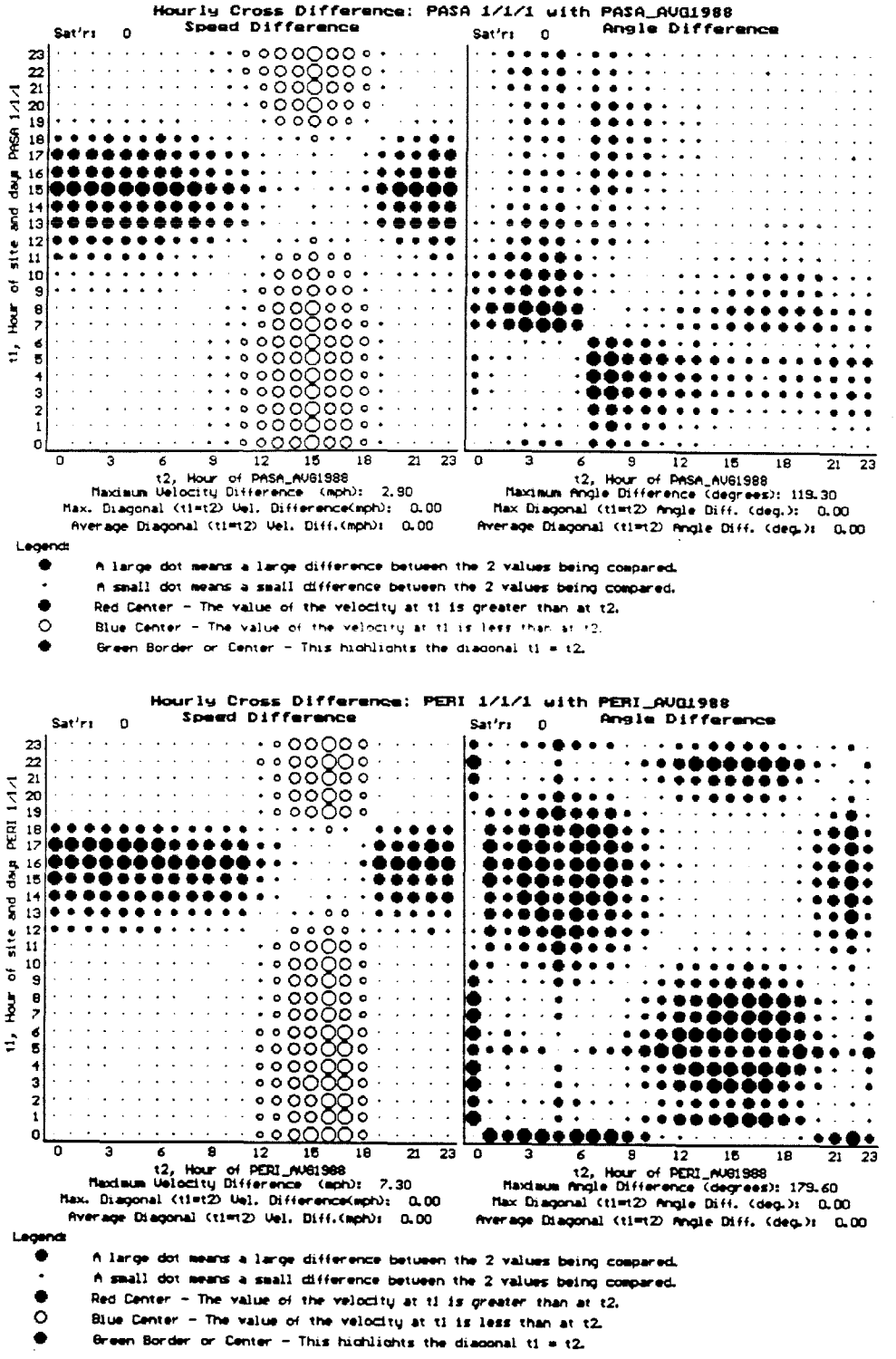

Figure 21. Speed and angle cross difference (top) Pasadena (PASA) average smog season day 1988 compared to itself, (bottom) Perris (PERI) average smog season day 1988 compared to itself.

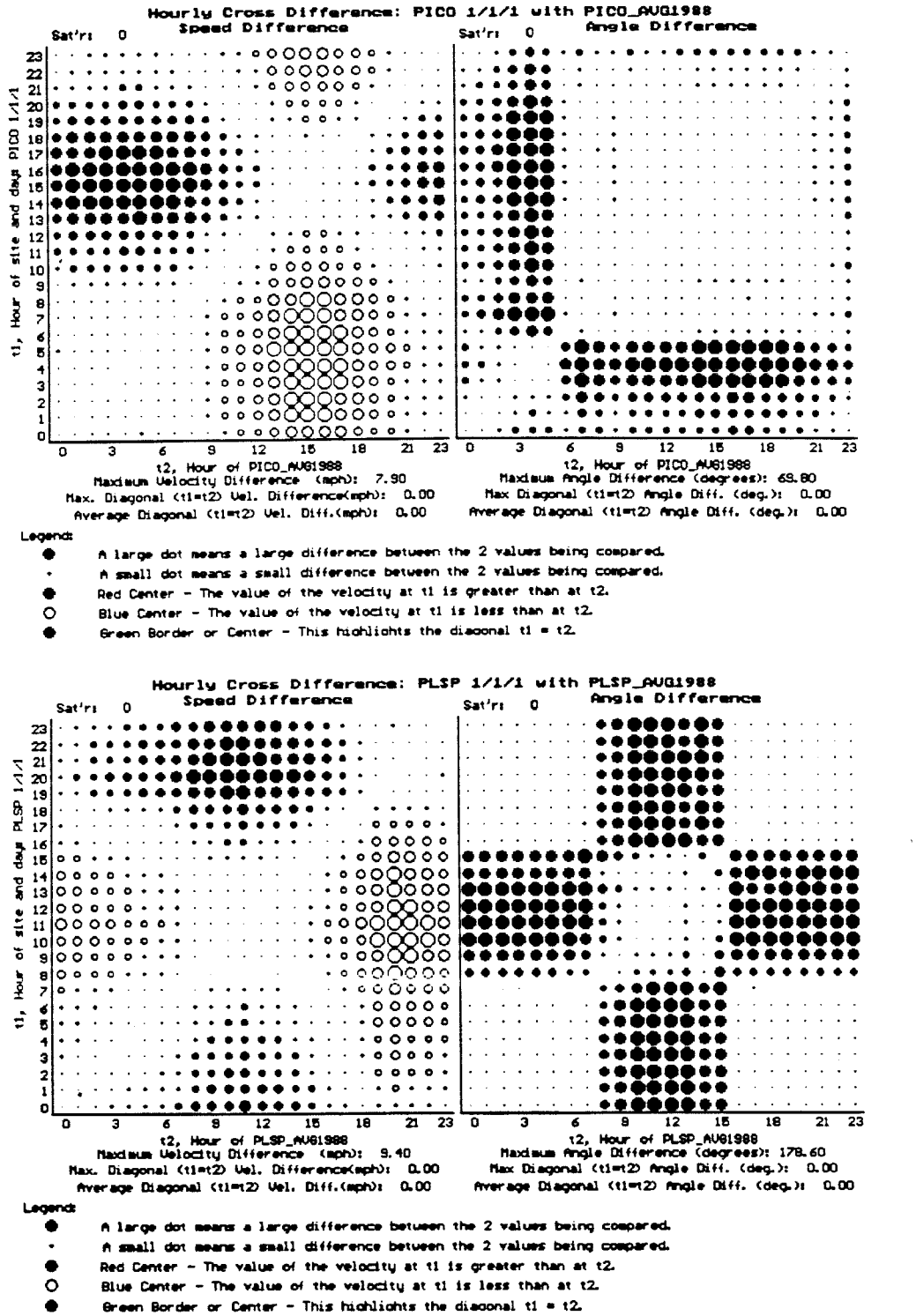

Figure 22. Speed and angle cross difference (top) Pico Rivera (PICO) average smog season day 1988 compared to itself, (bottom) Palm Springs (PLSP) average smog season day 1988 compared to itself.

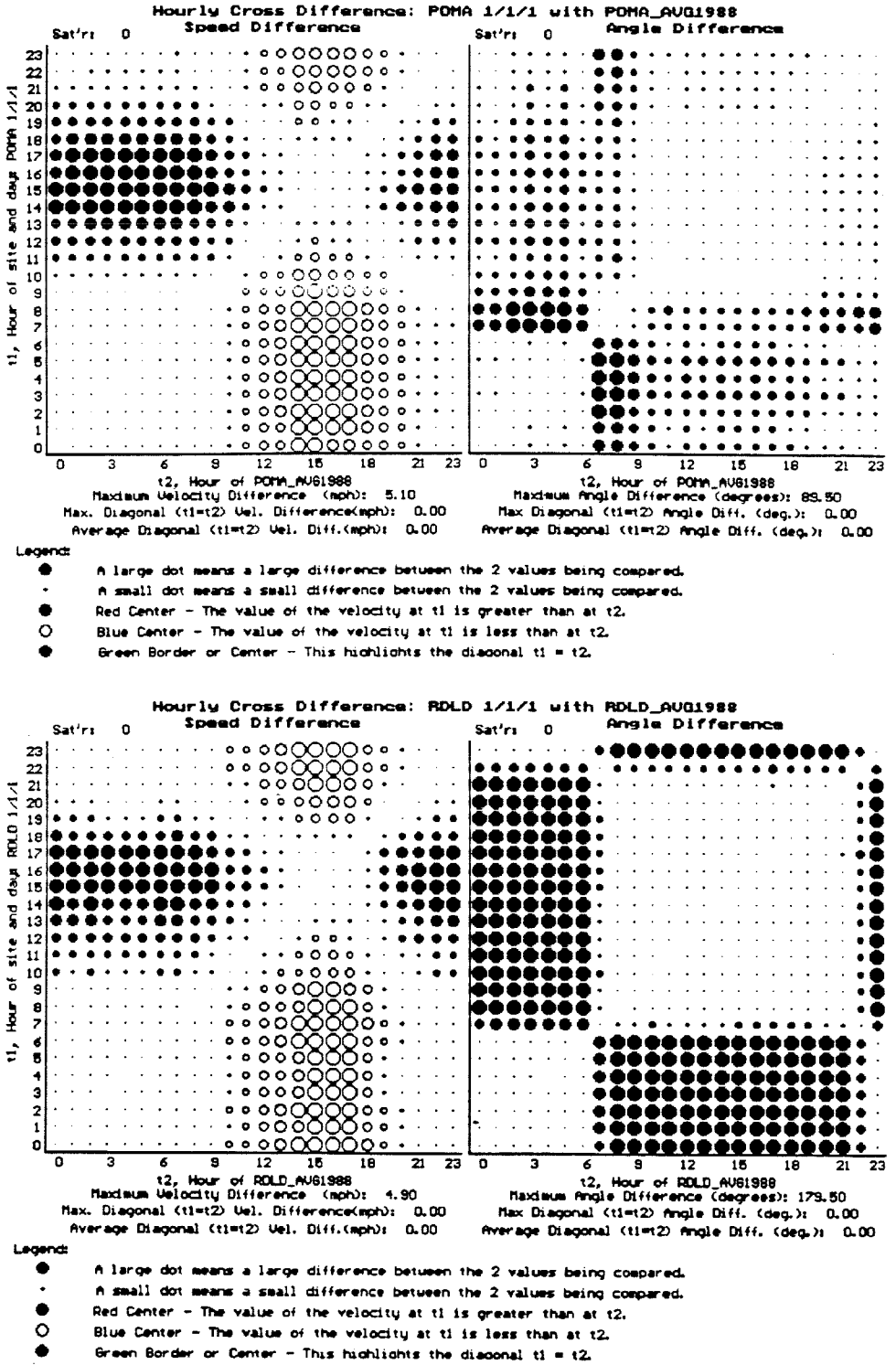

Figure 23. Speed and angle cross difference (top) Pomona (POMA) average smog season day 1988 compared to itself, (bottom) Redlands (RDLD) average smog season day 1988 compared to itself.

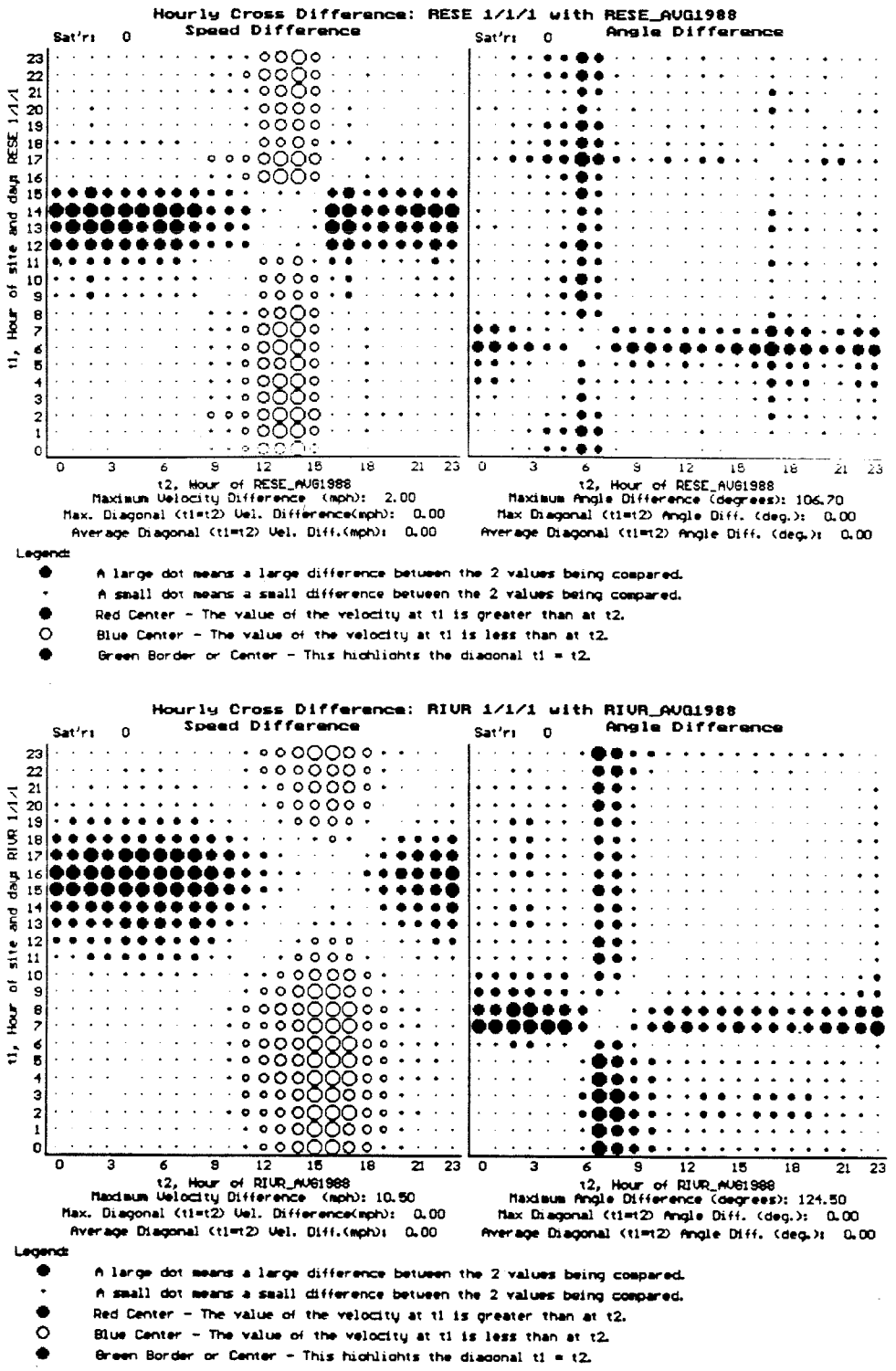

Figure 24. Speed and angle cross difference (top) Reseda (RESE) average smog season day 1988 compared to itself, (bottom) Riverside (RIVR) average smog season day 1988 compared to itself.

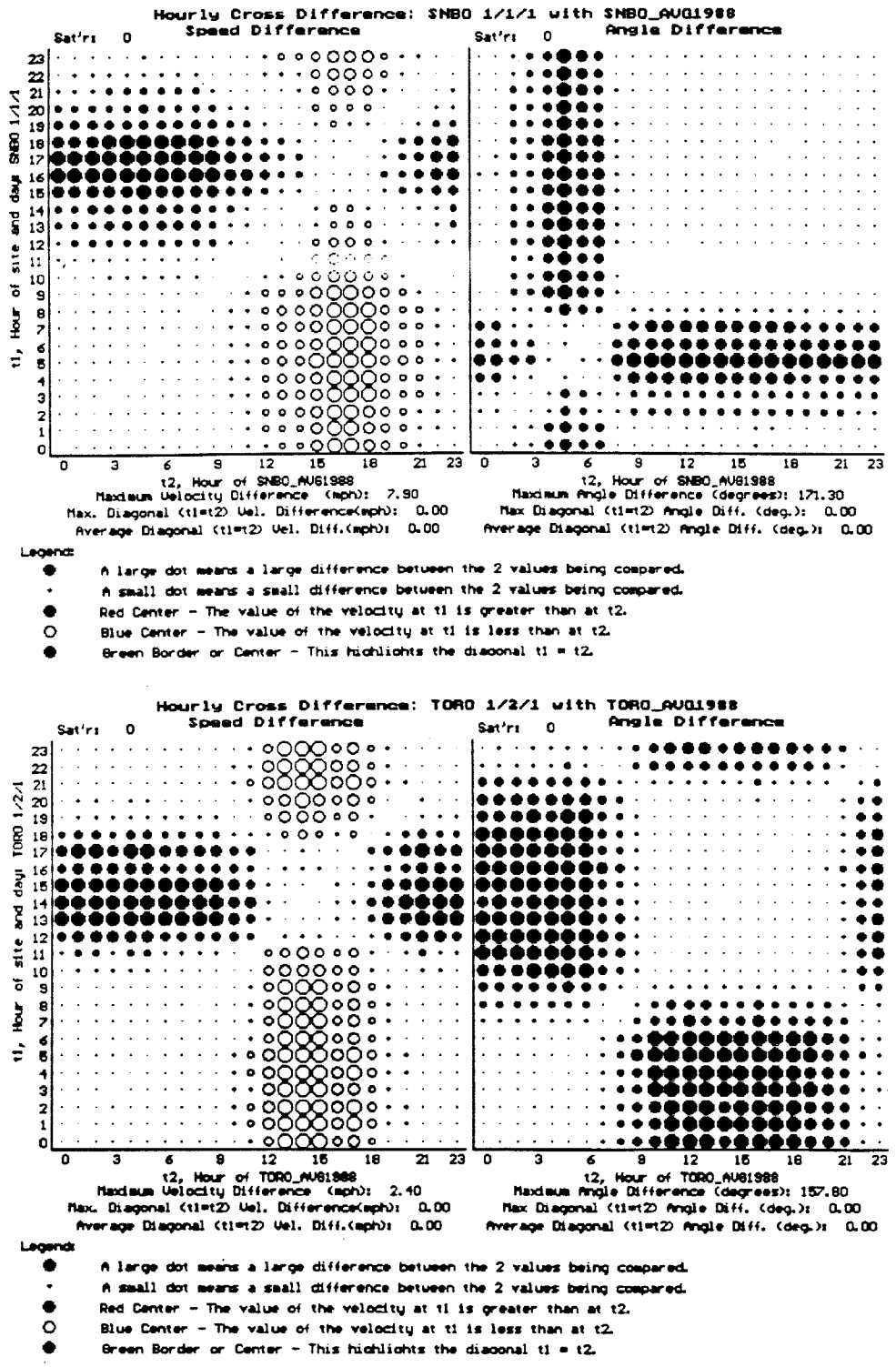

Figure 25. Speed and angle cross difference (top) San Bernardino (SNBO) average smog season day 1988 compared to itself, (bottom) El Toro (TORO) average smog season day 1988 compared to itself.

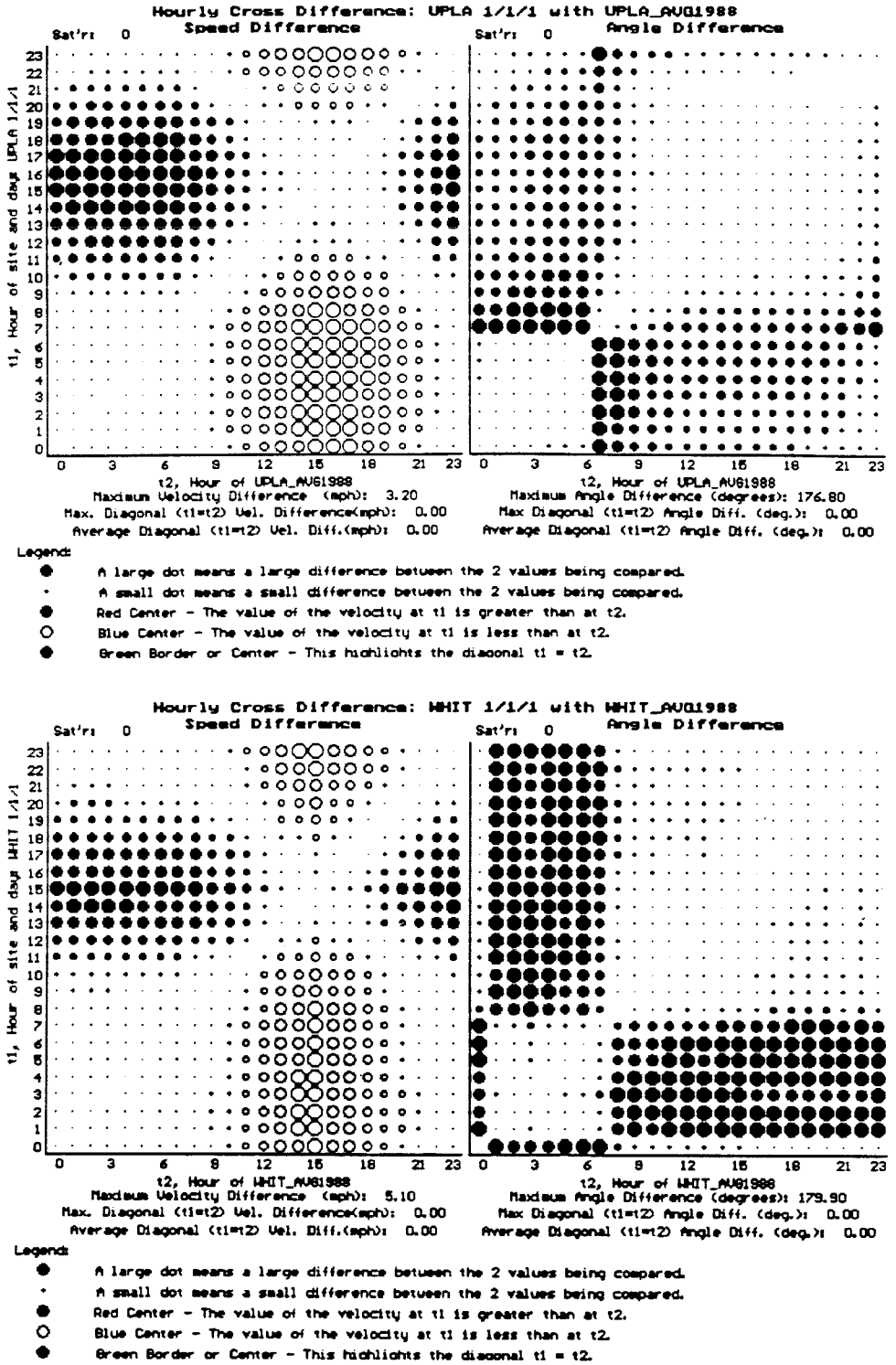

Figure 26. Speed and angle cross difference (top) Upland (UPLA) average smog season day 1988 compared to itself, (bottom) Whittier (WHIT) average smog season day 1988 compared to itself.

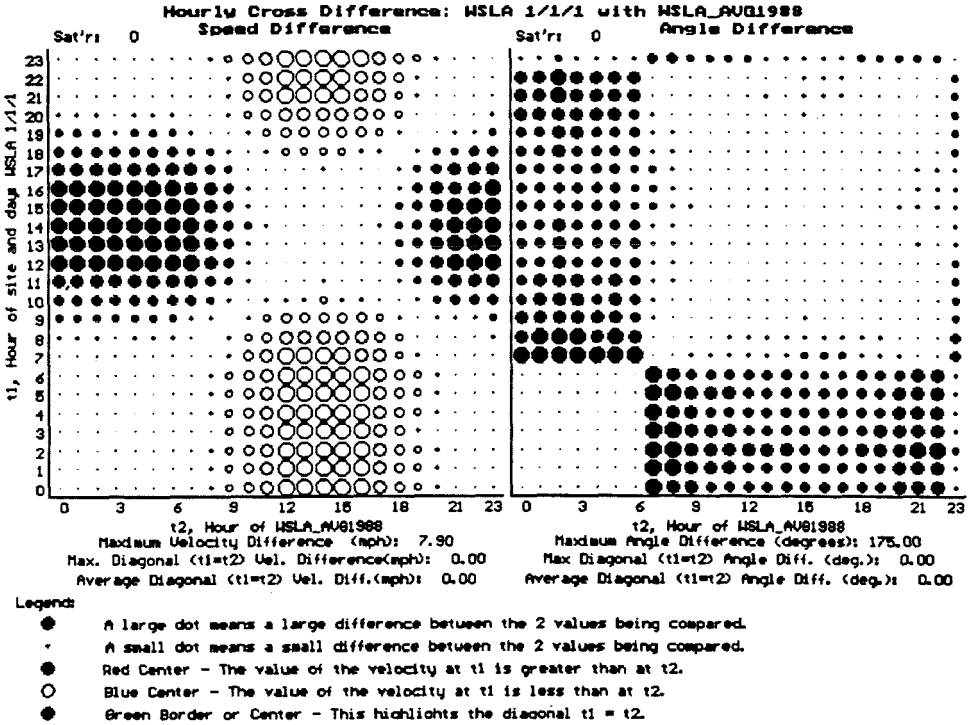

Figure 27. Speed and angle cross difference West Los Angeles (WSLA) average smog season day 1988 compared to itself.

References

1. Banta R. and Cotton W. R. (1981), "An Analysis of the Structure of Local Wind Systems in a Broad Mountain Basin," Journal of Applied Meteorology, **20** (11), pp. 1255-1266.
2. Blumen W. (1984), "An Observational Study of Instability and Turbulence in Nighttime Drainage Winds," Boundary-Layer Meteorology, **28**, pp. 245-269.
3. Defant F. (1951), "Local Winds," Compendium of Meteorology, Am. Met. Soc., Boston, MA, pp. 655-663.
4. Doran J.C. and Horst T. W. (1983), "Observations and Models of Simple Nocturnal Slope Flows," Journal of the Atmospheric Sciences, **40** (3), pp. 708-717.
5. Edinger J. G. (1959), "Changes in the Depth of the Marine Layer over Los Angeles Basin," Env. Sci. and Tech., **16** (3), p. 219.
6. Horrell R. S. (1987), "Atmospheric Buoyancy Driven Downslope Flows with Entrainment from a Ground Source," Masters Thesis, Department of Chemical Engineering, California Institute of Technology, Pasadena, CA 91125.
7. Horrell R. S., Deem M., Wyckoff P., Shair F. and Crawford N. (1989), "Ground Release SF_6 Tracer Experiments Used to Characterize Transport and Dispersion of Atmospheric Pollutants During the Southern California Air Quality Study of 1987," Air and Waste Association 82nd Annual Meeting, paper 89-138.2.
8. Kondo J. and Takeshi S. (1988), "A Simple Model of Drainage Flow on a Slope," Boundary-Layer Meteorology, **43**, pp. 103-123.
9. Scorer R.S. (1978), "Environmental Aerodynamics," Ellis Horwod, Chichester, U.K., p. 488.
10. Schroeder M.J. (1961), "Down-Canyon Afternoon Winds," Bulletin American Meteorological Society, **42** (8), pp. 527-542.

11. Shair et al. (1982), "Transport and Dispersion of Airborne Pollutants Associated with the Land Breeze-Sea Breeze System," Atmospheric Environment, **16** (9), pp. 2043-2053.

Chapter Three

Neural Network Computing Techniques to Process Air Quality Data

3.1 Introduction

The recent rapid growth in the field of collective computational systems frequently referred to as neuro-computing or neural networks is attributable to the recent work of Hopfield (1982) on associative memories, which showed how a collection of neuron-like processing units could be used to perform computationally intensive tasks. Further work by Rumelhart (1986) showed how networks which are strictly feedforward could be taught to map inputs to outputs even when the problem is not linearly separable. These authors and others have demonstrated how the parallel processing strategies utilized by biological systems can be emulated, and used in significant engineering and scientific applications.

Neural networks are attractive for several reasons. First, they are composed of many processing elements connected in a very parallel fashion. Therefore, a physical embodiment of such a system (Holler, 1989) capable of parallel data processing, will scale in time with the number of layers, rather than the number of weights as is the case with a sequential processor. Second, such systems are adaptive. If the circumstances in which the network performs its computations change, the network can be retrained to accommodate. Additionally, if trained properly, these networks can generalize. That is, they can interpolate and extrapolate over the input set, not suffering from the same deficiencies that expert systems suffer from when data is incomplete or not part of the training set (Fozzard, 1988).

Lapedes and Farber (1987) show that neural networks are able to accurately approximate a large class of functions. Additionally, they are capable of predicting the future for chaotic functions as well or better than known methods.

Recent developments have expanded the field to systems which are capable of handling time-dependent functions by means of information feedback within the network (Fang, 1990). Applications such as stock-market price pattern recognition, Kamijo (1990), and word recognition from a stream of characters (Benson,

1989) are among topics commonly being explored with recurrent networks.

An obscure application of neuro-computing exists which is relevant to the field of meteorology (Hu, 1964). Hu describes the use of an adaptive linear element (Adaline) system to do weather forecasting, specifically the occurrence of rain in the San Francisco Bay Area. He was able to conclude that the technique compared favorably with the U. S. Weather Bureau forecasts up to 24 hours into the future and was better from 24 to 36 hours into the future. More recently, good preliminary results have been obtained using a neuro-computing technique applied to the meteorological classification of satellite data (Smotroff, 1990). In both cases networks were proven capable of making classifications or forecasts which were traditionally done by experts.

The purpose of this paper is to demonstrate with two examples that additional applications in the science of meteorology and air quality data processing exist for neural networks. The first example demonstrates how automated Air Quality (AQ) data reconstruction can be accomplished using a network. The second example demonstrates the forecasting ability which can be embodied in a network. In both cases the examples were chosen to be representative of a class of commonly confronted AQ problems, and to produce results which were in and of themselves worthy of note. A second purpose was to explore an alternative approach for forecasting to the traditional approaches of numerical computing which have come under scrutiny (Zannetti, 1989).

3.2 Neuro – computing Strategy

The following section summarizes a general neuro-computing strategy. Persons unfamiliar with neuro-computing may find these introductory sections informative, and a useful preparation for the material that follows. Neuro-computing consists of 6 major steps:

1. Deciding whether a neuro-computing tactic is appropriate for a given computing task;
2. collecting and preprocessing the training data;
3. selecting a network architecture;
4. choosing the appropriate learning algorithm;
5. training the network;
6. computing with the trained network.

Often, when a physical system is being modeled with a neural network the state variables for the system are the inputs to the neural network, and the next or future states of the system are the outputs. In the discussion below the word "system" will be understood to mean physical system, and the word "task" will be understood to mean the task of modeling a physical system.

On the Appropriateness of a Neuro-computing Strategy

The decision to use a neuro-computing strategy to perform a given computing task is based on any combination of the following reasons:

1. The computing job would benefit from the speed of parallel processing or is inherently a parallel process. To actually obtain a speedup due to parallelism, it is necessary to utilize a physical system, i.e. an embodiment in hardware of a neural network, which takes advantage of the parallelism.
2. The functional mapping from input to output is not known, or understood, or practically obtained by known analytical methods.
3. The computing task to be accomplished would benefit from the ability to be updated as new or changing data are acquired.

4. An associative memory of past functional relationships is desired. Recurrent networks can perform "pattern completion," as well as, "pattern recognition" of inputs which are presented temporally.
5. The set of state variables for the system is incomplete. In this case, the network learns to generalize.

Collection of Training Data

The collection of data for training a neural network involves gathering data from a representative set of input variables and the associated output variables for the system being studied. Networks typically have multiple inputs and outputs, and are therefore referred to as input and output vectors. The notation convention I_i refers to the ith input element, and O_j refers to the output from the jth neuron. The outputs which are part of the training set are typically referred to as *target outputs*, *target vectors*, or just *targets*. The notation for targets is the same as for outputs except the letter T is used. The set of input and target vectors used to train the network is referred to as the *training set*. When the number of input variables is large or thought to contain duplicate or spurious inputs a principal component analysis (PCA) may be used to reduce the number of inputs down to the most significant subset of inputs (Baldi, 1989).

Training of a Network

Training a neural network is defined, for the purpose of this manuscript, as the process of presenting input vectors from the training set to the network (in its current state), and comparing the associated output vectors the network computes to the target output. The difference between the output and target vectors determines the error for that presentation. A vector of errors is computed for each input in the training set, one error for each output which is to be compared with a target. An algorithm such as error back propagation (Rumelhart, 1986), Madaline III, Real-Time Recurrent Learning Algorithm (Williams, 1988), etc. is used to adjust the internal parameters of the network to minimize

the error at each output. This definition applies to a mainstream class of neuro-computing strategies and is generally referred to as supervised training. This is a general definition, but it does not apply to all types of networks. Specific training algorithms will be discussed below.

Computation with the Network

The neural networks discussed herein achieve their computational power by performing the following calculation for a given input. The output of neuron j, O_j, is computed using Equations 3.2.1 - 3.2.4.

$$O_j = f_j[\sigma(I,O,W)] \tag{3.2.1}$$

where I and O are the input and output vectors, and W is the weight matrix which connects the inputs to the outputs and which also connects each of the outputs to all of the output units. The function, $f_j[\sigma]$, is the transfer function, and is typically a sigmoidal function like,

$$f(\sigma) = a + b \cdot tanh(\sigma), \tag{3.2.2}$$

or the so-called sigmoidal squashing function

$$f(\sigma) = a + \frac{b}{1 + e^{-\beta\sigma}}. \tag{3.2.3}$$

The function σ_j is computed by,

$$\sigma_j(I,O,W) = \sum_{k=1}^{m} I_k W_{jk} + \sum_{k=m}^{m+n} O_k W_{jk} - \gamma_j \tag{3.2.4}$$

where there are m inputs and n outputs. The symbol γ_j represents the adjustable bias weight associated with each neuron. Each neuron sums the contributions of all the inputs (the first sum in Equation 3.2.4) with the contributions from all of the neurons (the second sum in Equation 3.2.4), and subtracts off a fixed bias (γ in Equation 3.2.4). This sum is then passed through a nonlinear function (eg Equations 3.2.2 or 3.2.3) to produce the output of each of the neurons.

The above formulation describes a general, fully interconnected network which includes feedback. This definition can be reduced to a feedforward system by holding all weights which feed information backward in the system to zero. Something quite noteworthy is that a fully connected recurrent network can actually be trained to zero out any connections which feedback if the problem is inherently feedforward. The network learns that the recurrent weights are superfluous. From an engineering and application point of view this is of considerable value since the architecture of the network need not be assumed, only the number of neurons.

One measure of a network's performance and an indicator of the degree to which a network has been trained is the sum squared error defined in Equation 3.2.5 for input-output pattern q.

$$\epsilon_q = \frac{\sum_{j=1}^{n}[T_j - O_j]^2}{n} \tag{3.2.5}$$

where n is the number of output units. The sum squared error is computed for each input-output pair. A means of comparing network performance between two separate input-ouput pattern files is the *average epoch sum squared error* defined by Equation 3.2.6. It is the average of the sum squared errors in a single training set,

$$E = \frac{\sum_{j=1}^{p}\epsilon_j}{p} \tag{3.2.6}$$

where p is the number of pattern pairs presented in an epoch. Epoch is defined as the corpus of input and output pairs presented to the network for training.

Training Algorithms

Two network training algorithms are employed in the simulations to be described below: the feedforward form of the Madaline III algorithm by Andes (1989) is used in Section 3.3, and the recurrent algorithm of Williams and Zipser (1988) in Section 3.4.

Training Feedforward Networks

There are several algorithms to train feedforward networks of the architecture discussed in Section 3.2. Among them are backpropagation (Rumelhart, 1986) which has been discussed and used extensively in neuro-computing literature, and more recently Madaline III (Andes, 1989). The Madaline III algorithm is the most recent form of the Adaline (Widrow, 1988) family of adaptive element training algorithms. This algorithm has the particular distinction of being capable of learning on analog devices where the transfer functions are not as precisely described as in Equations 3.2.1 to 3.2.4. To obtain the increased speed benefit which neural networks offer, the use of hardware implementations is essential. The feasibility of such a use was sought, and therefore Madaline III was used. Madaline III is a very straight forward algorithm which performs gradient descent on the sum squared error in weight space. The reason it is useful for hardware implementations of a neural network is that it accounts for the nonidealities of the processing elements. Simply put, Madaline III perturbs the inputs of each neuron at every layer and determines whether the mean squared error is reduced or not. With this information and the input to each weight, a weight update rule is obtained.

Training Recurrent Networks

A network which has feedback among neurons is termed a recurrent network. Algorithms to train this sort or network have appeared only recently and have been authored by Williams and Zipser (1988), Pineda (1989), and Pearlmutter (1989). Additional computational overhead is acquired when training recurrent

networks compared to feedforward only networks. From an engineering point of view the additional effort may be worthwhile since this form of network is capable of organizing itself into its own architecture. The algorithm used by Williams and Zipser begins training with each neuron connected to every other neuron, and every input from the outside world. As training proceeds the elements of the weight matrix which connects some neurons to the external inputs, and to other neurons disappear. This process of zeroing weights isolates neurons into hidden layers. In applications where the required number of neurons, and layering of the neurons is not known *a priori*, training a recurrent network can provide the answers.

Among other things, recurrent connections confer upon a network the ability to identify patterns in a time series, and to predict future patterns. For this reason recurrent networks are well suited to forecasting applications.

3.3 A Feedforward Network for Ozone Data Reconstruction

A two-layer feedforward network was used to reconstruct air quality (AQ) data from incomplete data sets. The task of reconstructing missing AQ data is commonly done by hand by an air quality expert. For small data sets this is practical, but for the larger data sets which are generated in an urban area, i.e. Los Angeles, this may require a considerable amount of man-hours. Consider for example that roughly 100 air quality variables are being measured and recorded from 30 stations for each of the 24 hours in a single day by the South Coast Air Quality Management District in the Los Angeles Basin. Somewhere between four to eight percent of this data is routinely missing or upwards of 5760 data points daily, or approximately two million data points yearly. (This estimate is made based on the ozone data reported by the SCAQMD for 1987).

Neuro-computing offers a viable means of handling missing AQ data. The restoration technique can be used to minimize the time devoted to data reconstruction by AQ experts. This can be done as a pre-processing step prior to data archival or as an imbedded data filter in an existing application which accepts the raw data.

The neuro-computing solution offers an alternative approach for handling AQ data records with missing entries. It uses historical data as a basis for the data reconstruction, and can be updated continuously as new data is collected. Seasonal variations can easily be incorporated into the neural network solution by training individual networks on single seasons. It can reconstruct data across missing "peaks," a deficiency in the data which often leads to the data being discarded, and at minimum requires an expert's judgement to reconstruct the missing data. It can generate a flag which is a measure of the likely performance of the network's restoration based on previous restoration performance.

The simulations performed were done to: (1) validate the above claims, and (2) qualitatively assess the performance of the network in performing data

reconstruction.

Method

A 24 input 24 output, two-layer feedforward network was used to perform ozone data reconstruction. The network was presented with 24 one-hour-averaged values of ozone measured at Newhall, CA, one hour at each input. The network was then trained to output the identical pattern, filling in data at any missing hours. Figure 1 (top) shows the input, output, target, and error of the trained network for July 14, 1989 with a full input set. Figure 1 (bottom) shows the same networks output when an incomplete input is applied to the network.

The network was trained on a single month's worth of data, the 30 days of June 1988. In addition, "missing data" days were created by introducing defects into the training data set in the following way. A day in the data set was duplicated, then one, two, or three inputs were zeroed indicating that the data was missing. The corresponding outputs were kept intact. At least one duplicate day was made for each day of June.

Because the peak in the ozone occurs at approximately the same time of the day during this month it was clear from preliminary training simulations that the network would be incapable of generalizing to be able to reconstruct peaks when the peak occurred more than a couple hours from the average. To alleviate this problem ten additional days were created from the June days by shifting the data forwards or backwards in time up to five hours. (Actual days where the peak was shifted were too infrequent to justify collecting them). "Missing data" days were created for the time shifted days also. In total, there were 70 I/O pairs in the training set.

The sigmoid transfer function was adjusted to give it an output range from 0 to 30, which corresponds to the part per hundred million range of nearly all ozone observations in Los Angeles. To achieve this, the following characteristic parameters were used: $a = 0, b = 30$, and the gain, β was 0.001. The number

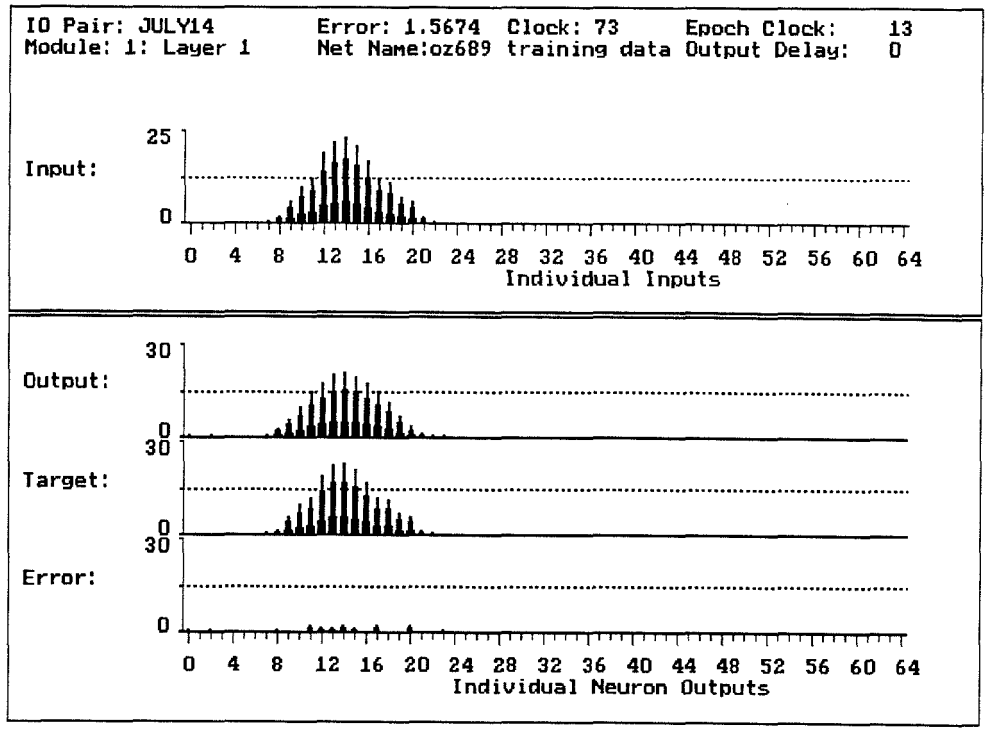

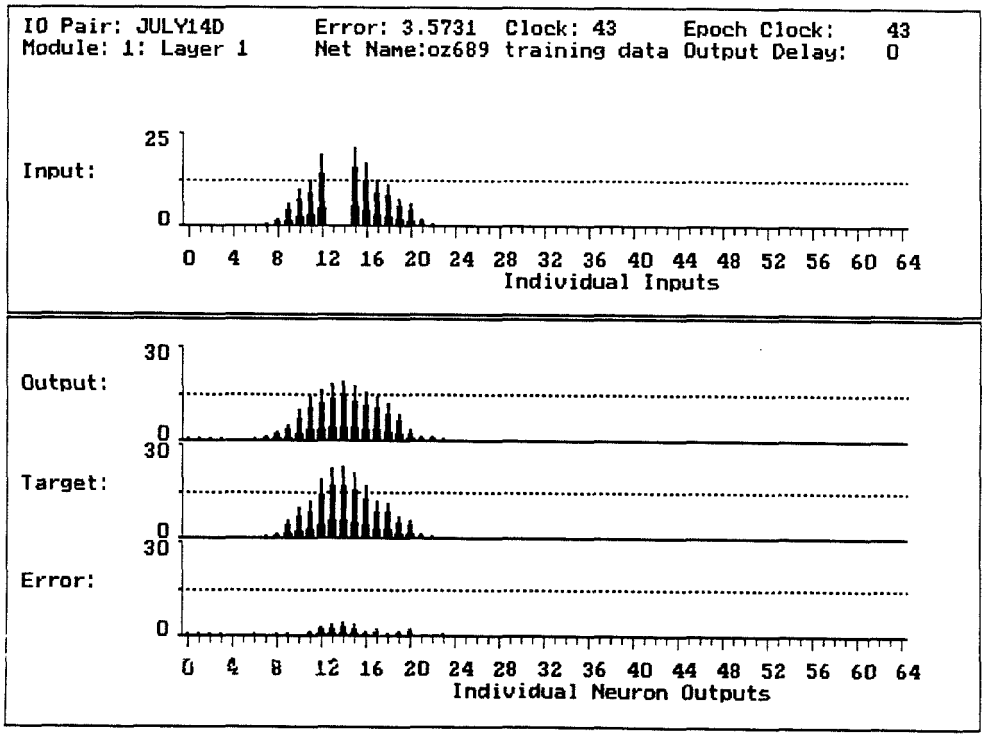

Figure 1. Input, output, target and error for the sample input July 14, 1989: (top) complete input, (bottom) input with two deletions at hours 13 and 14.

of neurons in the second (or hidden) layer was fixed at 24.

The Madaline III algorithm was used to train the network. The algorithm was implemented via DynaMind version 0.8 (NeuroDynamX 1990) PC-based simulator. Training was done on a Zenith Z-386/20 with 80387 math coprocessor. Approximately 500 epochs were required to train the network. Following training the network was tested on two month's worth of data from July 1989 and August 1989. Each simulation required approximately 2 hours. The learning rate was set to 0.05, and was found easily by trial and error.

Results

The average epoch sum squared error, Equation 3.2.6, for the June training data was 1.43 and for the July and August test set it was 2.04. A network with randomized weights has a value of 227 for the June training data. The similarity between these two values indicates that the network was able to process the new data nearly as well as the training data. In physical terms it means the filtering process imposed by the network alters each ozone value by approximately one pphm. For small ozone values, around one pphm, this is of course significant, however it is the large values which are of the greatest concern. For the larger ozone readings, 15 pphm, this means less than 7 percent error.

The effectiveness of the network for data reconstruction can be summarized qualitatively as successful with the following caveats. An increasing number of missing data points decreases the capacity for the network to fill in the missing points. Contiguous missing data points are reconstructed with greater accuracy than missing data which is scattered, especially when the missing points lie within several hours of one another. Figure 2 shows data reconstruction where deletions are not contiguous. Compare this to Figure 1, a similar day, noting the larger error which occurs in reconstruction when the missing hours of data are separated. In cases where the reconstruction of the data was poor, the ozone values surrounding the missing data points tends to be altered, generally in the

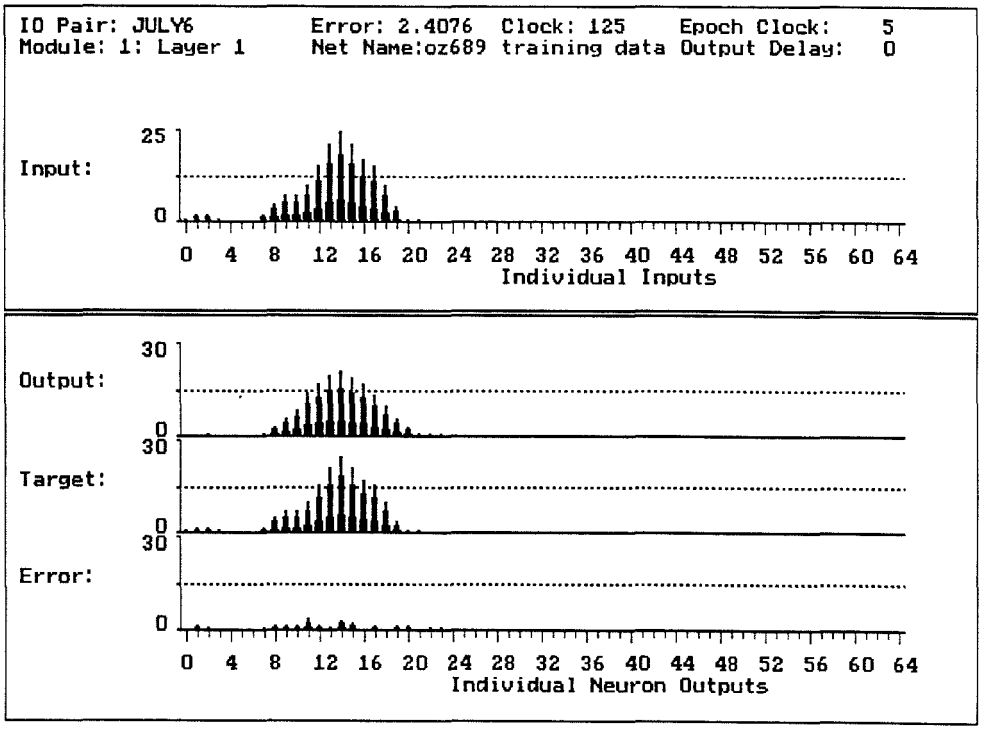

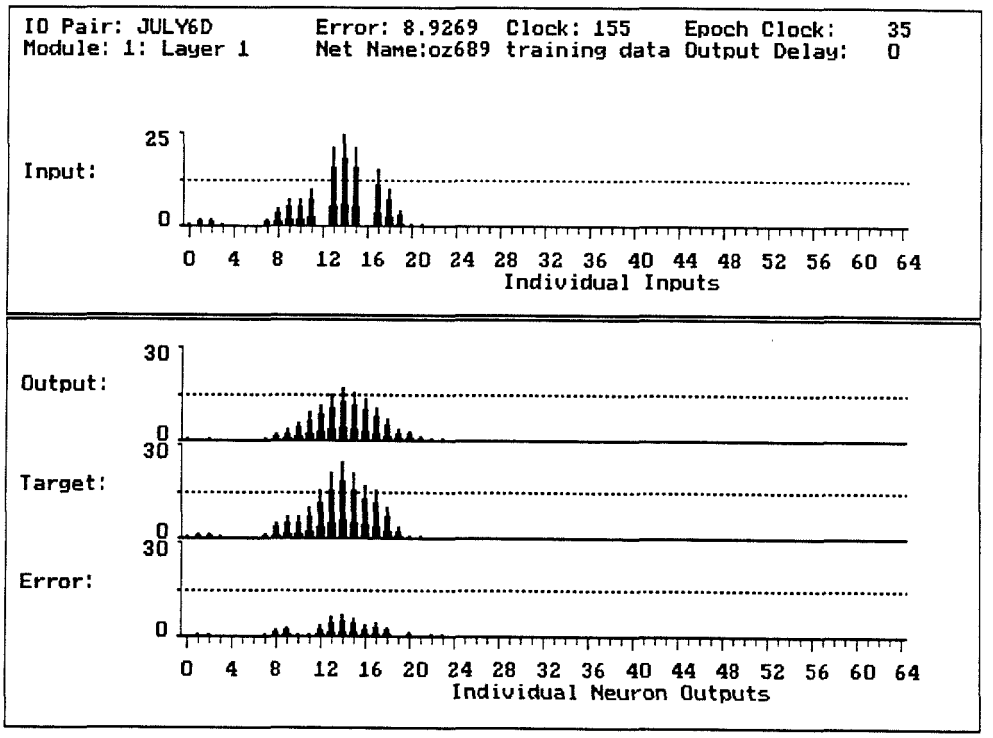

Figure 2. Input, output, target and error for the sample input July 6, 1989: (top) complete input, (bottom) input with two deletions at hours 12 and 16.

direction of being reduced.

Quantitatively the network is capable of reconstructing most missing points, on average, to better than $\pm$ 10 percent of their true value.

3.4 A Recurrent Network for Short – term Ozone Forecasting

Method

A fully interconnected recurrent network was used to continuously forecast short-term ozone levels at a single location based on the previous sequence of hourly averaged ozone levels observed at that location. The network is presented with a single ozone level in pphm from a single site in the Los Angeles Basin and trained to continuously make three predictions of the ozone levels at either: one, two and three hours, or at four, five, and six hours following the hour of the presented value. Through the use of the recurrent connections it is expected that the network will learn how many time steps from the past series of ozone presentations it requires to make its prediction.

The William and Zipser algorithm was used to do the training. The protocol was to present a single input, the ozone from a single hour, to the network and use the ozone levels at three future hours as targets for training. Each day (starting at hour 0) was treated as an independent series, and series were shown to the network in random order. This limited the network to making its prediction based only on the portion of the current day's series which it had seen as input. This decouples the prediction from the time series of the previous day. 24 one hour ozone levels for a given day. The training data for the network was the 30 days' of June 1989 taken at Newhall, CA.

The sigmoidal transfer function used by the network was identical to the one described above for the data reconstructing application. The learning rate was 0.3, which was determined by past experience using this algorithm. Approximately 500 epochs were required to train the network. Following training, the network's performance was tested on one month's worth of data from June 1988.

Since the optimum number of neurons which was obtained for the simulation was not known *a priori*, this was determined by simulation experiments. Three neurons is the lower limit, since three outputs are desired for each input (as

described above). Since simulation time with this algorithm scales with the number of neurons to the fourth power it is desirable to find the fewest number of neurons, above three, after which the epoch average sum squared error does not decrease. Simulations were done using from three to nine neurons. Each simulation was allowed to converge, but was trained on no less than 500 epochs in order to assure comparability between runs. Two simulations were done for each number of neurons. Figure 1 shows a plot of the epoch average sum squared error versus the number of neurons. From this figure it was determined that six neurons was the optimum choice for the rest of the simulations. Two networks were then trained using six neurons each, the first to make predictions for hours one, two and three, the second to make predictions for hours four, five, and six into the future. Under these conditions the first three neurons were arbitrarily assigned the job of making the prediction and neurons four, five, and six were allowed to "float" without being trained. To allow these neurons to float gives them the opportunity to arrange themselves into a hidden layer by the mechanisms discussed previously.

Results

Figures 2 and 3 display the ability of the two networks to predict from one to six hours into the future, from each hour of the day. Each error point is the average error for the forecasts based on 30 days' worth of data. Figure 2 shows the errors obtained from the test data set, and for comparison Figure 3 shows the errors associated with the training data. Note how the test data set has nearly identical errors to the training data indicating that the performance of the network is as good on the test set as it is on the training data. The peak centered around hour 9, seen in the error curves of all the predictions longer than two hours into the future has a useful interpretaion. It results from the increased uncertainty of predicting the peak ozone value which occurs diurnally around hour 14 at Newhall. Logically, each hour further into the future has increased

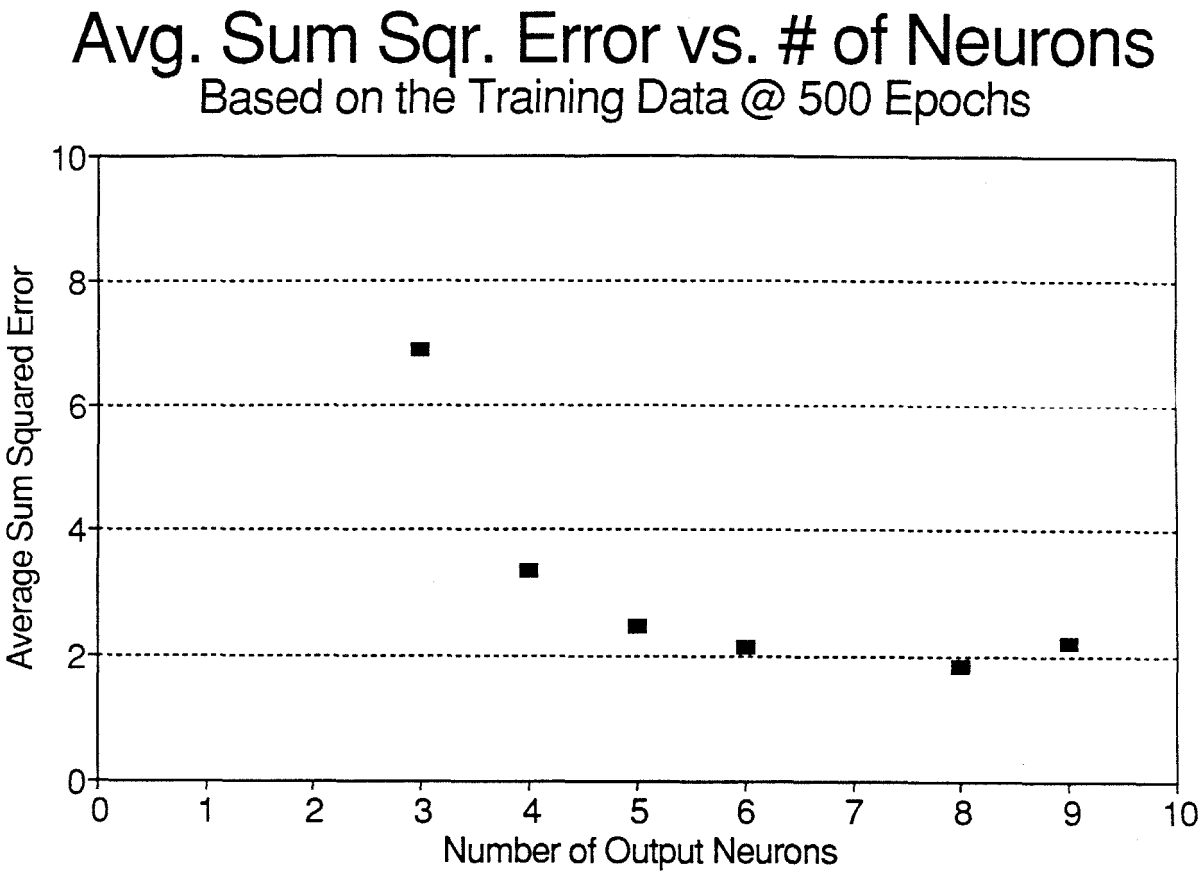

Figure 1. Average sum square error versus the number of neurons.

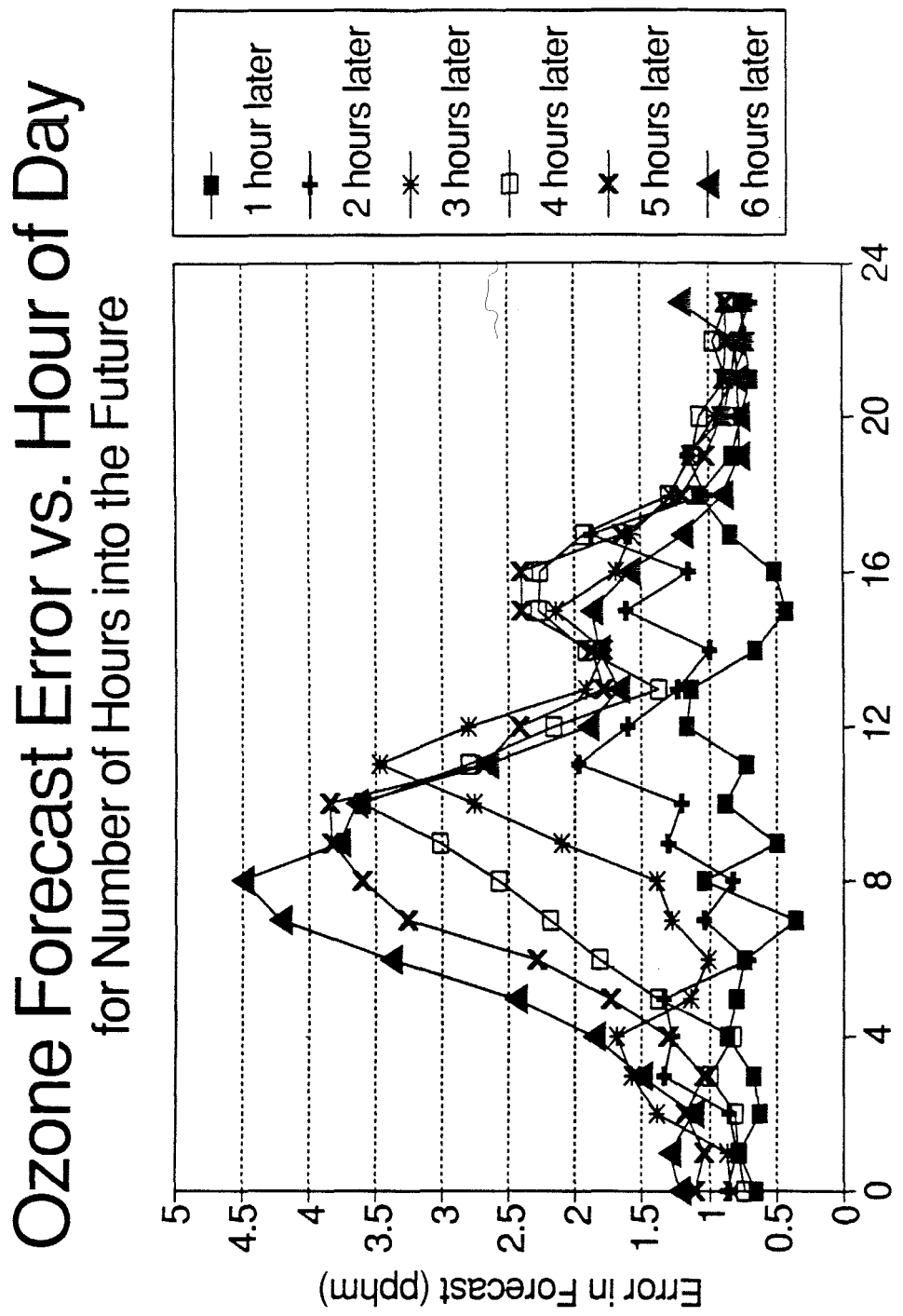

Figure 2. Test data: ozone forecast error versus the hour of the day.

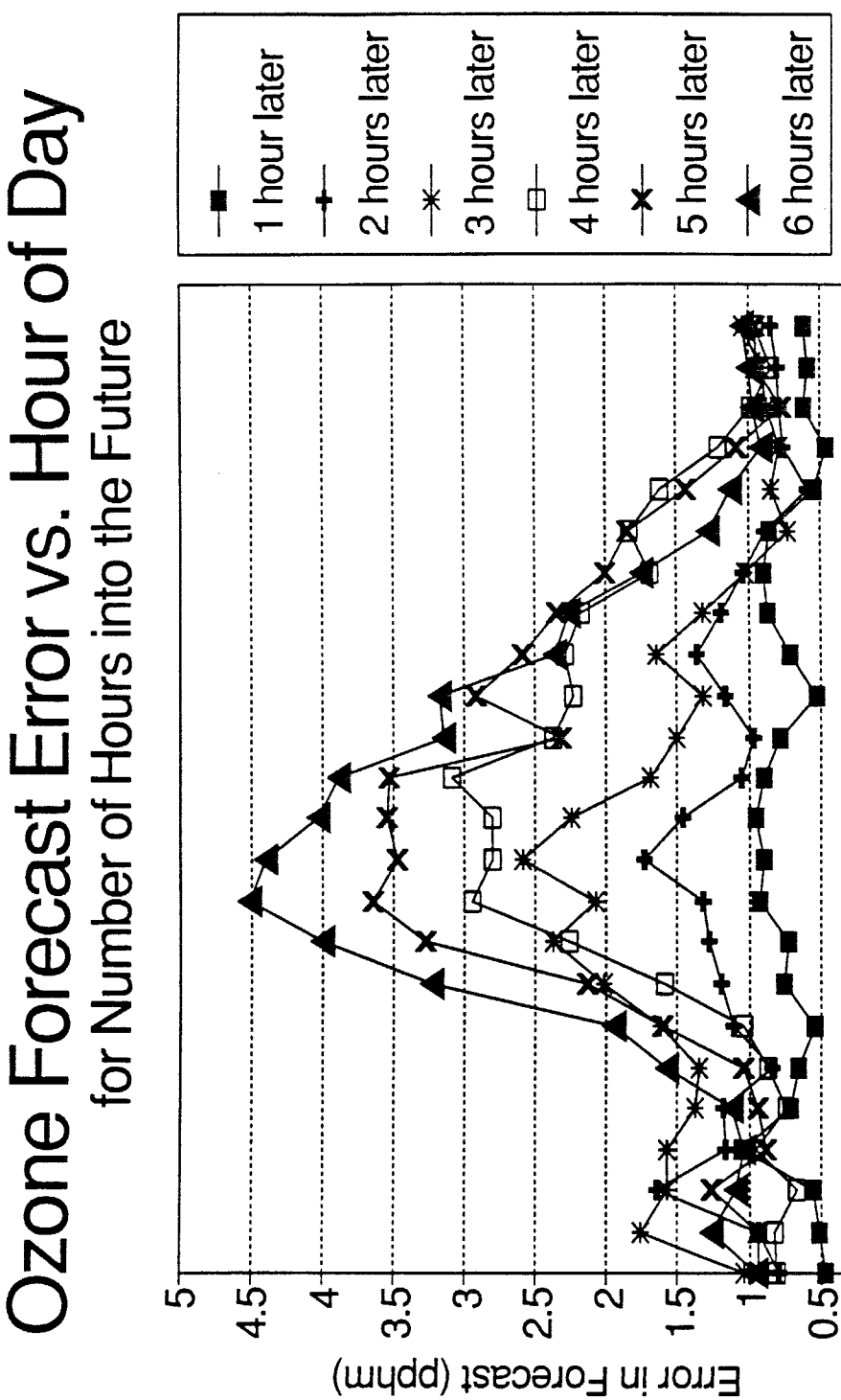

Figure 3. Training data: ozone forecast error versus the hour of the day.

uncertainty in the prediction, and that is the trend borne out in Figures 2 and 3.

Figure 4 shows the comparison of the actual versus the predicted value for a forecast three hours into the future. The network is clearly capable of following the true trajectory of the ozone in time very accurately. The correlation coefficient of the forecast to the observed value is 0.82 with a standard deviation of 2.2 for Figure 4. The performance of the network decays steadily to a correlation coefficient of 0.46 and a standard deviation of 6.1 for a six hour prediction. Figure 5 shows the output from the network for the longer predictions, four, five, and six hours into the future. Besides showing a time series of the networks longer term predictions it demonstrates the oscillating behavior which the network may be subject to on start-up. After approximately one day's worth of data the network settles into the desired forecasting mode. The possibility of a start-up instability is present when the network contains recurrent connections. In this case, predictions are not valid for approximately one day's worth of data.

The outputs of neurons four, five, and six (ie. the hidden units) as a function of time are shown in Figure 6. This figure provides some insight as to how the recurrent network is storing state information and using this information to make predictions. Notice that each hidden unit's output is an oscillator, each with a different amplitude, and phase. Though the mechanism is not completely understood, it appears that the input affects the amplitude of each of these outputs, and then collectively these three hidden outputs are combined to make the prediction. Thus it appears that the state of the network is maintained by three oscillators. The strong feedback coupling is observed during the start-up of the network which makes predictions farther into the future. This is reasonable since such a network may be predicting the future decline in the ozone level while it is experiencing an increase in the level at its input (see Figure 5).

The novelty of this approach makes it hard to compare to other methods

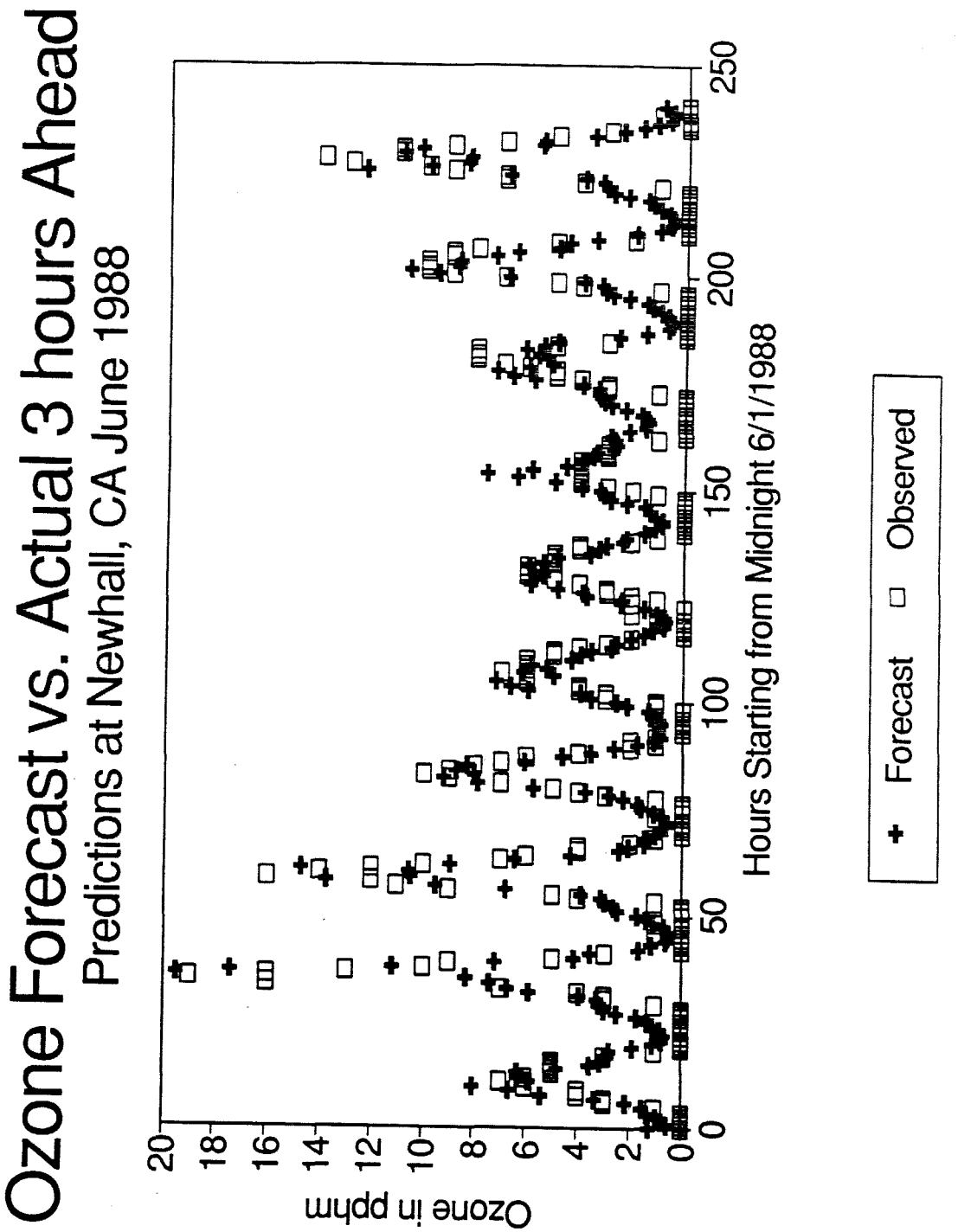

Figure 4. Ozone forecast versus the actual observed level three hours ahead.

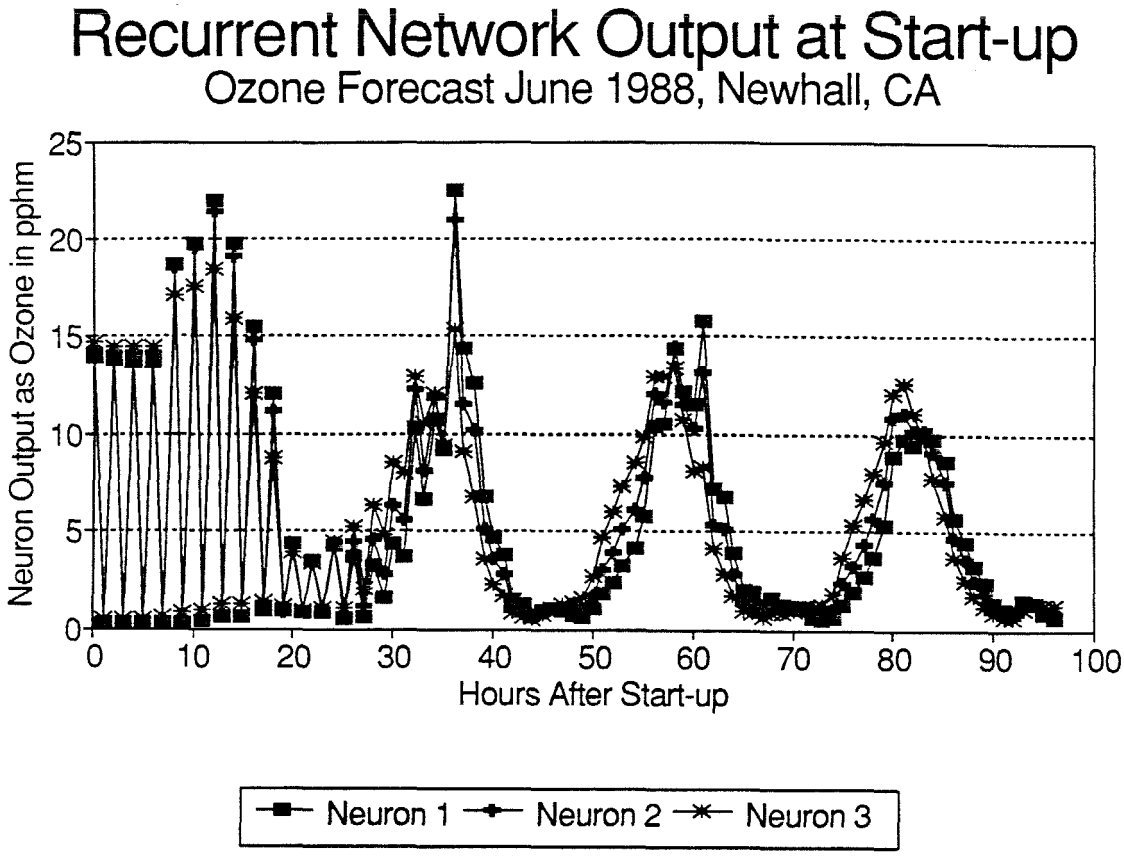

Figure 5. Recurrent network output at start-up for predictions four, five, and six hours into the future.

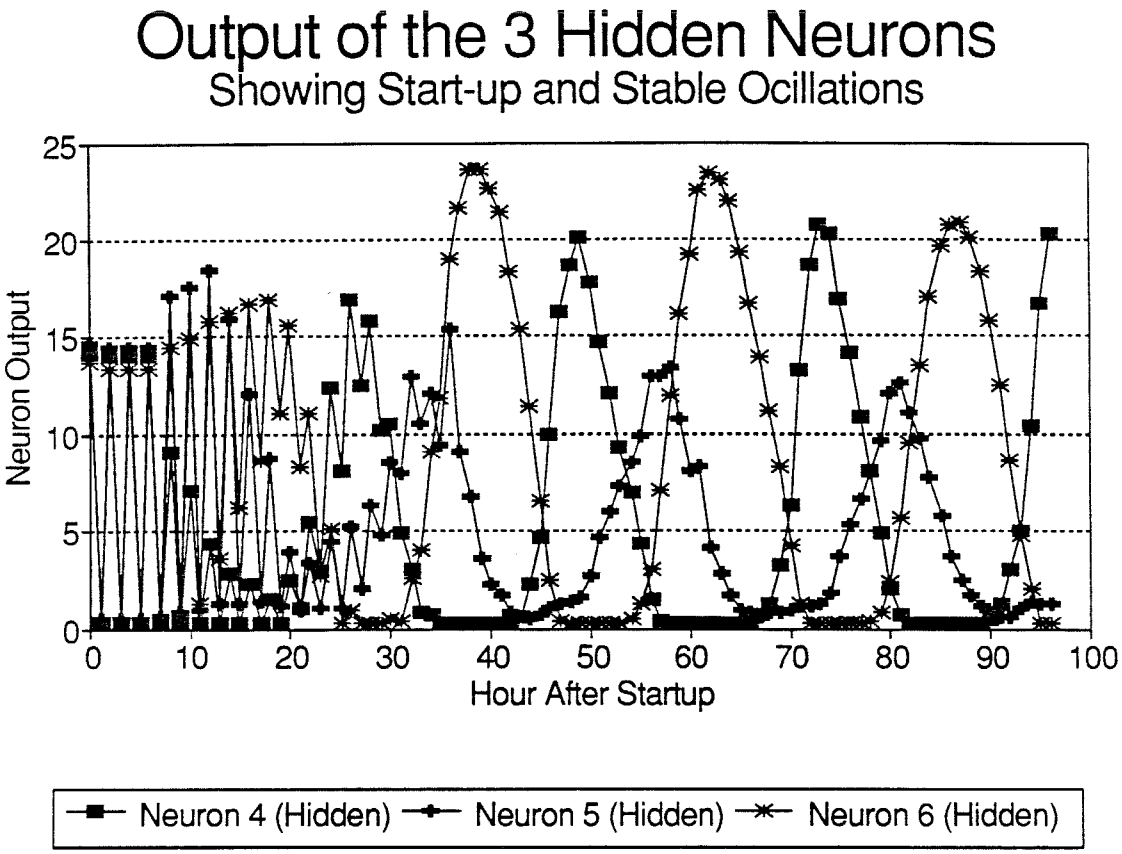

Figure 6. Output of the three hidden neurons as a function of time when predicting four, five, and six hours into the future.

such as the statistical forecast models for daily maximum ozone concentration (Robeson, 1990), though it is clear that this method can be generalized to do this type of forecasting. In lieu of a direct comparison two comparisons were constructed. (1) A linear regression was done using the value of ozone at hour nine to forecast from one to five hours into the future. (2) The 30 day average value was computed from the training set and used as a guess. Hour nine was chosen because the network produced the largest errors a this time when forecasting into the future. The relatively large error suggests that this is the most difficult time from which to forecast, and might be a weak point for the network. The resulting comparison of the methods is made in Figure 7. The neural network systematically had a lower error than either of the other two approaches. It should be noted that the standard deviation of all three methods was sufficiently large so as to prevent the three methods from being statistically distinguished from one another.

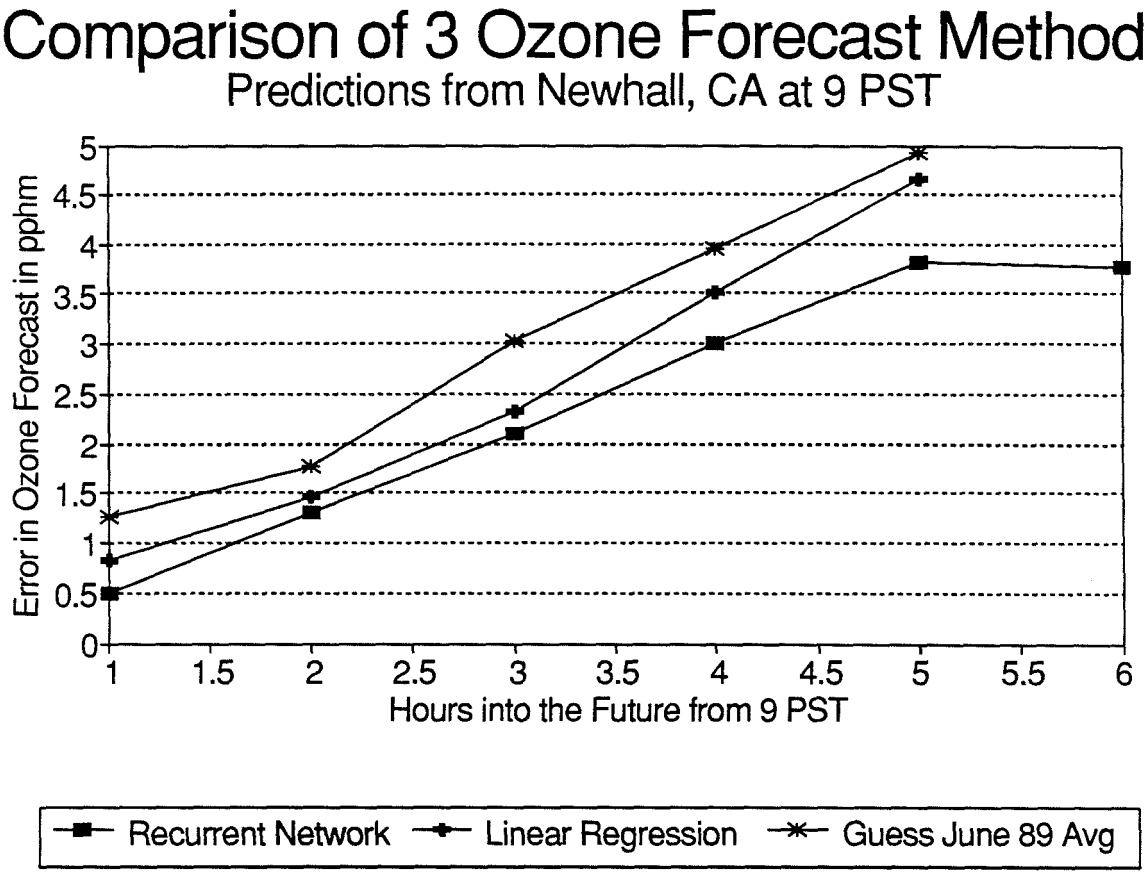

Figure 7. Comparison of three ozone forecast methods: (1) Recurrent network, (2)Linear regression, and (3) Seasonal Average.

Conclusions

Neural networks were capable of being configured and trained for the two classes of problems discussed. In both cases the network's performance was adequate for the task being performed, though direct comparisons with other methods were lacking as a definitive yardstick for comparison. Though it was not elaborated on, neuro-computing is the only method known to this author where the prediction or reconstruction made by the network can also include a measure of the networks confidence in its result.

The techniques employed can be extended to more complex cases with more diverse input sets. For instance, the temperature dependence, wind speed, atmospheric mixing depth, and ozone levels at other locations can all serve as inputs to either the data reconstruction or forecasting network. From the previous discussion it is also clear how networks might be trained to generate wind field forecasts at least several hours into the future. Such a tool might be useful to meteorologists and AQ specialists.

Acknowledgements

I would like to thank Bernard Widrow of the Department of Electrical Engineering at Stanford University for time spent in several discussions on adaptive learning as it pertains to weather forecasting related to the work of his former student Michael Hu. I would also like to thank Dr. John Hopfield, and Ron Benson for helpful suggestions and criticisms in conducting this research and preparing this document. I would also like to thank Rod Brittner of NeuroDynamX Inc. for the unrestricted use of the DynaMind 1.0 simulator for the purpose of conducting research, and Mark Holler of Intel Corporation for discussions on hardware implementation.

I would also like to thank the South Coast Air Quality Management District for access to ozone data, and the helpful suggestions of their senior meteorologist Joe Cassmassi in conducting this research.

References

1. Andes D. (1989), MRIII: A Robust Algorithm for Training Analog Neural Networks, pp. 533-536.
2. Baldi P. and Hornik K. (1989), Neural Networks and Principal Component Analysis: Learning From Examples without Local Minima, Neural Networks **II**, pp. 53-58.
3. Benson R. G. Horrell R. S. and Brittner R. (1989), "Word Recognition from a Stream of Characters," Intel Technical Project Summary.
4. Fang Y. and Sejnowski T. J. (1990), Faster Learning for Dynamic Recurrent Backpropagation, Neural Computation **2**, pp. 270-273.
5. Fozzard R. Bradshaw G. and Ceci L. (1988), A Connectionist Expert System that Actually Works, Neural Information Processing Systems **I**, pp. 248-255.
6. Lapedes A. and Farber R. (1987), How Neural Nets Work, Proceedings of IEEE, Denver Conference on Neural Nets.
7. Hopfield(1982), Neural Networks and Physical Systems with Emergent Collective Computational Abilities, Proceedings of the National Academy of Science **79**, pp. 2554-2558.
8. Holler M. Tam S. Castro H. and Benson R. (1989), An Electrically Trainable Artificial Neural Network (ETANN) with 10240 "Floating Gate" Synapses, IJCNN **II**, pp.191-196.
9. Hu M. J. C. (1964), Application of the Adaline System to Weather Forecasting, Technical Report No. 6775-1.
10. Kamijo K. and Tanigawa T. (1990), Stock Price Pattern Recognition - A Recurrent Neural Network Approach, IJCNN **I.**, pp. 215-221.
11. Pearlmutter B. A. (1989), Learning State Space Trajectories in Recurrent Neural Networks, Neural Computation **1**, pp. 263-269.
12. Pineda F. J. (1989), Recurrent Backpropogation and the Dynamical Approach to Adaptive Neural Computation, Neural Computation **1**, pp 161-172.
13. Robeson S. M. and Steyn D. G. (1990), Evaluation and Comparison of Statistical Forecast Models for Daily Maximum Ozone Concentrations, Atmos. Env. **24b** 2, pp. 303-312.
14. Rumelhart D. E. McClelland J. L. and the PPDP Research Group (1986), Parallel Distributed Processing: Explorations in the Microstructure of Cognition, Vol 1 Foundations.
15. Smotroff I. G. Howells T. P. and Lehar S. (1990), Meteorological Classification of Satellite Imagery Using Neural Network Data Fusion, IJCNN **II**, pp. 23-28.

16. Widrow B. Winter R. G. and Baxter R. A. (1988), Layered Neural Nets for Pattern Recognition, IEEE Transactions on Acoustics, Speech, and Signal Processing, **36** 7, pp. 1109-1118.

17. Williams R. J. and Zipser D. (1989), A Learning Algorithm for Continually Running Fully Recurrent Neural Networks, Neural Computation **1**, pp. 270-280.

18. Zannetti P. (1989), Can We Continue to Apply Dispersion Models Without a Proper Linkage with Meteorlogical Models?, Air and Waste Management Association Annual Meeting paper 89-43.1.